



universität
wien

MASTERARBEIT

Titel der Masterarbeit

NET-PET: Novel Radiotracers for the Norepinephrine
Transporter and Metabolic Considerations

verfasst von

Nadine Eberherr, BSc

angestrebter akademischer Grad

Master of Science (MSc)

Wien, 2015

Studienkennzahl lt. Studienblatt: A 066 862

Studienrichtung lt. Studienblatt: Masterstudium Chemie

Betreut von: Assoc.-Prof. Dr. Wolfgang Wadsak

Acknowledgements

First of all, I want to thank Ao. Univ.-Prof. Dr. Wolfgang Wadsak for the opportunity to accomplish this thesis in his working group. I'm sincerely grateful for the very interesting and widespread topic in this field of medicinal chemistry.

In particular, I would like to thank Dr. Christina Rami-Mark for her proficient support during the whole thesis, especially the practical work. Her permanent enthusiasm and her expertise in the field of radiochemistry was very inspiring and made it a pleasure to work with her and learn from her.

Moreover, I want to express sincere thanks to the whole working group for the readiness to help in every respect.

I am very grateful for the support of the Department of Drug and Natural Product Synthesis, Faculty of Life Sciences, University of Vienna. I would like to thank Ao. Univ.-Prof. Dr. Helmut Spreitzer for the possibility to work in his synthesis lab. Special thanks go to Dr. Catharina Neudorfer for the measurement of 1D NMR spectra and Ao. Univ.-Prof. Dr. Wolfgang Holzer for the measurement and interpretation of some 2D NMR spectra.

Furthermore, I want to thank Dipl. Ing. Alexander Roller for the measurement and refinement of crystal structures.

Finally, I wish to express my gratitude to all my friends for supporting me during the last years.

Last but most important I want to thank my family, especially my parents, for their support in every possible way during my whole life.

*“The important thing in science is not so much to
obtain new facts as to discover new ways of
thinking about them.”*

(William Lawrence Bragg)

To my parents

ABSTRACT

The norepinephrine transporter (NET) is relevant for important physiological and pathophysiological functions of the brain. Dysregulation of NET expression in various brain regions is assumed to be involved in diseases such as depression, schizophrenia, attention deficit hyperactivity disorder (ADHD) and Alzheimer's disease. In this context, it is of high interest to quantify the changes in NET density in healthy and treated individuals to provide information about the course of a disease and therapeutic outcome on a molecular basis. [^{18}F]FMeNER-D2, a derivative of the antidepressant reboxetine, has shown best results as a molecular biomarker of the reuptake transporter of noradrenaline when using positron emission tomography (PET) as the diagnostic method. However, its application faces limitations due to unspecific binding in neighboring regions of the brain, which impedes a correct quantification of the NET signal in defined brain areas. This background signal in PET images is presumed to be caused by radioactive metabolites of [^{18}F]FMeNER-D2 or the intact tracer itself via binding to the skull bone or adjacent tissues.

The aim of the thesis was to compare [^{18}F]FMeNER-D2 with other PET tracers concerning its bone affinity before the implementation of *in vitro* metabolic stability tests. These studies ought to give information about the localization of [^{18}F]FMeNER-D2 metabolism using monoamine oxidase A (MAO A), MAO B and catechol-*O*-methyltransferase (COMT) as primarily centrally occurring enzymes, and human liver microsomes (HLM), rat liver microsomes (RLM) and seven human cytochrome P450 single enzymes (hCYP450) to mimic hepatic metabolism *in vivo*. Stability of our radioactive tracer against mammalian esterases was tested using three different isozymes of human carboxylesterase (hCES) and porcine carboxyl esterase. To identify the responsible CYP450 isoforms, inhibition experiments in HLM and RLM were carried out using CYP450 selective chemical inhibitors. The detection and identification of radiometabolites was achieved using reversed-phase high performance liquid chromatography (RP-HPLC) with radiodetection.

Since reboxetine-derived analogues such as [^{18}F]FMeNER-D2 exhibit limitations in their applicability as NET-PET tracers in terms of metabolic stability, complex radiosynthesis and specific binding, there is still need for further investigation of different ligands for this important monoamine transporter. One of these promising candidates is [^{11}C]Me@APPI, which already underwent full *in vitro* evaluation. Computational "*in silico*" studies of fluoro-substituted structural analogues of methylated APPI indicate even higher affinity towards NET. In the second section of the thesis, two novel PET precursors possessing a benzo[*d*]imidazole core structure, namely FAPPI1:0 and FAPPI3:0, were synthesized and characterized. Beyond that, optimum conditions for small-scale radiolabeling of both substances as a basis for up-scaling experiments were found and a suitable purification method for the crude tracer was evaluated.

In vitro tests revealed that only minor increase in binding of [^{18}F]FMeNER-D2 to hydroxyapatite or human bone material (diaphysis) compared to clinically applied PET-tracers can be observed. Incubation experiments showed degradation via human CYP2D6, CYP2C19 and CYP3A4, whereas CYP1A2 might as well be responsible for reduced stability of [^{18}F]FMeNER-D2 against human enzymes *in vitro*. Intense signals in cranial bone cannot be explained via enzymatic defluorination, as no free [^{18}F]fluoride was detected in any experiment. Comparison of the RP-HPLC retention

times of the emerging polar radiometabolites with those of the labeling progenitor [^{18}F]bromofluoromethane does not indicate partial *O*-demethylation of our tracer *in vitro*. In summary, these results constitute the basis for further *in vivo* investigations of [^{18}F]FMeNER-D2 metabolism to finally enable an interference in tracer degradation, facilitating the evaluation of NET-PET images.

Beyond that, the novel precursors FAPPI1:0 and FAPPI3:0 were successfully prepared in a 4- and 7-step synthesis, respectively. Successful preparation of FAPPI1:0 was achieved starting from 1-phenyl-1*H*-benzo[*d*]imidazole-2(3*H*)-one in an overall yield of 12.6%. FAPPI3:0 was obtained using 2-fluoroaniline and 1-fluoro-2-nitrobenzene as starting materials giving the precursor in 2.0% overall yield. Radiochemical labeling gave the final tracers [^{11}C]Me@FAPPI1 and [^{11}C]Me@FAPPI3 in high radiochemical yields, while an optimum setup for purification has yet to be found.

Zusammenfassung

Der Norepinephrin-Transporter (NET) besitzt eine Schlüsselrolle in der Aufrechterhaltung physiologischer Prozesse im gesamten Körper und wird mit wichtigen pathophysiologischen Zuständen des Gehirns in Zusammenhang gebracht. Es gibt Hinweise darauf, dass eine Fehlregulation der Expression dieses Transporters in verschiedenen Gehirnregionen bei Krankheiten wie Depression, Schizophrenie, Aufmerksamkeitsdefizit-/Hyperaktivitätsstörung (ADHS) und Alzheimer vorliegt. In diesem Zusammenhang besteht starkes Interesse daran, die Veränderungen der Transporterdichten im Gehirn quantifizieren zu können, um Informationen über den jeweiligen Krankheitsverlauf und ein Therapieansprechen auf molekularer Basis zu erhalten. Unter Verwendung von Positronenemissionstomographie (PET) als nichtinvasive, diagnostische Methode der Wahl, konnten bereits durch den Einsatz des radioaktiven Tracers [¹⁸F]FMeNER-D2, einem Derivat des Antidepressivums Reboxetin, sehr gute Resultate bezüglich der Visualisierung des Wiederaufnahmetransporters NET erzielt werden. Seine Anwendung erlaubt jedoch momentan keine Quantifizierung des Transporters in allen Gehirnarealen, da es aufgrund eines bis dato unbekanntes Mechanismus zu einer unspezifischen Anreicherung von Radioaktivität in gehirnnahen Regionen kommt, wodurch ein störendes Hintergrundsignal vorliegt. Es wird angenommen, dass dieses Störsignal durch die Bindung des intakten Tracers oder seiner radioaktiven Metaboliten an Schädelknochen oder angrenzende Gewebe hervorgerufen wird.

Das primäre Ziel der Arbeit war es, Stabilitätstests von [¹⁸F]FMeNER-D2 *in vitro* durchzuführen, um Aussagen über den Metabolismus *in vivo* treffen zu können. Im Voraus sollte dabei die Bindungsaffinität des Tracers an Knochen mit anderen klinisch relevanten PET-Tracern sowie einigen Forschungstracern verglichen werden. Anhand von Inkubationsuntersuchungen mit zentral vorkommenden Enzymen wie Monoaminoxidase A und B (MAO A /B) und Catechol-O-methyltransferase (COMT), sowie mit in erster Linie hepatischen Multienzymkomplexen von Mensch (HLM) bzw. Ratte (RLM) und sieben humanen Cytochrom-P450 Einzelenzymen soll der Tracer-Abbau *in vivo* nachgeahmt werden. Die Stabilität gegenüber Esterasen wurde mittels 3 unterschiedlicher Isoenzyme der humanen Carboxylesterase (hCES) und Schweineleberesterase (CE porcine) überprüft. Inhibitionsassays mit chemischen Inhibitoren von humanen CYP450 Isoformen in HLM- und RLM-Inkubationen sollen der Identifizierung von für den Abbau verantwortlichen CYP450-Enzymen dienen.

Da die Anwendbarkeit von [¹⁸F]FMeNER-D2 und die Aussagekraft von erhaltenen PET-Scans aufgrund seiner geringen Stabilität, begrenzter spezifischer Bindung und komplexer Radiosynthese eingeschränkt wird, ist die Erforschung neuer Liganden für diesen Monoamintransporter von großer Wichtigkeit. Hierbei repräsentiert [¹¹C]Me@APPI einen vielversprechenden Kandidaten der bereits *in-vitro* evaluiert wurde und vergleichbare Ergebnisse bezüglich Selektivität sowie erhöhte Stabilität aufweist. Computergestützte „*in-silico*“ Analysen führten zu der Annahme, dass fluor-substituierte Strukturanaloga von Me@APPI eine darüber hinaus erhöhte Affinität gegenüber den NET zeigen sollen. Der zweite Teil der Arbeit widmet sich daher der Synthese und Charakterisierung von zwei neuen NET-PET Vorstufen mit einer Benzo[d]imidazol-Grundstruktur, FAPPI1:0 und FAPPI3:0. Außerdem sollen in Vorversuchen die

optimalen Bedingungen für die radioaktive Markierung als Basis für up-scaling Experimente gefunden werden und eine geeignete Trennmethode für das radioaktive Rohprodukt aufgestellt werden.

In-vitro Untersuchungen haben gezeigt, dass nur eine geringfügig erhöhte Bindung von [¹⁸F]FMeNER-D2 an Hydroxylapatit bzw. an humanes Knochenmaterial im Vergleich zu klinisch angewandten PET-Tracern stattfindet. Enzyminkubationen und Inhibitionstests haben ergeben, dass [¹⁸F]FMeNER-D2 dem Abbau durch die menschlichen Cytochrom-P450-Isoenzyme CYP2D6, CYP2C19 und CYP3A4 unterliegt, wobei darüber hinaus CYP1A2 eine reduzierte Stabilität bewirken könnte. Die durch PET-Bilder angedeutete starke Anreicherung im Schädelknochen kann nicht durch enzymatische Defluorierung erklärt werden, da in keinem der Experimente freies [¹⁸F]Fluorid nachgewiesen werden konnte. Ein Vergleich der Retentionszeiten der entstandenen radioaktiven Metaboliten aus HPLC-Messungen mit jener von [¹⁸F]Bromfluormethan macht die partielle *O*-Demethylierung des Tracers *in-vitro* unwahrscheinlich. Schlussendlich sollen die erbrachten Ergebnisse als Basis für Metabolismustudien *in-vivo* dienen, um Möglichkeiten zu finden, in die Biotransformation des NET-Liganden eingreifen zu können, was letztlich zu einer aufschlussreicheren Evaluierung von NET-PET Bildern führen soll.

Des Weiteren ist es gelungen zwei neue Vorstufen von potentiellen NET-Tracern, FAPPI1:0 und FAPPI3:0 in einer 4-stufigen bzw. 7-stufigen Synthese, herzustellen. Ausgehend von 1-Phenyl-1*H*-benzo[*d*]imidazol-2(3*H*)-on wurde FAPPI1:0 in einer Ausbeute von 12.6% erhalten. FAPPI:3 konnte im Zuge einer längeren Synthese anhand der Ausgangssubstanzen 2-Fluoranilin und 1-Fluor-2-nitrobenzol in einer Gesamtausbeute um 2% synthetisiert werden. Die radiochemische Markierung mittels [¹¹C]Methyltriflat lieferte die beiden Tracer in exzellenter radiochemischer Ausbeute, wobei letztlich noch die optimalen Bedingungen für eine chromatographische Trennung mittels semi-präparativer HPLC gefunden werden müssen.

Table of contents

ACKNOWLEDGEMENTS

ABSTRACT

ZUSAMMENFASSUNG

1	INTRODUCTION	1
1.1	RADIOACTIVE DECAY AS A PREREQUISITE FOR NUCLEAR IMAGING	1
1.1.1	<i>Decay modes</i>	1
1.2	PRODUCTION OF RADIOACTIVE ISOTOPES	3
1.2.1	<i>Cyclotron</i>	3
1.2.2	<i>Nuclear reactor</i>	4
1.2.3	<i>Generator</i>	5
1.3	POSITRON EMISSION TOMOGRAPHY (PET)	6
1.4	NOREPINEPHRINE (NE) AND NOREPINEPHRINE TRANSPORTER (NET)	7
1.4.1	<i>Tracers for NET</i>	10
1.4.2	<i>Function of NET in various diseases</i>	11
1.5	BIOTRANSFORMATION OF XENOBIOTICS.....	12
1.5.1	<i>Peripheral biotransformation</i>	12
1.5.2	<i>Central biotransformation</i>	16
1.6	<i>IN VITRO</i> METABOLISM STUDIES.....	18
1.6.1	<i>Microsomal preparations</i>	18
1.6.2	<i>Inhibition assays in Human Liver Microsomes (HLM)</i>	19
1.6.3	<i>Biotransformation in rats and chemical inhibitors for RLM</i>	23
1.7	AIM OF THE THESIS	25
2	EXPERIMENTAL PART I – METABOLISM STUDIES	27
2.1	MATERIALS	27
2.2	INSTRUMENTATION	28
2.3	METHODS	29
2.3.1	<i>Synthesis of [¹⁸F]FMeNER-D2</i>	29
2.3.2	<i>Enzyme assays</i>	33
2.3.3	<i>Bone binding studies</i>	41
3	RESULTS AND DISCUSSION I	43
3.1	SYNTHESIS OF [¹⁸ F]FMeNER-D2	43
3.2	RESULTS OF METABOLISM STUDIES.....	47
3.2.1	<i>Stability tests in HLM</i>	47
3.2.2	<i>Stability tests in RLM</i>	49
3.2.3	<i>Chemical inhibition experiments</i>	53
3.2.4	<i>Incubation of [¹⁸F]-FMeNER-D2 with recombinant human CYP450s</i>	64
3.2.5	<i>Incubation of [¹⁸F]-FMeNER-D2 with centrally occurring enzymes</i>	70
3.2.6	<i>Bone binding experiments</i>	70
4	EXPERIMENTAL PART II – SYNTHESIS OF NOVEL NET-PET TRACERS	73
4.1	GENERAL WORKING METHODS.....	73
4.1.1	<i>Characterization of precursors</i>	73
4.1.2	<i>Instrumentation for radiochemical labeling</i>	73
4.1.3	<i>Materials</i>	74

4.2	PRECURSOR CHEMISTRY – EXPERIMENTAL PROCEDURES	74
4.2.1	<i>FAPPI3:0</i>	76
4.2.2	<i>FAPPI1:0</i>	85
4.3	METHODS FOR RADIOCHEMICAL LABELING	91
4.3.1	<i>Preparations of the hot cell</i>	91
4.3.2	<i>Production of [¹¹C]CH₃I and [¹¹C]CH₃OTf</i>	91
4.3.3	<i>Small-scale reactions</i>	93
4.3.4	<i>Automation of radiosynthesis</i>	93
5	RESULTS AND DISCUSSION II	95
5.1	SYNTHESIS OF PRECURSORS	95
5.2	RESULTS OF <i>N</i> -[¹¹ C] METHYLATION OF FAPPI1:0 AND FAPPI3:0	97
5.2.1	<i>Small scale reactions</i>	97
5.2.2	<i>Full automation of radiosyntheses</i>	98
6	CONCLUSION	103
6.1	METABOLIC CONSIDERATIONS OF [¹⁸ F]FMENER-D2.....	103
6.2	SYNTHESIS OF NOVEL FLUORO-SUBSTITUTED NET-PET TRACERS.....	104
7	OUTLOOK	105
7.1	FURTHER <i>IN VITRO</i> AND <i>IN VIVO</i> TESTS OF [¹⁸ F]FMENER-D2	105
7.2	FUTURE OF ME@FAPPI DERIVATIVES.....	106
8	REFERENCES	107
9	APPENDIX.....	114
9.1	SUPPLEMENTARY DATA.....	114
9.1.1	<i>Detailed information about batch mixtures for chemical inhibition experiments</i>	114
9.1.2	<i>SPSS analyses</i>	117
9.1.3	<i>Analytical HPLC – chromatogram: Crude [¹⁸F]FMeNER-D2</i>	118
9.1.4	<i>Complete data table for metabolism experiments</i>	118
9.1.5	<i>Data tables for chemical inhibition experiments in RLM</i>	121
9.1.6	<i>Complete data for bone binding experiments</i>	123
9.1.7	<i>NMR spectra of novel compounds</i>	125
9.1.8	<i>El-MS spectra</i>	128
9.1.9	<i>Crystallographic data of 1-(1-(4-Fluorophenyl)-3-iodopropyl)-3-phenyl-1,3-dihydro-2H-benzo[d]imidazol-2-one</i>	129
9.2	LIST OF ABBREVIATIONS	130
9.3	LIST OF TABLES.....	131
9.4	LIST OF FIGURES	133
9.5	CURRICULUM VITAE	136

1 INTRODUCTION

The role of nuclear medicine in treatment and diagnostics is undeniable when looking at the constantly growing numbers of positron emission tomography (PET) and single photon emission computed tomography (SPECT) scans in clinical routine. The reason for this rising trend since the first intravenous injection of a radioactive sodium ^{24}Na for the treatment of leukemia in 1936 is that it presents a valuable tool for functional molecular imaging of organs in various fields like oncology, cardiology and neurology.^[1] By then, physicians were only able to gain structural information about parts of the body via methods like x-ray or computed tomography (CT) using electromagnetic waves. Since the development of PET and SPECT as the diagnostic subdivisions of nuclear medicine as well as functional MRT (fMRT) as a distinct radiological technique, detailed information about functional processes such as organ perfusion and metabolic activity can be gained in a non-invasive way. Nuclear medicine uses selective radioactive compounds and measures their distribution and accumulation *in vivo*. Fortunately, PET and SPECT represent very sensitive methods allowing the application of smallest quantities of these radioactive substances in the picomolar and nanomolar range.^[2] Nonetheless, the application of ionizing radiation and the concomitant stochastic risk has to be weighed carefully against its benefits. When used for the approved medical indications, this imaging technique allows a better understanding of the pathophysiology of diseases, helps us monitor treatment effects and assures medical diagnoses.

1.1 Radioactive decay as a prerequisite for nuclear imaging

The process of radioactivity describes the emission of corpuscular or electromagnetic radiation from instable nuclei and therefore, only refers to nuclear transformations. An important requirement for radioactive decay is an excess of either protons or neutrons, both of which cohere by nuclear binding energies in order to form the atomic nucleus. The binding energy conserves the part of mass, which is lost when unbound constituents form a bound entity. This interchangeability of matter and energy enables a release of parts of the nuclear binding energy upon nuclear decay. It should be noted, that not every type of decay leads to a change in the number of neutrons or protons as shown by isomeric transition (IT) and internal conversion (IC).^[3] The following chapter should give a brief outline of potential decay modes, some of them being important for nuclear medical diagnostics and therapy.^[4, 5]

1.1.1 Decay modes

1.1.1.1 Fission processes

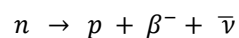
Fission can only occur for heavy, neutron-rich nuclei (atomic number ≥ 90), which can decay spontaneously (natural radioactivity) or under bombardment with particles (artificial radioactivity). Fission products are two fragments with nearly the same mass, two or three neutrons and thermal energy. Some naturally unstable nuclides used for fission processes are for example ^{235}U and ^{238}U (also see chapter 1.2.2).^[4]

1.1.1.2 α – decay

The alpha particle is equivalent to a helium nucleus consisting of two protons and two neutrons. The particles emitted by heavy, α -emitting nuclides are always monoenergetic. Due to their mass and their (positive) electric charge they can be easily absorbed by surrounding matter. The high ionization potential and the high absorption of α -particles in matter can be used for the destruction of tumor tissue in targeted radiation therapy.^[6]

1.1.1.3 β^- – decay

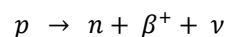
Neutron rich nuclei decay by β^- -emission. There results a difference between the decay energy, which is the energy difference between daughter and parent nuclide, and the particular beta energy, which can be variable. This remaining energy difference is released in form of an antineutrino $\bar{\nu}$.



Very characteristic for β^- decay is the production of *bremsstrahlung* when the particle interacts with the surroundings and loses kinetic energy. This excess energy is continuously converted into photons, and corresponds to the generation of x-rays for e.g. x-ray examinations and CT.^[4, 5]

1.1.1.4 β^+ – decay

Neutron deficient nuclei can decay by β^+ -emission to elevate the proportion of neutrons to protons. As for β^- , positrons (β^+) can also have various energies and, thus, a neutrino ν is emitted simultaneously.

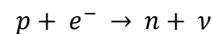


The consequence of the decrease in atomic number by one unit is that, at the same time, the electron shell has to unleash an electron. It can therefore be concluded, that the daughter nuclide has lost at least two times the mass of an electron, which equals twice 511 keV. Thus, the transition energy of this process accounts for at least 1.022 MeV. The lifetime of the ejected positrons is very short, as they represent the antimatter of electrons. They combine with electrons within microseconds forming the so-called positronium which annihilates into two photons of exact 511 keV, which are emitted in opposite directions at an angle of 180 degrees.^[7] Several positron emitters are used in nuclear medicine for diagnostic purposes, e.g. fluorine-18 or carbon-11.

1.1.1.5 Electron Capture (EC)

The competing reaction for proton-rich nuclides is electron capture (EC), where electrons from inner electron shells, mostly K- and L-shells, are captured by protons of the nucleus.^[4, 5] EC as well as β^+ decay can occur in radionuclides with transition energies exceeding 1.022 MeV. Lower energy differences between mother and daughter isotope are not sufficient for the formation of a positron and hence, only EC will occur. In these cases, the K-shell electron can be captured, if the transition energy amounts to at least K-shell binding energy. Otherwise, L-shell electrons are

captured. This nuclear transformation goes along with the production of a neutron and a neutrino according to the following nuclear reaction:



Thereby, the neutrino receives the whole amount of transition energy unless a daughter nuclide in some excited state is produced, where part of the energy is carried off by the γ -ray.^[4, 5]

1.1.1.6 Isomeric Transition (IT)

Isomeric Transition (IT) is the nuclide process for the application of ^{99m}Tc representing the most important radioactive tracer for diagnostic imaging, which is employed in more than 80% of all nuclear medical investigations.^[8] It occurs when an excited nucleus changes into ground state and emits surplus energy by emission of a gamma ray. Commonly, excited nuclei arise from radioactive decay processes. Isomeric states that are long lived are denoted by “m”, which means metastable.^[4, 5]

1.1.1.7 Internal Conversion (IC)

If the energy released from an excited nucleus is transferred to inner-shell electrons, this is called internal conversion (IC). It results in the emission of a “conversion electron” and is an alternative way to the direct generation of γ -rays. The daughter nuclide, however, emits a characteristic K-x-ray as an upper shell electron falls into the vacancy of the K-shell.^[4, 5]

1.1.1.8 γ -radiation

Gamma radiation may appear in every decay process mentioned above. The diagnostic fields of nuclear medicine, SPECT and PET, are both based on detection of gamma rays emerging from nuclear transitions. In the cases of EC or IC, energy differences can be transferred to electrons instead of the release of energy via x-rays. The ejected electrons are called *Auger electrons* and this process is again followed by filling of the empty space with electrons from upper shells.^[4, 5]

1.2 Production of radioactive isotopes

All radionuclides for nuclear medicine are produced artificially. In the following, the three sources of radionuclide production, namely, cyclotron, nuclear reactor and generator are outlined.^[4]

1.2.1 Cyclotron

A cyclotron serves for the production of radioactive isotopes via spiral acceleration of either a positively charged beam of protons or negatively charged hydrogen ions. Basically, it consists of two hollow semicircular chambers, the so-called Dees, which are metal electrodes placed in a static magnetic field and a high-frequency electrical field and are kept under high vacuum. The magnetic field forces the particles on their spiral trajectory due to the Lorentz force, while the electric field accelerates the particles due to the rapidly changing potential difference (10^7 times per sec) between the two chambers.

When a proton (or a deuteron) is released from the center between the Dees, it is attracted into the negatively charged Dee. At the time when the proton reaches the gap between the chambers, the charge of the Dees is inverted coinciding with their movement direction, which causes the proton to cross the gap and speed up. Following its trajectory in the second Dee, the radius of its path increases compared to the first Dee due to the particle's higher kinetic energy. This process is repeated until the proton reaches high energies and the aperture to the target on the outer border of the Dees. The resulting proton beam is directed towards the target via deflection plates and the bombardment of the target – i.e. the nuclear reaction – takes place. When a negatively charged hydrogen ion ($^1\text{H}^-$ or $^2\text{H}^-$) reaches this target entry, it passes a carbon foil (“stripping foil”), which strips away the electrons leaving the naked proton (or deuteron, respectively). The advantage of negative-ion machines is that higher beam currents can be generated using the stripping technique. Various target materials in different physical states (solid, liquid, gaseous) may be used depending on the desired secondary (radioactive) particles.^[5] Cyclotron-produced radionuclides usually have a deficiency in neutrons and thus, decay by β^+ emission or electron capture (EC).

It should be further mentioned that the use of cyclotrons in medicine is not restricted to production of radioactive nuclides for nuclear therapy and diagnostics. Another growing sector is particle therapy in the treatment of cancer. In proton therapy, ion beams produced by the cyclotron can be directly applied to the patient to destroy tumor tissue by radiation damage.^[9]

1.2.2 Nuclear reactor

Elements that can undergo fission have atomic numbers greater than 90 and break up into two approximately equal fragments through absorption of thermal neutrons and simultaneous emission of two or three neutrons. The release of new neutrons leads to a chain reaction, which has to be controlled via control rods consisting of boron or cadmium. The capture of neutrons by fissile heavy atoms is possible due to the moderator (e.g. D_2O) which surrounds the fuel rods and reduces the kinetic energy of emitted neutrons. Examples for heavy elements that are used in nuclear reactors include ^{235}U , ^{233}U , ^{239}Pu , ^{237}Np and ^{232}Th . Radionuclides produced via fission are often neutron rich and their preferred decay mode is β^- emission. ^{99}Mo and ^{131}I are important nuclides for nuclear medicine and are byproducts of ^{235}U fission. After chemical separation, the desired nuclides are carrier-free and therefore, high specific activities are possible. ^{99}Mo is used for radionuclide generators for the production of $^{99\text{m}}\text{Tc}$, which is needed for e.g. thyroid scintigraphy while ^{131}I can be applied in the treatment of thyroid cancer due to its longer half-life (8.02 d) and decay mode (β^-). If the production of other radionuclides is the main purpose of the nuclear reactor, stable target material can be inserted into the reactor. Depending on the energy of the neutrons different types of nuclear reactions are possible. The most common type of reaction with low-energy neutrons (thermal) is the (n,γ) -reaction. Thereby, the product is an isotope of the parent nuclide, hampering a chemical separation and resulting in low specific activity since only a small fraction of target atoms is converted (e.g. $^{98}\text{Mo}(n,\gamma)^{99}\text{Mo}$). For this reason, $A(n,\gamma)A^* \rightarrow B$ reactions giving a short-lived intermediate A^* and a longer-lived radionuclide B, induced by thermal neutrons, and $A(n,p)B$ reactions, obtained via fast neutrons, are more favorable. In both cases the chemical separation of target and product nuclides is possible and

high specific activities can be achieved. Another important possible reaction via neutron capture is $^{130}\text{Te}(n, \gamma)^{131}\text{Te}$, which decays to ^{131}I (via β^-).

1.2.3 Generator

Radionuclide generators serve as convenient sources for the production of short-lived radionuclides. As better images can be obtained by administration of large amounts of radioactivity, radiation burden can only be kept low when using nuclides with a short half-life comparable to the scan duration. Generally, a generator must consist of a long-lived parent nuclide that decays to a short-lived progeny whereas the progeny is no isotope of the mother radionuclide. As a result, the generator is able to provide the short-lived daughter, which can be isolated due to different chemical properties. The outstanding benefits of these systems are that, because of their small size and their lifetime, they can be transported and used at facilities far away from their place of production. It is of utmost importance that the separated daughter activity contains only minimal quantities of the parent nuclide owing to the parents' long half-life and the associated radiation dose.^[4, 5] Today, the most important systems in clinical use are the ^{99}Mo - $^{99\text{m}}\text{Tc}$, ^{82}Sr - ^{82}Rb , ^{90}Sr - ^{90}Y and the ^{68}Ge - ^{68}Ga generators (see *Table 1*). These generators consist of columns filled with different materials such as Al_2O_3 , SnO_2 or ion exchange resins, where the parent nuclide is adsorbed and can be eluted using an appropriate eluent (e.g. water and NaCl-, EDTA-, HCl-solutions).

Table 1: Important generators for nuclear medicine.

Nuclear reaction	Parent	Parent $t_{1/2}$ (decay mode)	Daughter	Daughter $t_{1/2}$ (decay mode)	Photon energy [keV]	Application
Fission or $^{98}\text{Mo}(n, \gamma)$	^{99}Mo	66 h (β^-)	$^{99\text{m}}\text{Tc}$	6 h (IT)	140	thyroid scintigraphy
$^{69}\text{Ga}(p, 2n)$	^{68}Ge	271 d (EC)	^{68}Ga	68 min (β^+)	511	diagnostics of neuroendocrine tumors
Fission	^{90}Sr	28.6 a (β^-)	^{90}Y	64.1 h (β^-)	-	therapy of neuroendocrine tumors (e.g. ^{90}Y -DOTATOC)
$^{63}\text{Cu}(p, 2n)$	^{62}Zn	9.3 h (β^+)	^{62}Cu	9.7 min (β^+)	511	^{62}Cu -ATSM ^[10] or PTSM ^[11] for tumor hypoxia and vascular diseases (clinical studies)
$^{79}\text{Br}(\alpha, 2n)$	^{81}Rb	4.6 h (β^+)	$^{81\text{m}}\text{Kr}$	13 s (IT)	190	lung ventilation studies ^[12, 13] (pulmonary embolism) ¹
$^{85}\text{Rb}(p, 4n)$	^{82}Sr	25.5 d (β^+)	^{82}Rb	75 s (β^+)	511	myocardial perfusion imaging ^[14]

¹ Besides $^{88\text{m}}\text{Kr}$, ^{133}Xe or $^{99\text{m}}\text{Tc}$ -DTPA are widely used for lung scintigraphy.

1.3 Positron Emission Tomography (PET)

Positron emission tomography, as mentioned before, is based on decay of proton rich nuclei via emission of positrons. The photons that originate from annihilation of electrons and positrons are emitted in an angle of 180°. Therefore, the pair of emitted photons is travelling along the straight line of coincidence (or line of response (LOR)) and can be detected via scintillation detectors surrounding the patient's body. Photons can only produce a signal if both gamma rays are detected simultaneously within a "coincidence time window", if they lie on a line and if showing an energy of 511 keV each. Due to the 360° arrangement of detectors, it is possible to reconstruct the distribution of the radioactive substance in three dimensions.^[15] To increase the informative value of the molecular data gained by PET scans, it is very common to combine these images with 3D anatomical data of the investigated organ acquired by MRT or CT imaging.

Table 2: Diagnostically relevant PET nuclides; CYC = cyclotron, GEN = generator.

Nuclide	Production mode	Production reaction	Target material	Half-life	% EC	Typical tracer + application
¹¹ C	CYC	¹⁴ N(p,α) ¹¹ CO ₂ , ¹⁴ N(p,α) ¹¹ CH ₄	gaseous +O ₂ +H ₂	20.4 min	0.21 ^[16]	[¹¹ C]-PIB: Alzheimer's disease
¹³ N	CYC	¹⁶ O(p,α)	liquid	10 min	-	[¹³ N]NH ₃ : myocardial perfusion
¹⁵ O	CYC	¹⁵ N(p,n)	gaseous	2 min	-	H ₂ ¹⁵ O: perfusion of organs
¹⁸ F	CYC	¹⁸ O (p,n)	liquid	110 min	3.0	[¹⁸ F]FDG: glucose uptake in oncology, metabolic status of organs
⁶⁸ Ga	GEN	⁶⁸ Ge(EC)		68 min	11.1 ^[17]	[⁶⁸ Ga]-DOTATOC: neuroendocrine tumors
⁸² Rb	GEN	⁸² Sr (β ⁺)		75 sec	-	[⁸² Rb]Cl: myocardial perfusion
¹²⁴ I	CYC	¹²⁴ Te(d,2n) or ¹²⁴ Te(p,n)	solid	4.2 d	25.6	Na ¹²⁴ I: thyroid carcinoma ^[18]

Fluorine-18 is the most attractive PET nuclide featuring a physical half-life of 109.77 min (*Table 2*), which prolongs possible imaging periods to several hours. The target material for [¹⁸F]fluoride is isotopically enriched H₂¹⁸O, which is commercially available.

In this context, it should be mentioned that for every form of diagnostic nuclear medical measurement, it is important to ensure, that an adequate amount of the radioactive drug is able to bind to the specific receptor or can be taken up by the targeted transporter. The proportion of the tracer which has already decayed and the part of tracer which has been synthesized in a non-radioactive form due to isotopic impurities of the starting synthon, can drastically influence the binding capacity of the radioactive tracer. This property can be described by the specific activity,

which is defined as the activity of the radionuclide [Bq] per unit mass of the chemical substance or the respective element.^[5] As this ratio decreases with time, a quick application of the tracer after synthesis and quality control is essential for accurate measurements.

Since the norepinephrine transporter (NET) is the biological target structure for the examined tracers within this thesis, some facts about its structure, molecular function and previous investigations on NET-ligands are given in the next chapter.

1.4 Norepinephrine (NE) and Norepinephrine Transporter (NET)

Norepinephrine (NE) is mainly produced in the locus coeruleus (LC), which is located in the rostral pons in the rhomboid fossa of the brainstem. It represents the principal site for synthesis of norepinephrine within the brain, while peripheral organs are supplied with this monoamine transmitter via the adrenal medulla. CNS functions of NE pathways include arousal reactions, enhanced attention, motivation, stress related actions as well as memory functions.^[19]

The norepinephrine transporter is a transmembrane glycoprotein consisting of 617 amino acids with 12 membrane-spanning domains and is responsible for the reuptake of norepinephrine into presynaptic nerve terminals and glial cells regulating the levels of NE in the synaptic cleft (see *Figure 1*).^[20, 21] A termination mechanism for neurotransmitter action of this kind can also be found for e.g. GABA, L-glutamate, glycine, dopamine and serotonin. Attenuation of NE removal enables a potentiation of the transmitters' effect. The NET is a sodium-chloride (Na^+/Cl^-)-dependent norepinephrine cotransporter, which transports ions and transmitter into the cell in an equimolar ratio. The cellular resting potential that is needed for this active transport is maintained by the Na^+/K^+ -ATPase.

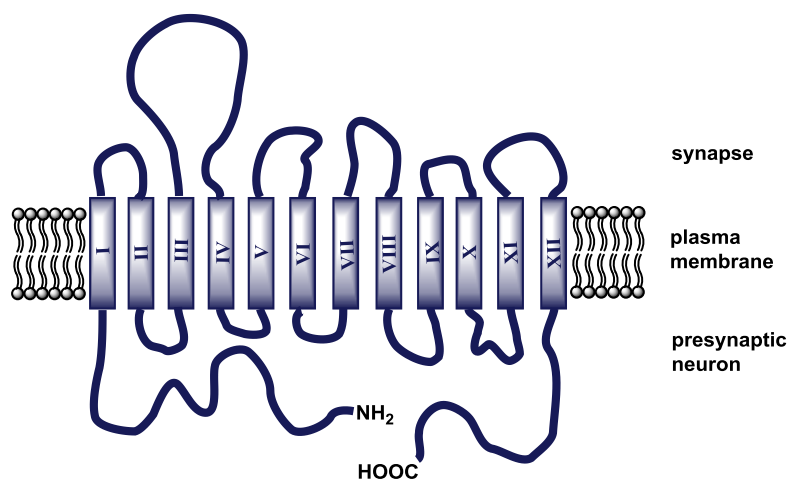


Figure 1: Schematic representation of NET with its 12 transmembrane segments (shown as numbered rectangles): C- and N-terminus are located on the cytoplasmic side of the plasma membrane, glycosylation sites were found on the largest loop between helix 3 and 4.^[20, 21]

Details about the synthesis, release and uptake of NE are given below (see *Figure 2*):

Tyrosine is transported into the noradrenergic nerve axon and converted to dihydroxyphenylalanine (DOPA) by tyrosine hydroxylase (TH), which represents the rate-limiting

step for the synthesis of NE. Further conversion to dopamine is catalyzed by DOPA decarboxylase (DD). After uptake of dopamine into transport vesicles via the vesicular monoamine transporter-2 (VMAT-2), dopamine is modified by dopamine β -hydroxylase (DBH) to finally give NE.

If an action potential is propagated across the axon and reaches the nerve terminal, depolarization of the cell causes the opening of voltage-dependent Ca^{2+} -channels and thus, an influx of calcium into the presynaptic neuron. The increase in intracellular calcium levels leads to a fusion of storage vesicles with the membrane and a subsequent release of NE into the synaptic cleft together with other substances such as ATP. NE stimulates the postsynaptic adrenergic α and β receptors and exhibits a negative feedback on its own release via inhibitory α_2 receptors. Besides, a small part of the NE is metabolized in the extracellular space. After reuptake of the majority of NE by NET, it is either encased by vesicles via VMAT-2, or it is degraded by a combination of monoamine oxidase (MAO), catechol-*O*-methyltransferase (COMT) and aldehyde reductase (ALDR) to yield 3-methoxy-4-hydroxyphenylglycol (MHPG) as the principal metabolite of NE in the brain.^[22, 23]

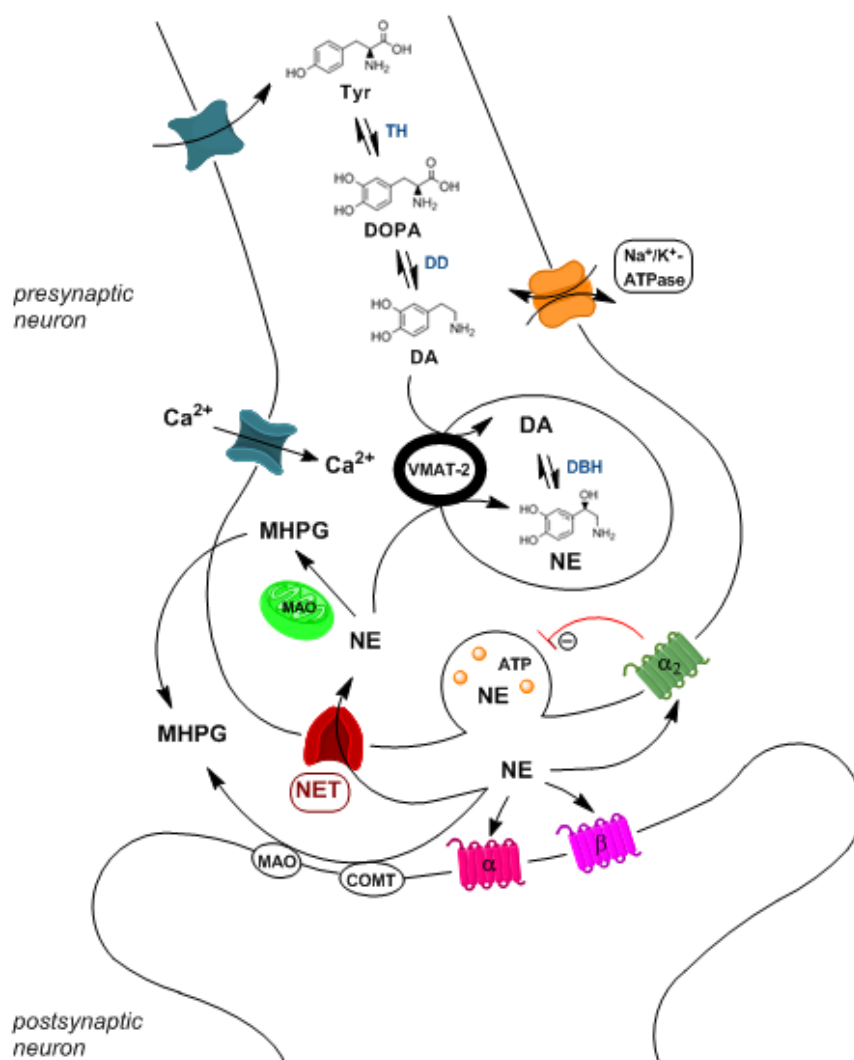


Figure 2: Schematic figure showing norepinephrine homeostasis: biosynthesis, release, reuptake and metabolism. Legend: COMT = catechol-*O*-methyl transferase, DA = dopamine, DBH = dopamine β -hydroxylase, DD = DOPA decarboxylase, DOPA = 3,4-dihydroxyphenylalanine, MAO = monoamine oxidase, MHPG = 3-methoxy-4-hydroxyphenylglycol, NE = norepinephrine, NET = norepinephrine transporter, TH = tyroxine hydroxylase.^[22]

Just as the dopamine transporter (DAT) is able to transport NE, NET is capable of dopamine uptake. Remarkably, NET is not expressed in neurons that release dopamine or epinephrine and, therefore, these neurons are called noradrenergic.^[24] NET can be regulated not only by antidepressants but also cocaine and the substance group of amphetamines.

It is known that NET density is very high in the locus coeruleus (LC) while the caudate nucleus serves as a reference region with negligible NET appearance.^[25, 26] As axons of LC-noradrenergic neurons extend into various other regions, above all the thalamus, the amygdala, the cingulate cortex, the striatum as well as hypothalamus and hippocampus, NET can be found in all of these brain areas, especially the thalamus (see *Figure 3*).^[27] Unlike the LC (0.1 cm³), the thalamus is big enough for routine PET diagnostics without a high resolution research scanner exhibiting a volume of 8.1 cm³ in females and 9 cm³ in males and therefore, represents the most promising structure for NET-PET studies to date.^[27, 28] With increasing age, a decrease in NET density in the human brain was observed.^[29, 30]

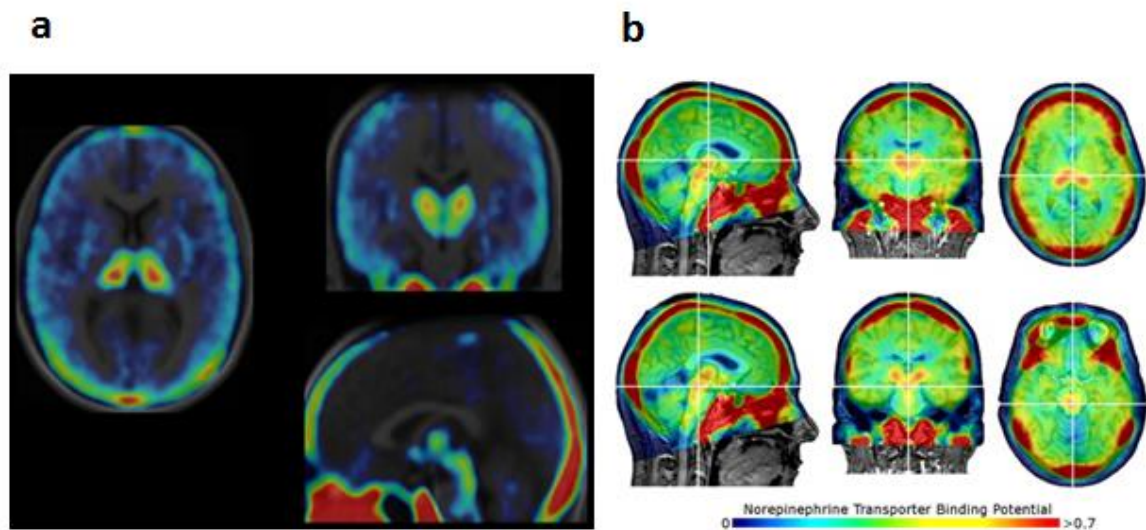


Figure 3: PET images of ¹⁸F]FMeNER-D2: a. transaxial (left), coronal (upper right) and sagittal (lower right) images in a healthy volunteer^[31]; b. PET-MR images in a healthy subject, white crosses display the thalamus (upper row) and the LC (lower row)^[32]; both PET scans indicate extensively high uptake in extra-cerebral tissue such as cranial bone and nasal mucosa.

1.4.1 Tracers for NET

Given the undeniable role of NE and its related transporter in various physiological as well as pathophysiological states, the measurement of regional NET levels in human brain is desirable. (*S,S*)-[¹¹C]MeNER was the first reboxetine analogue which showed remarkable binding to NET (Figure 4). However, a longer-lived PET-ligand was found to be more suitable due to time-dependent specific binding. Therefore, the fluorinated tracer (*S,S*)-[¹⁸F]FMeNER was developed, showing considerable skull-bound radioactivity, indicating a fast defluorination of the ligand. These disturbing background signals could be significantly reduced by introduction of the di-deuterated structural analogue (*S,S*)-[¹⁸F]FMeNER-D2 which is more stable against *in vivo* defluorination due to the deuterium isotope effect.^[31] With the development of [¹⁸F]FMeNER-D2 as a suitable radioligand for NET, it is possible to determine NET occupancy by antidepressants in the human brain.

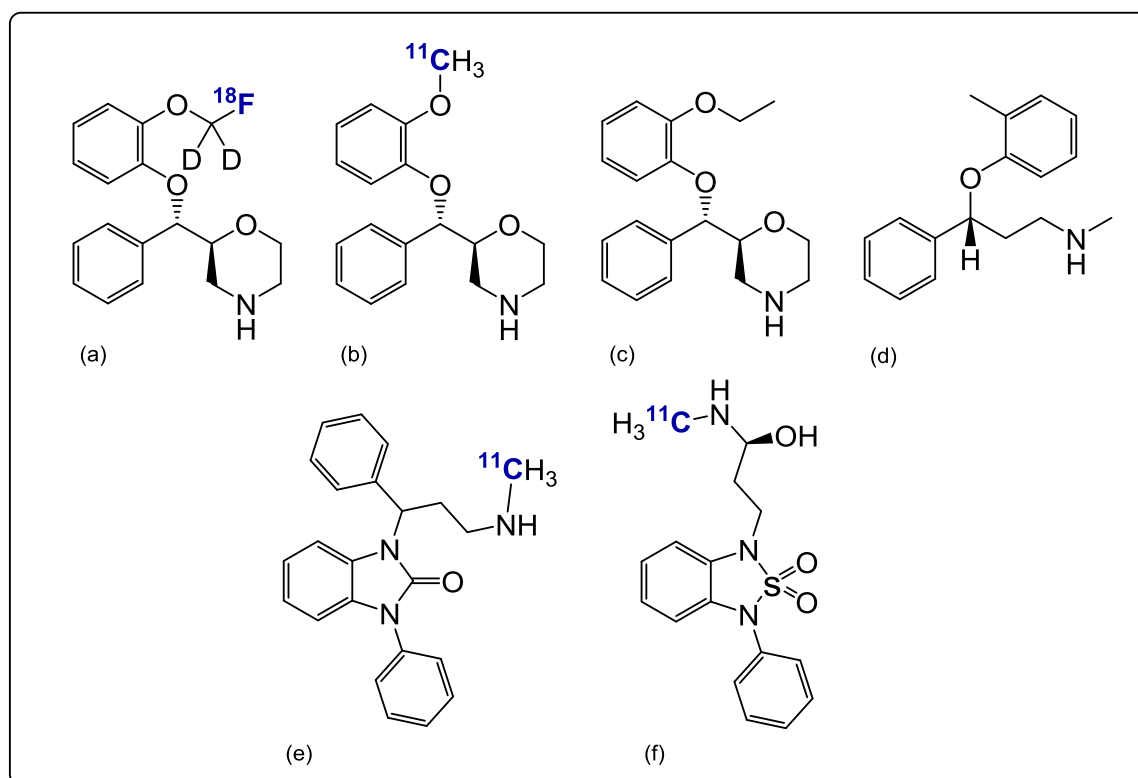


Figure 4: Diagnostically and therapeutically active ligands for norepinephrine transporter (NET): (a) (*S,S*)-[¹⁸F]FMeNER-D2, (b) (*S,S*)-[¹¹C]MeNER, (c) reboxetine, (d) atomoxetine; c) and d) are clinically approved therapeutics used for the treatment of depression and ADHD, respectively. Novel tracers for NET are listed in the bottom row: Me@APPI (e) and Me@HAPTHI (f).

Other NET affine ligands were found to be 1-(3-(methylamino)-1-phenylpropyl)-3-phenyl-1,3-dihydro-2*H*-benzimidazol-2-one (Me@APPI) and (*S*)-1-(3-hydroxy-4-([¹¹C]methylamino)butyl)-3-phenyl-1,3-dihydrobenzo[*c*][1,2,5]thiadiazole-2,2-dioxide (Me@HAPTHI) showing good results concerning *in vitro* testing (see Figure 4).^[32, 33]

1.4.2 Function of NET in various diseases

1.4.2.1 Alzheimer's Disease (AD)

In brains of patients with Alzheimer's disease a significant reduction of cell numbers in the LC as well as the thalamus is known and is accompanied with a regional decrease of NET. This was recently demonstrated in numerous autoradiographic studies also using NET-PET ligand (*S,S*)-FMeNER-D2 as a biomarker. Besides amyloid plaques and insoluble A β peptides, change in NET levels can serve as a valuable disease biomarker. Still further studies are needed to find out whether this tracer is a useful biomarker for identification of AD in an early stage.^[27]

1.4.2.2 Depression

Some very characteristic symptoms of major depressive disorder (MDD) such as psychomotor retardation, which is mainly characterized by restricted speech and thoughts, and poor concentration, are related to dysregulation of NE.^[34, 35] Antidepressants are not only acting as inhibitors of the reuptake of serotonin (SSRI) but also the NET serves as a main therapeutic target. Tricyclic antidepressants (TCA) which represent the oldest group of antidepressant substances exhibit very unspecific binding to a plethora of cellular targets of the brain also including NET. Their high affinity for NET partly explains their antidepressant activity but their application is constrained due to their poorly tolerable adverse reactions.^[36, 37] A relatively new class of antidepressant drugs are the so-called serotonin and norepinephrine reuptake inhibitors (SNRIs), which might result in higher responder rates than well-tolerated, but poorly effective SSRIs and exhibit less side effects than TCAs in the case of major depressive disorder.^[38]

1.4.2.3 Attention-deficit/hyperactivity disorder (ADHD)

Attention-deficit/hyperactivity disorder (ADHD) is the most frequently diagnosed disorder in children and adolescents (affecting about 5%) and is commonly persisting into adulthood. It is characterized by inattention, impulsiveness and locomotive unrest due to a lack of inhibitory and attentional control.^[39] There is evidence that not only the dopaminergic but also the noradrenergic system are involved in the etiology of ADHD, since anti-ADHD drugs are exhibiting a positive therapeutic effect by targeting both, DAT and NET.

The first PET study comparing NET densities in adult ADHD patients with age and sex matched controls did not reveal significant differences in (*S,S*)-FMeNER-D2 distribution.^[29] Although, it is known that pharmacological treatment with substances blocking the NET leads to a relief in symptoms. To further exclude NET involvement in ADHD additional occupancy studies have to be performed to investigate NET in the cerebral cortex. Up to now, structural as well as functional imaging points to a dysregulation of dopaminergic and noradrenergic fronto-subcortical pathways.^[40]

1.5 Biotransformation of xenobiotics

Like any other pharmaceutical, radioactive tracers are subject to metabolic processes *in vivo* meaning that not only their physical but also their biological half-life determines their applicability in a crucial way. For this work, metabolic transformations of NET-PET ligands are of considerable interest and will be outlined in the aim of the thesis and therefore, a focus is laid on the theoretical background of *in vivo* and *in vitro* metabolism.

1.5.1 Peripheral biotransformation

1.5.1.1 Cytochrome CYP450

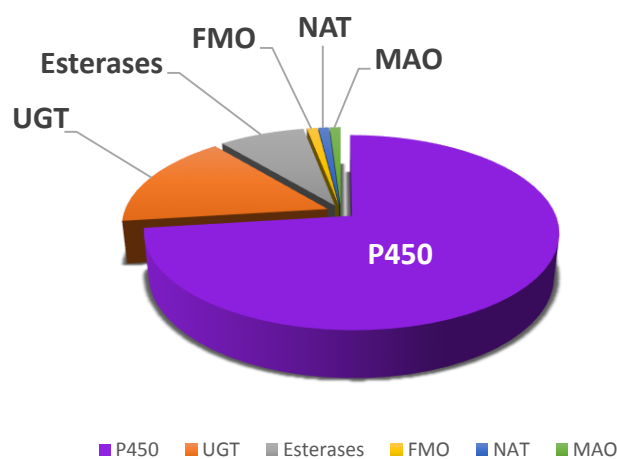


Figure 5: Overview of clearance mechanisms for the top 200 drugs in the US in 2002^[41]: UGT, UDP-glucuronosyltransferase; FMO, flavin monooxygenase; NAT, N-acetyltransferase; MAO, monoamine oxidase.

The cytochrome P450 (CYP) subfamily is of utmost importance in the biotransformation of endogenous compounds as well as xenobiotics, accounting for about 75% of total drug metabolism (see *Figure 5*).^[41, 42] Altogether, a total of 57 human CYP genes are known, but only members of the first three families CYP1, CYP2 and CYP3 are responsible for the modification of drugs.^[43, 44] Human CYPs are present in most tissues of the body and are principally membrane-associated proteins, which can be located in the inner membrane of mitochondria or in the endoplasmic reticulum.^[45] The term P450 derives its origin from the spectrophotometric property showing an absorption maximum at 450 nm in its reduced state (Fe (II)) and complexed with carbon monoxide. Cytochromes P450 belong to the superfamily of heme proteins and require an electron delivery system for their monooxygenase function. These electron transport proteins of P450 are needed to accept the two electrons from the cofactor NADPH and to transfer them to the P450 during the reaction. Based on the known electron transport components, P450 systems can be divided into the following groups^[46]:

1. If the mitochondrial system includes *adrenodoxin reductase*, which is NAD(P)H specific and has a FAD cofactor, and adrenodoxin (FDX1), an iron-sulfur protein, the electron transfer can be summarized by the following cascade: $\text{NAD(P)H} \rightarrow \text{FAD} \rightarrow \text{adrenodoxin (Fe}_2\text{S}_2) \rightarrow \text{P450} \rightarrow \text{O}_2$. In this case, adrenodoxin serves as a single electron carrier.

2. Some microsomal systems depend on a *NADPH reductase*, which is NADPH specific and contains flavin adenine dinucleotide (FAD) and flavin mononucleotide (FMN) as cofactors. Electron flow can be depicted as follows: $\text{NADPH} \rightarrow \text{FAD} \rightarrow \text{FMN} \rightarrow \text{P450} \rightarrow \text{O}_2$. In these microsomal P450s an ubiquitous electron-transport protein, namely, cytochrome b_5 can be responsible for the transfer of the second electron to P450, receiving electrons from cytochrome P450 reductase or cytochrome b_5 reductase with the latter being NADH dependent. Flow chart: $\text{NAD(P)H} \rightarrow \text{FAD} \rightarrow b_5 \rightarrow \text{P450} \rightarrow \text{O}_2$.

The other two missing groups comprise bacterial cytochrome P450 systems, which are of minor interest in our context. In summary, besides the well-known NADPH-cytochrome P450 reductase (CPR) as the major electron donor for the reduction of the iron center, adrenodoxin may serve as an additional electron transfer protein.^[47]

A simplified but generally accepted mechanism for the catalytic activity of P450 reactions is shown in Figure 6.^[48-51] It depicts the mechanism for the oxygenation of C-H bonds, which is from the chemical point of view the most extraordinary feature of CYPs besides a variety of other oxidative reactions such as N-, O- and S-dealkylations, heteroatom oxygenations, desaturations and epoxidations.^[51]

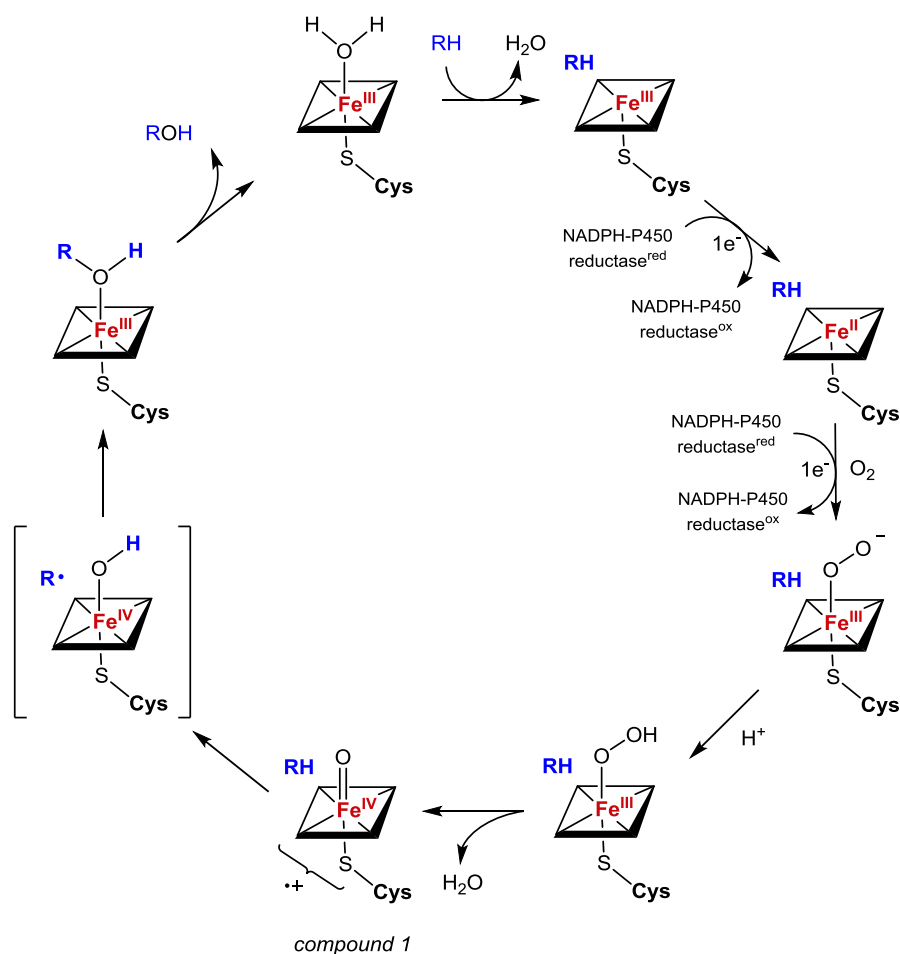


Figure 6: Cytochrome P450 catalytic cycle.

The binding of the substrate near the catalytic center leads to the displacement of water and a shift from the low spin to high spin ferric enzyme. The formed complex has a greater reduction potential and after the first reduction via its redox partner (e.g. NADPH reductase), oxygen is bound by the heme. This oxyferrous protein receives a second electron and after twofold protonation the oxygen double bond is cleaved under release of water. The newly formed compound is an iron(IV)oxo cation species where the radical is delocalized over the porphyrin and the thiolate ligands. The oxygenation of the substrate takes place via abstraction of a hydrogen radical from the substrate, followed by recombination of the substrate radical and the hydroxyl radical. The heme returns to the initial low spin state and the monooxygenated product may rearrange to form more stable products.^[47, 48]

The most important CYP subfamilies that are involved in the catalysis of small-molecule drug metabolism and their amount relative to the total CYP concentration are given in *Table 3*.^[43] In comparison to these data, the work of Williams et al. (2004) show similar results (see *Figure 7*^[41]).

Table 3: Human CYP450s in the liver responsible for drug metabolism.

CYP isoform	% of total amount
CYP3A ²	15 – 58
CYP2C ³	8 – 35
CYP1A2	2 – 28
CYP2A6	1 – 14
CYP2E1	2 – 13
CYP2D6	0.1 – 6
CYP2B6	0.1 – 0.8

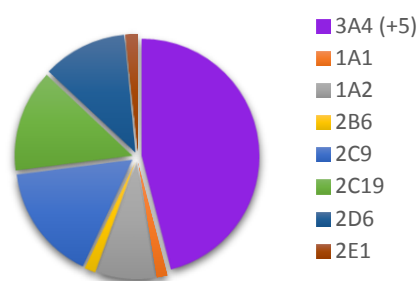


Figure 7: Fractions of CYP450 subfamilies responsible for the metabolism of cytochrome P450 substrates.

Among these, the CYP3A4 isoform is the most abundant and metabolizes the majority of drugs. CYP isozymes that are also responsible for degradation of xenobiotics include CYP1A1, CYP2A13, CYP2C8 and CYP2F1, which play a minor part and are not listed above. All other families or subfamilies are obligatory for the bioconversion of endogenous substances like sterols, fatty acids, eicosanoids and vitamins.^[44]

The deviation of relative percentages in *Table 3* is caused by interindividual differences in CYP gene expression.^[43] The effect of variation in human P450 activities on pharmacokinetics can be significant and therefore, individuals can be classified as normal (extensive) or poor metabolizers. Due to genetics, for some CYP enzymes not only deficiencies but also an absence of a specific CYP as well as the duplication/multiplication of the enzyme is known which leads to missing or ultrarapid metabolism. CYP2D6 shows the widest spectrum of genetic variants among all other major drug metabolizing CYP450 isozymes.^[52]

² comprises CYP3A4, CYP3A5 and CYP3A7.

³ contains CYP2C9, CYP2C18 and CYP2C19.

CYP2D6 deficiency

Cytochrome P450 2D6 is of relevant clinical interest even though it accounts for only a small percentage of liver P450 enzymes. It catalyzes the metabolism of a huge number of largely lipophilic drugs including antidepressants, neuroleptics, antiarrhythmics, antiemetics, opioids and β -adrenoceptor blockers, which cover about a quarter of currently prescribed drugs. CYP2D6 deficiency is most commonly caused by point mutations in the coding region of the gene, which results in amino acid substitution and hence an alteration in catalytic activity. The CYP2D6 gene is localized on chromosome 22q13.1 and modification of the only functional gene of the CYP2D subfamily represents an autosomal recessive trait. The different known polymorphisms may lead to a lack of functional enzyme showing ethnic prevalence in 7% of Caucasians and 1% of Orientals. These individuals are the so-called “poor metabolizers”, while among the rest, which carries further allelic variants, a small part exhibits either ultrarapid to normal metabolism or, for the bigger part, notably reduced metabolism (“intermediate metabolizers”).^[53, 54] CYP2D6 can primarily be found in liver, brain^[55], prostate^[56] and bone marrow.^[57] Furthermore, it is stated that CYP2D6 is the important cytochrome isozyme in the brain responsible for homeostasis of neuronal transmission since it plays a role in the regeneration of serotonin from 5-methoxytryptamine.^[58]

CYP450 enzymes in the brain

Cytochrome P450 enzymes are not only highly abundant in mammalian liver, but are also expressed in a far lower extent in extra-hepatic tissues including the brain. The total amount of CYPs in the brain comes to about 0.5 – 2% of hepatic levels, so the central metabolism is unlikely to influence systemic metabolite levels.^[59] An interesting difference between liver and brain concerning CYP450 enzyme distribution is, that it is far more heterogeneous in cerebral tissue and very specific for every single cytochrome P450 monooxygenase. Due to the concentration of a special CYP enzyme in a defined region of the brain, its activity can have a considerable impact on metabolite formation and may affect a certain microenvironment or the entire brain.^[60] In the end, the regional neuronal levels of CYPs may even be higher than in hepatocytes.^[61] While CYP2D6 can be found in the frontal cortical layers III-V in pyramidal neurons and in the white matter, CYP2B6 is highly expressed in astrocytes close to cerebral blood vessels.^[62] Centrally active CYP450 families involved in the metabolism of exogenous substrates are given in *Table 4*.^[58]

Table 4: CYP families expressed in the brain and their exogenous substrates.

Clinical drug		
Antidepressants	Antipsychotics	Other centrally acting substrate
CYP1A	CYP1A	CYP1A
CYP2B	-	CYP2B
CYP2C	-	CYP2C
CYP2D	CYP2D	CYP2D
CYP3A	CYP3A	CYP3A
-	-	CYP2E1

1.5.2 Central biotransformation

Besides the monooxygenases of the cytochrome P450 system, flavin-containing monooxygenases (FMO), molybdenum hydroxylases, alcohol and aldehyde dehydrogenases, as well as amine oxidases are important enzymatic systems responsible for the metabolism of xenobiotics.^[63] Hereafter, two important enzymatic classes, which are responsible for the homeostasis of neuronal transmitters are discussed.

1.5.2.1 Monoamine oxidases (MAOs)

Monoamine oxidase (MAO) represents a mitochondrial outer-membrane flavozyme, which can be found in the brain and is also responsible for oxidative catabolism in peripheral organs. It can be predominantly found in the liver, intestinal mucosa, renal cortex, lung, myocardium and spleen.^[64-66] MAO consists of two distinct non-covalently bound subunits, whereby each unit covalently binds one cofactor molecule flavin-adenin dinucleotide (FAD) via a thioether. Two distinct MAO isozymes have been characterized, MAO-A and MAO-B, which catalyze the oxidative deamination of the neurotransmitters norepinephrine, dopamine and serotonin. Moreover, MAO plays an important role in the conversion of further biogenic amines such as tyramine, tryptamin and MPTP (N-Methyl-4-phenyl-1,2,3,6-tetrahydropyridine), with the latter one being a synthetic and well-known proneurotoxin causing symptoms of Parkinson's disease via its metabolite MPP⁺.^[64, 65] To the present knowledge, the contribution of MAOs to the metabolism of xenobiotics has for the most part been neglected. However, it has been shown, that important classes of pharmaceutical substances (e.g. some β -adrenoceptor agonists and antagonists, serotonin 5HT₁-receptor agonists and MAO inhibitors) can be substrates for these enzymes. In general, monoamine oxidases A and B, which have a sequence identity of about 70%, are both able to oxidize primary, secondary and tertiary amines. An introduction of a methyl group at C_α with respect to the amino group of the substrate is described to inhibit the oxidation reaction by MAO.^[63]

Reaction mechanism

The abstraction of C_α-hydrogen leads to the formation of an imine while FAD is reduced to FADH₂. In the next non-enzymatic step, the imine is hydrolyzed to the carbonyl (incorporating oxygen taken from water) to form the product. FADH₂ is subsequently reoxidized by molecular oxygen producing H₂O₂.^[67] The final reaction products are hydrogen peroxide, the corresponding amine and the aldehyde (*Figure 8*).

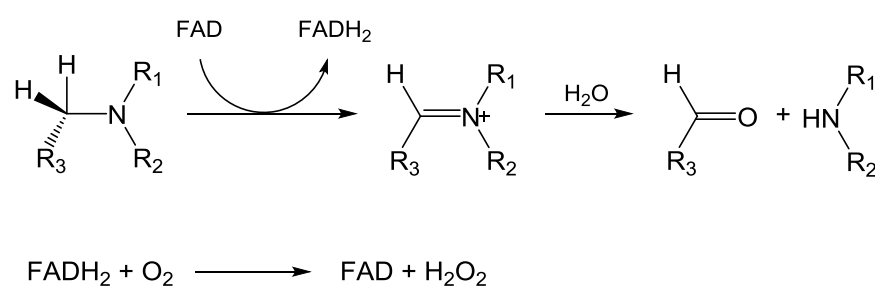


Figure 8: Reaction catalyzed by MAO.

1.5.2.2 Catechol-*O*-methyltransferase (COMT)

Human catechol-*O*-methyltransferase plays a central role in the metabolism of catecholamine neurotransmitters (norepinephrine, epinephrine, dopamine), catechol steroids and catechol drugs (e.g. L-DOPA). The enzyme inactivates the abovementioned neurotransmitters and therefore, its inhibition leads to an improvement in the treatment of Parkinson's disease as dopamine levels are raised.^[68] COMT regulates the amounts of active neurotransmitters in the brain and thus, is related to changes in mental processes and mood.

The methyl transferase is ubiquitously expressed and exists in a membrane-bound endoplasmic reticulum (MB) and soluble (S) cytosolic form, whereby S-COMT is expressed at higher levels in peripheral tissues and MB-COMT is more predominant in human brain.^[69, 70] The monomeric S-COMT protein consists of 221 amino acid residues. The only difference between the two forms is the NH₂-terminal extension of 50 additional lipophilic amino acids in the human MB-COMT serving as a hydrophobic anchor. Human MB-COMT has a significantly higher affinity for catechol substrates than S-COMT. As there is no conformational change in the structure of MB-COMT, the difference in catalytic activity compared to the soluble form is attributed to the charged membrane, which causes favorable binding interactions.^[71] The most abundant tissue for hCOMT is the liver, followed by the kidneys, stomach, intestines and lung. In the brain most of its activity is located in glial cells or in postsynaptic dopaminergic neurons.^[70]

Reaction mechanism

COMT catalyzes the transfer of a methyl group to the phenolic hydroxyl-group of the catechol substrate with *S*-adenosyl-L-methionine (AdoMet) acting as the methyl donor in the presence of Mg²⁺ ions.^[72] The AdoMet-binding domain is part of the catalytic site of COMT, which is formed by amino acid residues that are important for the binding of the substrate, Mg²⁺ and water. The reaction follows a sequential mechanism where *S*-adenosyl-L-methionine (SAM) binds before the magnesium ion and the catechol substrate placing one of the catechol hydroxyls close to the activated methylsulfonium group of SAM.^[73, 74] The Mg²⁺ ion facilitates the deprotonation of the hydroxyl group while the basic lysine residue (Lys144) serves as a proton acceptor in this nucleophilic methyl transfer.^[70]

Rat and human liver COMT have not been as extensively examined as the pig liver form in terms of structure and function. Thus, in many investigations e.g. the search for new potent inhibitors, porcine COMT is still used for enzymatic assays as an alternative.^[68, 75] Human S-COMT displays 81% structural homology in primary amino acid sequence with rat S-COMT compared to 82% with porcine COMT.^[73] More precisely, pig liver COMT differs from rat and human variants by having an arginine residue in position 38 instead of tryptophan. The substitution of the hydrophobic Trp to a highly polar Arg leads to reduced affinity (K_M) and increased K_i values for COMT inhibitors.^[70] The use of porcine COMT instead of purified human recombinant COMT is reasonable due to the very similar specificity of both enzymes and the easier handling of commercially available porcine COMT.^[76]

1.6 *In vitro* metabolism studies

To ensure the safety of a drug candidate it is necessary to predict its metabolic fate in humans. Information about stability, drug clearance and possible drug-drug interactions are hence a prerequisite for further drug development and are acquired via preclinical *in vitro* testing. Due to identical degradation mechanisms as well as inductive or inhibitory effects of different therapeutics, drug interactions *in vivo* are a common phenomenon.

Such compulsory preclinical investigations include for example, simple stability tests in human plasma as well as the identification of major metabolic pathways in human or mammalian tissues (e.g. microsomal extracts of human or rat liver) and purified or recombinant human cytochrome P450s.

In the case of PET or SPECT-diagnostic agents, adverse drug events can be neglected due to the very small amounts of administration (picomolar to nanomolar range). Therefore, stability tests are obligatory but it is not established to investigate drug metabolism in detail.

In the following last sections standard *in vitro* stability tests for drug candidates are presented.

1.6.1 Microsomal preparations

1.6.1.1 Human Liver Microsomes (HLM) and Rat Liver Microsomes (RLM)

A common initial *in vitro* study in drug development is to test bioavailability using liver microsomal incubations to quantify the amount of substance eliminated in a simulated first-pass effect. In general, microsomes are obtained from liver tissue via a special homogenization and centrifugation sequence. Consequently, microsomal preparations provide a source of membrane bound drug metabolizing enzymes such as members of the cytochrome P450 superfamily as well as uridine 5'-diphospho-glucuronosyltransferase (UGT) and many others.

HLM

According to *Pelkonen et al.* (1998) human liver microsomes contain 13 major CYP450 isozymes, listed hereafter in decreasing abundance: CYP3A4, CYP3A5, CYP 3A7 (ca. 30%), CYP2C8, CYP2C9, CYP2C18 (ca. 20%), CYP1A2 (ca. 15%), CYP2E1 (ca. 10%), CYP2C19 (less than 5%), CYP2D6 (less than 5%), CYP2A6 (less than 5%), CYP2B6 and CYP1A1.^[77] It has to be stated that CYP3A7 seems to be existing only in fetal liver. Apart from cytochrome P450 enzymes pooled human liver microsomes also contain UDP-glucuronosyltransferases and flavin-containing monooxygenase, whereby UGTs are part of the phase II metabolism allowing substances to be eliminated by the kidneys.

Cofactor

NADPH is the required cofactor for the activation of phase I CYP-mediated metabolism for human liver microsomes (HLM), rat liver microsomes (RLM) or recombinant human cytochrome P450 (rhCYP) assays and must be added for CYP activity. In such systems oxidative metabolism is generated either, like in our case, with NADPH-regenerating system or with an excess of NADPH. For UGT activity, uridine diphosphate glucuronic acid (UDPGA) cofactor must be supplied.

Cofactor recycling

The addition of NADPH regenerating system supports reactions of cytochrome P450, flavin-containing monooxygenases, NADPH-P450 reductase and certain other enzymes. Recycling of NADPH using glucose 6-phosphate dehydrogenase (G6PDH) follows the given mechanism (see Figure 9).

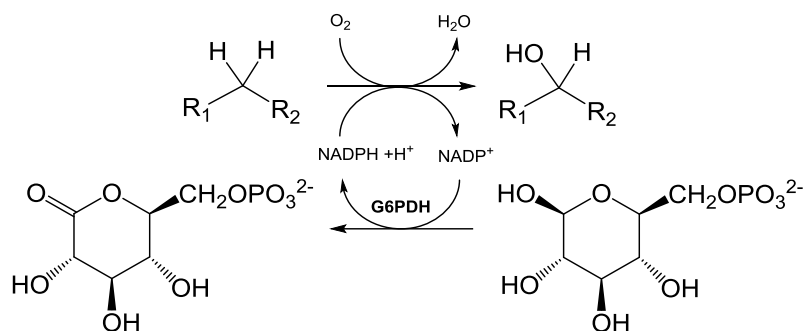


Figure 9: NADPH regeneration converting glucose 6-phosphate into 6-phosphogluconate.

Organic solvents in the incubation mixture

The known sensitivity of CYP activity to organic solvents presents a significant issue, indicating that the portion of organic solvent should be kept to a minimum of 0.5 – 1% v/v. The usage of organic solvents in incubation mixtures is justified due to the enhancement of the solubility of some compounds (e.g. inhibitors) and arises from the dilution of stock solutions.^[78] For incubation batches of the different enzymes recommended values concerning percentage of organic solvent (DMSO, EtOH) have been considered.^[79] In human liver microsomes (HLM) the content of organic solvent (acetonitrile, methanol, DMSO) in each batch should not exceed 1%. For several P450-mediated reactions - 2E1, 2C19, 3A4 and 2C8/2C9 - DMSO affects metabolism at even lower concentrations (0.2%).^[80] The activities of CYP2D and CYP2E are fully inhibited by DMSO (and acetone) already at very low concentrations around 0.2%. Therefore, acetonitrile is recommended for RLM incubations, which has no significant interference when the content of organic solvent is kept below 1 % v/v.

1.6.2 Inhibition assays in Human Liver Microsomes (HLM)

Another method for determining degradation with a certain CYP isozyme involves the use of selective inhibitors in human and rat liver microsomal incubations. The choice of a selective inhibitor, which is effective even at low concentrations (high potency) for a single CYP isoform is the crucial step to spot the involvement of a particular enzyme. For study design, it is of prime importance to consider inhibitor concentrations as with choosing an inappropriate concentration range of the inhibitor, the reduction of enzymatic turnover may not only be dedicated to one presumed CYP450. Inhibition can be achieved using either specific antibodies against hCYP450 or by using specific chemical inhibitors. The following table (Table 5) gives a summary of well-established chemical CYP inhibitors for the most abundant hepatic CYP450 enzymes.^[43, 81-83] In general, chemical inhibitors of CYP isoenzymes are ligands that act upon direct ligation to the

heme iron via a nitrogen atom provided by imidazole, pyridine and primary amino groups, which results in a lowering of redox potential.^[50]

Table 5: List of important inhibitors and substrates for hCYP450 enzymes; the main reaction for the given substrate (probe substance) to monitor CYP isozyme activity used for the evaluation of inhibitory effects of a drug candidate is quoted in the rightmost column; K_i values (third column) for inhibitors (second column) are given.

Enzyme	Inhibitor	K_i [μ M]	Probe substance	Probe reaction
CYP1A2	α -Naphthoflavone	0.013	Phenacetin	Phenacetin <i>O</i> -deethylation
	Furafylline	0.6 – 4.44		
CYP2C9	Sulfaphenazole	0.12 – 0.7	Diclophenac Tolbutamide	Tolbutamide methyl-hydroxylation
	(+)-N-3-Benzylirivanol	0.25	(S)-Mephenytoin	(S)-Mephenytoin 4'-hydroxylation
Ticlopidine	0.02 – 3.7			
(-)-N-3-Benzylpenobarbital	0.079			
CYP2D6	Quinidine	0.03 – 0.4	Dextromethorphan Bufuralol	Dextromethorphan <i>O</i> -demethylation; Bufuralol 1'-hydroxylation
	Ketoconazole	0.0037 – 0.13	Midazolam, Testosteron	Midazolam 1'-hydroxylation; Testosterone 6 β -hydroxylation
Azamulin	-			
Troleandomycin	0.14 – 2.4			
CYP2B6	2-Phenyl-2-(1-piperidinyl)propane (PPP)	5.6	Bupropion	Bupropion hydroxylation
	Ticlopidine	0.2		
CYP2C8	Montelukast	0.15	Paclitaxel	Paclitaxel 6 α -hydroxylation
	Quercetin	1.14 - 10.1		
CYP2A6	(R)-Tranylcypromine	0.04 – 0.2	Coumarin	Coumarin 7-hydroxylation
	3-(2-Methyl-1 <i>H</i> -imidazol-1-yl)pyridine (MIP)	0.25		
	3-(Pyridin-3-yl)-1 <i>H</i> -pyrazol-5-yl)methanamine (PPM)	0.3		
CYP2E1	4-Methylpyrazole	IC ₅₀ = 1 μ M	Chlorzoxazone	Chlorzoxazone 6-hydroxylation
	Diethyldithiocarbamate	-		

In the following subchapters, the used chemical inhibitors are outlined in detail.

Selectivity of established chemical inhibitors [43, 81-83]

CYP1A2 Inhibitors

Furafylline

Furafylline represents a competitive and mechanism-based⁴ inhibitor of CYP1A2 with an outstanding selectivity against other CYP450 isoforms. Its K_i range measured by phenacetin *O*-deethylase activity is 0.6 – 4.44 μM . α -Naphthoflavone is also an extremely potent inhibitor of CYP1A2 (K_i : 0.013 μM ^[84]) but inhibits the extrahepatic enzymes CYP1A1 (K_i : 0.01 μM ^[85]) and CYP1B1 (K_i : 0.0028 μM ^[86]) at very low concentrations. Thus, furafylline is so far the most selective inhibitor for CYP1A2.^[43]

CYP2C9 inhibitors

Sulfaphenazole

Sulfaphenazole is a selective and potent inhibitor for CYP2C9.^[43] Even at high concentrations of 100 μM in HLM incubations, sulfaphenazole fails to inhibit other cytochrome P450 mediated reactions of CYP3A4, CYP2E1, CYP1A2 or CYP2D6.^[82] However, it is also a weak inhibitor of CYP2C18 (K_i : 29 μM ^[87]), CYP2C19 (K_i : 10 – 14 μM ^[88]) as well as CYP2C8 ($K_i > 50 \mu\text{M}$) but solely at high concentrations.

CYP2C19 inhibitors

(+)-N-Benzylirivanol

Compared to the most favorable inhibitor (-)-N-3-benzylpenobarbital, benzylirivanol exhibits significantly less selectivity, but is easier commercially available. It selectively inhibits CYP2C19 activity in HLM at maximum concentrations of 30 μM .^[89]

Ticlopidine

Ticlopidine also represents a potent inhibitor, but shows least selectivity of all mentioned inhibitors, as it also reduces activities of CYP2B6 (K_i : 0.2 μM ^[90]) and CYP2D6 (K_i : 0.4 - 10 μM).^[43]

CYP2D6 inhibitors

Quinidine

Quinidine is by far the most commonly used inhibitor of CYP2D6 isozyme exhibiting K_i values in the low micromolar range. However, it is also known as a weak inhibitor of the CYP2A family (K_i : 5.3 – 20 μM).^[43]

⁴ Mechanism-based inhibition typically results in an irreversible inhibition of the enzyme, thus, making it completely nonfunctional until new protein is synthesized.

CYP2E1 inhibitors4-Methylpyrazole

4-Methylpyrazole is an inhibitor of the CYP2E1 isoenzyme. However, it is known to inhibit CYP2A6 (K_i : 78 μM ^[91]) and CYP2C9 activity (K_i : 166 μM ^[92]) in human liver microsomes, but still is the most selective CYP2E1 inhibitor currently available.

Diethyldithiocarbamate, orphenadrine and clomethiazole are alternative CYP2E1 inhibitors, which are neither very selective nor well studied concerning their applicability.

CYP3A inhibitors

For the most part both isoforms of CYP3A, namely, CYP3A4 and CYP3A5, convert the same substrates, while CYP3A5 shows a slower turnover.

Ketoconazole

Ketoconazole is an antifungal drug that binds to the P450 heme via its azole nitrogen and represents the most frequently used inhibitor for CYP3A. However, its application is only selective if used in sub-micromolar concentrations. It inhibits all of the following enzymes as soon as concentrations in the micromolar range are used: CYP2A6, CYP2B6, CYP2C8, CYP2C9, CYP2C19, CYP2D6 and CYP2E1.^[43]

Azamulin

Stresser et al. suggest that azamulin is the best inhibitor for CYP3A inhibition showing at least 100-fold selectivity over other isoforms except for CYP2J2.^[93]

Troleandomycin is also a potent inhibitor but its selectivity towards other CYP isozymes is not well studied.

CYP2C8 inhibitorsMontelukast

For the competitive inhibitor Montelukast K_i values in the sub-micromolar range are reported.^[94] At higher concentrations it also suppresses the enzymatic activity of several other CYP450 isoforms: CYP3A4, CYP2C9, CYP2D6 and CYP2B6.

Another extensively studied but less selective inhibitor is quercetin. It also inhibits CYP1A1 and CYP1B1 in the sub-micromolar range, as well as CYP1A2, CYP2C19 and CYP2C9 in low micromolar concentrations. Other inhibitors of CYP2C8 are the so-called “insulin-sensitizers” of the thiazolidinedione group, namely, rosiglitazone and pioglitazone as well as the antibiotic agent trimethoprim and the fibrate gemfibrozil.^[43]

CYP2B6 inhibitors2-Phenyl-2-(1-piperidiny)propane (PPP)

It has been shown that if PPP is used in HLM incubations at a concentration of 30 μM only the desired CYP was inhibited almost exclusively. Other CYPs were affected in an extent accounting for less than 10% inhibition.^[95]

Ticlopidine

Ticlopidine is a known substrate of CYP2B6, but it primarily inhibits the isoenzyme CYP2C19.

Furthermore, clopidogrel, sertraline and amlodipine are alternative but less selective inhibitors of CYP2B6.

CYP2A6 inhibitors

When studying extrahepatic metabolism it has to be taken into consideration, that CYP2A6 and CYP2A13 have a marked sequence homology (93.5%), whereas the latter one can only be found in extrahepatic tissues.^[96]

Tranlycypromine

Tranlycypromine, especially the (R)-isoform, is a potent inhibitor showing acceptable selectivity towards CYP2A6. At higher than sub-micromolar concentrations it also affects the following CYPs: CYP1A2, CYP2C19, CYP2C8, CYP2C9, CYP2D6 and CYP2E1. Efforts are made concerning the evaluation of new inhibitors superior to tranlycypromine in respect to selectivity. Promising candidates are 3-(2-Methyl-1H-imidazol-1-yl)pyridine (MIP) and 3-(Pyridin-3-yl)-1H-pyrazol-5-yl)methanamine (PPM) but their commercial access is well limited.^[43]

1.6.3 Biotransformation in rats and chemical inhibitors for RLM

As already mentioned for the drug metabolism in humans, the same three subfamilies – CYP1, CYP2 and CYP3 – are responsible also for the biotransformation of xenobiotics in rats.^[97]

Hitherto, it is still challenging to determine the role of a CYP450 isoform in metabolism of a tested drug in rat liver microsomes by chemical inhibition. The main reason for this lies in the insufficient number of investigations in this area of research.

Moreover, it has been shown that chemical inhibitors of human CYP450 isozymes are not always selective for the corresponding rat isoform. Especially ketoconazole and quinidine showed little effect and minor selectivity towards the respective rat CYP3A and CYP2D6 isoforms.

In contrast, sulfaphenazole exhibits high selectivity for rat CYP2C6, when used in the low micromolar concentration range. In addition, furafylline can be used as a potent inhibitor of CYP1A2 in rat liver microsomes. Even concentrations $> 1 \mu\text{M}$ do not affect CYP2D2, CYP2E1 and CYP3A1 activity, but may result in additional inhibition of CYP2C6.^[98]

Table 6 lists a range of inhibitors which can be used for rat liver microsomes according to previously published work.^[99-109]

Inhibitors not well studied concerning their effects on rat liver microsomes include 4-methylpyrazole and ticlopidine, which are primarily known for their evident applicability in human liver microsomes.

Table 6: Inhibitors for RLM; cross-reactivity should be avoided in the given concentration range.

Rat CYP isoform	Inhibitor	Recommended conc. range [μM] ^[110]
CYP1A2	α -Naphthoflavone	0.5 – 4
	Furafylline	< 1
CYP2A1	Pilocarpin	2.5 - 20
CYP2B1	Orphenadrine	2.5 - 20
	Antirat CYP2B1 antibody	-
CYP2C6	Sulfaphenazole	5 – 40
	Furafylline	-
	Quinidine	0.1
CYP2C11	Cimetidine	1 – 10
	Fluoxetine	-
	Antirat CYP2C11 antibody	-
	Sulfaphenazole	-
	Ticlopidine ^[108]	-
CYP2D1	Quinidine	2.5 – 20
CYP2D1/2	Quinine	-
CYP3A1/2	Ketoconazole	0.5 – 4 , nonselective
	Clotrimazole	nonselective
CYP3A2	Antirat CYP3A2 antibody	-
CYP2E1	Diethyldithiocarbamate	12.5 – 100
	4-Methylpyrazole ^[108]	-

1.7 AIM of the thesis

Preclinical and clinical studies in non-human as well as human brain have clearly demonstrated the utility of (*S,S*)-[¹⁸F]FMeNER-D2 as a PET radioligand for the visualization of the NET.^[35, 111-115] An important prerequisite for its application is its selectivity towards NET ($K_i = 3.1$ nM) compared to other monoamine receptors such as 5-HTT and DAT (both: $K_i > 1000$ nM).^[31] However, as a result of a low signal to noise ratio, a proper quantification of the NET signal is hampered in various brain regions. Accumulation of radioactivity in bone marrow is thought to be the main cause for restricted PET image quality and, up to now, there is a broad consensus about defluorination being the underlying mechanism.^[31, 114] Still, the evaluation of the thalamus, an important NET-rich region, within the scope of diverse neuropathological diseases using this tracer is feasible. Further ambitious goals in NET research are the visualization of the multiple nuclei of the thalamus and their connections to associated cortical areas as well as an improved quantification of NET densities in the locus coeruleus (LC). The major prerequisites for achieving these objectives are on the one hand clinical implementation of high-resolution PET scanners and on the other, a suitable NET-PET tracer with high specific binding. Even though [¹⁸F]FMeNER-D2 is showing the abovementioned restrictions, it is a routinely available, clinically advanced PET tracer. Therefore, it is worth investigating the metabolic fate of this tracer to identify the involved mechanisms, which restrain its stability. An intervention in such biodegradation mechanisms might be able to enhance bioavailability *in vivo*, which may allow an improved quantification of NET in wider areas of the human brain.

Thus, the major goal of the thesis was to give a detailed characterization of [¹⁸F]FMeNER-D2 central and peripheral metabolism *in vitro*. The hypothesis about extensive defluorination as the major cause for the observed bone uptake should be verified or falsified and a discussion about the exact nature of the binding structures other than NET and the bound species should be induced.

Therefore, *in vitro* tests were performed using single enzyme incubations as well as hepatic multi-enzyme complexes in combination with chemical inhibitors to identify the responsible isoenzymes. The intact tracer as well as the arising metabolites were tested for binding to inorganic bone mineral (hydroxyl apatite) or human diaphyseal osseous matter. Attempts were made to characterize and identify the formed metabolite species. A better understanding of the enzymatic reactions reducing tracer stability *in vivo* and the identification of the disturbing radioactive species might enable potential measures against these unspecific accumulations hampering PET image interpretation.

Nevertheless, application of [¹⁸F]FMeNER-D2 is accompanied by some restraints such as low signal to noise ratio, as a consequence of limited specific binding and reduced sensitivity as well as gradual kinetics.^[26, 36, 116] Hence, it is still reasonable to continue with the search for alternative NET-PET tracers, which meet these requirements. Another promising class of substances are based on a benzo[*d*]imidazole core structure whose hitherto only representative [¹¹C]Me@APPI has shown remarkable selectivity to NET comparable to [¹⁸F]FMeNER-D2. The intention of the thesis was therefore, to expand this group of substances for another two representatives, which are estimated to have higher affinity towards NET than towards DAT or SERT based on preceding

in silico calculations.^[117] The structural modifications performed on [¹¹C]Me@APPI were the fluorination of either the aromatic core structure or the aromatic side-chain.

2 EXPERIMENTAL PART I – Metabolism studies

2.1 Materials

The precursor (*S,S*)-NER [= (*S,S*)-norethyl-reboxetine = (2*S*,3*S*)-2-[α -(2-hydroxyphenoxy)benzyl]-morpholine) was obtained from PharmaSynth AS (Tartu, Estonia).

Acetonitrile ($\geq 99.9\%$ (GC)) and ACN (HPLC grade), methanol (CHROMASOLV[®], for HPLC, $\geq 99.9\%$), ethanol, dimethylformamide (DMF, p.a.), sodium hydroxide, ammonium formate, hydroxyapatite (reagent grade), dibromomethane-d₂ (99 atom%D, copper stabilized) and Kryptofix K2.2.2 (4,7,13,16,21,24-hexaoxa-1,10-diazabicyclo[8.8.8]hexacosane) were purchased from Sigma-Aldrich (Vienna, Austria). Sterile water was obtained from a MilliQ water purification system (Merck Millipore, Germany). Phosphate buffer (125 mM) was prepared by dissolving 0.224 g sodium dihydrogenphosphate-monohydrate and 1.935 g disodiumhydrogenphosphate-dihydrate (both from Merck, Darmstadt, Germany) in 100 mL sterile water. Kryptofix solution was prepared taking 440 mg of crypt-222 and 90 mg of potassium carbonate dissolved in 16 mL ACN and 4 mL water. The following inhibitors for chemical inhibition assays were acquired from Sigma Aldrich (Vienna, Austria): quinidine (cystallized, $\geq 98\%$, ca. 10% hydroquinidine^[118])⁵, montelukast sodium (EP-reference standard), ketoconazole (EP-reference standard), 4-methylpyrazole hydrochloride ($\geq 95\%$), furafylline ($\geq 98\%$, HPLC), (+)-*N*-3-benzylirivanol ($\geq 98\%$, HPLC), sulfaphenazole ($\geq 98\%$), ticlopidine hydrochloride (EP-reference standard). 2-Phenyl-2-(1-piperidinyl)propane was purchased from abcam[®] (Cambridge, UK).

Chemicals and solvents, which are not particularly mentioned above were received from Merck (Darmstadt, Germany) and Sigma-Aldrich (Vienna, Austria) having at least analytical grade and were therefore used without further purification.

6-[¹⁸F]Fluoro-L-DOPA (0.3 GBq/mL solution for injection) and fluorocholine [¹⁸F]-chloride (1 GBq/mL solution for injection) for bone binding experiments were purchased from IASON GmbH (Graz-Seiersberg, Austria). All other radioactive tracers were synthesized at the Department of Biomedical Imaging and Image-Guided Therapy, Division of Nuclear Medicine, Medical University of Vienna.

Purified diaphyseal bone material was obtained from the central bone bank (Vienna Austria) and grinded manually (80 μ m, date: 09.11.2012). Frozen hepatic human microsomes and rat microsomes from Sprague Dawley rats (pooled HLM and RLM; 20 mg/mL in 250 mM sucrose) for stability assays were obtained from BD Biosciences (NJ, USA) and stored at -80°C until use. NADPH-regenerating system, including solution A (26 mM NADP⁺, 66 mM Glucose-6-phosphate, 66 mM MgCl₂ in H₂O) and solution B (40 U/mL glucose-6-phosphate dehydrogenase in 5 mM sodium citrate) was obtained from Corning[®] (NY, USA). Single enzyme preparations were purchased from Sigma Aldrich in the case of CYP3A4, CYP2E1, CYP1A1 and CYP1B1 as well as monoamine oxidase

⁵ Quinidine and its impurity hydroquinidine are both important inhibitors of CYP2D6.

A or B, catechol-*O*-methyl transferase (porcine) and carboxylesterase (porcine). The remaining CYP450 isozymes 2D6, 2A6 and 2C19 and human carboxylesterases 1b, 1c and 2 were received from Corning® (NY, USA).

Anion exchange cartridges (PS-HCO₃) for the adsorption of [¹⁸F]fluoride were purchased from Macherey-Nagel (Dueren, Germany). Solid phase extraction was carried out using C18 plus Sep-Pak® cartridges and Silica plus Sep-Pak® cartridges obtained from Waters Corporation (Milford, USA). The end-product was formulated with 0.9% saline solution from B. Braun (Melsungen, Germany), 3% saline solution (Landesapothek Salzburg, Austria) and phosphate buffer (125 mM). Millex® sterile filters (GS 0.22 µm) for the delivery of the product were obtained from Millipore (Bedford, USA).

2.2 Instrumentation

The PET nuclide [¹⁸F]Fluoride was produced within a GE PET trace cyclotron (GE Medical Systems, Uppsala, Sweden) via ¹⁸O(p,n)¹⁸F reaction (16.5 MeV protons). H₂¹⁸O enriched water was obtained from Rotem Europe (Leipzig, Germany). Automated synthesis was performed in a Nuclear Interface synthesizer (GE Healthcare, Sweden) which was remotely operated by a laptop equipped with designated software.

Semi-preparative RP-high-performance liquid chromatography (RP-HPLC) for the on-line purification of the crude [¹⁸F]FMeNER-D2 was carried out using a system consisting of a LaPrep HPLC pump (VWR International, Radnor, USA), a radioactivity- and a UV-detector (Linear Instruments Model 200 Detector). The chromatographic separation system included a TMS-endcapped C18 Phenomenex® Gemini column (250 x 100 mm, 10 µm; Phenomenex®, Aschaffenburg, Germany) and a mobile phase of MeOH/0.1 M ammonium formate (AMF) in water 50/50% v/v at a flow rate of 12 mL/min.

Analytical RP-HPLC analyses were performed on a Merck-Hitachi LaChrom HPLC system equipped with an isocratic pump (L-7100), a degasser, a UV detector (LaChrom L-7400, at 254 nm), a gamma detector (NaI radiodetector, Berthold Technologies, Bad Wildbach, Germany) using Raytest software (Raytest, Straubenhardt, Germany) and an autosampler. The applied chromatographic system was composed of a Phenomenex Prodigy Phenyl-PH3 column (250 x 4.6 mm, 5 µm; Phenomenex®, Aschaffenburg, Germany) and a mobile phase of ACN/0.1 M AMF in H₂O 50/50% v/v employing 1.5–2 mL/min flow rate. Radio-thin layer chromatography (TLC) was performed on silica gel 60 RP-18 F₂₅₄S plates from Merck (Darmstadt, Germany) using a mobile phase consisting of ACN/water 70/30% v/v. Analyses of radio TLC plates was done on a Canberra-Packard Instant Imager (Perkin Elmer, Watford, UK).

Measurements for bone binding experiments were carried out on a Perkin Elmer 2480 Wizard² automatic gamma-counter (Perkin Elmer, USA).

Data processing was performed with Microsoft Excel 2013 and SPSS 15.0 for Windows.

2.3 Methods

Enzymatic experiments were carried out via degradation of radioactive [^{18}F]FMeNER-D2, which was synthesized according to the previously published procedure of *Rami-Mark et al.* (2013) which is based on work of *Schou et al.* (2004).^[31, 119] The radioactive tracer had to be freshly prepared for every metabolic experiment (*Figure 10*).

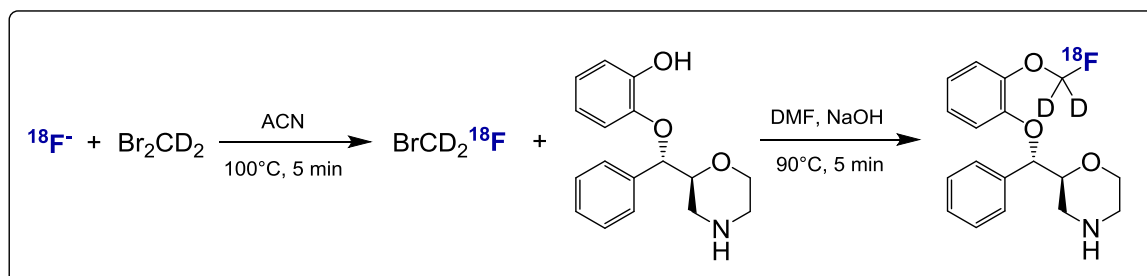


Figure 10: Synthesis steps for preparation of [^{18}F]FMeNER-D2.

2.3.1 Synthesis of [^{18}F]FMeNER-D2

The synthesis of [^{18}F]FMeNER-D2 was performed in a Nuclear Interface synthesizer, following the flow scheme in *Figure 11*.

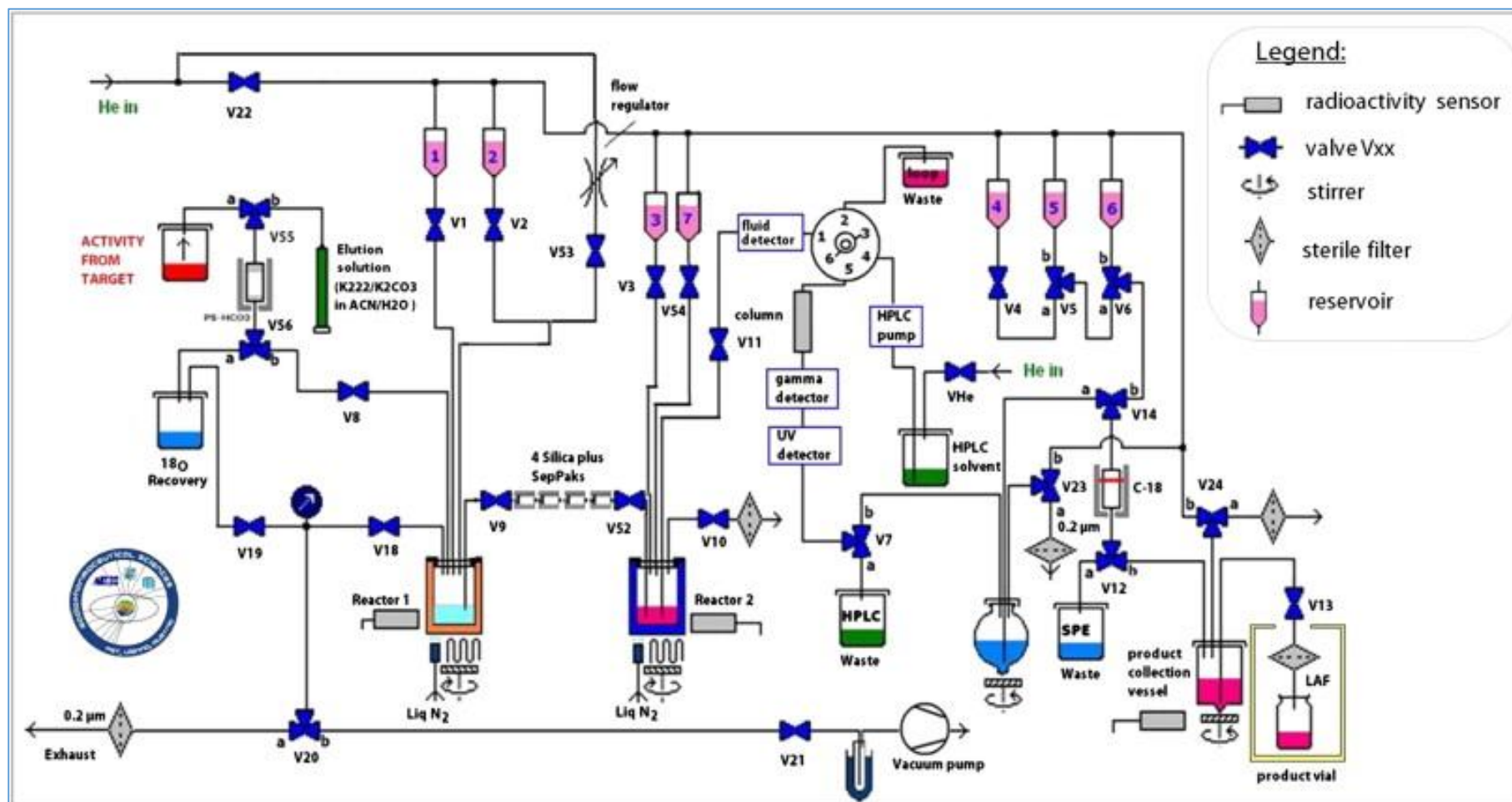


Figure 11: Process flow chart of $[^{18}\text{F}]\text{FMeNER-D2}$ synthesis.

2.3.1.1 Preparations of the hot cell

Storage vessels V1-V3 and transfer tubings were rinsed thrice with each water, acetonitrile and acetone (see *Figure 11*). V4 and V6 were washed twice with water, while V5 was flushed with EtOH. All tubings were dried under He-stream and the reactor 1 was dried using an external argon stream. All vessels, including the product collection vial (PCV), were equipped with the required solutions given below. The Sep-Pak[®] was preconditioned using 10 mL EtOH and 20 mL of water. The preparative HPLC column was equilibrated with the mobile phase starting with 2 mL/min flow rate progressing to 10 mL/min for 10 min while the pressure of the HPLC pump was checked.

2.3.1.2 Synthesis and preparation of [¹⁸F]fluoride

30 – 40 GBq of [¹⁸F]fluoride were produced within the cyclotron, transferred into the lead shielded cell and connected to V55 (*Figure 11*). Radioactive fluoride was trapped on an anion exchange cartridge (PS-HCO₃) using a vacuum pump (V55(a)→V56(a)→TW Waste→V19→V20(b)→V21), whereby the ¹⁸O-enriched water was collected in an interconnected target water vial (TW Waste) for recovery. It was eluted from the trap into reactor 1 (V55(b)→V56(b)→V8→V18→V20(b)→V21) with 0.7 mL of a crypt-222 solution (58.4 mM Kryptofix 2.2.2, 32.6 mM K₂CO₃ in ACN/"trace select H₂O" 80/20% v/v).

2.3.1.3 Azeotropic drying

Subsequently, [¹⁸F]fluoride was azeotropically dried by heating the reactor to 100°C and applying a slight He-stream of 40 – 50 mL/min via V53. Following 3 min of evaporation time, the temperature was raised to 110°C for 2 min and further to 120°C for another 2 min. The reactor was cooled to 40°C before addition of 0.6 mL ACN via the same way as the elution solution. After another drying cycle the last portion of ACN was transferred into reactor 1 from vial 1 (He from V22→V1→V18→V20(b)→Exhaust), evaporated to dryness and cooled to 20°C.

2.3.1.4 Synthesis of 1-bromo-2-[¹⁸F]fluoromethane-d₂ ([¹⁸F]BFM)

Dibromomethane-d₂ stored in V2 (50 µL in 500 µL ACN) was added and after manual closure of the exhaust valve (V18) the reaction vessel was heated to 100°C for 5 min. During this reaction time, the reactor 2 - containing 400 µL DMF - was cooled to -20°C. Subsequently, the reactor 1 was cooled to 24°C and the formed radioactive BFM was distilled into reactor 2 over four silica plus Sep-Pak[®] cartridges connected in series. A gentle supportive He-stream was applied (V53→V9→V52→V10) after manual opening of all of the four valves. The initial flow rate of 10 mL in the first minute was raised to 40 mL/min for the main part of the distillation process varying between 7 – 15 min. Trapping in liquid nitrogen-cooled DMF (at -20 to -50°C) was achieved by bubbling the gaseous He-BFM mixture through a PEEK tubing (V52).

2.3.1.5 Synthesis of [¹⁸F]FMeNER-D2 and formulation of the product

After reaching a plateau of activity in reactor 2, the distillation was stopped including manual closure of V52 and precursor (*S,S*)-NER (1 – 1.2 mg in 200 µL DMF + 6 µL 5M NaOH via vial 3) was transferred into reactor 2. The reaction mixture was immediately sealed by hand (V10) and nucleophilic substitution was performed for 5 min at 90°C. The crude reaction mixture was cooled to 25°C and quenched by addition of 1 mL water via V54. The raw product mixture was injected

onto the preparative HPLC column (Phenomenex® Gemini, MeOH/0.1 M AMF 50/50 % v/v) using a fluid detector and applying a flow rate of 12 mL/min. At the expected retention time, when the measured activity at the gamma-detector had risen above 100 cps, the peak was cut manually into the bulb containing 80 mL water. The diluted pure product was transferred over a C18 plus Sep-Pak® cartridge (V23(b)→V14(a)→V12(a)) and washed with 10 mL water from V6 (V6(b)→V14(b)→V12(a)). Elution of the product into the product collection vessel (PCV) was accomplished via 1.5 mL EtOH from V5 (V5(b)→V6(a)→V14(b)→V12(b)→V24(a)). The PCV already contained 4 mL 0.9% saline, 1 mL 3% saline and 1 mL 125 mM phosphate buffer. After the tubings were washed into the PCV with further 5 mL 0.9% saline from vial 4, the solution was filtered over a sterile filter (0.22 µm, Millex®) into a sealed and sterile vial (20 mL, pressure compensation via sterile air-filter (22 µm, Millex®) containing another 5 mL of 0.9% saline. This final formulation of our product comprised 8.5% of organic solvent (EtOH) in a total volume of 17.5 mL.

Quality control

Radiochemical purity was determined by analytical HPLC and TLC. Chemical purity was analyzed by analytical HPLC using UV detection. Specific activities were ranging from 150 – 1400 GBq/µmol.

Since the product was not administered to study participants but was only used for *in vitro* experiments, a GC analysis for the quantification of organic solvents as well as osmolarity and pH measurements were not required.

2.3.2 Enzyme assays

2.3.2.1 General procedure

All of the described enzymatic tests were carried out on a shaking water bath (450 rpm) at 37°C and were initiated by the addition of the radioactive tracer [¹⁸F]FMeNER-D2. Aliquots were taken after defined time intervals and quenched by 1:1 dilution with ice-cold ACN/MeOH (9/1) solution. After centrifugation of the samples for 5 min at 22 600 g, the supernatant was analyzed by RP-HPLC. Each incubation mixture was at least performed in duplicates while using the enzyme-free mixture at the same time as a reference.

2.3.2.2 Microsomal multi-enzyme assays

HLM and RLM

All incubations were carried out in a 100 µM phosphate buffer (for HLM) or phosphate buffered saline (PBS; for RLM) containing HLM or RLM (0.3 mg/mL), 3.3 mM MgCl₂, 1.3 mM β-NADP, 3.3 mM glucose-6-phosphate and 1.0 U/mL glucose-6-phosphate dehydrogenase. The mixtures were pre-incubated for 5 min at 37°C and then the metabolic degradation process initiated by addition of 10 µL of the freshly prepared [¹⁸F]FMeNER-D2.

Concentrations of the required stock solutions are given in *Table 7 and 8*.

Table 7: Components of stock solution A (on the left) and stock solution B (on the right)

Substance	Conc. [mM]	Substance	Amount
NADP ⁺	26	Glc-6-P-DH	40 U/mL
Glucose-6-P	66	NADP ⁺ Reductase	0.48 µmol/(min*mL)
MgCl ₂	66	Na-citrate	5 mM
NADP ⁺ Reductase	0.34 µmol/(min*mL)		

Table 8: Microsomal incubation batch

Solution	Amount [µL]
PBS	257
Solution A	15
Solution B	3
Microsomes	15
Tracer	10

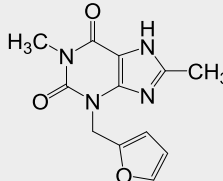
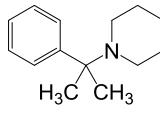
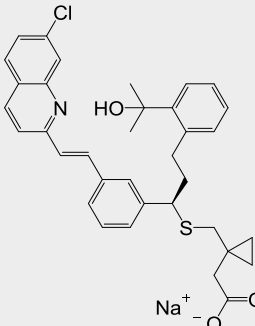
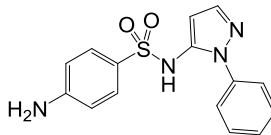
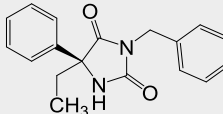
2.3.2.3 Chemical inhibition experiments

Inhibition assays in RLM and HLM were performed according to the abovementioned microsomal incubations using three concentrations of each inhibitor in one series. The concentration of organic solvent (DMSO or EtOH) was equal to the batch with the highest concentration of inhibitor (see appendix: *Table 53*). For each assay, a stock solution of the respective inhibitor was prepared.

Multi-enzyme complexes with inhibitor and the NADPH regenerating system at 37°C was extended to 30 min to guarantee a sufficient inhibition of the respective single enzyme, before addition of the radioactive tracer.

The chemical inhibitors used and the tested concentration range were as follows (Table 9)^[81]:

Table 9: Chemical inhibitors for CYP450 isozymes.

CYP	Inhibitor	M [g/mol]	Concentration range [μM]	Structure
1A2	Furafylline	260.25	20 – 100 (HLM) 20 – 100 (RLM)	C ₁₂ H ₁₂ N ₄ O ₃ 
2B6	2-Phenyl-2-(1-piperidinyl)-propane	203.32	10 – 50 (HLM) 10 – 50 (RLM)	C ₁₄ H ₂₁ N 
2C8	Montelukast.Na	608.17	10 – 100 (HLM) 1 – 10 (RLM)	C ₃₅ H ₃₅ ClINNaO ₃ S 
2C9	Sulfaphenazole	314.36	10 – 50 (HLM) 10 – 50 (RLM)	C ₁₅ H ₁₄ N ₄ O ₂ S 
2C19	(+)-N-3-Benzylnirvanol	294.35	2 – 100 (HLM) 2 – 100 (RLM)	C ₁₈ H ₁₈ N ₂ O ₂ 

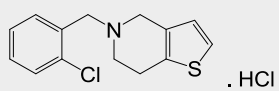
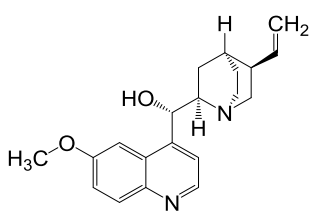
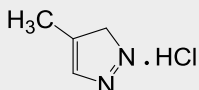
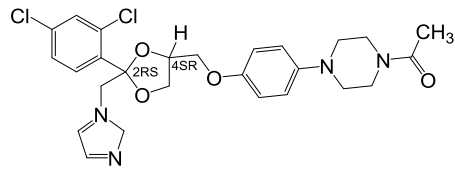
CYP	Inhibitor	M [g/mol]	Concentration range [μ M]	Structure
	Ticlopidine.HCl	300.25	10 – 100 (HLM) 10 – 200 (RLM)	$C_{14}H_{15}Cl_2NS$ 
2D6	Quinidine	324.42	0.4 – 20 (HLM) 5 – 50 (RLM)	$C_{20}H_{24}N_2O_2$ 
2E1	4-Methyl-pyrazole.HCl	118.56	5 – 20 (HLM) 1 – 10 (RLM)	$C_4H_7ClN_2$ 
3A4	Ketoconazole	532.43	2 – 100 (HLM) 2 – 100 (RLM)	$C_{26}H_{29}ClN_4O_4$ 

Table 10 and *Table 11* give a short overview on the completed assays for each inhibitor in human or rat liver microsomes. Details about assay preparations are given in the appendix (see chapter 9.1.1).

Table 10: HLM Inhibition assay.

Inhibitor	Batch-#	Conc. [μ M]	Replicates
Furafylline	8	20, 50, 100	2
2-Phenyl-2-(1-piperidinyl)propane	6	10, 20, 50	1
Montelukast.Na	7	10, 50, 100	1
Sulfaphenazole	6	10, 20, 50	1
Ticlopidine	7	10, 50, 100	1
	9	50, 100, 200	1
(+)-N-Benzylnirvanol	8	20, 50, 100	2
Quinidine	1	0.4, 0.8, 2	1
	2	1, 2, 5	1
	5	5, 10, 20	1
4-Methylpyrazole.HCl	5	5, 10, 20	1
Ketoconazole	4	2, 5, 10	1
	8	20, 50, 100	2

Table 11: RLM inhibition assays.

Inhibitor	Batch-#	Conc. [μ M]	Replicates
Furafylline	8	20, 50, 100	1
2-Phenyl-2-(1-piperidinyl)propane	6	10, 20, 50	1
Montelukast.Na	3	1, 5, 10	1
Sulfaphenazole	6	10, 20, 50	1
Ticlopidine	7	10, 50, 100	1
	9	50, 100, 200	1
(+)-N-Benzylnirvanol	8	20, 50, 100	2
Quinidine	5	5, 10, 20	1
	6	10, 20, 50	1
4-Methylpyrazole.HCl	3	1, 5, 10	1
Ketoconazole	4	2, 5, 10	3
	8	20, 50, 100	1

2.3.2.4 Single enzyme assays

2.3.2.4.1 CYP450

Single-enzyme incubations were carried out based on standard procedures.^[120] The assays contained the tested enzyme, $MgCl_2$, β -NADP, glucose-6-phosphate and glucose-6-phosphate dehydrogenase in defined concentrations given below (*Table 12 - Table 18*). Incubations were performed in phosphate buffered saline (PBS), sodium phosphate (PB, 50 or

100 mM) or Tris (50 mM) buffer, depending on the respective CYP isozyme. Stock solutions of Solution A and B had the same concentrations as mentioned above (see *Table 7*). To gain higher evidence about metabolic stability the concentrations of the enzymes were raised in certain experiments.

CYP1A1 (+ P450 reductase)

Enzyme stock: 10 mg/mL protein; 420 pmole/mL CYP1A1.

Table 12: CYP1A1 batch, 300 μ L.

Solution	Amount [μ L]
PB (100 mM) or PBS	257
Solution A	15
Solution B	3
Enzyme	15
Tracer	10

CYP1B1 (+ P450 reductase)

Enzyme stock: 6.5 mg/mL protein; 1000 pmole/mL CYP1B1.

Table 13: CYP1B1 batches, 300 μ L (left) and 1000 μ L (right).

Solution	Amount [μ L]	Solution	Amount [μ L]
PB (100 mM)	266	PBS	970
Solution A	15	Solution A	12.5
Solution B	3	Solution B	2.5
Microsomes	6	Microsomes	5
Tracer	10	Tracer	10

CYP2A6 (+ P450 reductase + cytochrome b₅)

Enzyme stock: 2.2 mg/mL protein; 1000 pmole/mL CYP2A6.

Table 14: CYP2A6 batch, 500 μ L.

Solution	Amount [μ L]
50 mM Tris (pH 7.4)	450
Solution A	25
Solution B	5
Microsomes	10
Tracer	10

CYP2C19 (+ P450 reductase + cytochrome b₅)

Enzyme stock: 3.2 mg/mL protein; 1000 pmole/mL CYP2C19.

Table 15: CYP2C19 batch, 300 µL.

Solution	Amount [µL]
50 mM PB (pH 7.4)	245
Solution A	25
Solution B	5
Microsomes	15
Tracer	10

CYP2D6*1 (+ P450 reductase)⁶

Enzyme stock: 8.7 mg/mL protein; 1000 pmole/mL CYP2D6.

Table 16: CYP2D6 batches, 1000 µL (left) and 300 µL (right).

Solution	Amount [µL]	Solution	Amount [µL]
100 mM PB (pH 7.4)	950	100 mM PB (pH 7.4)	250
Solution A	25	Solution A	25
Solution B	5	Solution B	5
Microsomes	10	Microsomes	10
Tracer	10	Tracer	10

CYP2E1 (+ P450 reductase + cytochrome b₅)

Enzyme stock: 1000 pmole/mL CYP2E1.

Table 17: CYP2E1 batches, 500 µL (left) and 300 µL (right).

Solution	Amount [µL]	Solution	Amount [µL]
PBS	410	PB (50 mM)	210
Solution A	25	Solution A	25
Solution B	5	Solution B	5
Microsomes	50	Microsomes	50
Tracer	10	Tracer	10

⁶ Both preparations contain CYP2D6 catalytic activity considerably higher than in HLM.

CYP3A4 (+ P450 reductase + cytochrome b₅)

Enzyme stock: 1000 pmole/mL CYP1A1.

Table 18: CYP3A4 batches, 500 μ L (left) and 300 μ L (right).

Solution	Amount [μ L]	Solution	Amount [μ L]
PBS	450	PBS or PB (100 mM)	257
Solution A	25	Solution A	15
Solution B	5	Solution B	3
Microsomes	10	Microsomes	15
Tracer	10	Tracer	10

A different incubation medium quoted in previous work uses Tris-H₂SO₄ (118mM) and MgSO₄ (0.5 mM) for CYP3A4 assays.^[121]

2.3.2.4.2 MAO A and MAO B

Incubation mixtures with human, recombinant monoamine oxidase A or B were carried out applying two different enzyme concentrations [100 μ g/mL (22 U/mL) or 800 μ g/mL (176 U/mL)] in 100 mM sodium phosphate buffer with pH 7.4 according to *Table 19*.^[65]

Enzyme stock: 5 mg/mL (220 U/mg protein).

Table 19: MAO A/B incubation mixtures, 1000 μ L (left) and 250 μ L (right) batch.

Solution	Amount [μ L]	Solution	Amount [μ L]
PBS	970	PB (100 mM, pH 7.4)	200
Enzyme	20	Enzyme	40
Tracer	10	Tracer	10

2.3.2.4.3 Catechol-O-methyltransferase (COMT)

The purified COMT (porcine liver) was dissolved in 1 mL of buffer-#1 containing 25 mM sodium phosphate buffer (PB, pH 7.8) and 0.5 mM dithiothreitol. A 90 μ L aliquot (batch-#A) or 90 μ L of its dilution (1:9, batch-#B) was incubated in 250 μ L sodium phosphate buffer (25 mM, pH 7.8) containing 2 mM MgCl₂ and 500 μ M SAME for batch-#A, and 0.8 mM MgCl₂ and 200 μ M SAME for batch-#B, respectively. The mixture was incubated at 37°C for 30 min in a shaking water bath before the tracer was added. After t = 30, 60, 120, 180 and 240 min of incubation time the reaction was terminated using a 50 μ L aliquot and adding an equal volume of cold ACN/MeOH (9/1) (see *Table 20 - Table 22*).

Table 20: Resulting concentrations for COMT assays.

Batch-#	A	B	Reference
BP [mM]	25	25	25
pH	7.8	7.8	7.8
Enzyme [U/mL]	19.3	1.9	0
SAM [μ M]	357	143	357
MgCl ₂ [mM]	1.4	0.6	1.4
DTT [μ M]	130	130	130

Table 21: Stock solutions for COMT incubation assays.

Buffer-#	PB [mM]	DTT [mM]	pH	MgCl ₂ [mM]	SAM [μ M]	COMT [U/mL]	Preparation
0	25		7.8				
1	25	0.5	7.8				
2	25		7.8	2	500		
3	25		7.8	0.8	200		buffer-#2 diluted with buffer-#0: 1/1.5
4	25	0.5	7.8			75	0.5 mg of COMT dissolved in 1 mL buffer-#1
5	25	0.5	7.8			7.5	dilution of buffer-#4 1:9

Table 22: Preparation of COMT incubations using stock solutions given above (Table 21).

Buffer-#	Batch-#				Reference ref
	A		B		
	1	2	1	2	
#1 [μ L]					90
#2 [μ L]	250	250			250
#3 [μ L]			250	250	
#4 [μ L]	90	90			
#5 [μ L]			90	90	
Tracer [μ L]	10	10	10	10	10
Vol [μ L]	350	350	350	350	350

2.3.2.4.4 *Human carboxylesterases (hCES)*

The effect of human carboxylesterases (hCES) on the stability of [¹⁸F]FMeNER-D2 was examined using a one-pot mixture of the specific isoforms hCES 1b, 1c and 2 according to the assay in Table 23.

Stock solutions: 5 mg/mL protein.

Table 23: hCES batch, 300 μ L.

Solution	Amount [μ L]
Phosphate buffer (100 mM, pH 7,4)	270
Enzyme each (3x)	3 x 8
Tracer	6

2.3.2.4.5 Porcine carboxylesterase (CE, porcine)

The tested enzymatic incubations contained 80 IU/mL of porcine carboxylesterase under physiological conditions (PBS, pH 7.4, 37°C) (Table 24).^[122]

Stock solution: 3.7 mg/mL esterase (100 U/mL)

Table 24: porcine CE-batch, 500 μ L.

Solution	Amount [μ L]
PBS	90
Enzyme	400
Tracer	10

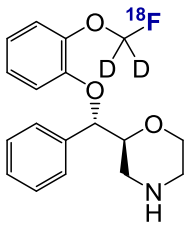
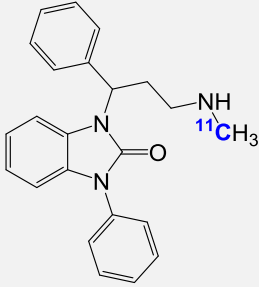
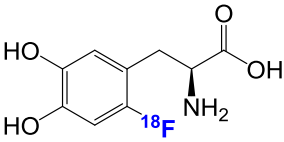
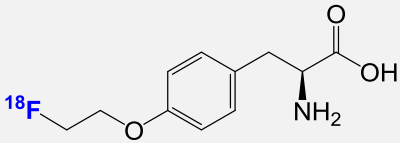
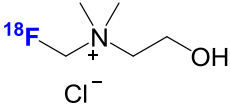
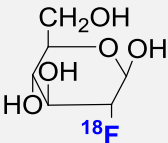
2.3.3 Bone binding studies

To find out whether bone matter represents the preferred compartment for our radiotracer or its metabolites, incubations of [¹⁸F]FMeNER-D2 using hydroxyapatite (HA) or grounded diaphysis were performed. The proportion bound to bone matrix was compared to clinically used tracers as well as some research tracers. The examined tracers and their structures are listed in Table 25.

An amount of 3 mg of HA or diaphysis was suspended in 245 μ L phosphate buffered saline (PBS) before 5 μ L of the respective tracer were added. After determination of the exact activity of each batch with a gamma counter, the suspensions were incubated at 37°C and 450 rpm in a thermomixer for 30, 60 or 90 min. After the defined time intervals, the incubation mixtures were centrifuged and the pellet was washed twice with buffer. The pellet, the supernatant and the washing solutions were measured in a gamma counter and the percentage of binding to bone or HA was determined for each radiotracer.

Attempts to gain information about the binding affinity of metabolites of [¹⁸F]FMeNER-D2 were made using the supernatant of rat liver microsomes (RLM) containing fully metabolized tracer after precipitation of biological material with ACN or cold H₂O and subsequent centrifugation. Water was used for precipitation as a reference to see whether organic solvents (up to 1%) have an influence on bone binding.

Table 25: Radioactive tracers tested for their binding properties to bone or hydroxyapatite as its inorganic mineral.

[¹⁸F]FMeNER-D2	
[¹¹C]Me@APPI	
6-[¹⁸F]Fluoro-L-DOPA	
[¹⁸F]FET	
[¹⁸F]Fluorocholine chloride	
[¹⁸F]FDG	
Sodium [¹⁸F]fluoride	$\text{Na}^{+}\text{18F}^{-}$

3 RESULTS and DISCUSSION I

3.1 Synthesis of [¹⁸F]FMeNER-D2

In a total of 22 radiosyntheses mean radiochemical yields of 0.6 ± 0.3 GBq ($3.5 \pm 1.5\%$ corrected for decay) were obtained.⁷ Reaction times from the end of target bombardment to the delivery of the final product accounted for 103 ± 7.0 min. Radiochemical and chemical purity exceeded 98% in every synthesis. In TLC and analytical HPLC the amount of [¹⁸F]fluoride and [¹⁸F]BFM was quantified as $\leq 1\%$.

Trapping on the [¹⁸F]fluoride cartridge was found to work better than the subsequent elution using crypt.-222 when comparing the activities found in the target water waste and the remnant activity on the cartridge after elution (see *Table 26*). Besides, the transfer of activity from the target vial into reactor 1 involved a loss of up to 41% of the produced activity in some hitherto unknown way, but is assumed to be attributed to fluoride-18 sticking to the tubings. In the following azeotropic drying procedure greater losses could be observed which is indicated by the amount of activity in the exhaust vial of reactor 1 (see *Table 26*). In about half of the syntheses more than 2 GBq (up to 10 GBq, corrected for decay) could be detected in the exhaust vial due to superheating effects which represents an average loss of $9.5 \pm 11.1\%$ of the starting activity. This marked reduction of radioactivity in the reaction system might be caused by an inappropriately low He-flow (up to 50 mL/min) during the reaction. Moreover, higher filling volumes were thought to be the reason for higher activities detected in the exhaust vial. However, not only reactions when reactor 1 was equipped with 100 μ L acetonitrile prior to transfer of radioactive [¹⁸F]fluoride lead to an overflow into the exhaust. In some cases an overflow could be observed when [¹⁸F]fluoride was eluted from the cartridge but was not associated with a higher filling volume. These observations suggest an influence of the transfer velocity or the position of tubings in reactor 1, which may have been adjusted at a level, which was too low for the achieved filling volume. The use of additional ACN in reactor 1 intended to improve the drying of [¹⁸F]fluoride for the following reaction step. Though, no increase in trapped [¹⁸F]BFM could be obtained via this simple modification in synthesis conditions.

In this series of syntheses it could be confirmed that, besides the drying of [¹⁸F]fluoride, the crucial step of the reaction was the distillation step of [¹⁸F]BFM. This purification step involves a major loss of activity that in the end determines the radiochemical yield (*Table 26*). After distillation, most of the activity remained in reactor 1, while only about 13% were trapped in reactor 2 accounting for $8.9 \pm 1.5\%$ of the starting activity. Higher flow rates than 50 mL/min (up to 100 mL/min) or longer distillation times were no effective options to raise the amount of trapped [¹⁸F]FBrCD₂. By increasing these two parameters only higher amounts of [¹⁸F]fluoride could be found in preparative HPLC-chromatograms while the yields of end product [¹⁸F]FMeNER-D2 seemed to be unaffected. It cannot be stated whether the entire activity (1.1 ± 0.4 GBq) found on Silica Sep-Paks[®] was attributed to [¹⁸F]FBrCD₂. Radioactive fluoride is also able to be transferred to the cartridges via evaporation of acetonitrile and therefore, the measured activity could be

⁷ Three syntheses were excluded from averaging due to known systematic errors (see *Table 27*, highlighted in red).

assigned to [^{18}F]fluoride to some extent. Another reason for high fluoride concentration in experiments where the distillation process was prolonged, is the possible defluorination of [^{18}F]bromofluoromethane-d₂ on the polar sorbent of the cartridge or in the trapping solution.

The volume of DMF for trapping as well as the trapping temperature could not be found to have a significant impact on [^{18}F]BFM yields. This can be stated for trapping volumes between 400 to 500 μL and temperatures in reactor 2 of -20°C to -50°C (see *Table 27*).

These findings suggest that it is very likely that the nucleophilic substitution of Br_2CD_2 is not able to provide [^{18}F]FBrCD₂ in the desired amount. In general, nucleophilic substitutions are known to be very sensitive to polar solvents like water. Therefore, the synthesis module was prepared carefully to avoid any additional contaminations with water or moisture during the synthesis by washing with acetone, drying of the reactors and flushing with argon. However, analytical HPLC of crude [^{18}F]BFM still showed fluoride not exceeding 10% of total radioactivity.

The last reaction between [^{18}F]BFM and the precursor (*S,S*)-NER in 5 M NaOH for 5 min at 90°C including the subsequent purification via HPLC and formulation gave our tracer in an average yield of about 40%. Thus, compared to the first part of the synthesis starting from dry [^{18}F]fluoride in reactor 1 to [^{18}F]BFM in reactor 2 showing about 15% of overall yield, this final part of the reaction sequence did not diminish product yields in a similar crucial way. Unfortunately, the doubling of reaction time did not result in increased product yields as decay compensates a possible slight rise in [^{18}F]FMeNER-D₂ formation. Therefore, no significant differences between reactions carried out for 5 or 10 min, respectively, could be detected. [^{18}F]Fluoromethylation of (*S,S*)-NER gave [^{18}F]FMeNER-D₂ in a very high radiochemical yield with less than 5% radiochemical impurities in the crude mixture. The preparative purification of the final precursor from other radioactive (BFM, fluoride) and non-radioactive substances (NER, Br_2CD_2) was performed quantitatively.

Moreover, only a negligible amount of radioactivity could be found in the loop waste. The purification step via the C-18 cartridge did not lead to a remarkable decrease in product yield. Residual activities remaining on the RP-cartridge were found to range between $0.3 \pm 0.2\%$ of starting activity (*Table 26*).

Table 26: Preparation of [¹⁸F]FMeNER-D2; Yields and loss of radioactivity between reaction steps and required time (MEAN±SD); R1 = reactor 1, R2 = reactor 2, TW=waste = target water waste.

n ≥ 21	Activity [GBq]	% of initial activity (corr. for decay)	Δ t to start of synthesis [min]
[¹⁸ F]Fluoride activity produced in cyclotron	31.7 ± 2.5	100	0
[¹⁸ F]Fluoride starting activity R1	16.4 ± 2.5	59.2 ± 8.6	21.3 ± 2.8
Activity before distillation	14.0 ± 2.7	64.9 ± 13.1	60.6 ± 5.0
Pure [¹⁸ F]BFM after distillation trapped in R2	1.8 ± 0.5	8.9 ± 1.5	73.9 ± 6.0
[¹⁸ F]FMeNER-D2 final product yield	0.6 ± 0.3	3.5 ± 1.5	103.5 ± 7.0
F-18 cartridge	0.4 ± 0.4	1.5 ± 1.0	
TW-waste	0.01 ± 0.02	0.1 ± 0.1	
Exhaust R1	2.0 ± 2.4	9.5 ± 11.1	
Silica Sep-Paks®	0.1 ± 0.1	0.7 ± 0.3	
	0.2 ± 0.2	0.9 ± 1.0	
	0.1 ± 0.0	0.7 ± 0.2	
	0.2 ± 0.1	1.1 ± 0.6	
Sum Silica Sep-Paks®	1.1 ± 0.4	3.4 ± 1.2	
Loop-waste	0.1 ± 0.2	0.3 ± 0.7	
C-18 Sep-Pak®	0.1 ± 0.0	0.3 ± 0.2	

The retention times for preparative HPLC were 1.27 min ($k' = 0$) for [¹⁸F]fluoride, 2.0 min ($k' = 0.57$) for (*S,S*)-NER, 2.2 min ($k' = 0.73$) for [¹⁸F]BFM, 5.02 min ($k' = 2.95$) for Br₂CD₂ and 6.31 min ($k' = 3.97$) for [¹⁸F]FMeNER-D2 (Figure 12, left).

Analytical HPLC did not show the presence of [¹⁸F]fluoride or any other radiochemical impurity besides the desired product which elutes after 5.0 min (Figure 12, right).

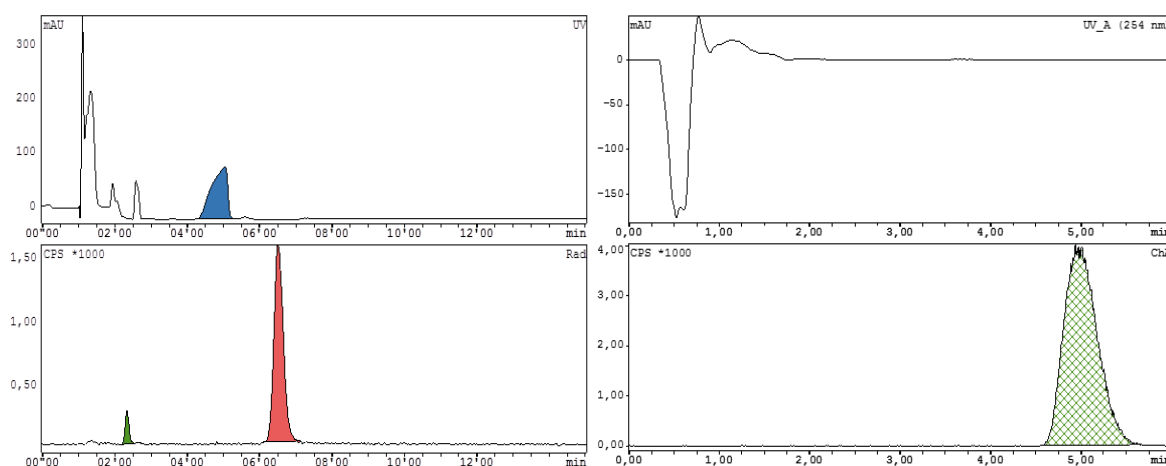


Figure 12: Exemplary preparative (left) and analytical (right) HPLC chromatograms of [¹⁸F]FMeNER-D2 (FMN-# 121).

Table 27: List showing all FMN syntheses and special modifications in the procedures.

Synth.-#	FMN-#	Yield [MBq]	Yield [%] (uncorr.)	T(R1) [°C]	Vol (R2) [μL]	Vol (R1) [μL]	Reaction time (R2)	Comments
1	91	388.9	1.3	-20	400	0	5	
2	92	497.3	1.2	-20	800	0	10	
3	93	1230	3.5	-20	400	0	5	
4	94	1380	3.9	-20	400	0	5	
5	95	644.7	2.1	-30	400	0	5	
6	97	68.8	0.2	-20	400	0	5	error: due to HPLC leakage
7	100	603.0	1.9	-20	400	0	5	
8	104	485.1	1.5	-20	400	0	5	
9	105	551.0	1.8	-50	400	0	5	
10	106	250.0	0.8	-50	400	0	5	error: only 50% of peak cut into the bulb
11	107	416.7	1.4	-20	400	0	5	
12	108	321.6	1.1	-20	400	0	5	
13	109	340.4	1.1	-20	500	0	5	
14	110	346.0	1.1	-20	500	100	5	
15	111	393.0	1.3	-20	500	0	5	
16	112	772.0	2.5	-50	500	0	5	azeotropic drying via V1
17	113	395.0	1.3	-50	500	100	10	
18	114	652.0	2.2	-20	400	100	10	
19	115	790.5	2.6	-50	500	100	5	azeotropic drying with two times 1 mL ACN, flow for trapping increased to 100 mL: lots of fluoride visible in preparative chromatogram
20	117	610.0	2.0	-50	500	100	5	increased flow for trapping due to reuse of Sep-Paks®
21	118	295.0	0.9	-50	500	100	5	
22	119	173.7	0.8	-30	500	100	5	error: enormous loss in exhaust of reactor 1
23	120	521.0	1.6	-30	500	100	5	He stream varied manually during azeotropic
24	121	558.0	1.8	-30	500	100	5	
25	122	581.3	1.9	-30	500	100	5	

3.2 Results of metabolism studies

3.2.1 Stability tests in HLM

Incubation in phosphate buffer (PB)

Incubation of [^{18}F]FMeNER-D2 with HLMs lead to a moderate degradation corresponding to $79.1 \pm 2.7\%$ ($n = 9$) of unmetabolized tracer after 90 min (see *Table 28*, *Figure 13*). Concomitantly performed TLC analysis did not reveal the formation of free [^{18}F]fluoride at any timepoint.

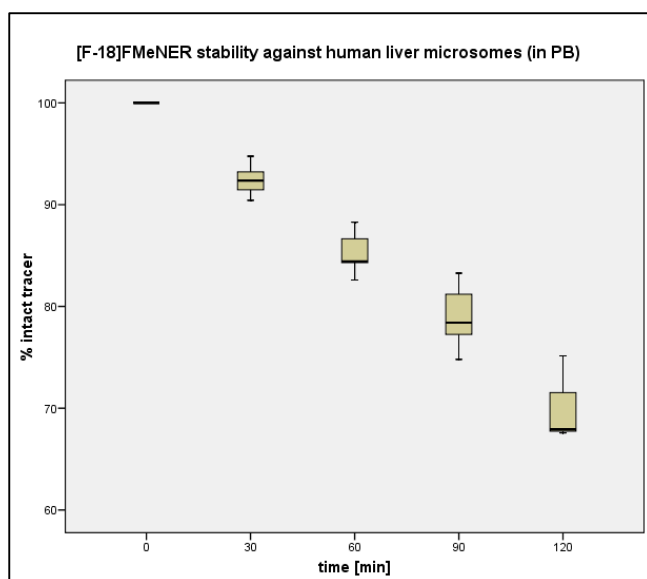


Table 28: Data for Figure 13.

t [min]	MEAN [% intact tracer]	SD	n
0	100.0	0.0	9
30	92.3	1.3	9
60	85.2	1.9	9
90	79.1	2.7	9
120	70.2	4.3	3

Figure 13: Boxplots showing degradation of radiotracer [^{18}F]FMeNER-D2 in HLM within 2 h; based on data from *Table 28*; statistically corrected for outliers (see appendix, chapter 9.1.2).

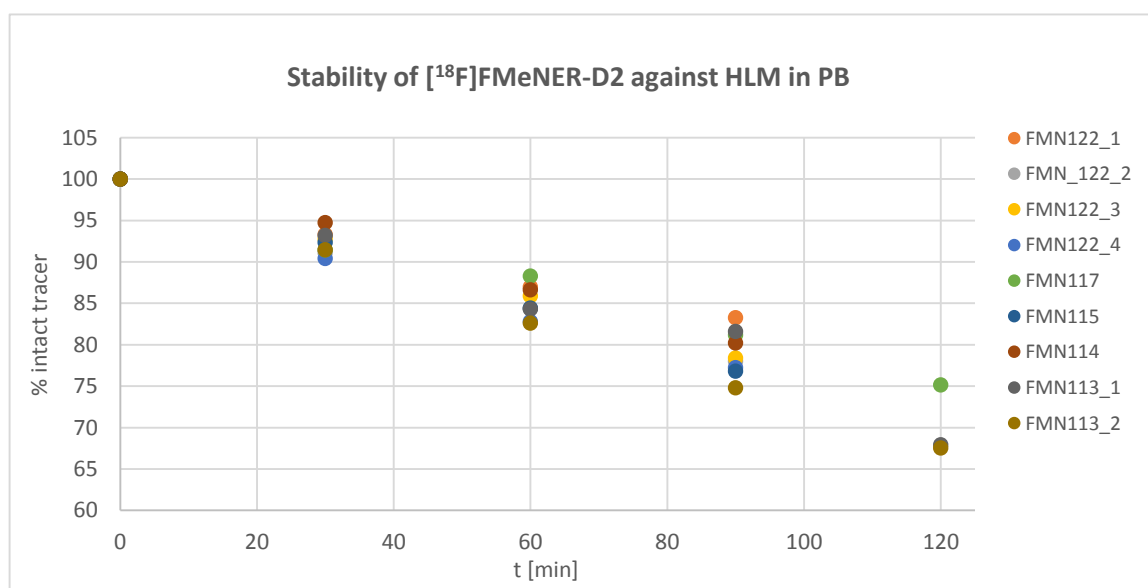


Figure 14: Individual series of measurements ($n = 9$) which were averaged in *Figure 13*.

Incubation in phosphate buffered saline (PBS)

When using a different buffer with higher ionic strength, the activity of cytochrome P450 enzymes in the microsomal mixtures was reduced leading to a significant reduction in turnover. After 90 min still $94.0 \pm 2.4\%$ of radiotracer were left intact (Figure 15 and Table 29).

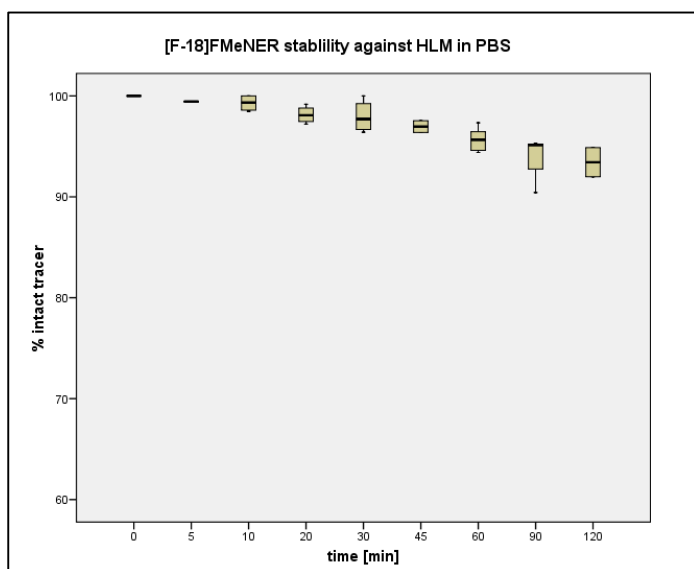


Table 29: Data for Figure 15.

t [min]	MEAN [% intact tracer]	SD	n
0	100.0	0.0	6
5	99.4	0.0	2
10	99.3	0.8	4
20	98.1	0.9	4
30	98.0	1,6	4
45	97.0	0.8	2
60	95.7	1.1	6
90	94.0	2.4	4
120	93.4	2.0	2

Figure 15: Shows higher stability of $[^{18}\text{F}]\text{FMeNER-D2}$ in PBS than in PB according to data from Table 29.

Interpretation of radiosignals in HLM

In human liver microsomes up to 2 different radiosignals could be detected ($k' = 0.7$ and 2.1). The radiosignal at $k' = 0.7$ can be interpreted as a protein-bound species as a UV-signal at 254 nm was present. In fact, it cannot be precluded that this signal corresponds to microsomal bound intact tracer impurities in the supernatant (due to insufficient precipitation). This hypothesis is corroborated by the observation that with increasing activity in the incubation mixture, the portion of this signal decreased and seemed to have almost constant intensity. At very high tracer activities this signal diminished to zero (see *Figure 16*). Therefore, only one single radio-metabolite could be observed in microsomal incubations of human liver besides the tracer signal ($k' = 3.2$).

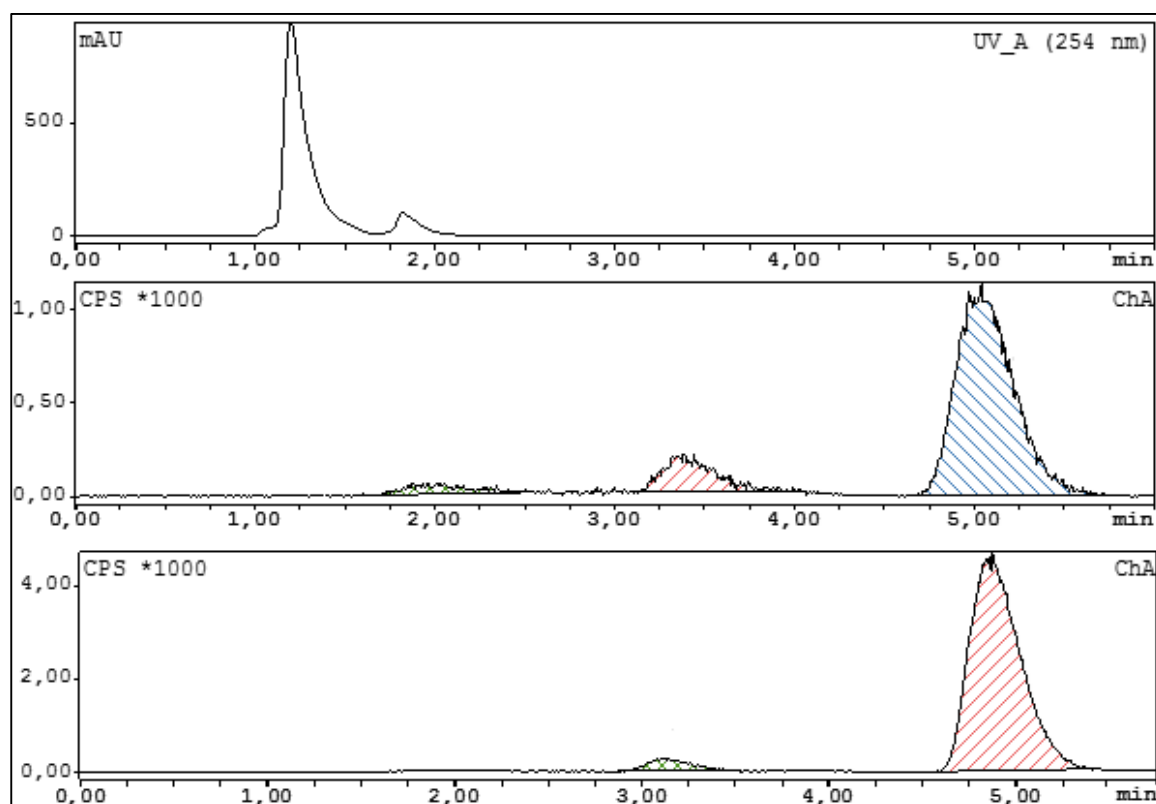


Figure 16: Analytical HPLC chromatograms showing radiosignals of metabolites and intact $[^{18}\text{F}]\text{FMeNer-D2}$ ($t_r = 5$ min) in HLM incubations after 60 min with different tracer concentrations.

3.2.2 Stability tests in RLM

Incubation in phosphate buffer (PBS)

Compared to human liver microsomes, a complete and significantly faster cleavage of the tracer was observed within 7 min (*Figure 17*). After 5 min of incubation time only $1.3 \pm 0.4\%$ ($n = 4$) of unmetabolized tracer could be found (*Table 30*). TLC analysis of the fully cleaved batches did not show ionic $[^{18}\text{F}]\text{fluoride}$ which corresponds to results in human liver microsomes.

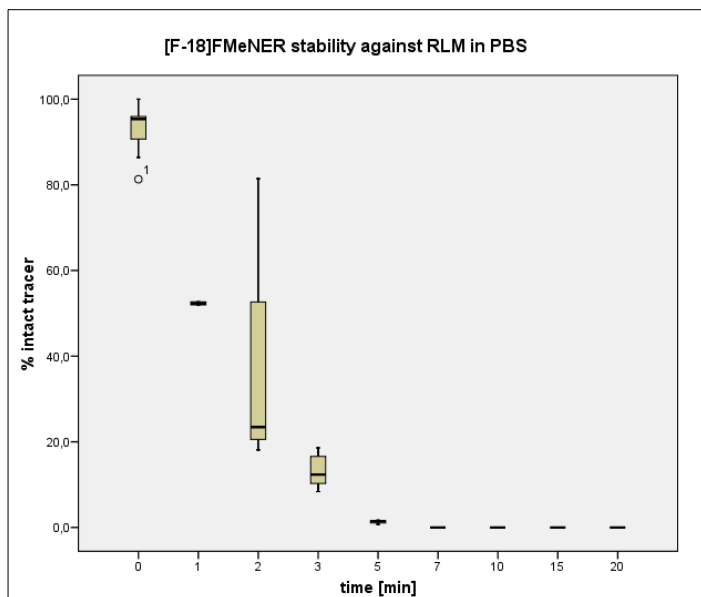


Table 30: Data for Figure 17.

t [min]	MEAN [% intact tracer]	SD	n
0	93.3	5.2	15
1	52.3	0.5	2
2	36.6	30.0	4
3	13.3	3.9	7
5	1.3	0.4	4
7	0.0	0.0	8
10	0.0	0.0	6
15	0.0	0.0	10
20	0.0	0.0	14

Figure 17: Boxplots showing degradation of radiotracer $[^{18}\text{F}]\text{FMeNER-D2}$ in RLM within 20 min; based on data from Table 30; statistically corrected for outliers (see appendix, chapter 9.1.2).

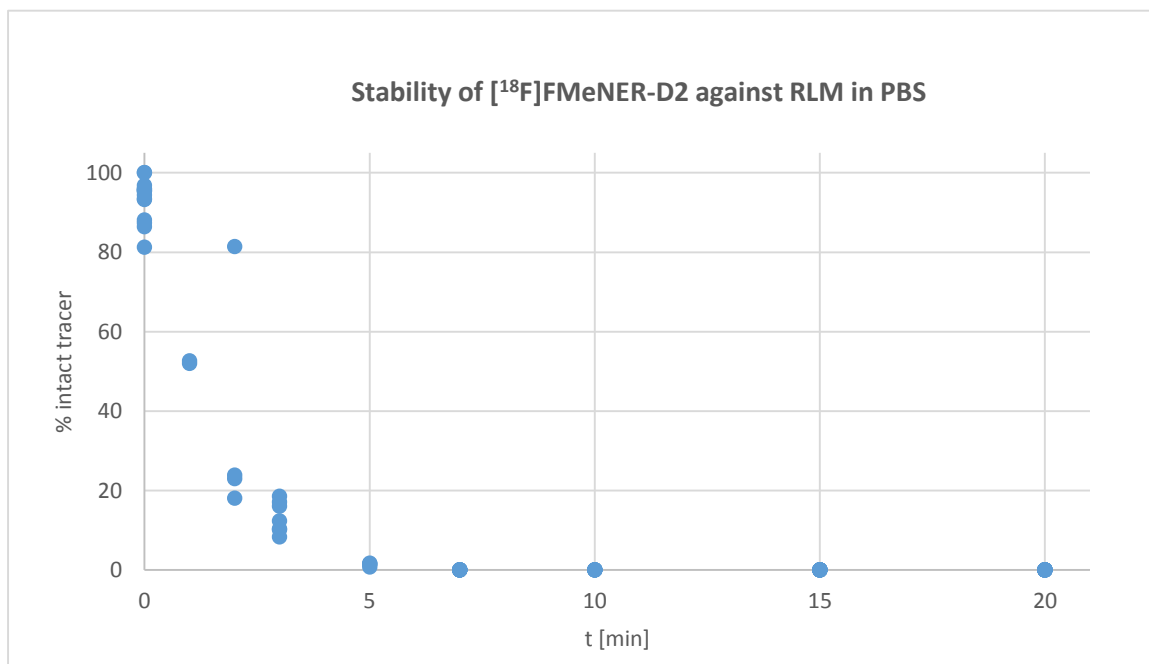


Figure 18: Individual datapoints of all series of measurements, which were averaged in Figure 17.

Effect of preincubation

A slight but remarkable effect of preincubation for high-turnover RLM incubations could be observed (*Figure 19*, $n = 1$). Based on these findings, conditions were strictly kept at 5 min of preincubation time in the following experiments.

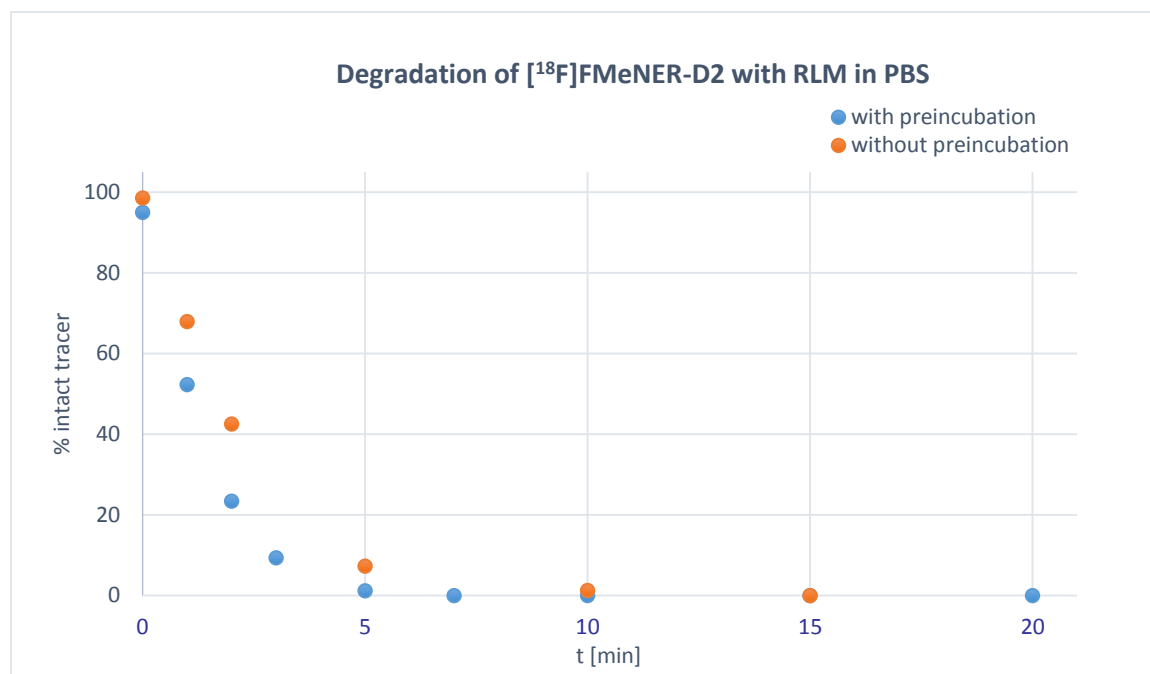


Figure 19: Effect of preincubation; $n = 1$.

Interpretation of radiosignals in RLM

In rat liver microsomes one major metabolite was rapidly formed at $k' = 1.8$ ($t_0 = 1.2$). In some cases, a second and third peak occurred after about 10 min of incubation time. With increasing time, metabolite 1 ($k' = 1.8$) decreased while other minor metabolites ($k' = 1.2$ and 1.4) rised marginally in intensity. As outlined in *Figure 20*, the uppermost chromatogram shows that only one single metabolite was formed. The second and last trace show, that at times when the tracer ($t_r = 5$ min) was almost or fully degraded two (second trace) or three (last trace) metabolites were detected.

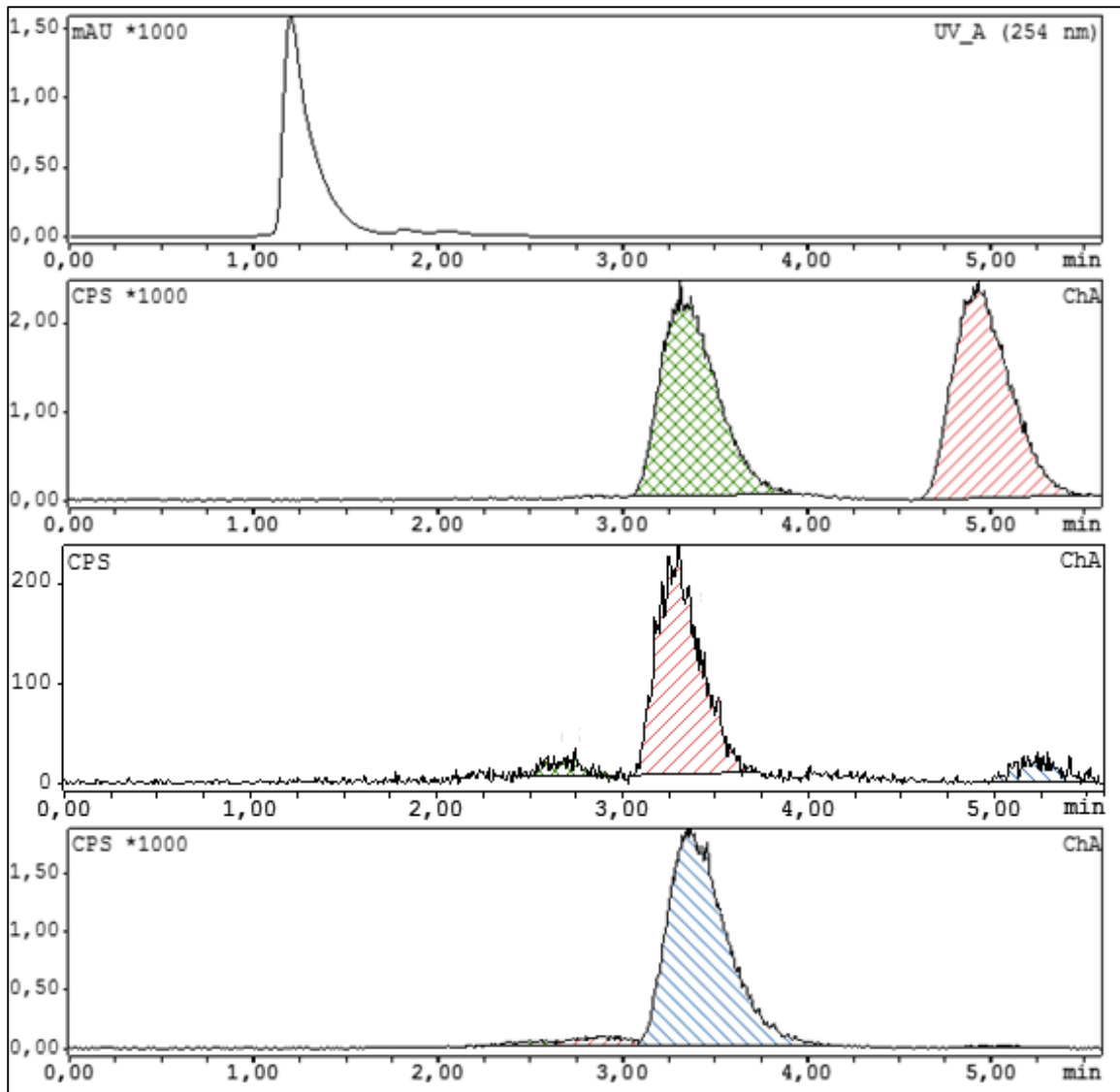


Figure 20: Supernatant of different RLM incubations showing up to three radioactive signals besides the tracer signal ($t_r = 5$ min).

3.2.3 Chemical inhibition experiments

In the following subchapters, the effects of selective inhibitors of CYPs on the formation of metabolites in human and rat liver microsomes is presented.

3.2.3.1 Chemical inhibition of HLM

Ketoconazole

HLM incubation with up to 20 μM ketoconazole did not lead to a significant inhibition of PET-tracer degradation, neither in PBS nor in PB. At concentrations of 50 – 100 μM , a significant slowdown of [^{18}F]FMeNER-D2 breakdown was observed (see *Figure 21, a.*). The influence of ketoconazole in PBS was not that obvious due to the generally reduced degradation rate in PBS (see *Figure 21, b.*). Experiment a. showed that 10.2% more tracer was left intact after 60 min compared to the reference.

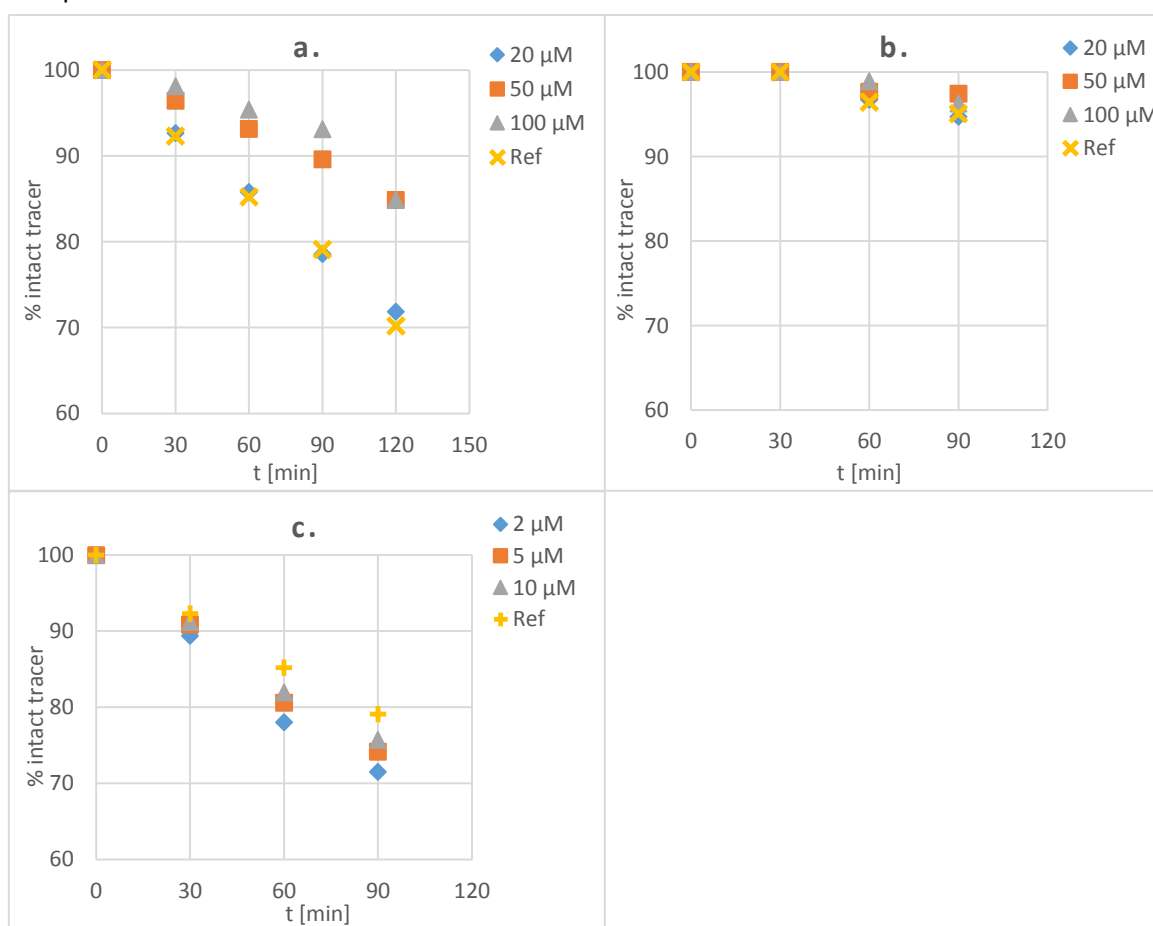


Figure 21: Inhibition of HLM metabolism of [^{18}F]FMeNER-D2 via ketoconazole; (a) 20, 50, 100 μM inhibitor in PB, (b) 20, 50, 100 μM inhibitor in PBS, (c) 2, 5, 10 μM inhibitor in PB; $n = 1$.

Quinidine

The selective CYP2D6 inhibitor quinidine induced full inhibitory effects at a concentration of 2 – 5 μM . After 120 min of incubation time degradation of [^{18}F]FMeNER-D2 was not observed, thus indicating a complete chemical inhibition of the respective CYP isoenzyme. Lower concentrations did not result in a complete block of cytochrome P450 activity as depicted in Figure 22. In Table 31, the dependence of the percentage of intact tracer on the amount of inhibitor including standard deviations is outlined.

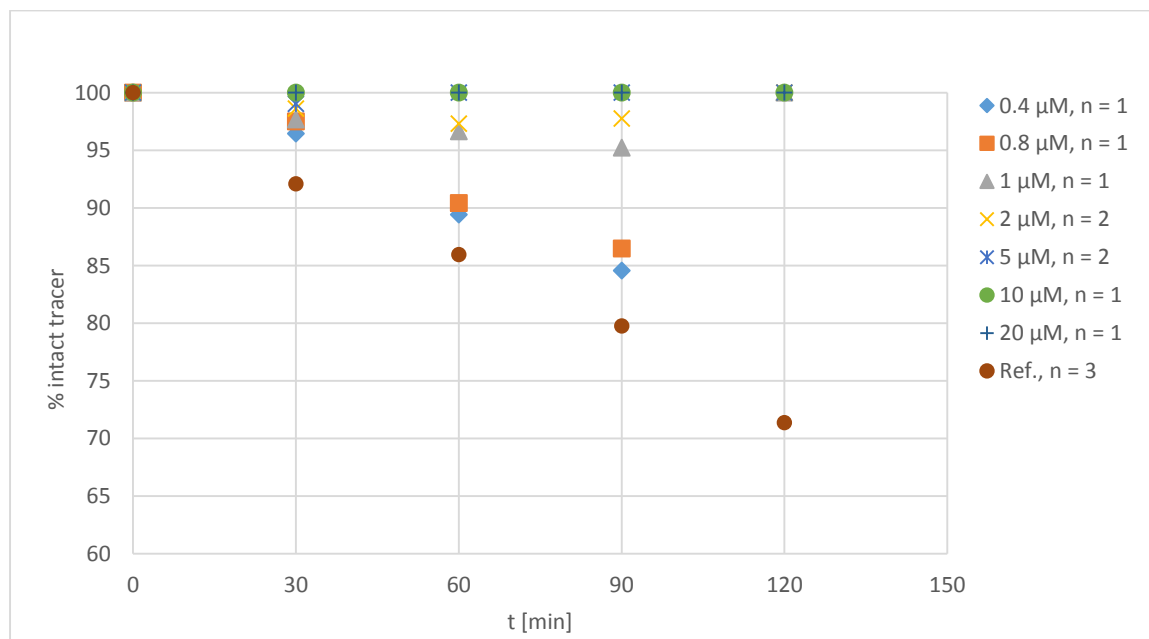


Figure 22: Inhibition of HLM activity with quinidine in a concentration range of 0.4 - 20 μM .

Table 31: Data table for Figure 22; Standard deviations (SD) are given for experiments, which were carried out more than once.

	% intact tracer				
t [min]	0.4 μM	0.8 μM	1 μM	2 μM (mean)	SD (2 μM)
0	100.0	100.0	100.0	100.0	0.0
30	96.4	97.5	97.7	98.6	1.1
60	89.4	90.4	96.7	97.3	0.9
90	84.6	86.5	95.2	97.8	3.2
120			100.0	100.0	0.0
t [min]	5 μM (mean)	SD (5 μM)	10 μM	20 μM	Ref
0	100.0	0.0	100.0	100.0	100.0
30	99.0	1.4	100.0	100.0	92.1
60	100.0	0.0	100.0	100.0	86.0
90	100.0	0.0	100.0	100.0	79.8
120	100.0	0.0	100.0	100.0	71.4

(+)-N-3-Benzylirivanol

Significant reduction of metabolism was not observed until 100 μM of (+)-N-3-benzylirivanol. After 60 min tracer activity was elevated by the portion of $4.2 \pm 1.8\%$ ($n = 2$) (Figure 23 and Table 32).

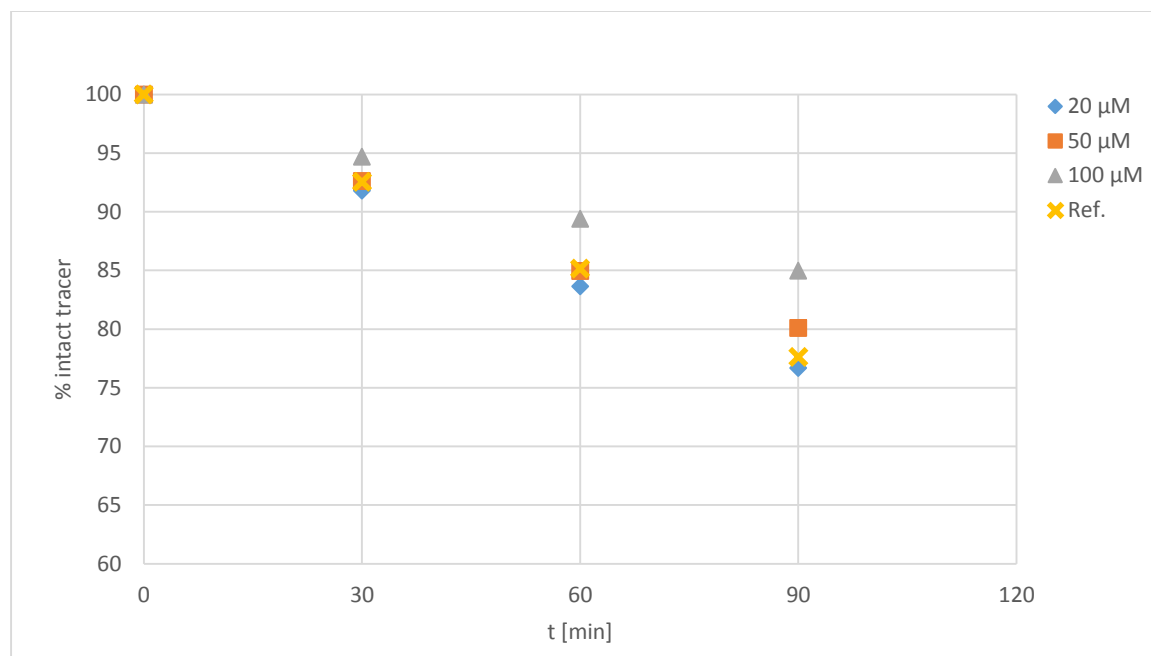


Figure 23: Inhibitor (+)-N-3-benzylirivanol tested for its effect in HLM incubations of [^{18}F]FMenER-D2; 20, 50, 100 μM in PB; $n = 2$.

Table 32: Data table for Figure 23.

n = 2	% intact tracer							
	20 μM		50 μM		100 μM		Ref	
t [min]	Mean	SD	Mean	SD	Mean	SD	Mean	SD
0	100.0	0.0	100.0	0.0	100.0	0.0	100.0	0.0
30	91.8	2.2	92.6	1.1	94.7	0.2	92.5	0.3
60	83.7	4.4	85.0	1.8	89.4	0.7	85.2	1.0
90	76.7	6.4	80.1	4.2	85.0	0.6	77.6	1.1

Ticlopidine hydrochloride

Ticlopidine strongly impeded the degradation of our PET-Tracer at concentrations of 50 – 100 μM . It lead to an increase of remaining intact tracer of 3.9% in PBS (50 or 100 μM), while tracer activities were elevated by 9.1% and 10.5% for 50 μM and 100 μM incubations in PB, respectively (Figure 24).

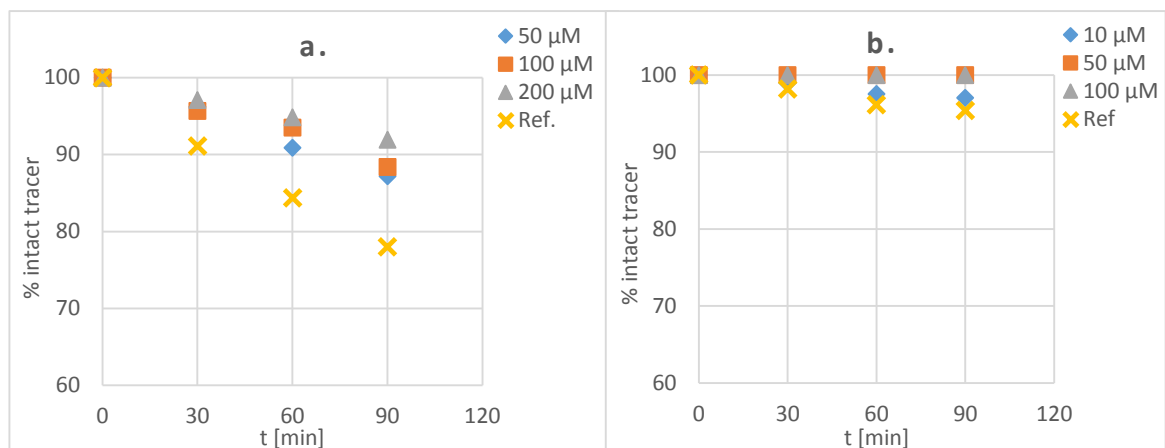


Figure 24: Ticlopidine.HCl inhibits metabolism of $[^{18}\text{F}]\text{FMeNER-D2}$ in HLM; a) 50, 100, 200 μM in PB; b) 10, 50, 100 μM in PBS.

2-Phenyl-2-(1-piperidinyl)-propane

This selective inhibitor of CYP2B6 did not show any effect on CYP450 metabolic activity when tested in PBS (Figure 25).

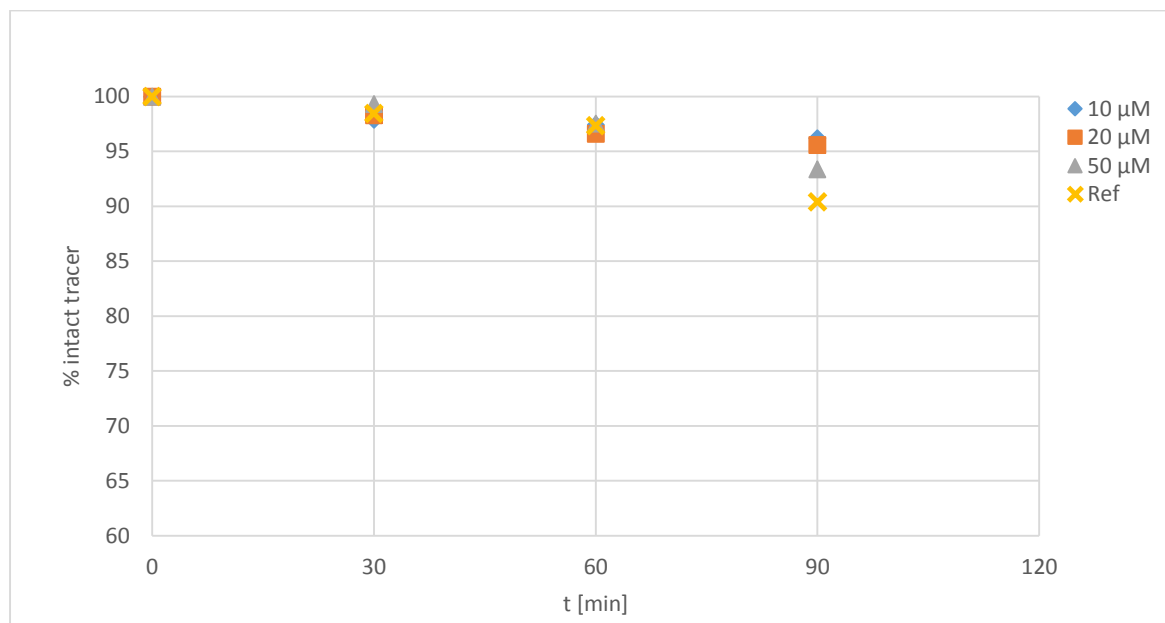


Figure 25: 10, 20, 50 μM incubations with inhibitor PPP in HLM, $n = 1$.

Sulfaphenazole

Inhibition of CYP2C9 using Sulfaphenazole failed to have an effect on tracer degradation in HLM as shown in Figure 26. The concentration range examined was 10 – 50 μM .

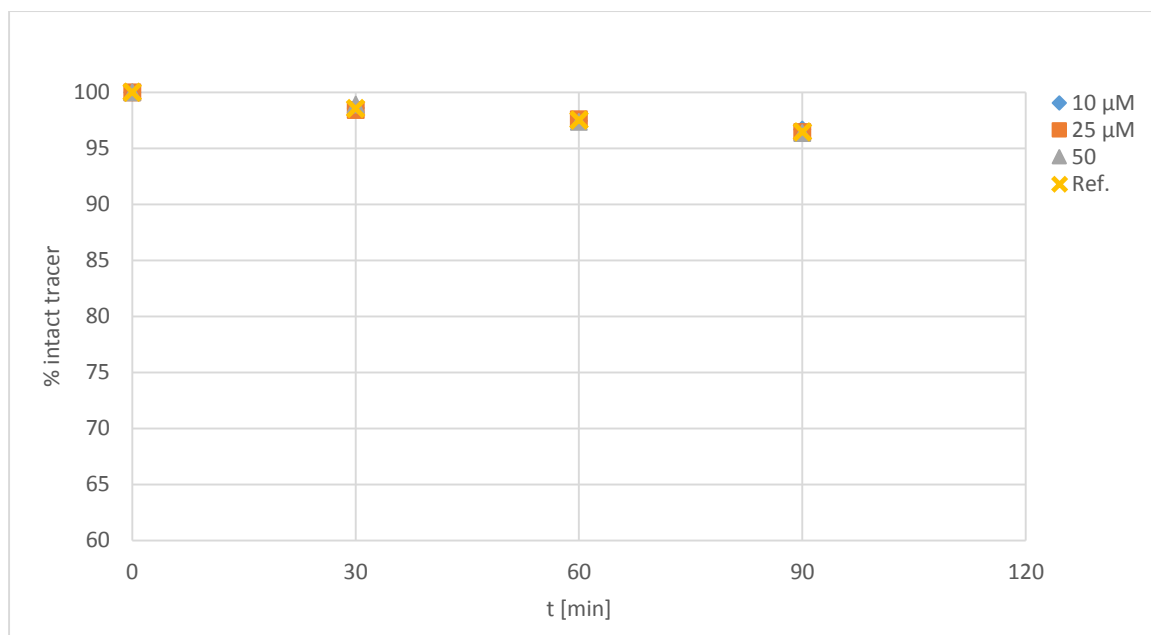


Figure 26: Selective CYP2C9 inhibitor sulfaphenazole used in 3 different concentrations in HLM incubations; 10, 20, 50 μM in PBS; $n = 1$.

Montelukast sodium

In a single experiment the involvement of Montelukast in tracer breakdown was investigated. Results did not suggest the inhibition of [^{18}F]FMeNER-D2 metabolism by 50 – 100 μM of the mentioned inhibitor. The deviating data obtained for the 10 μM batch might be caused by a systematic error (see Figure 27).

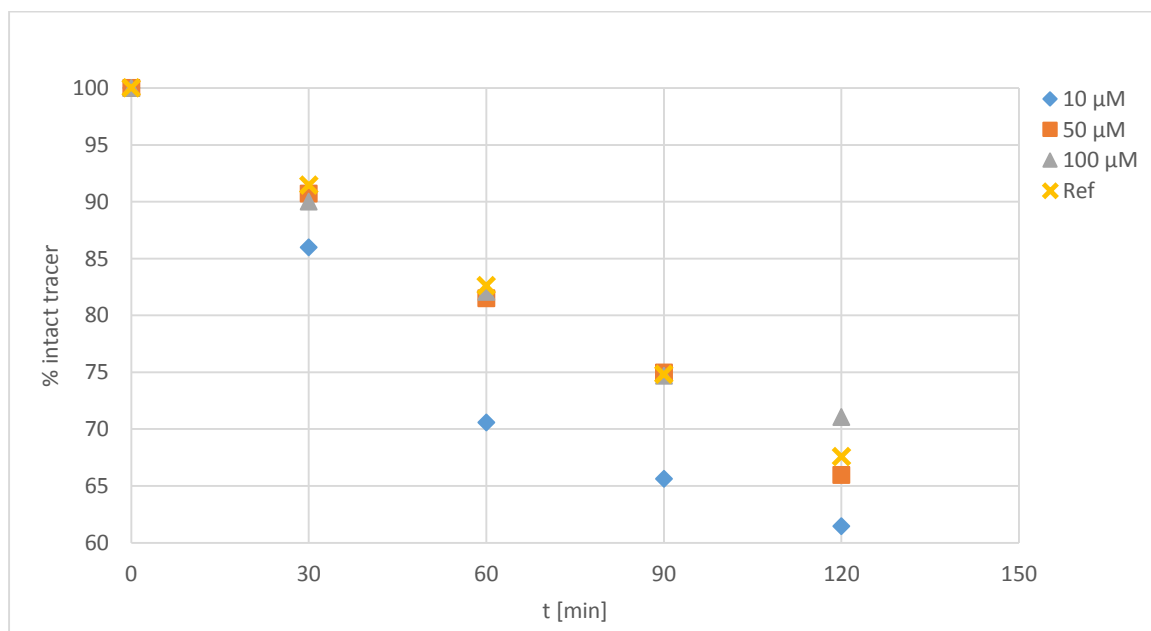


Figure 27: CYP450 inhibitor Montelukast sodium was tested for impairment of [^{18}F]FMeNER-D2 degradation; 10, 50, 100 μM in PB; $n = 1$.

4-Methylpyrazole hydrochloride

The chemical inhibitor usually applied for CYP2E1 inhibition did not show any effect on the metabolism of our radioactive tracer in the concentration range depicted in *Figure 28*.

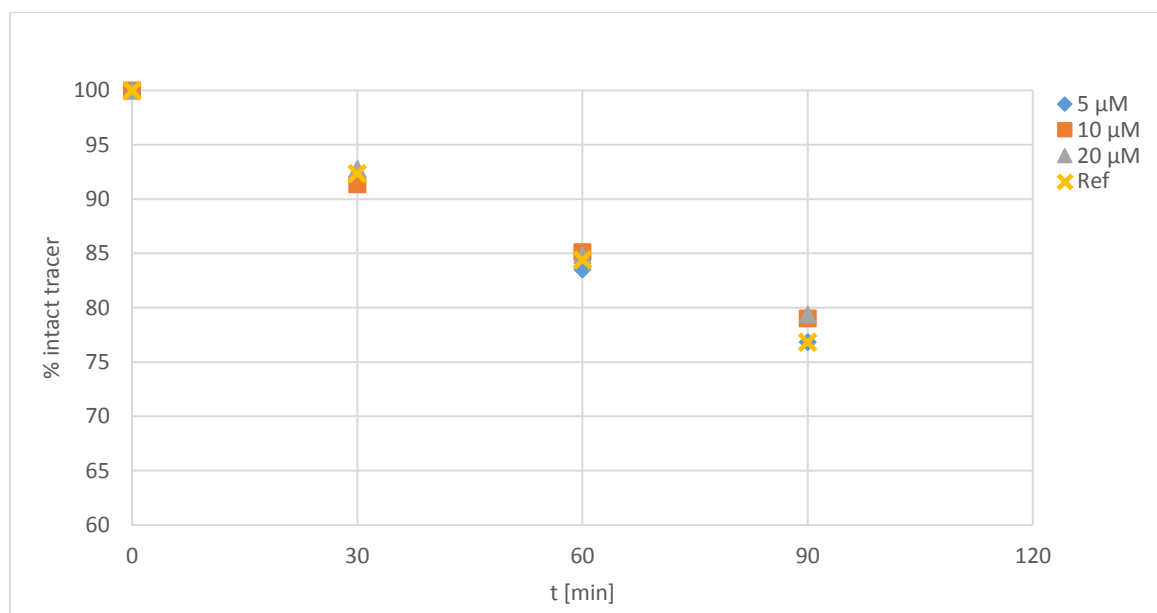


Figure 28: Involvement of 4-methylpyrazole.HCl in the metabolic stability of [18 F]FMeNER-D2; 5, 10, 20 μ M batches in PB were investigated; n = 1.

Furafylline

Incubations containing 100 μ M furafylline exhibited $5.4 \pm 1.5\%$ higher tracer activity compared to the reference without inhibitor (n = 2), depicted in *Figure 29* (for SD see *Table 33*).

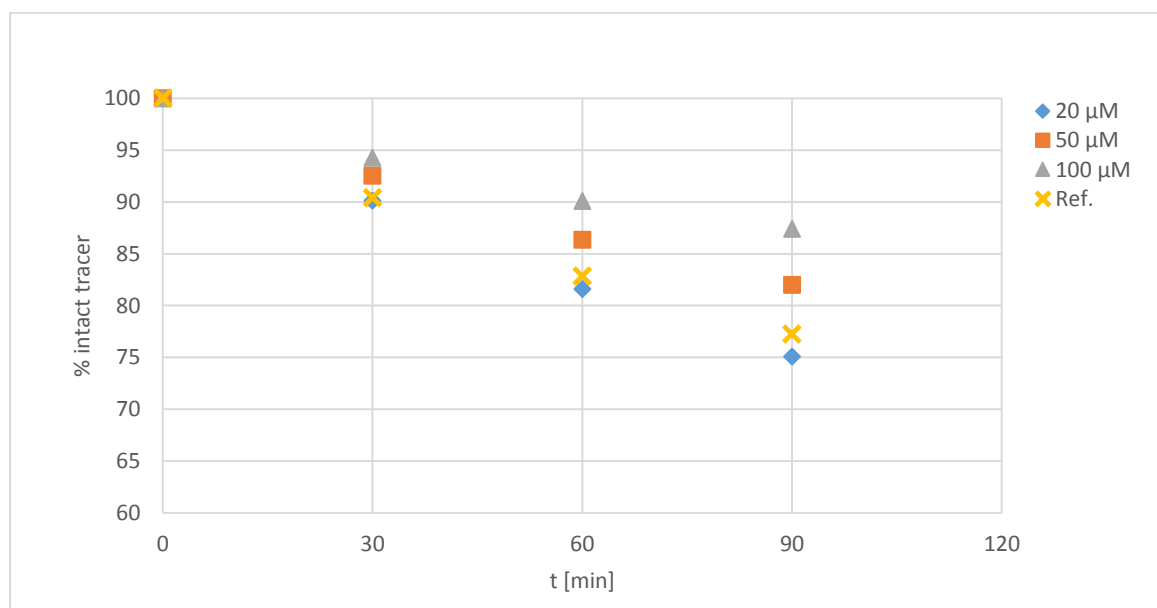


Figure 29: Stability of [18 F]FMeNER-D2 in HLM incubations spiked with three different concentrations of furafylline; 20, 50, 100 μ M in PB; n = 2.

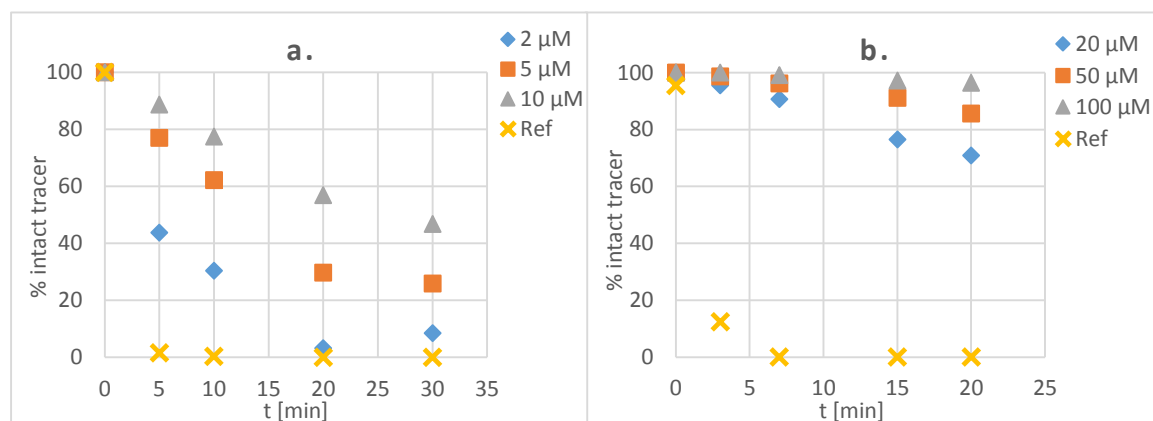
Table 33: Averaged data for Figure 29 including standard deviations.

% intact tracer								
t [min]	20 μ M		50 μ M		100 μ M		Ref	
	Mean	SD	Mean	SD	Mean	SD	Mean	SD
0	100.0	0.0	100.0	0.0	100.0	0.0	100.0	0.0
30	90.1	0.4	92.5	0.5	94.3	1.1	90.4	3.1
60	81.6	2.2	86.3	2.3	90.1	1.2	82.8	2.7
90	75.1	2.7	82.0	1.0	87.4	2.8	77.3	2.1

3.2.3.2 Chemical inhibition of RLM

Ketoconazole

Ketoconazole lead to a remarkable inhibition of tracer degradation in 10 μ M incubations accounting for an increase of [18 F]FMeNER-D2 of $56.9 \pm 1.6\%$ after 20 min compared to the reference. For the 100 μ M batch, almost full inhibition was achieved (96.4% of intact tracer) (Figure 30, Table 34).

**Figure 30:** Inhibition of RLM enzymatic activity via ketoconazole; a) 2, 5, 10 μ M in PB, $n = 3$, b) 20, 50, 100 μ M in PBS, $n=1$.**Table 34:** Data list for Figure 30.

% intact tracer								
t [min]	2 μ M		5 μ M		10 μ M		Ref	
	Mean	SD	Mean	SD	Mean	SD	Mean	SD
0	100.0	0.0	100.0	0.0	100.0	0.0	100.0	0.0
5	43.8	-	77.0	-	88.7	-	1.5	-
10	30.4	20.8	62.2	12.0	77.5	3.0	0.4	0.7
20	3.2	0.1	29.7	1.5	56.9	1.6	0.0	-
30	8.4	-	25.9	-	46.7	-	0.0	-

Quinidine

In this experimental series, a significant effect of quinidine on RLM metabolism of our tracer could be determined. Interestingly a high deviation of the observed values was obtained for lower molarities of inhibitor in the incubation solution (see *Table 35*).

Table 35: Data table for RLM inhibition via quinidine gives MEAN (\pm SD).

n = 1 - 2		% intact tracer					
t [min]	2 μ M	5 μ M	10 μ M	20 μ M	50 μ M	Ref	
0	95.3	97.8 (0.3)	99.4 (1.1)	99.7 (0.5)	100	93.3	
2	-	41.6	71.7 (12.9)	79.5	-	36.6	
3	-	-	60.5	93.5	89.4	13.3	
5	-	-	27.7	51.1	-	1.3	
7	-	-	31.6	83.0	78.1	0.0	
10	-	0.0	9.0	28.9	-	0.0	
15	0.0	1.5 (2.1)	10.6 (10.5)	39.1 (32.6)	53.6	0.0	
20	0.0	0.0	5.2 (7.1)	28.3 (31.1)	44.8	0.0	

(+)-N-3-Benzylirivanol

Benzylirivanol was able to inhibit tracer degradation significantly in 100 μ M concentration batches. Interestingly, distinct results were obtained for incubations carried out in PBS (*Figure 31, a.*) and PB (*b.*). The reason for this finding might be either favored interaction of benzylirivanol with inhibitor-sensitive enzymes in a medium with high ionic strength or a systematic error in the procedure.

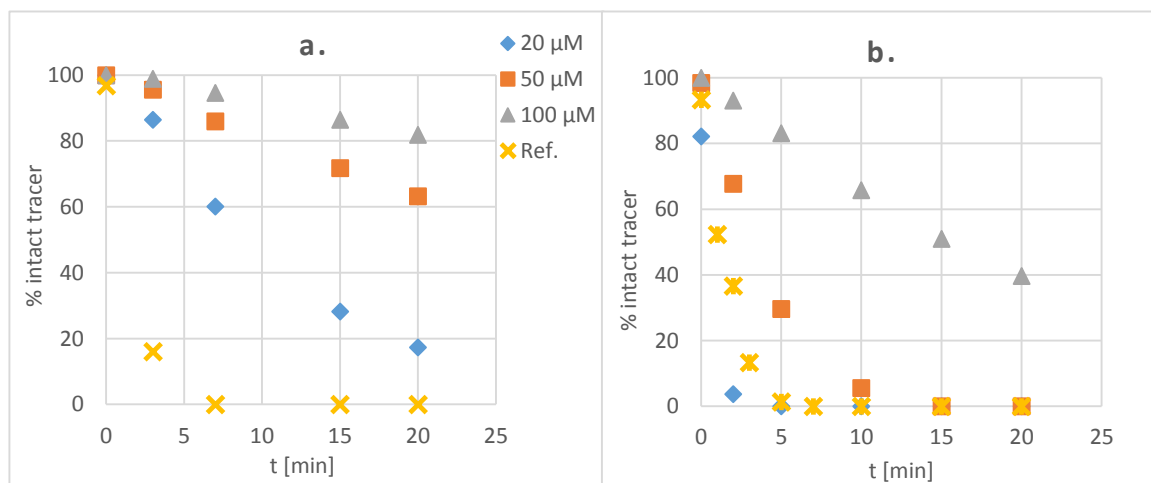


Figure 31: Inhibition via (+)-N-3-benzylirivanol in RLM, a) 20, 50, 100 μ M in PBS; 0.04 μ M DMSO, n = 1, b) 20, 50, 100 μ M, 0.14 μ M DMSO in PB, n = 1.

Ticlopidine hydrochloride

Ticlopidine hydrochloride, a not extensively studied inhibitor of CYP2C11, showed slight but significant effects in RLM incubations of the PET-tracer [¹⁸F]FMeNER-D2 (Figure 32 and Table 36).

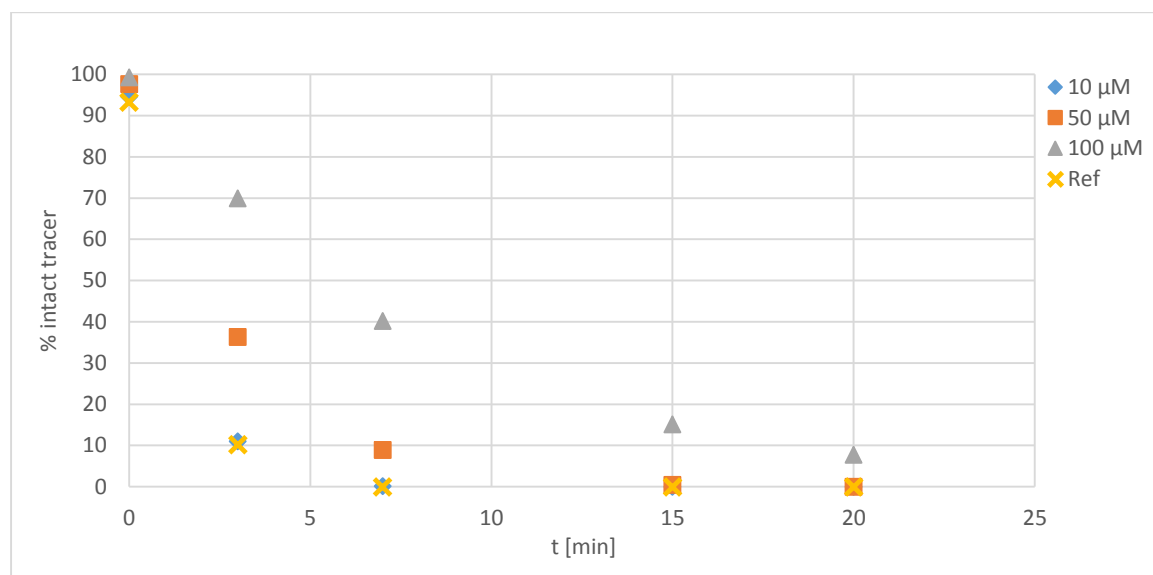


Figure 32: Evaluation of the effect of ticlopidine on RLM breakdown of [¹⁸F]FMeNER-D2; 10, 50, 100 μM in PBS; n = 2.

Table 36: Data list for Figure 32.

t [min]	% intact tracer						
	10 μM		50 μM		100 μM		Ref
	Mean	SD	Mean	SD	Mean	SD	
0	94.6	0.9	97.7	0.9	99.3	0.3	93.3
3	11.1	2.2	36.4	16.5	70.0	12.3	10.2
7	0.2	0.3	9.0	9.0	40.2	16.3	0.0
15	0.0	0.0	0.5	0.7	15.1	11.5	0.0
20	0.0	0.0	0.0	0.0	7.8	7.7	0.0

2-Phenyl-2-(1-piperidiny)-propane

2-Phenyl-2-(1-piperidiny)-propane, which has not been studied for CYP450 inhibition in rats yet, caused a substantial slowdown in [¹⁸F]FMeNER-D2 metabolic modification in RLM. In 50 μM inhibitor incubations 34.3 ± 8.6% more tracer were left after 20 min compared to control (n = 2, see Figure 33, Table 37).

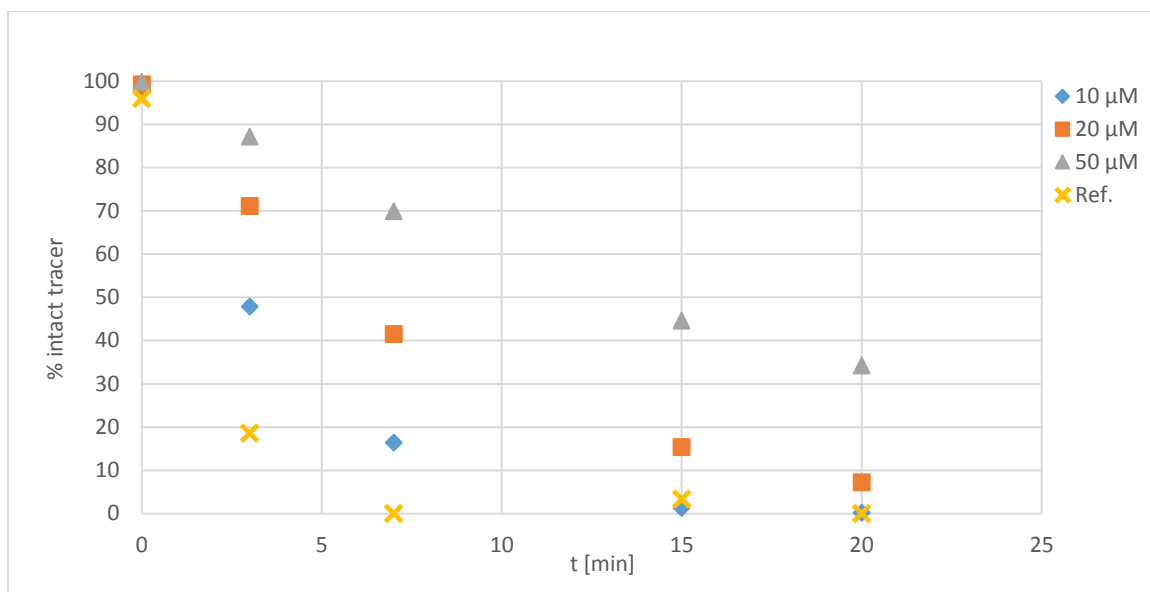


Figure 33: Inhibition of microsomal degradation of [¹⁸F]FMeNER-D2 via PPP in RLM; 10, 20, 50 μM in PBS; n = 2.

Table 37: Data set for Figure 33.

t [min]	% intact tracer						Ref
	10 μM		20 μM		50 μM		
	Mean	SD	Mean	SD	Mean	SD	
0	98.6	0.1	99.3	0.3	99.9	0.2	96.0
3	47.9	5.4	71.1	5.9	87.2	3.2	18.6
7	16.4	3.7	41.5	7.0	69.9	4.7	0.0
15	1.3	1.9	15.4	5.6	44.6	8.9	3.3
20	0.2	0.3	7.2	5.0	34.3	8.6	0.0

Sulfaphenazole, Montelukast sodium, 4-Methylpyrazole hydrochloride, Furafylline

All of these potential CYP450 inhibitors did not influence the metabolism of [¹⁸F]FMeNER-D2 in rat liver microsomes. In the interest of completeness, the obtained data for sulfaphenazole, montelukast sodium, 4-methylpyrazole and furafylline are listed in the appendix (see chapter 9.1.5).

3.2.3.2.1 Summary and comparison of inhibitory effects in HLM and RLM**Table 38:** Overview on inhibition experiments in HLM and RLM.

Inhibitor	HLM		RLM	
	Concentration required for effect [μM]	[% tracer (inh.)] – [% tracer (ref.)] after 60 min	Concentration required for effect [μM]	[% tracer (inh.)] – [% tracer (ref.)] after 20 min
Ketoconazole	50	7.9 (n = 1)	10	56 \pm 1.6 (n = 2)
	100	10.2 (n = 1)	100	96.4 (n = 1)
Quinidine	5	100 (n = 2)	50	44.8 (n = 1)
(+)-N-3-Benzylirvanol	100	4.2 \pm 1.8 (n = 2)	100	39.7 (PB) or 81.9 (PBS) (n = 1)
Ticlopidine.HCl	50	9.1	no effect	-
	100	10.5	100	7.8 \pm 7.7 (n = 2)
PPP	no effect	-	50	34.3 \pm 8.6 (n = 2)
Furafylline	100	5.4 \pm 1.5 (n = 2)	no effect	-
Sulfaphenazole	no effect	-	no effect	-
4-Methylpyrazole hydrochloride	no effect	-	no effect	-
Montelukast.Na	no effect	-	no effect	-

Ketoconazole is a frequently used inhibitor for CYP3A in HLM but is only selective for this isozyme when used in sub-micromolar concentrations. In higher concentrations significant influence on other CYP450 isoforms like CYP2A6, CYP2B6, CYP2C8, CYP2C9, CYP2C19, CYP2D6 and CYP2E1 were observed.^[43] However, a cross-inhibition of CYP2E1, CYP2C9, CYP2C8 and CYP2B6 can be excluded from inhibition experiments with 4-methylpyrazole, sulfaphenazole, montelukast sodium and 2-phenyl-2-(1-piperidinyl)propane, respectively.

Benzylirvanol and ticlopidine were tested as inhibitors for CYP2C19 and minor effects could be observed for both of them (*Table 38*). In this regard, a selective inhibition cannot be guaranteed for both inhibitors due to the high concentration required for a first significant effect. It was stated, that benzylirvanol selectively inhibits CYP2C19 activity in HLM at maximum concentrations of up to 30 μM .^[89] Besides that, ticlopidine gave an effect at 50 μM , which does not ensure selective inhibition of CYP2C19 (K_i -values: 0.4 – 10 μM , see chapter 1.6.2).

Furafylline exerted a minimal reduction of enzymatic activity against [^{18}F]FMeNER-D2 in HLM amounting to 5.4 \pm 1.5% (n = 2). To verify the involvement of CYP1A2 in the HLM metabolism, an even more potent CYP1A2 inhibitor, namely α -naphthoflavone, ought to be tested in future.

Furthermore, the well-marked effect of quinidine on tracer metabolism found in HLM incubations has to be emphasized. As quinidine fully inhibited tracer degradation in concentrations around its K_i – value, a selective blockage of CYP2D6 can be assumed.

In contrast to human liver microsomes, no complete inhibition of rat liver microsomal metabolism of our tracer was achieved. In this case, not quinidine but ketoconazole was able to exhibit the

strongest effect of all tested CYP450 chemical inhibitors. Unfortunately, ketoconazole is known to be a nonselective inhibitor in RLM and therefore, metabolic modification of our tracer via rat CYP3A1/2 solely could not be determined with certainty.

The second strongest effect after ketoconazole was observed for quinidine. The fact that sulfaphenazole did not impede enzymatic degradation via CYP2C6 suggests that quinidine selectively inhibits CYP2D1 activity in the used assay.^[98] As metabolism via CYP2C6 could be excluded, furafylline is only supposed to influence CYP1A2 activity. However, its effect on tracer metabolism could not be demonstrated.^[110] Moreover, the lack of alterations in metabolism with increasing content of 4-methylpyrazole indicates no involvement of CYP2E1 in [¹⁸F]FMeNER-D2 degradation.^[108] Unlike HLM, incubations with 2-phenyl-2-(1-piperidinyl)propane (PPP) in RLM were able to reduce degradation kinetics significantly but cannot be assigned to a defined CYP isoform. This is also the case for benzylnirvanol, which hampered metabolism of [¹⁸F]FMeNER-D2 to a noticeable degree, but is not established as CYP inhibitor for RLM so far. Ticlopidine and Montelukast on the other hand showed no effects on RLM metabolism of [¹⁸F]FMeNER-D2, however their inhibitory effect on RLM has not yet been sufficiently evaluated.

To recap, the results obtained for HLM and RLM incubations were comparable, only furafylline, ticlopidine and PPP represented exceptions.

From the chemical inhibition experiments, it can be concluded that CYP3A, CYP2C19 and CYP2D6 might be primarily responsible for the *in vitro* degradation of [¹⁸F]FMeNER-D2 in humans. CYP1A2 might also contribute to FMeNER-D2 degradation but it needs to be further examined. To validate the influence of the above identified single enzymes in the multi-enzyme complexes, [¹⁸F]FMeNER-D2 was incubated with individual recombinant CYP450 enzymes.

3.2.4 Incubation of [¹⁸F]-FMeNER-D2 with recombinant human CYP450s

Seven major drug-metabolizing isoforms of cDNA expressed human CYPs were tested to examine their capacities for metabolism of [¹⁸F]FMeNER-D2. The incubation of the investigated tracer with several cytochrome P450 isoforms, namely, CYP1A1, CYP1B1, CYP2A6 and CYP2E1 did not lead to a breakdown of the reboxetine-derived tracer within 240 min under the aforementioned conditions (n≥2). It has to be emphasized that higher concentrations of organic solvent (EtOH) had to be used for CYP2E1 than usually are tolerated. Normal formulation of the tracer leads to a content of 0.17% EtOH in the incubation mixture while 0.2% of organic solvent is supposed to lead to inhibition of this isoform.^[123] A higher dilution of our tracer would have provided not integrable radiosignals and was, therefore, not feasible.

3.2.4.1 CYP3A4

For this specific isoenzyme a significantly altered enzymatic activity was observed with varying buffer and ionic strength of the buffer solution. When using phosphate buffered saline enzymatic activity was fully inhibited in the first 90 min of incubation time (n = 4). Simple alteration of PBS to sodium phosphate buffer lead to a degradation of [¹⁸F]FMeNER-D2 accounting for 74.6 ± 5.9%

after 90 min (Figure 34). Separation via HPLC chromatography indicates the formation of three distinct metabolites (see Figure 35).

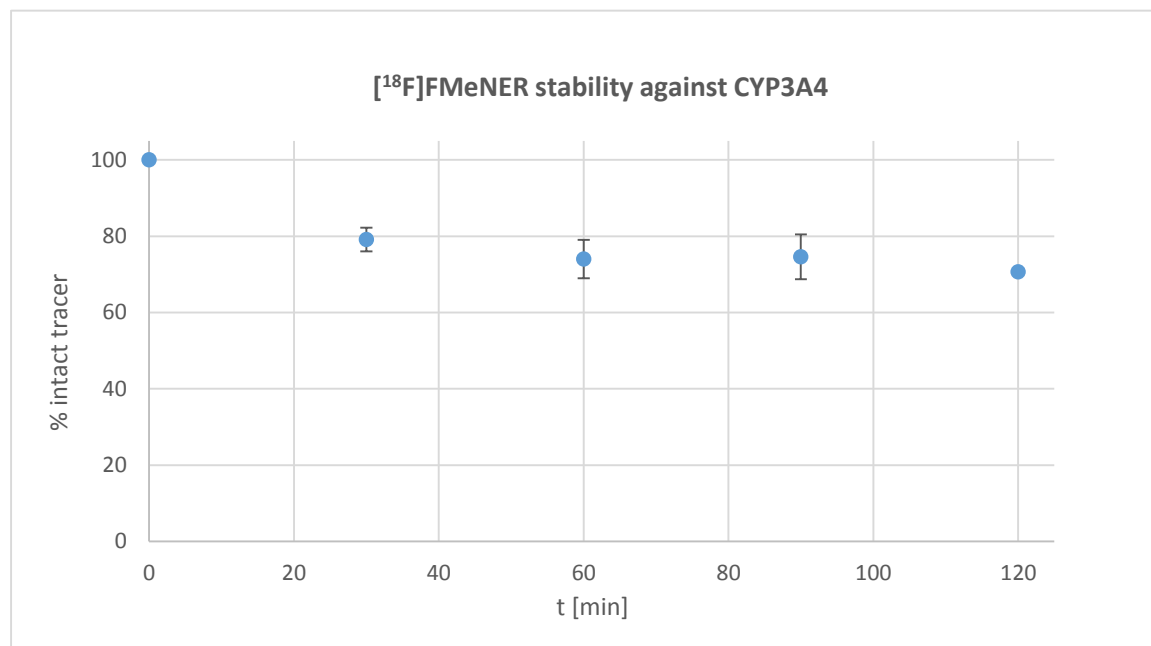


Figure 34: Time-dependent cleavage of [^{18}F]FMeNER-D2 via CYP3A4; (MEAN \pm SD); $n = 4$.

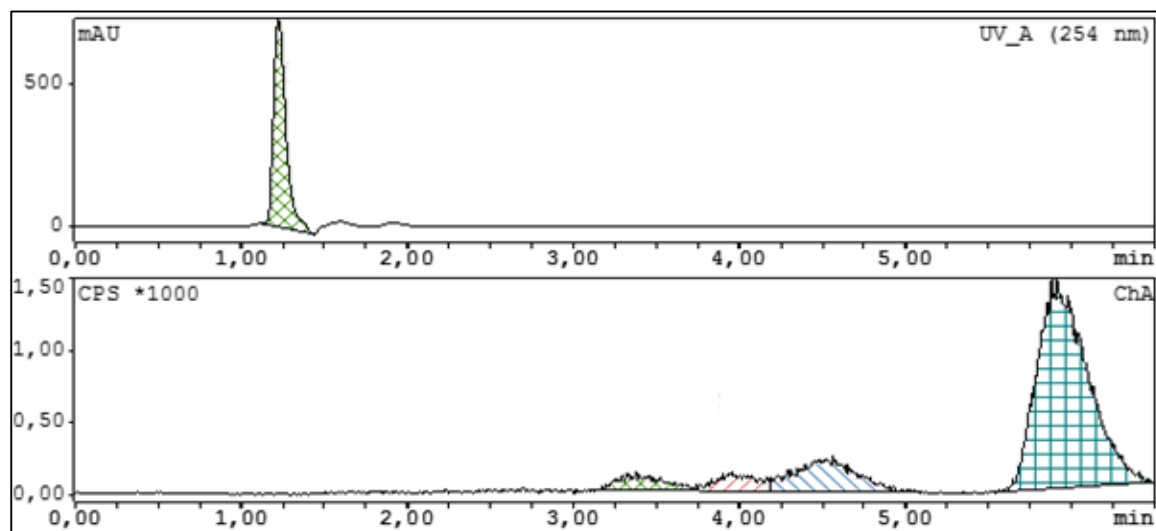


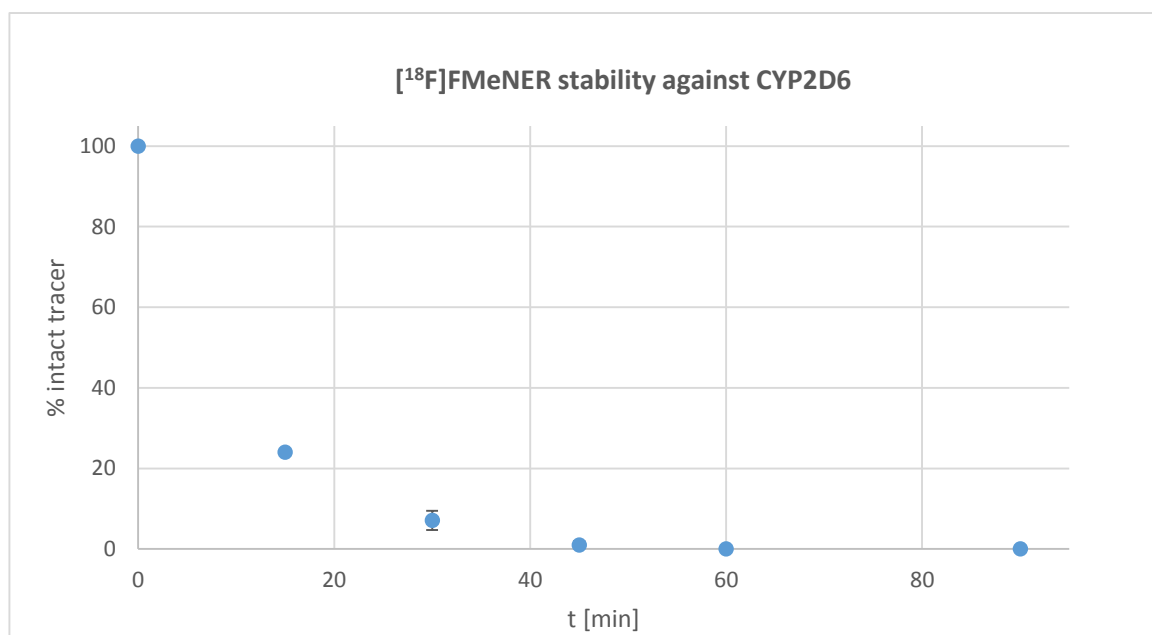
Figure 35: Exemplary chromatogram of CYP3A4 incubation showing the resulting radiosignals of metabolites after 60 min.

3.2.4.2 CYP 2D6

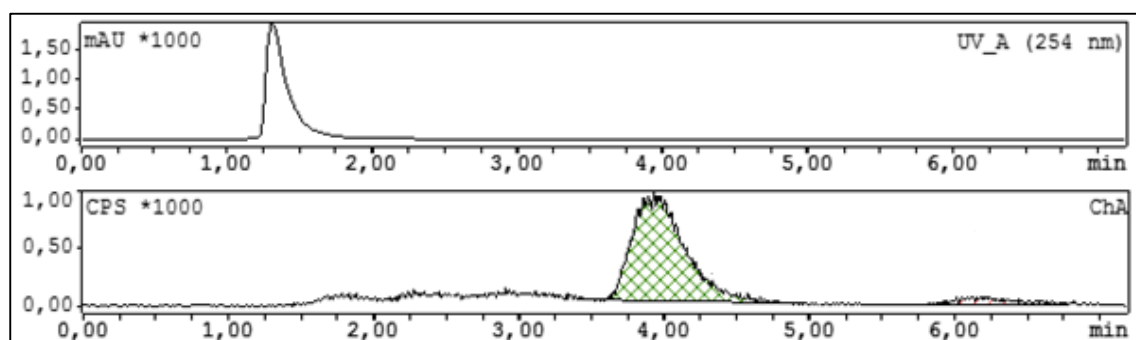
In Figure 36, a significant biodegradation of the fluoromethyl ether [^{18}F]FMeNER-D2 with CYP2D6 is shown, culminating in a complete decomposition within 60 min (Table 39).

Table 39: Degradation via CYP2D6, 1000 μL batch.

t [min]	MEAN [% intact tracer]	SD	n
0	100	0.0	5
15	24.1	0.4	2
30	7.1	2.4	5
45	1.0	1.0	5
60	0.0	0.0	5
90	0.0	0.0	5

**Figure 36:** Full depletion of NET-ligand $[^{18}\text{F}]\text{FMENER-D2}$ via the CYP2D6 isoform using 1000 μL batch; (MEAN \pm SD).

Interestingly, the 300 μL incubation batch (3.3-fold higher concentrated than 1000 μL batch) lead to a minimally reduced enzymatic turnover resulting in full depletion of $[^{18}\text{F}]\text{FMENER-D2}$ after 90 min. HPLC separation of single enzyme incubations showed one major metabolite, as depicted in Figure 37.

**Figure 37:** HPLC chromatogram showing enzymatic breakdown with CYP2D6 after 45 min incubation time, 1000 μL batch ($t_{\text{r}}(\text{FMN}) = 6 \text{ min}$, $t_{\text{r}}(\text{metabolite}) = 4 \text{ min}$).

3.2.4.3 CYP2C19

A significant metabolic degradation was observed in CYP2C19 incubations, yielding $88.9 \pm 2.0\%$ of intact $[^{18}\text{F}]\text{FMeNER-D2}$ after 90 min.

Using this enzyme, one metabolite with higher polarity than the parent tracer $[^{18}\text{F}]\text{FMeNER-D2}$ was detected by radio-HPLC (Figure 38).

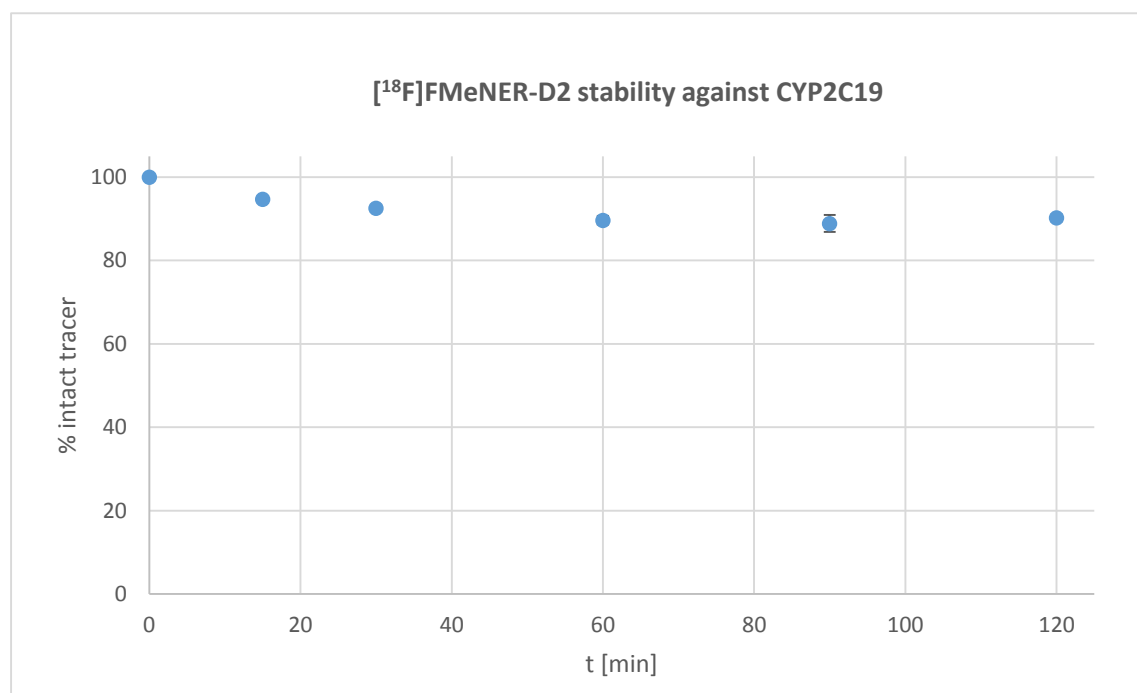


Figure 38: In-vitro depletion of intact $[^{18}\text{F}]\text{FMeNER-D2}$ via CYP2C19; (MEAN \pm SD); $n = 5$.

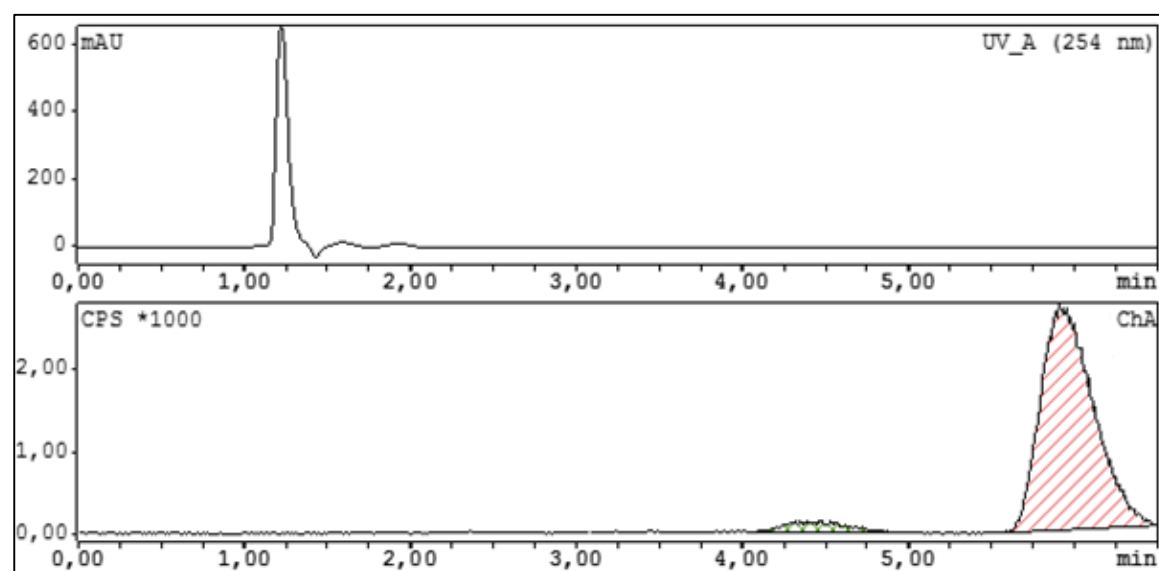


Figure 39: RP-chromatography reveals one major metabolite ($t_r = 4.5$ min) formed in enzymatic decomposition of $[^{18}\text{F}]\text{FMeNER-D2}$ ($t_r = 6$ min) with CYP2C19; after 15 min of incubation time.

Testing the selectivity of CYP2D6 and CYP3A4 inhibitors against the recombinant CYP450 isozyme

In the following single enzyme incubations, the inhibitory effect of CYP2D6 and CYP3A4 inhibitors on their respective enzyme was investigated. For CYP2D6 1 μM quinidine was sufficient to fully prevent any degradation of the tracer (*Figure 40*). Incubations were carried out according to the previously described procedures (300 μL batches, see methods: chapter 2.3.2.4.1).

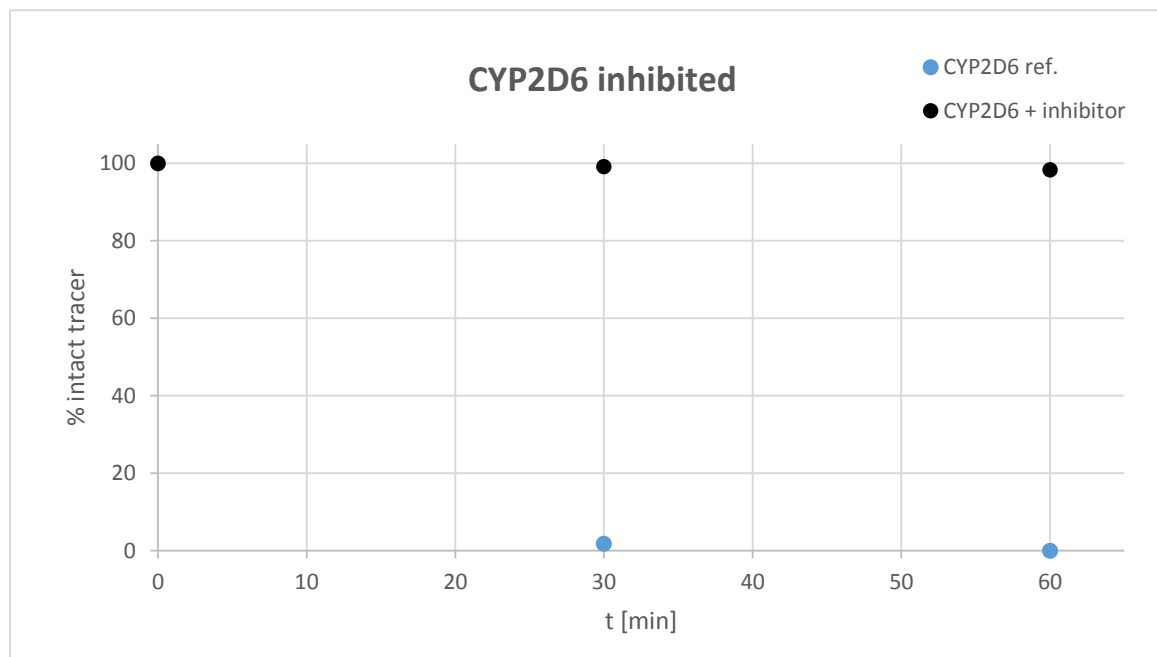


Figure 40: CYP2D6 inhibition via quinidine (1 μM) in the presence of [^{18}F]FMeNER-D2 versus control.

The same conditions were used for CYP3A4, but 1 μM ketoconazole was not able to stop the metabolism of [^{18}F]FMeNER-D2 to a significant extent (*Figure 41*).

Therefore, it might be questionable whether complete inhibition can be achieved using higher concentrations of inhibitor (up to 20 μM).

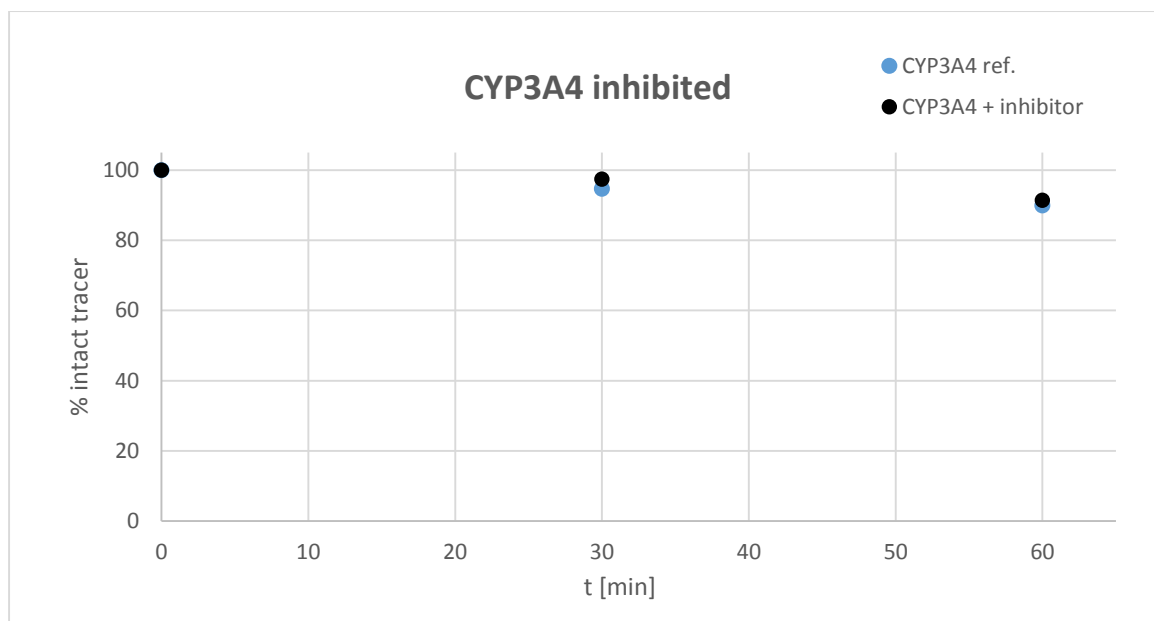


Figure 41: Effect of single enzyme CYP3A4 inhibition on tracer degradation; 1 μ M ketoconazole versus control without inhibitor.

Comparison of metabolites – Interpretation of radiosignals

When comparing radiosignals of the different experiments the retention times of each run have to be normalized to k' values, to enable an instrument-independent analysis.

Hence, k' values of the radiometabolites occurring in the incubation mixtures of HLM, RLM and single enzymes were compared (see *Table 40*).

Table 40: Radioactive signals listed for all experiments where degradation was observed (MEAN(\pm SD)); main signals are highlighted in bold.

	HLM	RLM	CYP2C19	CYP2D6	CYP3A4
k'					
met 1		1.6 (0.1)			1.7 (0.0)
met 2	2.1 (0.1)	2.2 (0.0)		2.0 (0.1)	2.2 (0.0)
met 3			2.7 (0.1)		2.7 (0.1)
FMN	3.8 (0.1)	4.0 (0.2)	3.9 (0.1)	3.6 (0.1)	3.8 (0.0)

It can be assumed that the main metabolite formed in HLM incubations was identical with the one found in RLM ($k' = 2.1$ and 2.2 , respectively). This radioactive signal could also be found in CYP2D6 batches, where it represented the most intense peak. In CYP3A4 degradation this signal appeared as well but played a subordinate role. Surprisingly, the main radioactive signal observed for CYP2C19 and CYP3A4 ($k' = 2.7$ on first column) did not occur in the case of HLM and RLM. The radioactive signal found in the loopwaste and in the crude mixture of reactor 1 and 2 showed a k' value of 1.4 and may be assigned to $[^{18}\text{F}]\text{BFM}$. Therefore, it can be concluded that the main

metabolites arising in our degradation mixtures are not attributed to *O*-demethylation of the tracer.

3.2.5 Incubation of [¹⁸F]-FMeNER-D2 with centrally occurring enzymes

Furthermore, centrally occurring enzymes like MAO A and B as well as COMT (porcine) did not influence the stability of [¹⁸F]FMeNER-D2 *in vitro*. Esterases such as human carboxylesterase 1b, 1c and 2 as well as a porcine CE did not result in a degradation of fluoromethyl ether [¹⁸F]FMeNER-D2. In contrast, the remaining CYP450 isoforms CYP3A4, CYP2C19 and CYP2D6 lead to the formation of radiometabolites and are discussed hereinafter in more detail.

3.2.6 Bone binding experiments

In bone binding studies, no inordinate adsorption was observed for the intact radiotracer [¹⁸F]FMeNER-D2 according to $5.9 \pm 1.1\%$ with HA and $2.8 \pm 0.3\%$ with diaphyseal bone. This uptake is comparable to 6-[¹⁸F]Fluoro-L-DOPA, a commercially available and well-established neurotracer for PET imaging of neuropsychiatric diseases (see *Figure 42*). The lowest levels of activity measured for the pellet were found for [¹⁸F]fluorocholine chloride, [¹⁸F]FET and [¹⁸F]FDG, whereas the latter one was intended to be used as a negative control ($1.7 \pm 0.5\%$ (HA) and $1.5 \pm 0.5\%$ (diaphysis) after 90 min). As incubations with [¹⁸F]F-choline resulted in a lower binding than [¹⁸F]FDG, these data were used as negative control. The scattering of values of bound fraction of [¹⁸F]FDG can be explained by varying proportions of radioactive fluoride in the formulated product (0.5 - 1.7%). [¹⁸F]NaF is known to be a bone seeker and represented the positive control in our measurements ($98.7 \pm 0.2\%$ (HA) and $97.9 \pm 0.2\%$ (diaphysis) after 90 min).

Incubation with metabolites of our tracer obtained from RLM (100% cleavage) did not show the expected significant increase in adsorption ($4.5 \pm 4.9\%$ (HA) and $1.6 \pm 0.3\%$ (diaphysis) after 30 min). An incubation time-dependent binding was only observed for 6-[¹⁸F]Fluoro-L-DOPA and [¹¹C]Me@APPI suggesting limited stability of the tracers under the aforementioned conditions.

[¹⁸F]F-DOPA is known to be less stable at pH values above 4.5 due to oxidation of the tracer.⁸ Interestingly, differences between uptake in inorganic mineral and bone material was only observed for the intact [¹⁸F]FMeNER-D2, its metabolites as well as [¹¹C]Me@APPI but not for [¹⁸F]F-DOPA. Diaphysis was able to bind only half as much tracer as hydroxyapatite indicating that binding is hampered by collagen, which can be found in bone matter in relevant quantities. Acetonitrile did not interfere in the experimental setup, since washing with ACN did not change the bound proportion compared to the reference washed with water.

⁸ according to SPC (Summary of Product Characteristics) of IASON GmbH; revised 16.05.2012.

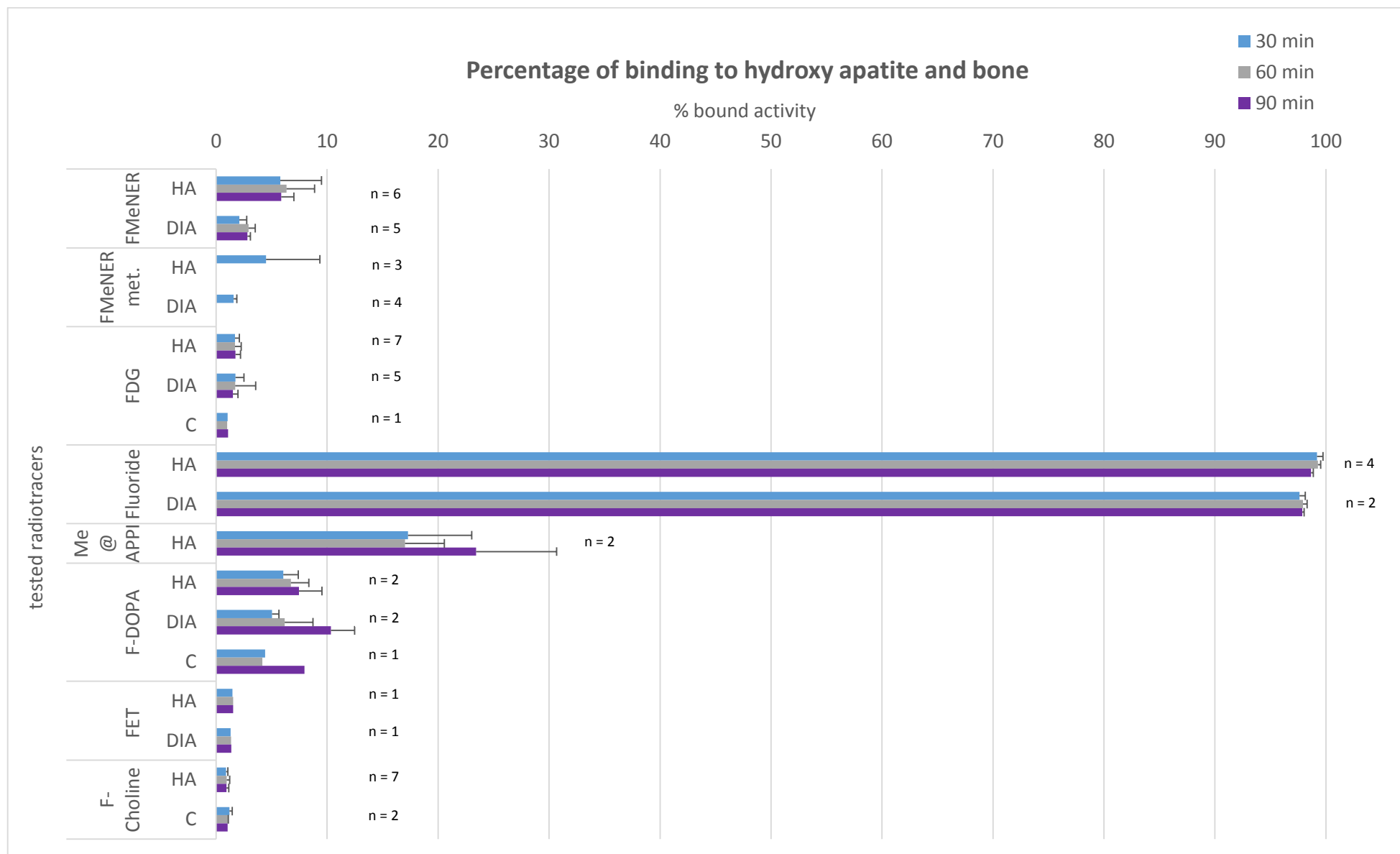


Figure 42: Overview on bone binding studies using the same amount (3 mg) of hydroxy apatite (HA), diaphysis (DIA) or corticalis (C), FMeNER met. stands for radiometabolites taken from RLM incubations; the complete data table is given in the appendix (see Table 58).

For metabolite suspensions obtained by microsomal degradation with RLM, results were identical for incubations which were stopped with acetonitrile or water (maximum final concentration of ACN: 1%). Therefore, binding does not seem to be impeded by minimal amounts of organic solvents. This also applies to the formulation of [¹⁸F]FMN (abbrev. for [¹⁸F]FMeNER-D2), giving concentrations of 0.06 – 0.4% EtOH in the final incubation batches, which was not found to correlate with the proportion of FMN bound to HA or diaphysis in the performed experiments (n = 5-6).

The obtained data demonstrated that [¹⁸F]FMN is stable under the abovementioned incubation conditions, as no increase or decrease in percentage of binding from 30 min to 90 min was observed. Beyond that, only very limited binding for [¹⁸F]FMN (about 5% to HA or 2% to bone, corrected for unspecific binding of negative control [¹⁸F]F-choline) and polar metabolites of FMN (4% to HA or 1% to bone) to inorganic bone matrix (HA) and human long bones occurred. TLC controls of [¹⁸F]FMN before and after incubation with HA or bone material did not show the presence of free [¹⁸F]fluoride. No significant loss of activity during incubations with metabolites from RLM was found, which indicates that the formed main metabolite is not highly volatile (boiling point of CH₂BrF = 19°C). In TLC controls of [¹⁸F]FMeNER-D2 a R_f value of 0.85 (RP-DC, ACN/H₂O 70/30) was observed. TLC plates of RLM incubations (100% cleavage according to HPLC) did not show a radioactive spot except for the intact tracer. However, this can only be explained by a very volatile metabolite species.

Moreover, one major drawback presents the unspecific binding of lipophilic tracers to the polypropylene vials (Eppis). Therefore, the binding of the tested compounds to empty tubes needs to be assessed prior to the experiments. To largely reduce the influence of this unspecific binding, the suspension should be transferred into a new vial after the incubation time and activity in the washed incubation tube should be measured.

4 EXPERIMENTAL PART II – Synthesis of novel NET-PET tracers

4.1 General working methods

4.1.1 Characterization of precursors

Nuclear Magnetic Resonance Spectroscopy

^1H and ^{13}C , ^{18}F , ^{15}N and two dimensional ^1H - ^1H COSY, ^1H - ^{13}C HSQC and ^1H - ^{13}C HMBC NMR spectra were recorded on a Bruker DPX200 spectrometer (200 MHz (^1H), 50 MHz (^{13}C)) or on a Bruker Avance III 400 spectrometer (400 MHz (^1H), 100 MHz (^{13}C), 40 MHz (^{15}N), 376 MHz (^{18}F)) at 25°C. All compounds were dissolved in CDCl_3 or DMSO-d_6 and therefore, the chemical shifts are quoted relative to the residual solvent signals. Spectra measured in CDCl_3 are referenced to 7.24 ppm for ^1H and 77.00 for ^{13}C . ^{15}N NMR data were obtained via ^1H , ^{15}N HSQC experiments and referenced against nitromethane.

Mass spectra were obtained by measurements on a Shimadzu QP 1000 instrument (EI, 70 eV, Kyoto Japan).

High resolution mass spectrometry (HRMS) was carried out on a maXis HD ESI-Qq-TOF mass spectrometer (Bruker Daltonics, Bremen, Germany) in the positive-ion mode (direct infusion).

Melting points were determined on a Reichert-Kofler hot-stage microscope.

X-ray diffraction data were recorded on a Bruker D8 Venture diffractometer at 100 K. Data were processed using Olex2 software working with the ShelXS structure solution program.^[124, 125] The structures were solved by direct methods and refined with the XL refinement package using least-squares minimization.

Thin layer chromatography (TLC) for reaction monitoring was performed using Silica Gel 60 F₂₅₄ and Silica Gel 60 RP-18 F₂₅₄ plates (Merck, Darmstadt, Germany).

4.1.2 Instrumentation for radiochemical labeling

^{11}C CO₂ was produced within a GE PET trace cyclotron (General Electric Medical System, Uppsala, Sweden) by a $^{14}\text{N}(p,\alpha)^{11}\text{C}$ reaction through irradiation of N₂ (+1% O₂) (Air Liquide, Schwechat, Austria). The production of radioactive methyl iodide [^{11}C]CH₃I, methyl triflate [^{11}C]CH₃OTf as well as the synthesis of the final tracers [^{11}C]Me@FAPPI1:0 and [^{11}C]Me@FAPPI1:3 was performed within a TRACERlab™ FX C Pro synthesizer (GE Healthcare, Uppsala, Sweden). The operation of the module was remotely controlled by a standard laptop including appropriate software.

For purification of the crude tracers different semi-preparative RP-columns were tested (see *Table 41*). The used HPLC system was equipped with a radioactivity detector and a UV-detector as well as a LaPrep HPLC pump (VWR International, Radnor, USA).

Analytical HPLC was performed using a Merck-Hitachi LaChrom HPLC system (pump L-7100) with a UV-detector (at 254 nm, LaChrom L-7400) and a NaI radio-detector (Bertholdt Technologies, Bad

Wildbach, Germany). The chromatographic system combined a Phenomenex® Prodigy, Phenyl-3-(PH-3) column (5 µm, 250 x 4.6 mm) with a mobile phase consisting of ACN/0.1 M AMF 50/50% v/v at a flow rate of 2 mL/min. For data processing GinaStar® software was used (Raytest, Straubenhardt, Germany).

4.1.3 Materials

Column chromatography was carried out using Merck Silica Gel 60 (70-230 mesh) or Merck LiChroprep RP-18 Silica Gel (40-63 µm). All chemicals were purchased from Sigma Aldrich, Thermo Fisher Scientific or VWR (Vienna, Austria). The reference standards Me@FAPPI1 and Me@FAPPI3 were kindly provided by the Department of Drug and Natural Product Synthesis, Faculty of Life Sciences, University of Vienna.

Dimethylsulfoxide (DMSO), 2-butanone (MEK), tetrabutylammonium hydroxide 30-hydrate (TBAH), triethylamine and Nickel nanopowder (< 100 nm, > 99%) was purchased from Sigma Aldrich (Vienna, Austria). Iodine (sublimated grade for analysis; Pharm. Eur.) was obtained from Merck (Darmstadt, Germany). Silver triflate impregnated carbon was prepared according to the procedure of Mark et al.^[32] using silver trifluoromethanesulfonate (Sigma Aldrich, Vienna, Austria) and Graphpac-GC (80/100 mesh, Alltech, Deerfield, USA). Solid phase extraction was carried out using C8 plus Sep-Pak® cartridges from Waters (Waters® Associates, Milford, USA).

All other products e.g. solvents, saline solutions, sterile water, sterile filters and phosphate buffer were purchased and prepared as given for [¹⁸F]FMeNER-D2 synthesis.

4.2 Precursor chemistry – Experimental procedures

The synthesis route is based on work of Zhang et al.^[126] as well as modifications of Neudorfer et al.^[117] In contrast to the literature, the last two steps of the synthesis were altered in order to facilitate the purification of the compounds and to give the product in higher yields. In Figure 43, an overview of the synthesis steps is given.

Briefly, core structure **3** and **16** were prepared before linkage to the racemic side chain **5** and **11**, respectively, via nucleophilic substitution. The resulting intermediates **6** and **12** were modified by two subsequent substitution reactions giving the azide derivatives **8** and **14**. The free amines **9** and **15** were obtained using a reduction step under *Staudinger* conditions.

Synthetic scheme

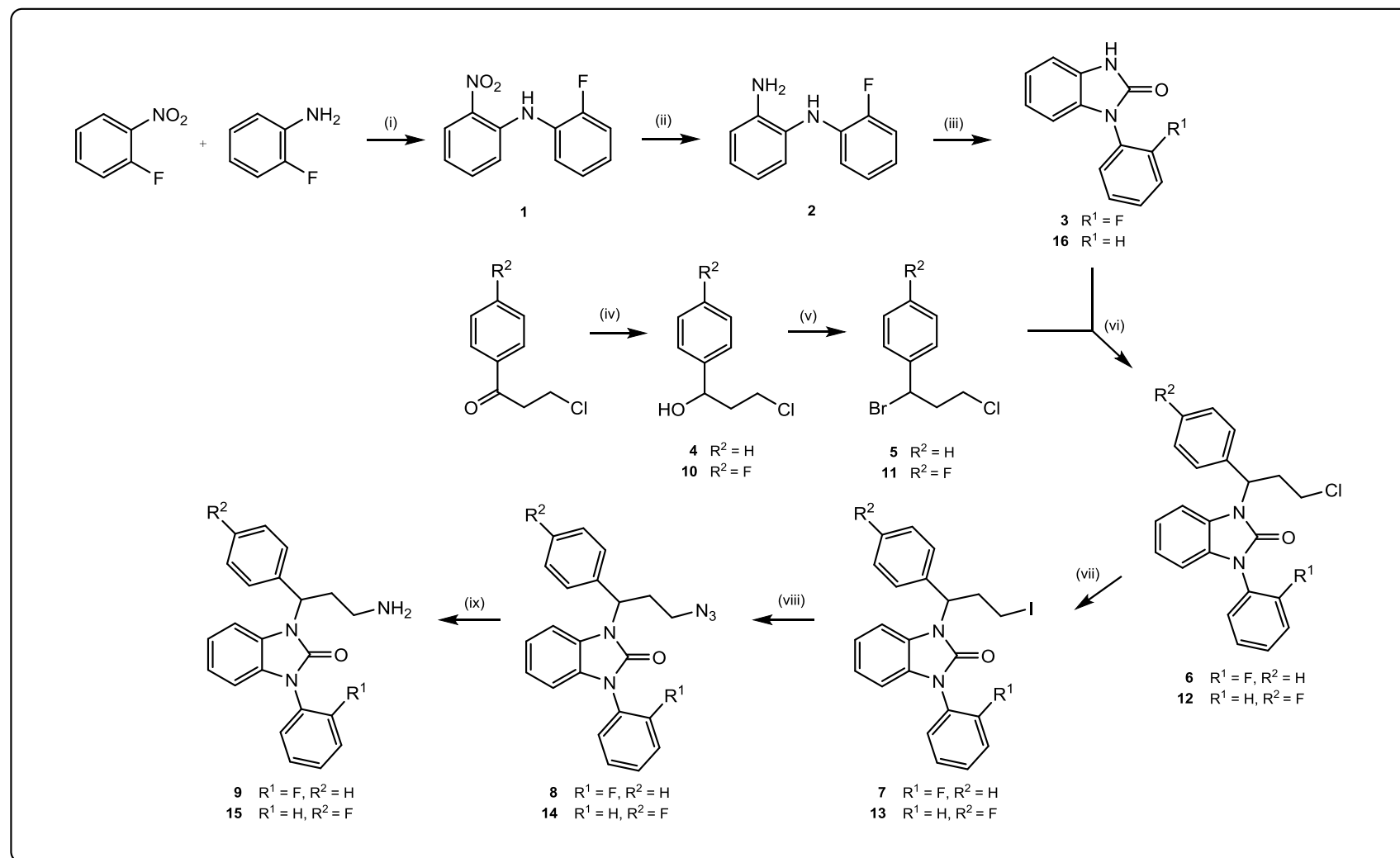
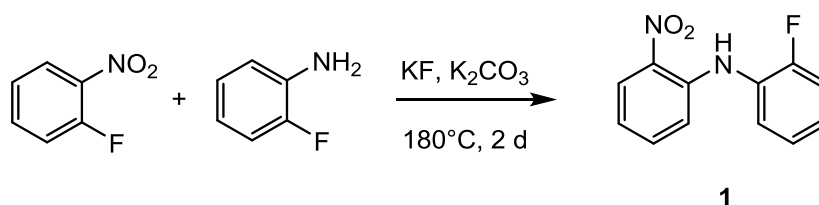


Figure 43: Reagents and Conditions: (i) KF, K₂CO₃, 180°C, 2 d, (1, 23%); (ii) CH₂Cl₂, DMF, Ar, Zn, 2 h: 0°C to rt (2, 97%); (iii) CDI, DMF, Ar, reflux, 2 h (3, 75%); (iv) EtOH/THFdry, NaBH₄, -10°C to rt, 3 - 4 h [(4, 92%), (10, 98%)]; (v) HBr (47%), rt, 3h (5, 95%), 18 h (11, 93%); (vi) K₂CO₃, DMF, rt, 24 h (6, 68%), 7 h or 24 h (12, 17%); (vii) NaI, acetone_{dry}, reflux, 18 - 20 h [(7, 52%), (13, 89%)]; (viii) NaN₃, DMF, 75%, 12 h [(8, 60%), (14, 98%)]; (ix) (1) PPh₃, THF, rt, 8-10 h; (2) H₂O, 12 - 16 h [(9, 57%), (15, 85%)].

4.2.1 FAPPI3:0

4.2.1.1 Synthesis of core structure

4.2.1.1.1 Step 1

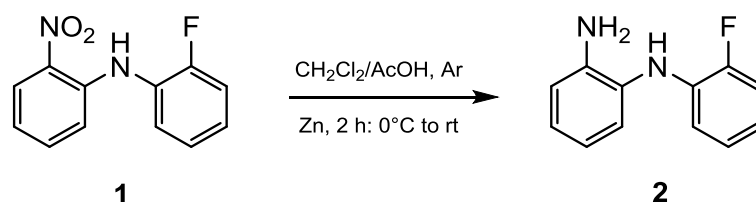
Substance	<i>M</i> [g/mol]	<i>m</i> [g]	<i>n</i> [mmol]	ρ [g/mL]	Eq.
2-Fluoroaniline	111.12	3.96	35.6	1.151	1.0
1-Fluoro-2-nitrobenzene	141.10	5.07	35.9	1.338	1.0
KF	58.10	2.07	24.3		0.7
K ₂ CO ₃	138.20	4.91	35.5		1.0

To a mixture of anhydrous KF and K₂CO₃, 2-fluoroaniline and 1-fluoro-2-nitrobenzene were added and refluxed at 180°C for 2 days. Thereafter, H₂O (50 mL) and dichloromethane (DCM, 50 mL) were added and the organic layer was washed with 10 mL of HCl (10%) and brine three times each. After re-extraction with DCM (2 x 20 mL) the combined organic layers were dried over Na₂SO₄ and the solvent was removed under reduced pressure. The resulting red-brown solid was purified by column chromatography (silica gel 60, PE/EtOAc: 9/1 → 8/2). Only one pure fraction was collected which was used in the next reaction step. The second fraction was discarded due to impurities.

Form and appearance: red-brown solid

Yield: 1.90 g, 23% (pure fraction), 1.04 g, 13% (mixed fraction; dark orange oil)

Spectroscopic data (¹H-, ¹³C-NMR) are in accordance with the literature.^[127]

4.2.1.1.2 Step 2

Substance	<i>M</i> [g/mol]	<i>m</i> [g]	<i>n</i> [mmol]	<i>V</i> [mL]	Eq.
2-Fluoro- <i>N</i> -(2-nitrophenyl) aniline	232.21	1.88	8.1		
Zn	65.38	7.28	111.0		14
AcOH	60.05			3.75	

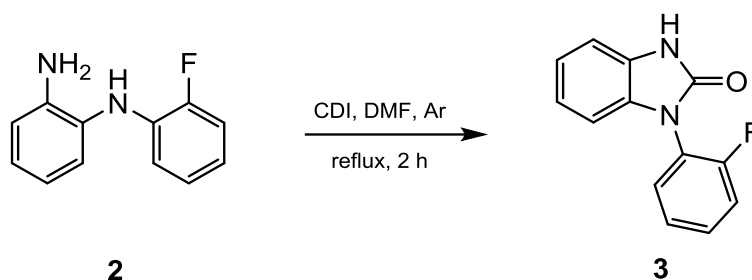
To a vigorously stirred solution of 2-fluoro-*N*-(2-nitrophenyl)aniline in dry DCM and glacial acetic acid at 0°C, powdered Zn⁰ was quickly added under argon atmosphere. Subsequently, the dark-brown mixture was stirred for 2 h at room temperature (rt) (after 1 h: color change to green-brown). Zn was filtered off and the pH of the solution was adjusted to about 8 – 9 (2 M NaOH). Another 30 mL of water were added before extraction with 600 mL DCM. The organic phase was washed twice with saturated NH₄Cl solution (pH 7-8) and once with brine (pH 7-8) and the combined aqueous phase was re-extracted with DCM. The solvent was removed under reduced pressure and used in the next reaction step without further purification. The product was identified via TLC.

$R_{f_{\text{educt}}}(\text{PE/EtOAc } 9/1) = 0.45$

$R_{f_{\text{product}}}(\text{PE/EtOAc } 9/1) = 0.23$

Form and appearance: dark-brown solid

Yield: 1.589 g, 97%

4.2.1.1.3 Step 3

Substance	<i>M</i> [g/mol]	<i>m</i> [g]	<i>n</i> [mmol]	Eq.
<i>N</i> ¹ -(2-Fluorophenyl)benzene-1,2-diamine	202.23	1.589	7.86	1.0
CDI	162.15	4.810	29.7	3.7

A solution of CDI in 39 mL DMF was added to the educt **2** in 14 mL DMF within 15 min under argon atmosphere. After stirring at rt for 5 min the solution was heated to 90°C and refluxed for 2 h. DMF was removed under reduced pressure and the reaction was quenched with 100 mL H₂O. The resulting precipitate was collected via filtration, dissolved in DCM and dried over Na₂SO₄. The solvent was removed under reduced pressure and the residue dried *in vacuo*. The dark-red oil was purified via column chromatography (PE/EtOAc/MeOH 4/5/1).

Form and appearance: red solid

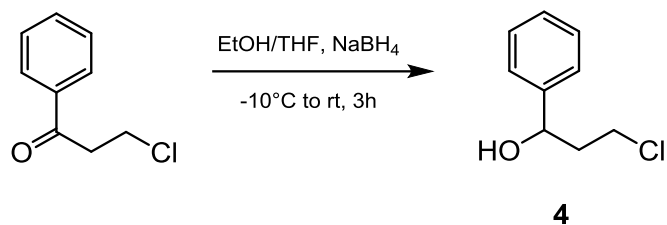
Yield: 1.344 g, 75%

Spectroscopic data (¹H-, ¹³C-NMR) are in accordance with the literature.^[117]

¹H NMR (200 MHz, CDCl₃, δ_H): 10.54 (bs, 1H), 7.60 – 7.42 (m, 2H), 7.89 – 7.26 (m, 2H), 7.19 – 7.00 (m, 3H), 6.85 – 6.82 (m, 1H).

¹³C NMR (50 MHz, CDCl₃, δ_C): 160.5, 155.4, 154.7, 130.4, 129.6, 128.2, 125.0, 124.9, 122.4, 121.9, 121.5, 121.5, 117.4, 117.0, 110.1, 108.9.

4.2.1.2 Synthesis of the sidechain

4.2.1.2.1 Step 4

Substance	<i>M</i> [g/mol]	<i>m</i> [g]	<i>n</i> [mmol]	Eq.
3-Chloro-1-phenylpropan-1-one	168.62	4.49	26.6	1.0
NaBH ₄	37.83	1.06	28.0	1.05

To a cooled solution (-10°C) of 3-chloro-1-phenylpropan-1-one in dry THF (25 mL) and EtOH_{abs.} (35 mL) was slowly added NaBH₄ over a period of 15 min. After stirring for additional 15 min, the mixture was allowed to warm to rt and these conditions were kept for another 3 h. The reaction was quenched by pouring the mixture onto ice (40 g) and saturated NH₄Cl (80 mL). The product was extracted with diethyl ether (4 x 80 mL), washed with water (2 x 40 mL), dried over Na₂SO₄ and the solvent was evaporated under reduced pressure.

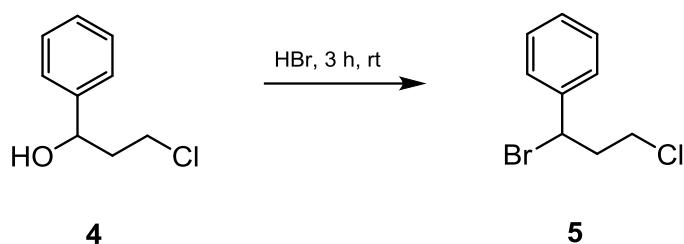
Form and appearance: light-yellow oil

Yield: 4.166, 92 %

Spectroscopic data are according to the literature.^[128]

¹H NMR (200 MHz, CDCl₃, δ_H): 7.39 – 7.34 (m, 5H), 4.95 (dd, ³*J* = 6.0 Hz and 2 Hz, 1H), 3.77 – 3.70 (m, 1H), 3.62 – 3.50 (m, 1H), 2.33 – 2.01 (m, 3H).

¹³C NMR (50 MHz, CDCl₃, δ_C): 143.7, 128.6, 127.9, 125.7, 71.3, 41.7, 41.4.

4.2.1.2.2 Step 5

Substance	<i>M</i> [g/mol]	<i>m</i> [g]	<i>n</i> [mmol]	<i>V</i> [mL]
3-Chloro-1-phenylpropan-1-ol	170.64	3.645	21.4	
HBr (47%)	80.91			70

3-Chloro-1-phenylpropan-1-ol and hydrobromic acid (47%) were stirred for 3 h at rt before slowly pouring the mixture into saturated K_2CO_3 (9 mL) with ice (55 g). After adjusting the pH of the solution to 7, the product was extracted with diethyl ether, dried over MgSO_4 and the solvent evaporated to dryness. The conversion of the educt was monitored via TLC and the substance was used for the next reaction step without further purification.

Form and appearance: transparent, grayish oil

Yield: 4.73 g, 95%

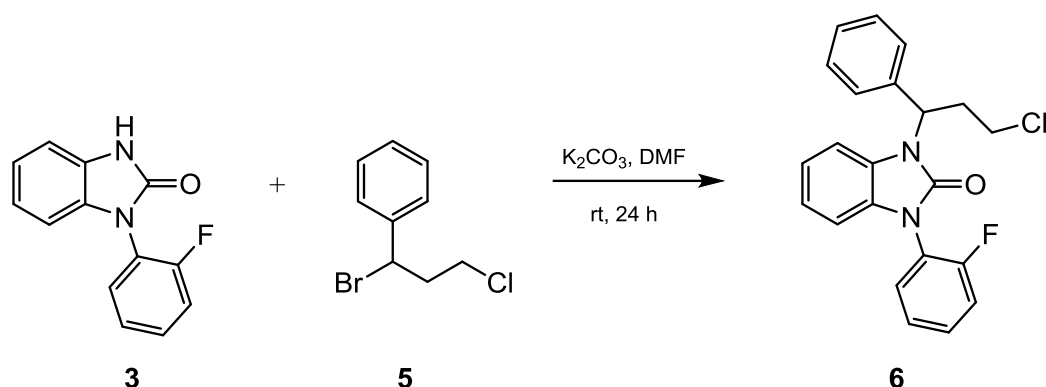
Spectroscopic data match with literature values.^[128]

^1H NMR (200 MHz, CDCl_3 , δ_{H}): 7.46 – 7.33 (m, 5H), 5.24 (dd, 1H, $^3J = 4.0$ Hz and 4.0 Hz), 3.81 – 3.54 (m, 2H), 2.82 – 2.65 (m, 1H), 2.58 – 2.41 (m, 1H).

^{13}C NMR (50 MHz, CDCl_3 , δ_{C}): 140.6, 128.6, 128.5, 127.1, 51.3, 42.5, 41.8.

4.2.1.3 Linkage and modifications

4.2.1.3.1 Step 6



Substance	<i>M</i> [g/mol]	<i>m</i> [g]	<i>n</i> [mmol]	Eq.
1-(2-Fluorophenyl)-1,3-dihydro-2H-benzo[d]imidazol-2-one	228.22	1.28	5.61	1.0
1-Bromo-3-chloropropylbenzene	233.53	1.97	8.41	1.5
K_2CO_3	138.21	1.55	11.21	2.0

A solution of 1-(2-fluorophenyl)-1,3-dihydro-2H-benzimidazol-2-one and K_2CO_3 in DMF (6 mL) was stirred for 20 min at rt before 1-bromo-3-chloropropylbenzene in DMF (0.5 mL) was slowly added. After the reaction took place over night (24 h), H_2O (10 mL) was added and the aqueous phase was extracted with EtOAc (3 x 170 mL) and washed with saturated NaCl solution (3 x 20 mL). The combined organic layers were dried over $MgSO_4$ and the solvent evaporated to dryness. The crude product was purified by column chromatography (silica gel 60, PE/EE 8/2) to yield the desired product as light-yellow resin (mixed fractions were discarded).

Form and appearance: light-yellow resin

Yield: 1.462, 68%

$R_{f, Cl}$ (PE/EtOAc 9/1) = 0.29

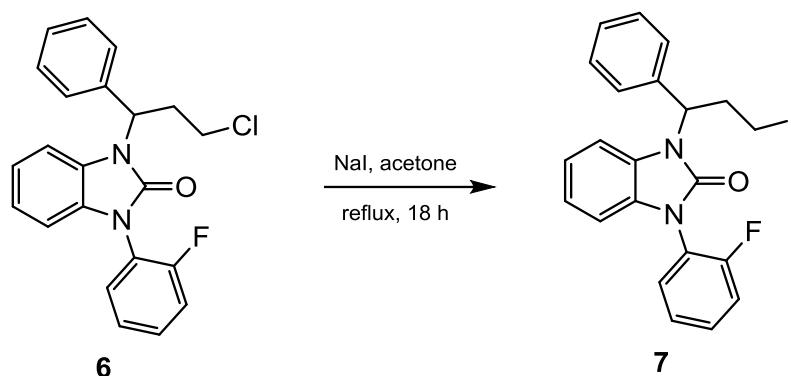
Spectroscopic measurements show product according to the literature.^[117]

1H NMR (400 MHz, $CDCl_3$, δ_H): 7.56 – 7.51 (m, 3H, C12, C16, C21), 7.48 – 7.43 (m, 1H, C20), 7.40 – 7.28 (m, 5H, C13, C14, C15, C19, C22), 7.08 – 7.03 (m, 3H, C5, C6, C7), 6.87 – 6.83 (m, 1H, C4), 5.81 – 5.77 (m, 1H, C8), 3.70 – 3.60 (m, 2H, 2 x C10), 3.21 – 3.25 (m, 1H, C9), 2.86 – 2.78 (m, 1H, C9).

$^{13}\text{C}\{^1\text{H}\}$ NMR (CDCl_3 , δ_{C}): 157.9 (d, $^1J = 253.2$ Hz, C18), 153.0 (C2), 138.4 (C11), 130.2 (d, $^3J = 7.8$ Hz, C20), 129.5 (C22), 129.4 (C3a), 128.8 (C13), 128.8 (C15), 128.1 (C14), 127.3 (C12), 127.3 (C16), 124.8 (d, $^4J = 3.8$ Hz, C21), 122.0 (C6), 121.9 (C17), 121.6 (C5), 117.1 (d, $^2J = 19.5$ Hz, C19), 109.0 (C7), 108.8 (d, $J^{\text{NOE}} = 1.7$ Hz, C4), 54.5 (C8), 41.9 (C10), 34.2 (C9), *undetected*: C7a.

^{19}F NMR (471 MHz, CDCl_3 , δ_{F}): -118.39 (m, C18)

4.2.1.3.2 Step 7



Substance	<i>M</i> [g/mol]	<i>m</i> [g]	<i>n</i> [mmol]	<i>V</i> [mL]	Eq.
1-(3-Chloro-1-phenylpropyl)-3-(2-fluorophenyl)-1,3-dihydro-2 <i>H</i> -benzimidazol-2-one	380.84	1.322	3.47		1.0
NaI	149.89	1.04	6,94		5.0
Acetone _{abs.}				24	

To a solution of educt **6** in dry acetone was added NaI and refluxed overnight. After cooling to rt the solvent was evaporated and the residue was resuspended in dry DCM. NaCl and NaI were separated via filtration and the solvent removed under reduced pressure. Purification via column chromatography (silica gel 60, PE/EtOAc 9/1) provides the product as a yellow solid.

Form and appearance: yellow solid

Yield: 0.845 g, 52% (pure fraction)

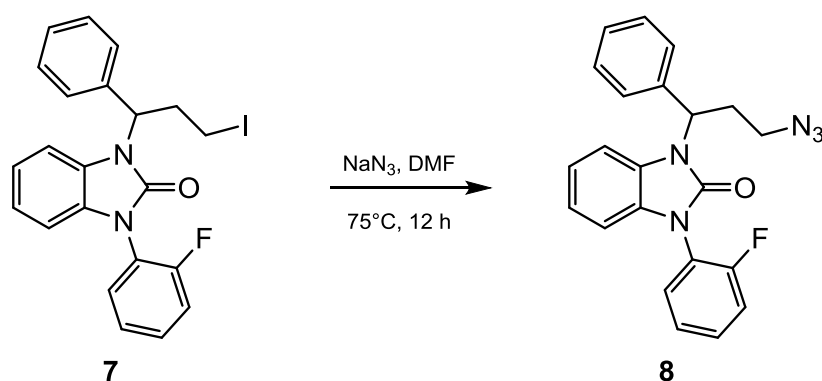
R_f (PE/EtOAc 9/1) = 0.35

Spectroscopic data are in accordance with the literature.^[117]

^1H NMR (400 MHz, CDCl_3 , δ_{H}): 7.58 – 7.47 (m, 4H, C12, C16, C20, C21), 7.45 – 7.26 (m, 5H, C13, C14, C15, C19, C22), 7.07 – 6.99 (m, 3H, C5, C6, C7), 6.88 – 6.85 (m, 1H, C4), 5.74 – 5.67 (m, 1H, C8), 3.36 – 3.13 (m, 3H, C9, 2 x C10), 2.98 – 2.80 (m, 1H, C9).

$^{13}\text{C}\{^1\text{H}\}$ NMR (CDCl_3 , δ_{C}): 157.8 (d, $^1J = 251.5$ Hz, C18), 153.0 (C2), 138.2 (C11), 130.2 (d, $^3J = 8.0$ Hz, C20), 129.5 (C22), 128.8 (C13), 128.8 (C15), 128.1 (C14), 127.3 (C12), 127.3 (C16), 124.8 (d, $^4J = 3.8$ Hz, C21), 122.0 (C6), 121.9 (C17), 121.6 (C5), 117.1 (d, $^2J = 19.0$ Hz, C19), 109.1 (C7), 108.9 (d, $J^{\text{NOE}} = 1.5$ Hz, C4), 57.6 (C8), 35.4 (C10), 2.3 (C9), *undetected*: C3a, C7a.

4.2.1.3.3 Step 8 ^[129-131]



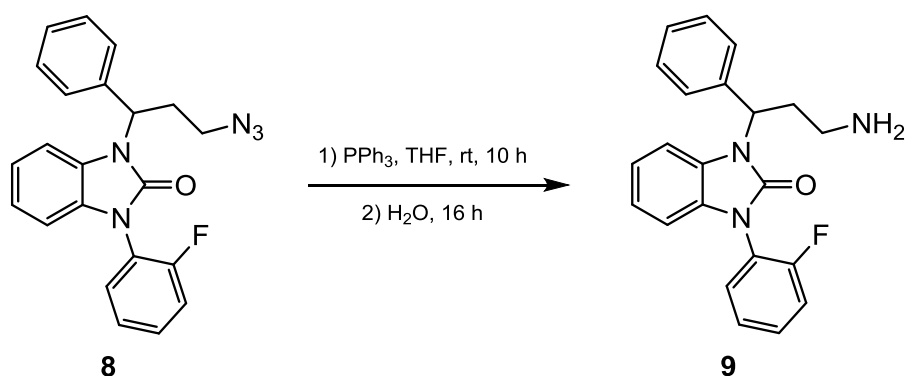
Substance	<i>M</i> [g/mol]	<i>m</i> [g]	<i>n</i> [mmol]	<i>V</i> [mL]	Eq.
1-(2-Fluorophenyl)-3-(3-iodo-1-phenylpropyl)-1,3-dihydro-2H-benzo[d]imidazol-2-one	472.29	0.150	0.32		1.0
NaN_3	65.02	0.048	0,65		2.0
DMF				3	

The iodine derivative was dissolved in DMF and heated to 75°C upon addition of NaN_3 . After 12 h reaction time, H_2O (10 mL) was added, which leads to a not filterable precipitation. The mixture was extracted with EtOAc (3 x 30 mL) and the organic phase washed with brine (3 x 10 mL). The combined organic layers were dried over Na_2SO_4 , filtered and concentrated under reduced pressure. The crude product was purified via column chromatography (PE/EE 8.5/1.5), which gave the desired azide **8**. It was used in the subsequent step without additional characterization except TLC.

Form and appearance: colorless, transparent oil

Yield: 75 mg, 60%

R_{fN_3} (PE/EtOAc 9/1) = 0.21

4.2.1.3.4 Step 9 ^[129, 130]

Substance	<i>M</i> [g/mol]	<i>m</i> [mg]	<i>n</i> [mmol]	<i>V</i> [mL]	Eq.
1-(3-Amino-1-phenylpropyl)-3-(2-fluorophenyl)-1H-benzo[d]imidazol-2(3H)-one	387.41	70	0.18		1.0
PPh ₃	262.29	71	0.27		1.5
THF				3	

Triphenylphosphine was added to a solution of azide **9** in THF and the mixture was stirred at rt for 10 h. Thereafter, 500 μL H₂O were added, and stirred for 16 h. The mixture was concentrated under reduced pressure. The crude product was purified by column chromatography (DCM/MeOH 9/1) to yield the final precursor as a colorless oil.

Form and appearance: colorless, transparent oil

Yield: 37 mg, 57%

¹H NMR (CDCl₃, δ_{H}): 7.59 – 7.51 (m, 1H, C22), 7.52 – 7.41 (m, 3H, C12, C16, C20), 7.37 – 7.26 (m, 5H, C13, C14, C15, C19, C21), 7.02 – 6.93 (m, 2H, C5, C6), 6.85 – 6.82 (m, 2H, C4, C7), 5.90–5.88 (m, 1H, C8), 2.84 – 2.73 (m, 2H, 2 x C10), 2.54 – 2.50 (m, 1H, 2 x C9), 2.44 (bs, 2H, NH₂).

¹³C{¹H} NMR (CDCl₃, δ_{C}): 157.9 (d, ¹*J*_{C,F} = 253.0 Hz, C18), 153.5 (C2), 138.7 (C11), 130.2 (d, ³*J*_{C,F} = 7.8 Hz, C20), 129.6 (C3a, C22), 128.7 (C13, C15), 128.1 (C7a), 127.7 (C14), 127.2 (C12, C16), 124.9 (d, ⁴*J*_{C,F} = 3.9 Hz, C21), 122.0 (C17), 121.9 (C6), 121.4 (C5), 117.1 (d, ²*J*_{C,F} = 19.5 Hz, C19), 109.9 (C7), 108.8 (d, *J*^{NOE} = 1.4 Hz, C4), 53.1 (C8), 38.6 (C10), 33.6 (C9). ¹⁹F NMR (471 MHz, CDCl₃, δ_{F}): -118.6 (m, C18)

¹⁵N NMR (40 MHz, CDCl₃, δ_{N}): 130.1 (N1), 124.0 (N3), 30.1 (NH₂).

El-MS, positive: *m/z* 361 [M]⁺, 228 [M – C₉H₁₁N]⁺.

HRMS (ESI-MS), positive: *m/z* Anal. Calcd for C₂₂H₂₁FN₃O 362.1663 [M+H]⁺: 362.1665.

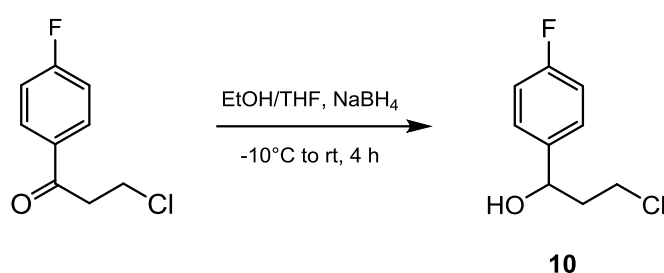
4.2.2 FAPPI1:0

The individual steps of the synthesis of FAPPI1:0 correspond to those of FAPPI3:0 concerning the type of reaction.

The core structure had been kindly provided by *Neudorfer et al.*^[117] (Department of Drug and Natural Product Synthesis, Faculty of Life Sciences, University of Vienna), therefore, the synthesis of the precursor FAPPI1:0 was confined to the synthesis of the side chain, the coupling and the modifications to provide the primary amine.

4.2.2.1 Synthesis of sidechain

4.2.2.1.1 *Step 4*



Substance	<i>M</i> [g/mol]	<i>m</i> [g]	<i>n</i> [mmol]	<i>V</i> [mL]	Eq.
3-Chloro-1-(4-fluorophenyl)propan-1-one	186.61	12.60	67.5		1.0
NaBH ₄	37.83	2.80	74.0		1.1
THF _{abs.}				70	
EtOH _{abs.}				70	

To the solution of 3-chloro-1-phenylpropan-1-one in dry THF (70 mL) and EtOH_{abs.} (70 mL) at -10°C was slowly added NaBH₄ over a period of 15 min. After stirring for additional 15 min, the mixture was allowed to warm to rt and these conditions were kept for another 4 h until the formation of gas stopped. The reaction was quenched by pouring the mixture onto ice (90 g) and saturated NH₄Cl (160 mL). The product was extracted with diethyl ether (4 x 150 mL), washed with water (2 x 100 mL) and dried over Na₂SO₄. Following filtration, the solvent was evaporated under reduced pressure and dried *in vacuo* to yield the corresponding alcohol (R_f (PE/EE 9/1) = 0.25).

Form and appearance: light-yellow oil

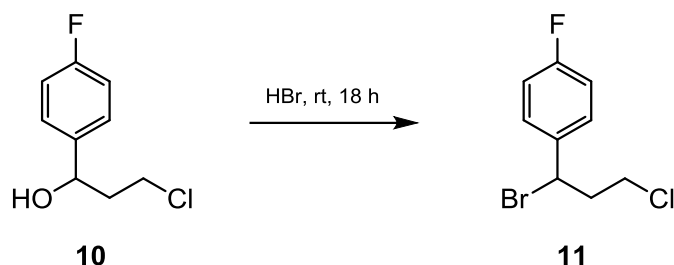
Yield: 12.47 g, 98 %

Spectroscopic data are according to the literature.^[132]

¹H NMR (200 MHz, CDCl₃, δ_H): 7.63-7.03 (m, 4H), 4.95 (m, 1H), 3.71-3.77 (m, 1H), 3.52-3.58 (m, 1H), 2.02-2.27 (m, 2H), 1.96 (d, *J* = 4.0 Hz, 1H).

^{13}C NMR (50 MHz, CDCl_3 , δ_{C}): 162.4 (d, $J = 244.3$ Hz), 139.6 (d, $J = 4.1$ Hz), 127.6 (d, $J = 8.0$ Hz), 115.6 (d, $J = 20.6$ Hz), 70.9, 41.7, 41.5

4.2.2.1.2 Step 5



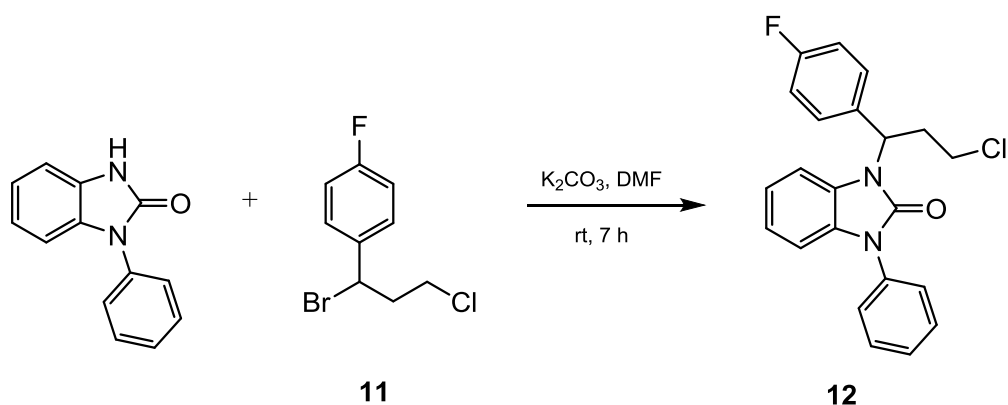
Substance	M [g/mol]	m [g]	n [mmol]	V [mL]
3-Chloro-1-(4-fluorophenyl)propan-1-ol	188.63	12.47	66.1	
HBr (47%)	80.91			220

3-Chloro-1-(4-fluorophenyl)propan-1-ol and hydrobromic acid (47%) are stirred for 18 h at rt before slowly pouring it into a mixture of saturated K_2CO_3 (100 mL) and ice (120 g). After adjusting the pH of the aqueous phase to 7 using solid K_2CO_3 , the product was extracted with diethyl ether (4 x 150 mL), washed two times with H_2O , dried over Na_2SO_4 and the solvent was evaporated to dryness. The conversion of the educt was monitored via TLC (R_f (PE/EE 9/1) = 0.70) and the resulting oil was used for the next reaction step without further purification.

Form and appearance: light-yellow oil

Yield: 15.49 g, 93%

Spectroscopic data match with literature values.^[133]

4.2.2.1.3 Step 6

Substance	<i>M</i> [g/mol]	<i>m</i> [g]	<i>n</i> [mmol]	<i>V</i> [mL]	Eq.
1-Phenyl-1 <i>H</i> -benzo[d]imidazol-2(3 <i>H</i>)-one	210.23	8.52	40.53		1.0
1-(1-Bromo-3-chloropropyl)-4-fluorobenzene	251.52	15.30	60.81		1.5
K ₂ CO ₃	138.21	11.20	81.04		2.0
DMF				70	

A solution of 1-phenyl-1*H*-benzo[d]imidazol-2(3*H*)-one in DMF (60 mL) was stirred with K₂CO₃ for 20 min at rt before 1-bromo-3-chloropropylbenzene in DMF (10 mL) was added. After a reaction time of 7 h quantitative conversion was obtained. Therefore, H₂O (100 mL) was added and the aqueous phase was extracted with EtOAc (3 x 200 mL) and washed with saturated NaCl solution (3 x 100 mL) until the aqueous phase had pH 7 - 8. The combined organic layers were dried over MgSO₄ and the solvent was evaporated to dryness. The crude product (dark-brown oil) was purified by column chromatography (PE/EE 9.5/0.5 → 9/1) to provide the desired product as light-yellow resin.

100 mg of 12 were recrystallized from PE/EE to yield colorless crystals.

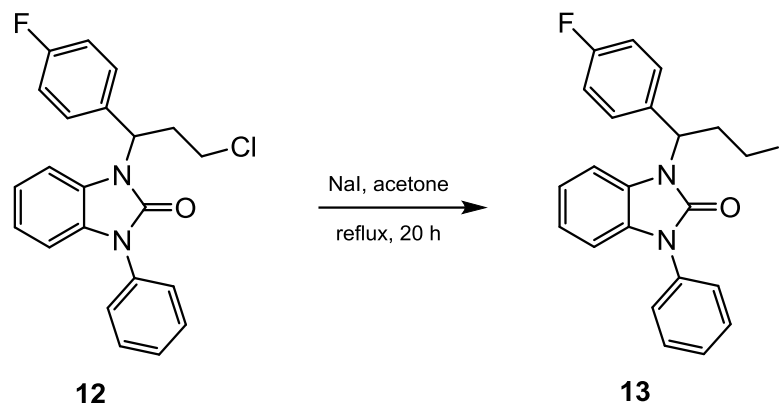
Form and appearance: colorless crystals, mp. 141-142°C

Yield: 2.035 g, 13% (pure fraction); 0.605 g, 4% (mixed fraction, yellow oil)

Spectroscopic measurements show product according to the literature.^[117]

¹H NMR (200 MHz, CDCl₃, δ_H): 7.57 – 7.39 (m, 7H), 7.11 – 7.00 (m, 6H), 5.76 – 5.70 (m, 1H), 3.60 – 3.65 (m, 2H), 3.30 – 3.12 (m, 1H), 2.87 – 2.70 (m, 1H).

¹³C NMR (50 MHz, CDCl₃, δ_C): 129.5, 129.4, 129.2, 127.8, 126.0, 122.0, 121.7, 115.9, 115.5, 109.0, 108.7, 53.8, 42.0, 34.4.

4.2.2.1.4 Step 7

Substance	M [g/mol]	m [g]	n [mmol]	V [mL]	Eq.
1-(3-Chloro-1-(4-fluorophenyl)propyl)-3-phenyl-1,3-dihydro-2H-benzo[d]imidazol-2-one	380.84	1.802	4.73		1.0
NaI	149.89	3.559	23.7		5.0
Acetone _{abs.}				35	

To a solution of **12** in dry acetone NaI was added and refluxed for 20 h. The dispersion was concentrated under reduced pressure, resuspended in dry DCM and filtered. The organic phase was evaporated *in vacuo* prior to purification via flash chromatography (PE/EE 8/2). The product (yellow oil) precipitated upon the addition of MeOH as a white solid.

A small amount (20 mg) was recrystallized from MeOH.

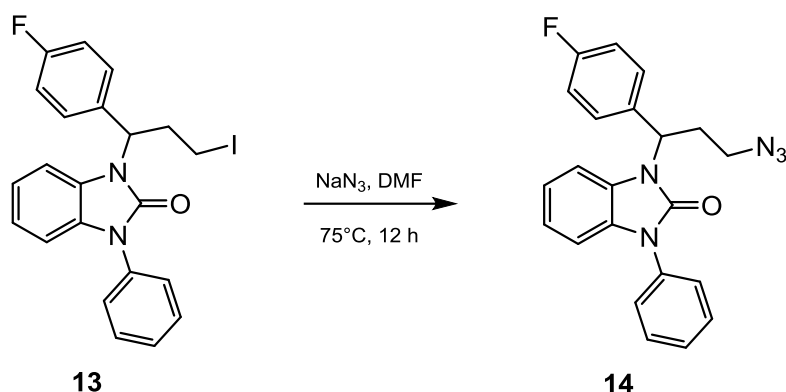
Form and appearance: colorless crystals, mp. 130-134°C

Yield: 1.982 g, 89%

Spectroscopic measurements show product according to the literature.^[117]

¹H NMR (200 MHz, CDCl₃, δ_H): 7.56 – 7.36 (m, 7H), 7.10 – 7.01 (m, 6H), 5.70 – 5.63 (m, 1H), 3.31 – 3.14 (m, 3H), 2.92 – 2.77 (m, 1H).

¹³C NMR (50 MHz, CDCl₃, δ_C): 164.8, 159.9, 153.0, 134.3, 134.1, 134.0, 129.4, 129.3, 129.1, 128.5, 127.7, 126.0, 122.0, 121.6, 115.9, 115.5, 108.9, 108.8, 57.0, 35.3, 2.3.

4.2.2.1.5 Step 8 ^[129-131]

Substance	<i>M</i> [g/mol]	<i>m</i> [g]	<i>n</i> [mmol]	<i>V</i> [mL]	Eq.
1-(1-(4-Fluorophenyl)-3-iodopropyl)-3-phenyl-1,3-dihydro-2H-benzo[d]imidazol-2-one	472.29	1.982	4.20		1.0
NaN ₃	65.02	0.410	6.31		1.5
DMF				40	

The iodine derivative was dissolved in DMF and heated to 75°C upon addition of NaN₃. After 12 h reaction time H₂O (40 mL) was added, the mixture was extracted with EtOAc (5 x 120 mL) and the organic phase washed with brine (2 x 100 mL). The combined organic layers were dried over Na₂SO₄, filtered and concentrated under reduced pressure. The crude product was purified via column chromatography (PE/EE 8.5/1.5), yielding the desired azide **14**.

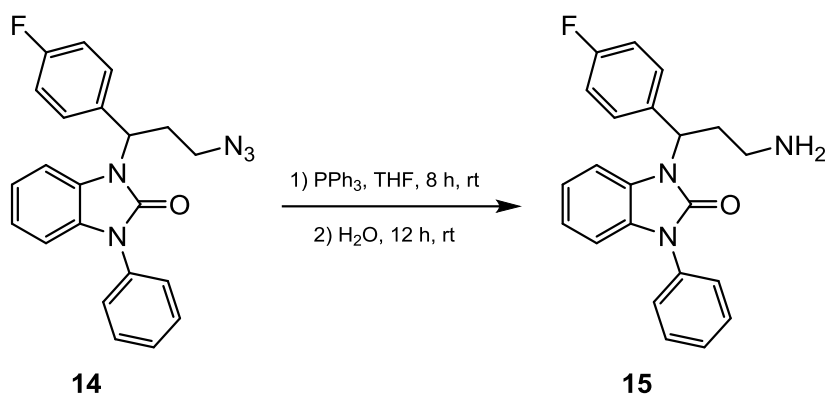
Form and appearance: colorless, transparent oil

Yield: 1.594 g, 98 %

¹H NMR (200 MHz, CDCl₃, δ_H): 7.58 – 7.48 (m, 6H, C18, C19, C21, C22), 7.46 – 7.38 (m, 1H, C20), 7.12 – 7.08 (m, 1H, C4), 7.08 – 7.02 (m, 4H, C5, C6, C13, C15), 7.01 – 6.98 (m, 1H, C7), 5.66 (dd, 1H, ³J(H_{C9}) = 10.3 Hz, ³J(H_{C9}) = 5.4 Hz), 3.48 – 3.42 (m, 2H, C10), 2.98 – 2.87 (m, 1H, C9), 2.65 – 2.55 (m, 1H, C9).

¹³C{¹H} NMR (CDCl₃, δ_C): 162.33 (d, ¹J_{C,F} = 247.1 Hz, C14), 153.20 (C2), 134.34 (d, ⁴J_{C,F} = 3.3 Hz, C11), 134.32 (C17), 129.48 (C3a, C19, C21), 129.14 (d, ³J_{C,F} = 8.2 Hz, C12, C16), 128.35 (C7a), 127.73 (C20), 126.00 (C18, C22), 121.98 (C6), 121.64 (C5), 115.70 (d, ²J_{C,F} = 21.5 Hz, C13, C15), 108.98 (C4 or C7), 108.78 (C4 or C7), 53.49 (C8), 48.72 (C10), 30.61 (C9).

¹⁹F NMR (471 MHz, CDCl₃, δ_F): -113.9 (m, C14)

4.2.2.1.6 Step 9 ^[129, 130]

Substance	M [g/mol]	m [mg]	n [mmol]	V [mL]	Eq.
1-(3-Azido-1-(4-fluorophenyl)propyl)-3-phenyl-1,3-dihydro-2H-benzo[d]imidazol-2-one	387.41	1.306	3.37		1.0
PPh ₃	262.29	1.331	5.07		1.5
THF				28	

Triphenylphosphine and a solution of azide 9 in THF were stirred at rt for 8 h before 3 mL of H₂O were added. After another 12 h of reaction time the mixture was concentrated under reduced pressure and the crude product purified by column chromatography (gradient: DCM/MeOH 9.5/0.5 → 8/2) to yield the final precursor as a colorless oil.

Form and appearance: colorless, transparent oil

Yield: 1.034 g, 85%

¹H NMR (200 MHz, CDCl₃, δ_H): 7.58 – 7.50 (m, 4H, C18, C19, C21, C22), 7.50 – 7.43 (m, 2H, C12, C16) 7.10 – 6.94 (m, 5H, C4, C5, C6, C13, C15), 6.87 – 6.82 (m, 1H, C7), 5.85 (dd, 1H, ³J(H_{C9}) = 10.8 Hz, ³J(H_{C9}) = 4.8 Hz, C8), 2.85 – 2.60 (m, 3H, C9, 2 x C10), 2.54 – 2.40 (m, 1H, C9), 2.28 (bs, 2H, NH₂).

¹³C{¹H} NMR (CDCl₃, δ_C): 162.10 (d, ¹J_{C,F} = 246.7 Hz, C14), 153.59 (C2), 134.63 (d, ⁴J_{C,F} = 3.3 Hz, C11), 134.40 (C17), 129.45 (C3a, C19, C21), 129.02 (d, ³J_{C,F} = 8.1 Hz, C12, C16), 127.86 (C7a), 127.69 (C20), 126.00 (C18, C22), 121.81 (C6), 121.44 (C5), 115.51 (d, ²J_{C,F} = 21.4 Hz, C13, C15), 109.55 (C4 or C7), 108.87 (C4 or C7), 52.43 (C8), 38.57 (C10), 33.82 (C9).

¹⁹F NMR (471 MHz, CDCl₃, δ_F): -114.4 (m, C14)

¹⁵N NMR (40 MHz, CDCl₃, δ_N): 130.1 (N1), 134.4 (N3), 30.2 (NH₂).

EI-MS, positive: m/z 361 [M]⁺, 210 [M – C₉H₁₀FN]⁺.

HRMS (ESI-MS), positive: m/z Anal. Calcd for C₂₂H₂₁FN₃O 362.1663 [M+H]⁺: 362.1666.

4.3 Methods for radiochemical labeling

The two precursors **9** and **15** were objected to further radiochemical labeling of their free amino group using carbon-11. The synthesis of the *N*-methylated radiotracers takes place according to the following scheme (Figure 44):

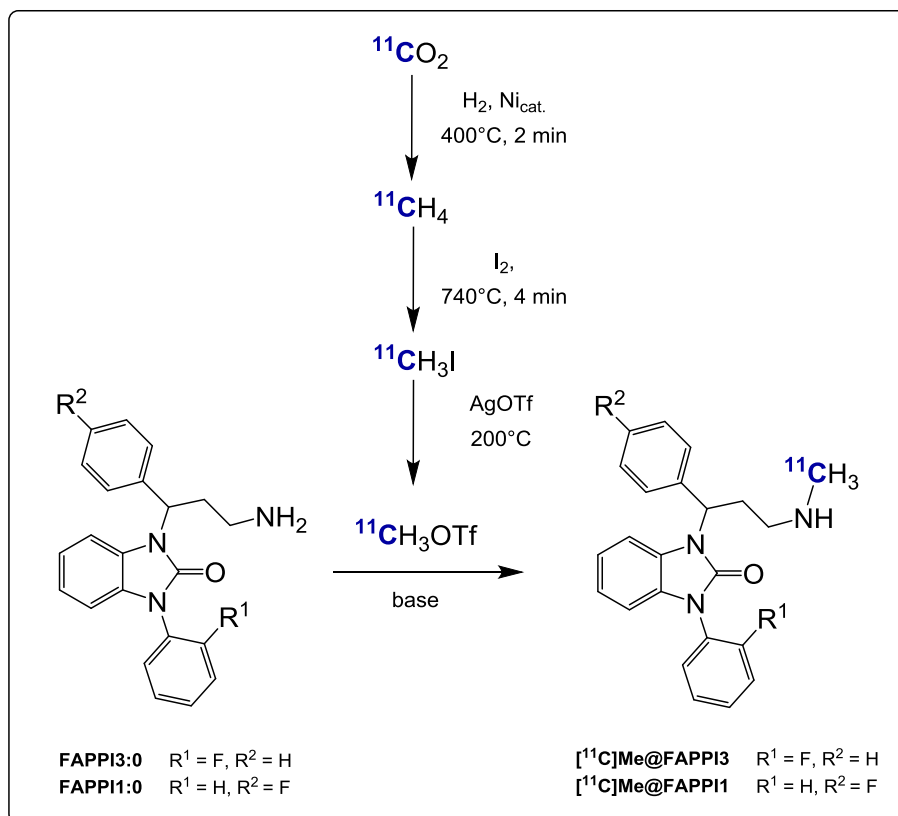


Figure 44: Radiosynthesis of [^{11}C]Me@FAPPI derivatives.

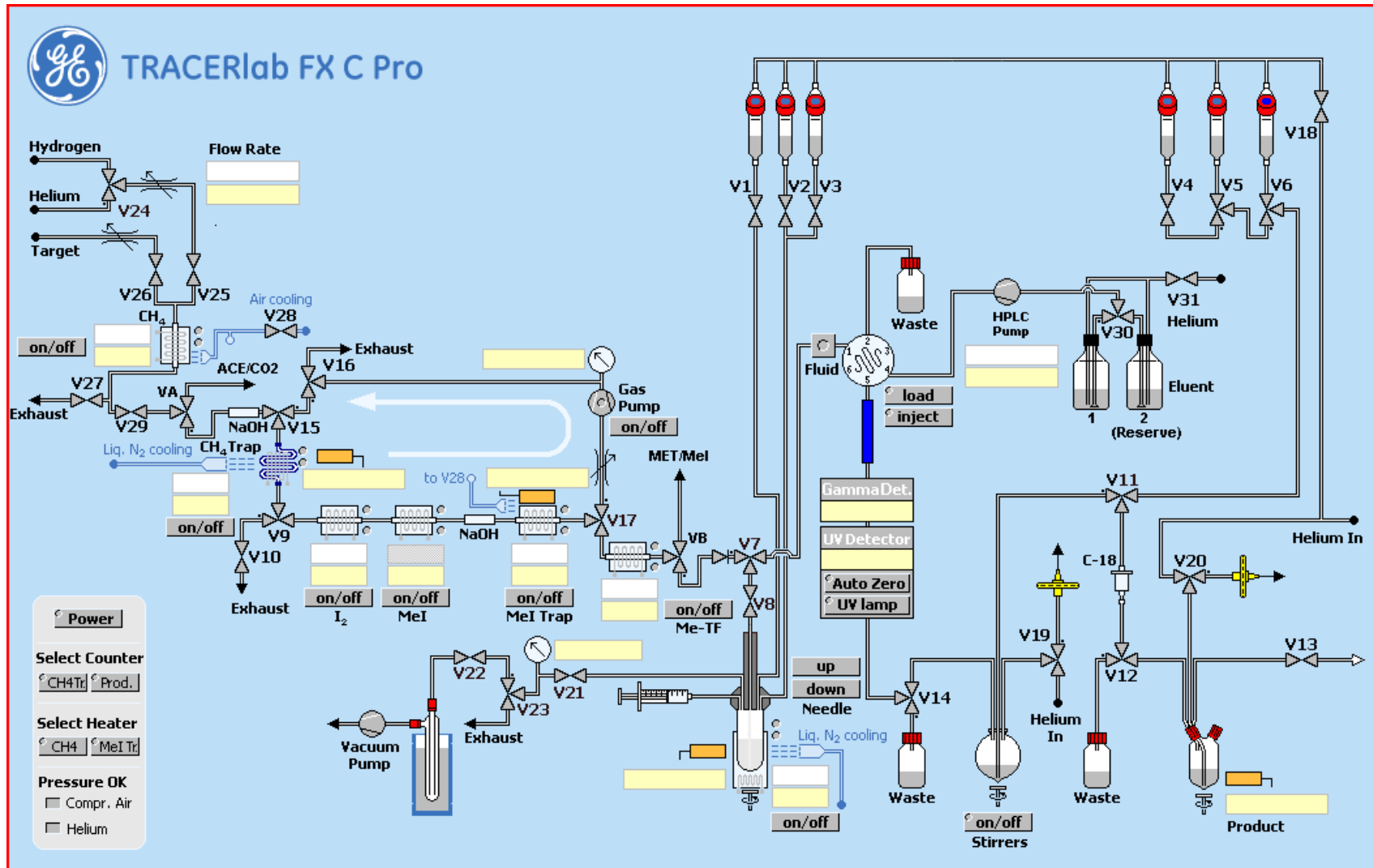
4.3.1 Preparations of the hot cell

Storage vessels V1-V3 (see Figure 45) and transfer tubings were rinsed each thrice with water and acetone. V4 and V6 were washed twice with water, while V5 was flushed with EtOH. All tubings were dried under He-stream, before all vessels including the product collecting vial (PCV) were equipped with the required solutions given below. The Sep-Pak[®] was preconditioned using 10 mL EtOH and 20 mL water and flushed with air. The AgOTf-oven for preparation of [^{11}C]CH₃OTf was preheated to 200°C and the [^{11}C]CO₂ trap was heated to 400°C under He-stream of 50 mL/min for quantitative removal of ¹²CO₂.

4.3.2 Production of [^{11}C]CH₃I and [^{11}C]CH₃OTf

The production of [^{11}C]CO₂ within the cyclotron was terminated at target activities of 30 to 50 GBq and the radioactive gas was trapped on a molecular sieve (4 Å) in the Tracerlab FxC Pro synthesizer (V26→V27→Exhaust). Radioactive carbon dioxide was converted into [^{11}C]CH₄ by hydrogenation at 400°C under Ni-catalysis (V24→V25) for 2 min in the closed system. Subsequent on-line conversion to [^{11}C]CH₃I was carried out in a gas phase reaction according to the literature^[134, 135]:

Figure 45: Production flow chart of $[^{11}\text{C}]\text{Me}@\text{FAPPI}$ synthesis.



Radioactive methane was dried by passing an Ascarite® column and trapped at -78°C (V24→V25→V29→V15→V9→V10). The released methane was converted into [¹¹C]CH₃I in a circulatory system where reaction with sublimated iodine at 740°C for 4 min at a flow rate of 50 mL/min takes place (V9→V17→V16→V15→V9). The iodinated product was trapped on a Porapak® N column and released by heating of the trap (190°C). [¹¹C]CH₃I further passed an AgOTf column (300 mg AgOTf) at 200°C giving [¹¹C]CH₃OTf which was trapped in 500 µL of ACN at a flow rate of 40 mL/min (V17→V7→V8→reactor→V21→V23).

4.3.3 Small-scale reactions

As reaction turnover was assumed to be the same for both precursors due to their similar structure, these small-scale investigations were only carried out for FAPPI3:0. Optimization of reaction conditions was performed using [¹¹C]CH₃OTf for substitution reactions varying the parameters temperature, reaction time, solvent and base.

For this purpose, [¹¹C]methyl trifluoromethanesulfonate was trapped in 500 µL of solvent in a 1.5 mL Eppendorf® tube. Aliquots of 25 µL were transferred manually into separate Wheaton V vials, which were prefilled with precursor dissolved in 25 µL of solvent and 0.5 µL of the respective base. After a reaction time of 1 or 3 min at rt or 75°C, the reaction was quenched using an equivolume of water or HPLC eluent.

The following reaction conditions were examined:

- ◆ Reaction temperature: 30°C, 75°C
- ◆ Base: NaOH, triethylamine (TEA), tetrabutylammonium hydroxide (TBAH)
- ◆ Solvent: DMSO, MEK, ACN

4.3.4 Automation of radiosynthesis

Optimum conditions from small scale reactions were used for automated large-scale syntheses.

After production of [¹¹C]CH₃OTf, it was trapped in the glass reactor containing the precursor FAPPI3:0 or FAPPI1:0 (1 – 1.2 mg) and 0.5 µL of 5 M NaOH in 25 µL ACN. The sealed reaction vessel was either heated to 75°C or kept at room temperature (30°C) for 1 min, before the reaction was cooled to 25°C and quenched with 1 mL of HPLC eluent. The crude reaction mixture was subsequently injected onto a semi-preparative HPLC column (varying type) and the product peak was cut manually into the bulb containing 80 mL water (column→V14→bulb→V19→exhaust). The diluted product was transferred over a C8 SPE Sep-Pak® (He pressure from V19→bulb→V11→cartridge→V12→waste). After washing the cartridge with water (V6→V11→C-18 cartridge→V12), the product was eluted with 1.5 mL EtOH into the product collecting vial (PCV)(V5→V11→V12→PCV→V13→waste). This PCV was equipped with 4 mL 0.9% saline, 1 mL 3% saline and 1 mL 125 mM phosphate buffer. The tubings were washed with 5 mL 0.9% saline (V4) into the PCV and the resulting volume of 12.5 mL was filtered over a filter (0.22 µm, Millex®) into a sterile vial (20 mL) containing 5 mL 0.9% saline under laminar air flow (He in→V20→PCV→V13).

4.3.4.1 Quality control

Radiochemical purity was determined by analytical radio-HPLC. Chemical purity was analyzed by analytical HPLC using UV detection. Radiochemical identity was determined via comparison of retention times with methylated reference substances.

5 RESULTS and DISCUSSION II

5.1 Synthesis of precursors

The mentioned reaction yield for product **1** (23%, see chapter 4.2.1.1.1) could be improved by using a less polar eluent for column chromatography (PE/EE 9.5/0.5 instead of PE/EE 9/1), as the resulting mixed fraction could be diminished. Nevertheless, TLC showed a number of side products, therefore, a higher yield than 30 – 40 % cannot be expected using the specified conditions.

NMR (^1H and ^{13}C) and TLC of intermediate **2** only showed minor impurities of the product after reduction and working up and thus, compound **2** was used in the next reaction step without purification.

Since the reduction of the carbonyl group as well as the bromination gave the particular products in high purity, further purification of compounds **3**, **4**, **10** and **11** was not necessary.

The extended reaction time of 18 h for bromination of compound **10** to give substance **11** was chosen for time reasons but was not necessary for complete conversion (compare compound **5**).

Chlorine derivative **6** could be obtained in a far higher yield (68%) compared to compound **12** (17%). This may be attributed to the fact, that core structure **16** was provided in a not perfectly pure form according to a second less intense spot on TLC and impurities in ^1H NMR. Reaction monitoring showed complete conversion of educt **16**, but at the same time extensive formation of byproducts could be observed. Therefore, it is highly recommended to use the purified substance **16**, which is accessible by cyclisation of *N*-phenylbenzene-1,2-diamine with carbonyldiimidazole (CDI) in a single-step reaction.

It has also been previously demonstrated, that a fluorine substituent at the phenyl group directly attached to the benzimidazolone leads to higher yields (FAPPI3:0, 55%) in this reaction step compared to the para-fluorosubstituted phenylpropyl side-chain of FAPPI1:0 (32 %), if the reaction is carried out under the same conditions.^[117] For compound **12**, a reduction of reaction time from 24 to 7 h does not affect the reaction yield.

Finkelstein reaction applying NaI in acetone gave the intermediates **7** and **13** in almost quantitative yields. The use of dry solvent and an excess of NaI are important prerequisites to influence the reaction equilibrium in a positive way. The relatively low yield (52%) of pure substance **7** resulted from an insufficient chromatographic separation of educt **6** and product. For the following reaction step impurities of **6** or **12**, respectively, did of course not influence the reaction, but substitution with sodium azide was not possible for the chlorine derivatives under the aforementioned conditions (75°C). Hence, smaller yields are expected when using mixed fractions.

Nucleophilic substitution of iodine **8** and **14** via azide could be performed in a simple manner with high conversion. The reaction temperature was raised to 75°C as the reaction rate was very slow

when using room temperature. The use of 2.0 equivalents of sodium azide compared to 1.5 equivalents did not have a significant effect on the speed of reaction. The difference between compound **8** and **14** regarding reaction yields can be explained by the small-scale reaction **14** compared to reaction **8**, which may have caused less turnover or lead to a higher percentage of loss during purification steps. In both cases, the side products were showing an irreversible binding to silica gel and can therefore be easily removed via filtration over silica gel.

Impurities of chlorine or iodine precursors did not affect any of the following reactions but chlorine substituted compounds and their corresponding azides showed a very similar retention on normal phase silica gel. Therefore, any residues of the halides have to be largely removed directly after iodination to guarantee a highly pure azide product.

The reduction of azides **8** and **14** was accomplished via a Staudinger reaction whereas both substances could be easily purified via flash chromatography.

Thereby, the occurring respective amine products, which have a far lower retention factor compared to the other derivatives (chlorine, iodine, azide), enabled a fast and time efficient purification by simple filtration over silica gel after each step if the starting material should not be recovered.

At first sight, the preparation of the free amine via nucleophilic substitution with ammonia is the method of choice. Unfortunately, it was found, that reactions with different concentrations of ammonia (in EtOH or isopropanol) at varying temperatures lead to several, inseparable byproducts (showing very similar retention on normal and reversed phase systems compared to the desired precursors) (see *Figure 46*). Therefore, even a repeated purification via column chromatography to obtain the pure substances was not successful. Hence, the more inconvenient synthetic way - via a first substitution with sodium azide and subsequent reduction of the azide - was able to yield pure compounds in decent (FAPPI 3, 34%) to high (FAPPI 1, 83%) yields.

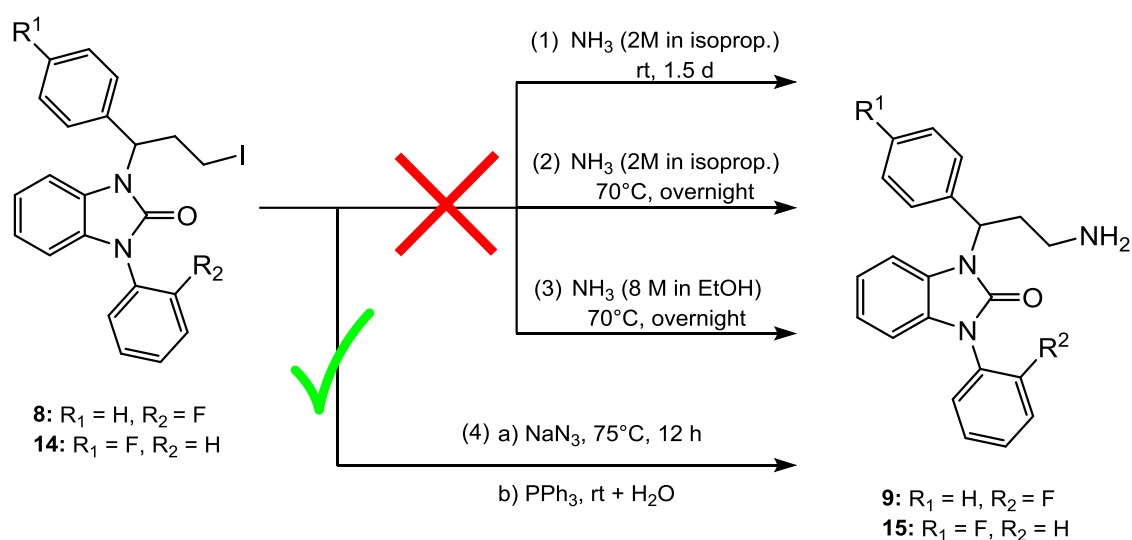


Figure 46: Synthesis of **9** and **15** with ammonia solutions: both precursors cannot be obtained under the abovementioned conditions due to no conversion (1) and the formation of numerous side products (2 + 3); synthesis route (4) was able to give the pure precursors.

5.2 Results of *N*-[¹¹C] Methylation of FAPPI1:0 and FAPPI3:0

5.2.1 Small scale reactions

The influence of different parameters – namely, solvent, reaction temperature and base – on radiochemical incorporation yields was examined for FAPPI3.

Using DMSO, radiochemical yields for any of the three bases and at any reaction temperature did not exceed 0.2%. Therefore, DMSO presented an inappropriate solvent for methylation reactions of FAPPI3:0 with [¹¹C]CH₃OTf.

Good results were achieved for reactions in 2-butanone (MEK) when using NaOH or TEA as a base (see *Figure 47*). Up to 21.0% (NaOH) and 53.7% (TEA) of radiochemical incorporation were obtained at room temperature after a reaction time of 3 min. Similar results were obtained for a reaction time of 1 min at 75°C (18.9% for NaOH and 48.6% for TEA), which indicates equivalent reaction conditions. Apparently, reaction temperature and reaction time did have less influence on conversion than the different nature of the base giving radiochemical yields up to 29.2% for NaOH and 62.1% for TEA. Thereby, TBAH was found to be unsuitable as a base for this reaction. (conversion <0.5%)

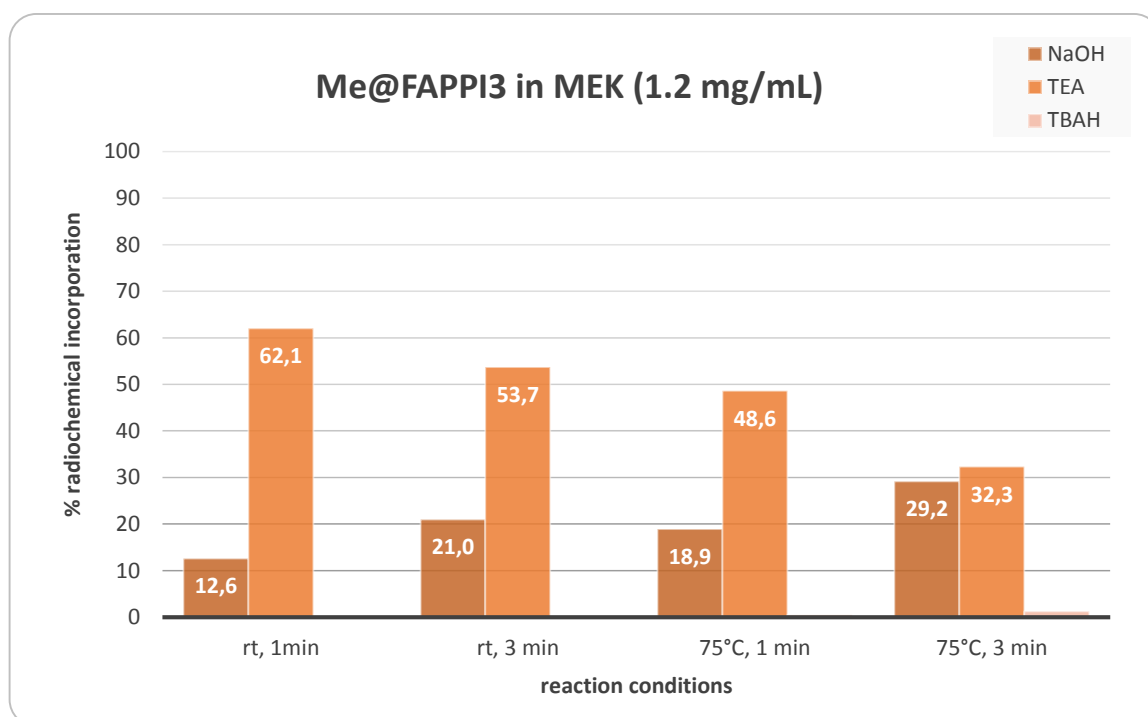


Figure 47: Influence of reaction time and temperature on radiochemical yield using different bases (NaOH, TEA and TBAH) in 2-butanone (*n* = 1).

Very high radiochemical yields were reached when using ACN as a reaction medium (see *Figure 48*). None of the tested parameters did have a significant effect, resulting in an average of 73.3% ($\pm 4.8\%$) of radiochemical conversion in an overall of 12 syntheses (*Figure 48*). Present data indicates, that for a larger number of measurements a significant but minor increase in yield may be noticed for TEA.

These results have to be considered under the aspect that higher concentrations of tracer were used for reactions in MEK (1.2 mg/mL compared to 1.0 mg/mL in ACN), which emphasizes the better effect of ACN over MEK even more.

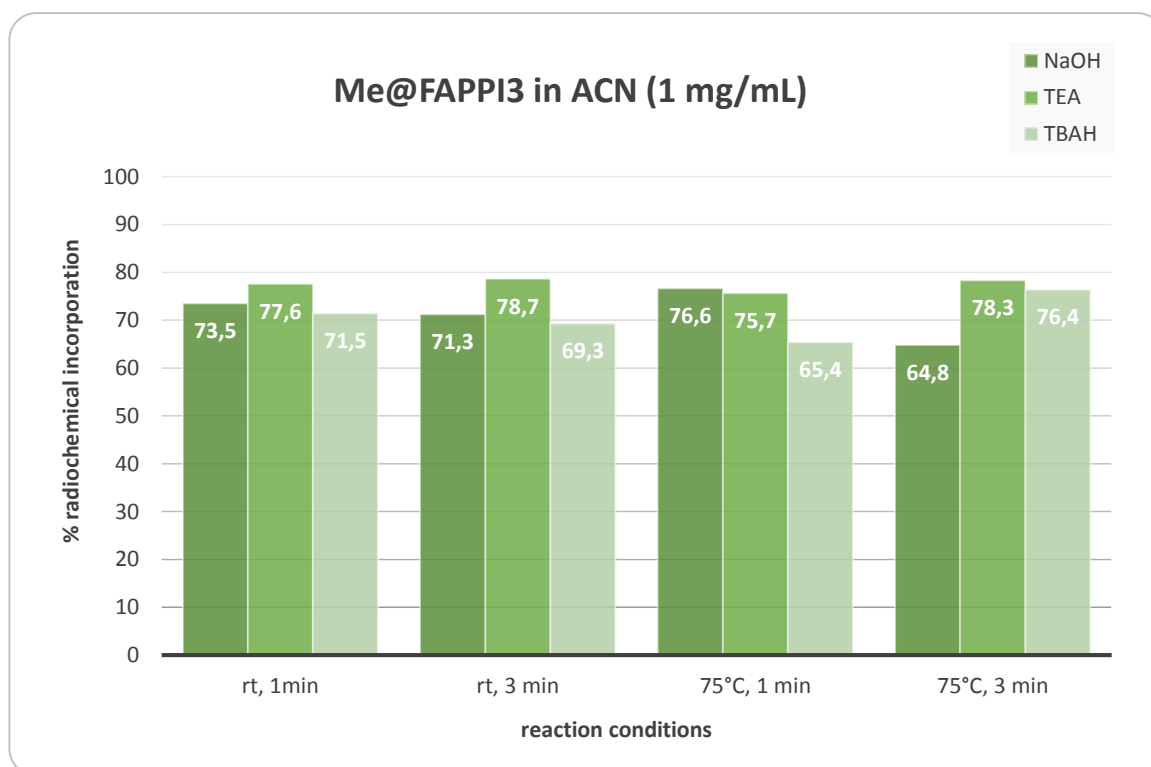


Figure 48: Dependence of radiochemical incorporation yield of the tracer [^{11}C]Me@FAPPI3 for the shown reaction conditions ($n = 1$).

5.2.2 Full automation of radiosyntheses

Optimum parameters were identified in the preceding small-scale reactions and used for large-scale experiments. Thus, all radiosyntheses were performed in acetonitrile within a fully automated process giving the readily formulated product. Based on the analogue structure compared to [^{11}C]Me@APPI, the same cartridge for purification of the tracer, a C8 plus SPE Sep-Pak[®] was used. So far, 2 large-scale syntheses of Me@FAPPI3 and one single synthesis of Me@FAPPI1 have been performed (see *Table 41*). Despite very good yields in these syntheses for both tracers comparable to those in small-scale tests, a purified final tracer has not yet been obtained due to very similar retention times of precursor and radioactive product. Thus, a preparative HPLC separation was hampered.

Performing the substitution reaction ($\text{S}_{\text{N}}2$) in the absence of base at 75°C was found to give approximately the same product yield of Me@FAPPI3 as the reaction with sodium hydroxide at 30°C. However, the base-free method was not further considered due to the formation of a side product with similar retention time (see *Figure 49*, a., #2, left).

Investigations showed that increased reaction temperatures of 75°C are not necessary for an outstanding turnover (see *Table 41*, Me@FAPPI1 and Me@FAPPI3_#2), just as it had been indicated by small-scale reactions in advance. The application of an eluent containing 3% TEA in the case of Me@FAPPI3 (*Table 41*, reaction #2) was favorable for minimizing peak tailing and peak

width of the methylated secondary amine. For this separating system, the minimum acceptable retention difference for precursor and tracer resulting in base line separation (resolution $R = 1.5$) accounts for about 2.0 min, which could not be met in our setup by far ($\Delta t = 1$ min).

Up to now, no satisfactory purification results were obtained for the three different used chromatographic systems. Therefore, the products of [^{11}C]Me@FAPPI3 reactions were not formulated in physiological solution and therefore, no overall yield could be determined. The *N*-[^{11}C]methylation product of FAPPI1:0 was formulated, but only about two thirds of the detected radioactive peak was collected (cut between 6 and 7 min, see *Figure 50*).

Table 41: Overview on large scale syntheses performed for Me@FAPPI1 and Me@FAPPI3 using different chromatographic systems; overall yield for Me@FAPPI1 given below is less than the real turnover as not the whole product peak was collected.

Parameters and settings	Me@FAPPI1	Me@FAPPI3_#1	Me@FAPPI3_#2
Conc. [mg/mL]	1.1	1.2	1.2
Solvent	ACN	ACN	ACN
Base	NaOH 5M	-	NaOH 5M
Reaction time	2 min	1 min	2 min
Temperature	30°C	75°C	30°C
Column	SUPERCOSIL™ LC-ABZ+Plus, alkylamide RP, 5 μm, 25 x 10 mm, endcapped, 120 Å	Phenomenex® Gemini, C-18, TMS endcapping, 10 μm, 250 x 10 mm, 110 Å	Phenomenex® Gemini, C-18, TMS endcapping, 10 μm, 250 x 10 mm, 110 Å
Eluent	ACN/0.1 M NH ₄ Ac + 2 M TEAA 60/40/0.2 % v/v/v	MeOH/0.1 M AMF 70/30 + 1% Et ₃ N	MeOH/0.1 M AMF 70/30 + 3% Et ₃ N
Flow	5	5	7
Retention time precursor [min]	5.8 (5.6 – 8.1)	10.3 (10.0 – 12.9)	7.7 (7.4 – 8.7)
Retention time product [min]	6.0 (5.8 – 7.5)	11.5 (11.0 – 13.9)	8.7 (8.3 – 9.8)
Retention time side product	7.6 (7.2 – 8.2)	14.5 (14.0 – 15.3)	-
Separation	insufficient	insufficient	insufficient (best of the tested conditions)
Starting activity [¹¹ C]CO ₂ [GBq]	45.3 (t = 0)	45.4 (t = 0)	49.5 (t = 0)
Activity [¹¹ C]CH ₄ -trap [GBq] (t [min])	37.8 (Δt = 7)	38.2 (Δt = 7)	31.4 (Δt = 8)
Activity [¹¹ C]MeI-trap [GBq] (t [min])	21.1 (Δt = 12)	21.7 (Δt = 13)	22.5 (Δt = 12)
Activity reactor trapped [GBq] (t [min])	14.2 (Δt = 17)	14.4 (Δt = 18)	15.0 (Δt = 18)
Yield [GBq] (% uncorr.) (time)	2.02 (4.5%) (Δt = 35)	-	-
Duration [min] (without irradiation of target)	35	-	-

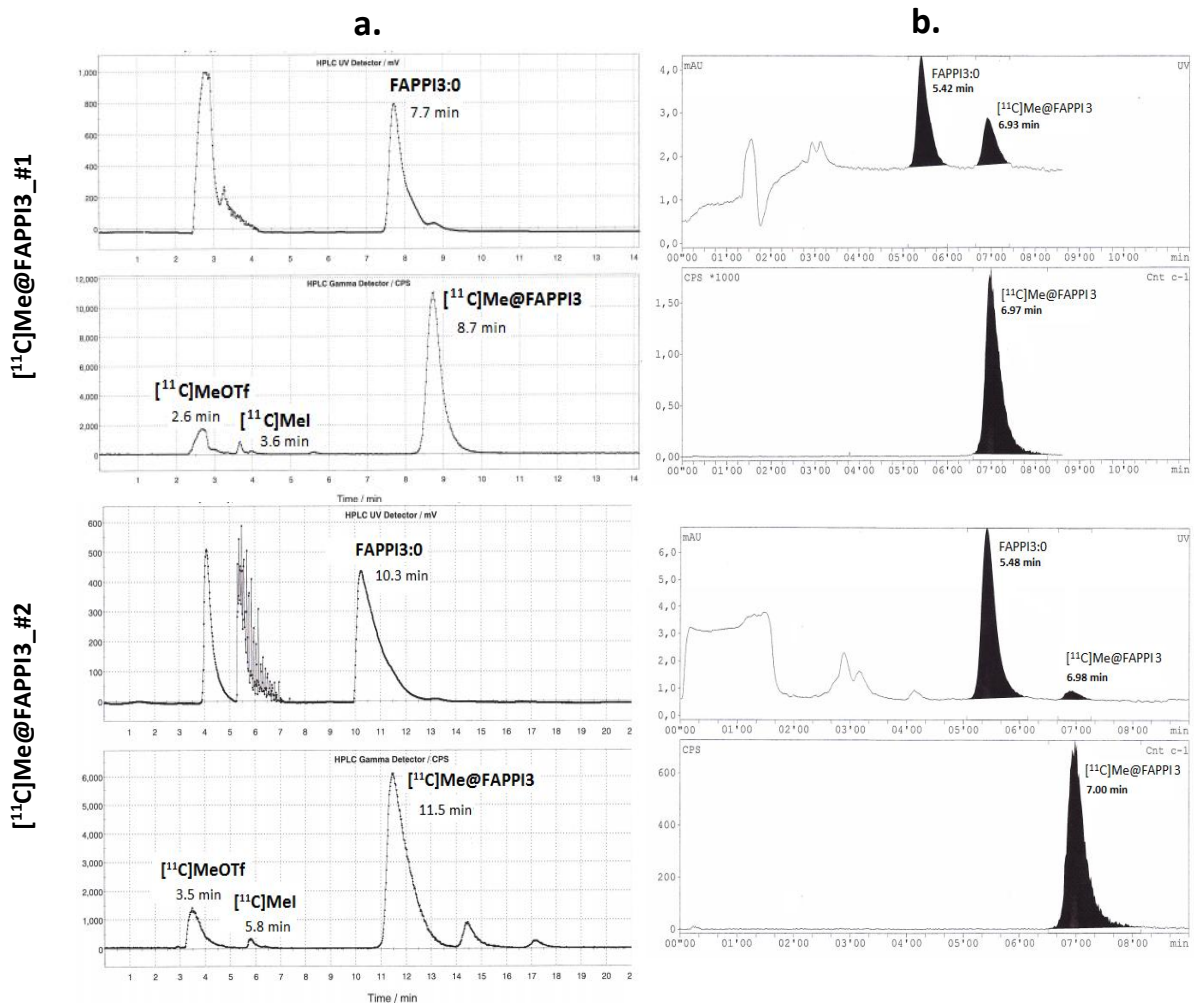


Figure 49: Semi-preparative (a.) and corresponding analytical (b.) HPLC chromatograms for both [¹¹C]Me@FAPPI3 syntheses: best separation was achieved via analytical separation showing retention times of 5.45 min for the precursor FAPPI3:0 (UV-channel) and 6.97 min.

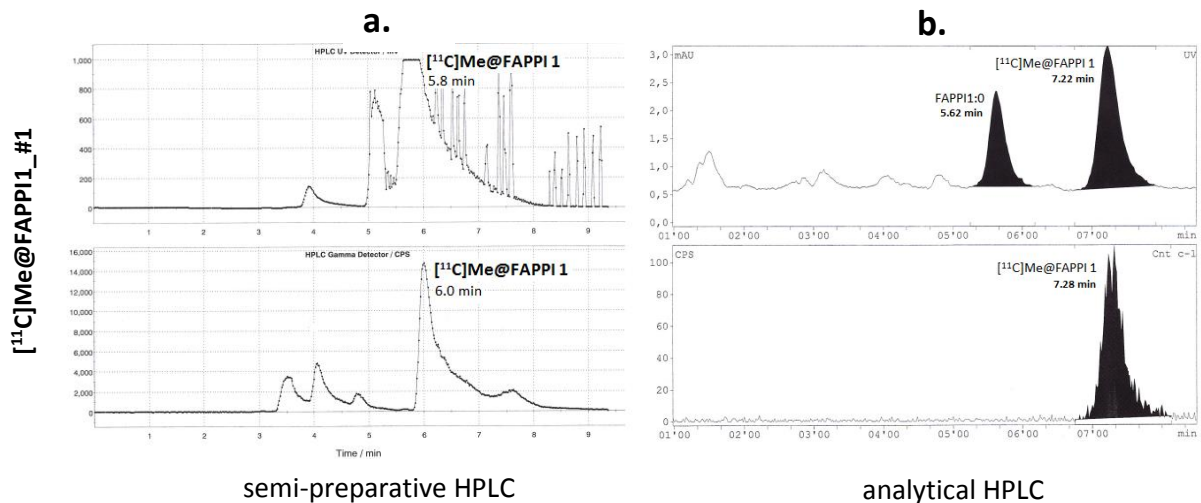


Figure 50: HPLC chromatograms of first [¹¹C]Me@FAPPI1 synthesis showing insufficient resolution. Analytical HPLC of the product peak shows very similar retention times of precursor (5.62 min) and tracer (7.25 min) compared to their analogues FAPPI3:0 and Me@FAPPI3.

6 CONCLUSION

6.1 Metabolic considerations of [¹⁸F]FMeNER-D2

In the present work, the metabolism of selective NET-radiotracer [¹⁸F]FMeNER-D2 in human and rat liver microsomes as well as selected centrally active enzymes such as MAO A/B and COMT was investigated.

The basis for these investigations was the successful preparation of [¹⁸F]FMeNER-D2 which could be accomplished following the procedure of Rami-Mark et al. (2013).^[119] The critical steps were found to be the preparation of absolutely dry [¹⁸F]fluoride for the subsequent moisture-sensitive formation of [¹⁸F]BFM on the one hand and the distillation and trapping of [¹⁸F]BFM on the other.

This study provides evidence, that CYP2D6, CYP3A4 as well as CYP2C19 are considered as the major enzymes in the biotransformation of the NET-ligand [¹⁸F]FMeNER-D2 in humans. Whether CYP1A2 is also involved has not yet been proven.

Since exclusively peripheral hepatic metabolism of the tracer could be verified, it has to be taken into consideration that – if the formed metabolites are held responsible for interfering with PET signals in the brain – they have to pass the blood-brain barrier (BBB) first. Therefore, the occurring radiometabolites must show adequate lipophilicity to penetrate the BBB.

The data derived from rat liver microsomal incubation point towards the contribution of CYP3A1/2 and CYP2D1 to [¹⁸F]FMeNER-D2 degradation in rodents. The inhibition of tracer metabolism in RLM via 2-phenyl-2-(1-piperidinyl)propane (PPP) and (+)-N-3-benzylirivanol cannot be interpreted due to insufficient knowledge about inhibitory properties and selectivities of these substances for rat CYP450 isoforms. However, an involvement of CYP2C6, CYP1A2, CYP2E1 and CYP2C11 in [¹⁸F]FMeNER-D2 metabolism could be excluded *in vitro*.

All radioactive metabolites were found to be more polar than the initial tracer [¹⁸F]FMeNER-D2, which is consistent with hydroxylation reactions generally performed by phase I metabolism of cytochrome P450 monooxygenases. Defluorination, as a major cause of metabolism, was excluded due to the lack of free [¹⁸F]fluoride in any TLC analysis. *O*-Demethylation is conceivable, but has not been proven due to missing peak identification in HPLC analyses.

In consideration of the restricted resolution of our analytical chromatographic system, remarkable similarities between the different radioactive signals of various incubation batches were observed. It is worth highlighting that the same major radio-metabolite was found in HLM, RLM and CYP2D6 assays. A radioactive peak displaying an identical capacity factor *k'* could be even found for CYP3A4.

Bone binding experiments did not demonstrate remarkable uptake of [¹⁸F]FMeNER-D2 and its radioactive metabolites in human bone material or hydroxyapatite. Therefore, accumulation in NET-PET scans cannot be explained by increased uptake in inorganic bone material. These data suggest that there is higher probability for the intact or the metabolized tracer to accumulate in

red or yellow bone marrow. Due to spatial proximity of cerebral membranes, an uptake in connective tissues is also possible.

Further *in vivo* research is needed to confirm the identified metabolic pathways and therefore to gain clinical significance. This future evidence for the presence of postulated radiometabolites *in vivo* can be supplied by blood sampling of future study populations during PET scans. The given results will also be valuable in the understanding and consideration of drug-drug interactions when [^{18}F]FMeNER-D2 is co-administered with medication exhibiting CYP450 inductive or inhibiting properties, which is of high importance as radioactive substances are only administered in the nanomolar range. Therefore, it might be possible to improve pharmacokinetic characteristics of our radiotracer [^{18}F]FMeNER-D2 in the future and to gain the ability to quantify the amount of norepinephrine transporter in hitherto impaired regions of the brain such as the prefrontal cortex.

6.2 Synthesis of novel fluoro-substituted NET-PET tracers

The syntheses of two novel fluoro-substituted APPI:0 analogues as potential NET-PET precursors have been successfully performed. The primary amines FAPPI1:0 and FAPPI3:0 could be obtained in a 4- and 7-step synthesis, respectively. Starting from 1-phenyl-1*H*-benzo[*d*]imidazole-2(3*H*)-one, FAPPI1:0 was synthesized in an overall yield of 12.6% while preparation of FAPPI3:0 started at a previous step using 2-fluoroaniline and 1-fluoro-2-nitrobenzene as starting materials, therefore, giving a reduced yield of 2.0%. For FAPPI3:0, an almost identical yield of 12.0% could be obtained when considering the last four steps of the synthesis.

Besides, the radiochemical labeling yielded the N-[^{11}C]methylated NET ligands in excellent conversions under mild conditions. For both tracers, a reaction time of 2 min using a temperature of 30°C and sodium hydroxide in acetonitrile were found to be ideal, giving about 73% of radiochemical incorporation. An ideal setup for the purification of both tracers yielding the required specific activity could not be established so far. However, phenyl ethyl RP-columns were found to be more suitable than alkylamide stationary phases or conventional C18-bonded silica.

7 OUTLOOK

7.1 Further *in vitro* and *in vivo* tests of [¹⁸F]FMeNER-D2

To complete the investigations of peripheral biotransformation of [¹⁸F]FMeNER-D2, another single enzyme assay using human CYP1A2 might be taken into consideration. Since the selective inhibitor furafylline showed a remarkable effect on HLM activity, there is high probability for the involvement of hCYP1A2 in [¹⁸F]FMeNER-D2 metabolism. To gain profound information about the role of CYP3A4, azamulin, the most selective inhibitor of CYP3A4 (15-fold higher activity against CYP3A4 compared to CYP3A5 or CYP3A7), can be tested for inhibitory properties in respect to [¹⁸F]FMeNER-D2 degradation.^[93]

To gain further significant evidence that FMeNER-D2 is no substrate of MAO isozymes in the liver, inhibition assays using irreversible inhibitors of MAO A and B (i.e. iproniazid, phenelzine, tranylcypromine) should be performed. However, these MAO inhibitors might show simultaneous unspecific inhibition of CYP450 enzymes.^[63] Besides, a more specific method for determination of stability against MAO activity represents the incubation in mitochondria suspensions of rat or human brain.^[136]

COMT assays were only carried out with enzyme from porcine origin. Further investigations should be done to evaluate the effect of recombinant hSCOMT (or hMBCOMT) on FMeNER-D2 stability.

To obtain a more detailed view of the [¹⁸F]FMeNER-D2 metabolism in rats and to assess the involvement of each individual CYP450, enzyme assays using an additional spectrum of inhibitors toward special CYP450 isozymes should be taken into account. Incubation of FMeNER-D2 with a panel of recombinant rat CYP450 enzymes should complete these data and might allow a better comparison between human and mouse.

Detailed statements about the metabolic pathways (e.g. demethylation, hydroxylation, hydrolysis of ether or ester bonds) of [¹⁸F]FMeNER-D2 cannot be made and were not part of this thesis. Characterization and identification of the metabolites of [¹⁸F]FMeNER-D2 could be achieved by using a suitable LC-MS method (MS²).

The restrictive factor limiting the amount of radioactive tracer added to the incubation mixtures was the content of organic solvent present in tracer formulations. Therefore, modification of the critical steps in the synthesis and thus leading to higher product yields might be desirable for future metabolic examinations of [¹⁸F]FMeNER-D2.

7.2 Future of Me@FAPPI derivatives

In addition to a compulsive, improved purification method for the new [^{11}C]Me@FAPPI tracers, some effort ought to be made to further enhance the synthesis of the labeling precursors. In the course of this thesis, it has not been tested whether the azide can be generated from the chloroalkyl derivative in a direct way by reactions at temperatures above 75°C. According to literature, however, reaction times and temperature ought to be sufficient for almost quantitative turnover. However, the most obvious way to simplify and shorten the synthesis is to use a Finkelstein reaction (involving catalytic amounts (0.15 Eq.) of sodium iodide) besides an excess of sodium azide in a one-pot reaction.^[137]

Concerning the purification of the radiolabeled [^{11}C]Me@FAPPI tracers, it would be reasonable to test semi-preparative phenyl columns with different spacers (ethyl, propyl, hexyl) or even more sophisticated modifications of silica such as diphenyl or biphenyl phases.

For the future, it might be of particular interest to synthesize the enantiopure unlabeled progenitors FAPPI1:0 and FAPPI3:0 and the respective enantiopure carbon-11 labeled NET-PET tracers. For instance, Zhang et al.^[126] compared (S)-Me@APPI with its corresponding (R)-enantiomer showing remarkably less potency and less selectivity of the (S)-form towards hNET against hSERT.

8 REFERENCES

1. Hamilton, J.G., *Excretion of radiosodium following intravenous administration to man*. Proc. Soc. Exper. Bio. Med., 1937. **35**: p. 595-598.
2. Fowler, J.S., et al., *Imaging the Addicted Human Brain*. Science & Practice Perspectives, 2007. **3**(2): p. 4-16.
3. Krieger, *Strahlenphysik, Dosimetrie und Strahlenschutz. Band 1. Grundlagen*. 1992.
4. Saha, G.B., *Fundamentals of Nuclear Pharmacy*. Sixth ed. 2010.
5. Kowalsky, R.J., *Radiopharmaceuticals in Nuclear Pharmacy and Nuclear Medicine*. Second ed. 2004.
6. Stigbrand, T.C., J.; Adams, G.P, *Targeted Radionuclide Tumor Therapy: Biological Aspects*. 2008.
7. Deutsch, M., *The discovery of the positronium*. The Superworld II, The Subnuclear Series, 1990. **25**: p. 517-524.
8. Zolle, I., *Technetium-99m Pharmaceuticals - Preparation and Quality Control in Nuclear Medicine*. 2007: Springer.
9. Foote, R.L., et al., *The clinical case for proton beam therapy*. Radiat Oncol, 2012. **7**: p. 174.
10. Fukumura, T., et al., *An improved $^{62}\text{Zn}/^{62}\text{Cu}$ generator based on a cation exchanger and its fully remote-controlled preparation for clinical use*. Nucl Med Biol, 2006. **33**(6): p. 821-7.
11. Zhang, T., et al., *PET with ^{62}Cu -ATSM and ^{62}Cu -PTSM is a useful imaging tool for hypoxia and perfusion in pulmonary lesions*. AJR Am J Roentgenol, 2013. **201**(5): p. W698-706.
12. Hartmann, I.J., et al., *Technegas versus (^{81}m)Kr ventilation-perfusion scintigraphy: a comparative study in patients with suspected acute pulmonary embolism*. J Nucl Med, 2001. **42**(3): p. 393-400.
13. Bajc, M., et al., *EANM guidelines for ventilation/perfusion scintigraphy : Part 1. Pulmonary imaging with ventilation/perfusion single photon emission tomography*. Eur J Nucl Med Mol Imaging, 2009. **36**(8): p. 1356-70.
14. Bengel, F.M., et al., *Cardiac Positron Emission Tomography*. Journal of the American College of Cardiology, 2009. **54**(1): p. 1-15.
15. Saha, G.B., *Physics and Radiobiology of Nuclear Medicine* Third ed. 2006.
16. Scobie, J. and G.M. Lewis, *K-capture in carbon 11*. Philosophical Magazine, 1957. **2**(21): p. 1089-1099.
17. Available from: http://www.nucleide.org/DDEP_WG/Nuclides/Ga-68_tables.pdf.
18. Phan, H.T., et al., *The diagnostic value of ^{124}I -PET in patients with differentiated thyroid cancer*. European Journal of Nuclear Medicine and Molecular Imaging, 2008. **35**(5): p. 958-965.
19. Foote, S.L., F.E. Bloom, and G. Aston-Jones, *Nucleus locus ceruleus: new evidence of anatomical and physiological specificity*. Physiol Rev, 1983. **63**(3): p. 844-914.
20. Gu, H.H., et al., *The NH(2)-terminus of norepinephrine transporter contains a basolateral localization signal for epithelial cells*. Mol Biol Cell, 2001. **12**(12): p. 3797-807.
21. Guo, L., et al., *Molecular cloning and structural analysis of human norepinephrine transporter gene(NETHG)[ast]*. Cell Res, 1995. **5**(1): p. 93-100.
22. Schroeder, C. and J. Jordan, *Norepinephrine transporter function and human cardiovascular disease*. Am J Physiol Heart Circ Physiol, 2012. **303**(11): p. H1273-82.
23. Ganapathy, V., *Drugs of abuse and human placenta*. Life Sci, 2011. **88**(21-22): p. 926-30.
24. Schroeter, S., et al., *Immunolocalization of the cocaine- and antidepressant-sensitive l-norepinephrine transporter*. J Comp Neurol, 2000. **420**(2): p. 211-32.
25. Nogami, T., et al., *Occupancy of serotonin and norepinephrine transporter by milnacipran in patients with major depressive disorder: a positron emission tomography study with*

- [(11)C]DASB and (S,S)-[(18)F]FMeNER-D(2). *Int J Neuropsychopharmacol*, 2013. **16**(5): p. 937-43.
26. Sekine, M., et al., *Norepinephrine transporter occupancy by antidepressant in human brain using positron emission tomography with (S,S)-[18F]FMeNER-D2*. *Psychopharmacology (Berl)*, 2010. **210**(3): p. 331-6.
27. Gulyas, B., et al., *The norepinephrine transporter (NET) radioligand (S,S)-[18F]FMeNER-D2 shows significant decreases in NET density in the human brain in Alzheimer's disease: a post-mortem autoradiographic study*. *Neurochem Int*, 2010. **56**(6-7): p. 789-98.
28. Tuohy, E., et al., *P1: An anatomical and MRI study of the human thalamus*. *Journal of Anatomy*, 2004. **205**(6): p. 527-527.
29. Vanicek, T., et al., *The norepinephrine transporter in attention-deficit/hyperactivity disorder investigated with positron emission tomography*. *JAMA Psychiatry*, 2014. **71**(12): p. 1340-9.
30. Ding, Y.S., et al., *PET imaging of the effects of age and cocaine on the norepinephrine transporter in the human brain using (S,S)-[(11)C]O-methylreboxetine and HRRT*. *Synapse*, 2010. **64**(1): p. 30-8.
31. Schou, M., et al., *PET evaluation of novel radiofluorinated reboxetine analogs as norepinephrine transporter probes in the monkey brain*. *Synapse*, 2004. **53**(2): p. 57-67.
32. Mark, C., et al., *Development and automation of a novel NET-PET tracer: [11C]Me@APPI*. *Nucl Med Biol*, 2013. **40**(2): p. 295-303.
33. Rami-Mark, C., et al., *Radiosynthesis and first preclinical evaluation of the novel norepinephrine transporter pet-ligand [(11)C]ME@HAPTHI*. *EJNMMI Res*, 2015. **5**(1): p. 113.
34. Greden, J.F. and B.J. Carroll, *Psychomotor function in affective disorders: an overview of new monitoring techniques*. *Am J Psychiatry*, 1981. **138**(11): p. 1441-8.
35. Takano, H., et al., *Norepinephrine transporter occupancy by nortriptyline in patients with depression: a positron emission tomography study with (S,S)-[(1)(8)F]FMeNER-D(2)*. *Int J Neuropsychopharmacol*, 2014. **17**(4): p. 553-60.
36. Nyberg, S., et al., *Norepinephrine transporter occupancy in the human brain after oral administration of quetiapine XR*. *Int J Neuropsychopharmacol*, 2013. **16**(10): p. 2235-44.
37. Deupree, J.D., M.D. Montgomery, and D.B. Bylund, *Pharmacological properties of the active metabolites of the antidepressants desipramine and citalopram*. *Eur J Pharmacol*, 2007. **576**(1-3): p. 55-60.
38. Papakostas, G.I., et al., *Are antidepressant drugs that combine serotonergic and noradrenergic mechanisms of action more effective than the selective serotonin reuptake inhibitors in treating major depressive disorder? A meta-analysis of studies of newer agents*. *Biol Psychiatry*, 2007. **62**(11): p. 1217-27.
39. Zimmer, L., *Positron emission tomography neuroimaging for a better understanding of the biology of ADHD*. *Neuropharmacology*, 2009. **57**(7-8): p. 601-7.
40. Biederman, J., *Attention-deficit/hyperactivity disorder: a selective overview*. *Biol Psychiatry*, 2005. **57**(11): p. 1215-20.
41. Williams, J.A., et al., *Drug-drug interactions for UDP-glucuronosyltransferase substrates: a pharmacokinetic explanation for typically observed low exposure (AUC_i/AUC) ratios*. *Drug Metab Dispos*, 2004. **32**(11): p. 1201-8.
42. Guengerich, F.P., *Cytochrome p450 and chemical toxicology*. *Chem Res Toxicol*, 2008. **21**(1): p. 70-83.
43. Khojasteh, S.C., et al., *Chemical inhibitors of cytochrome P450 isoforms in human liver microsomes: a re-evaluation of P450 isoform selectivity*. *Eur J Drug Metab Pharmacokin*, 2011. **36**(1): p. 1-16.
44. Guengerich, F.P., *Cytochrome P450s and other enzymes in drug metabolism and toxicity*. *AAPS J*, 2006. **8**(1): p. E101-11.

45. Berka, K., et al., *Membrane position of ibuprofen agrees with suggested access path entrance to cytochrome P450 2C9 active site*. J Phys Chem A, 2011. **115**(41): p. 11248-55.
46. Hanukoglu, I., *Electron transfer proteins of cytochrome P450 systems*. Adv. Mol. Cell Biol., 1996. **14**: p. 29-55.
47. Johnson, E.F., et al., *Correlating Structure and Function of Drug-Metabolizing Enzymes: Progress and Ongoing Challenges*. Drug Metabolism and Disposition, 2014. **42**(1): p. 9-22.
48. Rittle, J. and M.T. Green, *Cytochrome P450 compound I: capture, characterization, and C-H bond activation kinetics*. Science, 2010. **330**(6006): p. 933-7.
49. Im, S.C. and L. Waskell, *The interaction of microsomal cytochrome P450 2B4 with its redox partners, cytochrome P450 reductase and cytochrome b(5)*. Arch Biochem Biophys, 2011. **507**(1): p. 144-53.
50. Sevrioukova, I.F. and T.L. Poulos, *Understanding the mechanism of cytochrome P450 3A4: recent advances and remaining problems*. Dalton Transactions, 2013. **42**(9): p. 3116-3126.
51. Cooper, H.L.R. and J.T. Groves, *Molecular Probes of the Mechanism of Cytochrome P450. Oxygen Traps a Substrate Radical Intermediate*. Archives of biochemistry and biophysics, 2011. **507**(1): p. 111-118.
52. Zanger, U.M. and M. Schwab, *Cytochrome P450 enzymes in drug metabolism: Regulation of gene expression, enzyme activities, and impact of genetic variation*. Pharmacology & Therapeutics, 2013. **138**(1): p. 103-141.
53. Bertilsson, L., et al., *Molecular genetics of CYP2D6: clinical relevance with focus on psychotropic drugs*. Br J Clin Pharmacol, 2002. **53**(2): p. 111-22.
54. Teh, L.K. and L. Bertilsson, *Pharmacogenomics of <i>CYP2D6</i>: Molecular Genetics, Interethnic Differences and Clinical Importance*. Drug Metabolism and Pharmacokinetics, 2012. **27**(1): p. 55-67.
55. Hiroi, T., et al., *Progesterone oxidation by cytochrome P450 2D isoforms in the brain*. Endocrinology, 2001. **142**(9): p. 3901-8.
56. Finnstrom, N., et al., *Detection of cytochrome P450 mRNA transcripts in prostate samples by RT-PCR*. Eur J Clin Invest, 2001. **31**(10): p. 880-6.
57. Hodges, V.M., G.Y. Molloy, and S.N. Wickramasinghe, *Demonstration of mRNA for five species of cytochrome P450 in human bone marrow, bone marrow-derived macrophages and human haemopoietic cell lines*. Br J Haematol, 2000. **108**(1): p. 151-6.
58. Ferguson, C.S. and R.F. Tyndale, *Cytochromes P450 in the brain: Emerging evidence for biological significance*. Trends in pharmacological sciences, 2011. **32**(12): p. 708-714.
59. Hedlund, E., J.A. Gustafsson, and M. Warner, *Cytochrome P450 in the brain; a review*. Curr Drug Metab, 2001. **2**(3): p. 245-63.
60. Britto, M.R. and P.J. Wedlund, *Cytochrome P-450 in the brain. Potential evolutionary and therapeutic relevance of localization of drug-metabolizing enzymes*. Drug Metab Dispos, 1992. **20**(3): p. 446-50.
61. Miksys, S., E. Hoffmann, and R.F. Tyndale, *Regional and cellular induction of nicotine-metabolizing CYP2B1 in rat brain by chronic nicotine treatment*. Biochem Pharmacol, 2000. **59**(12): p. 1501-11.
62. Miksys, S., et al., *Smoking, alcoholism and genetic polymorphisms alter CYP2B6 levels in human brain*. Neuropharmacology, 2003. **45**(1): p. 122-32.
63. Benedetti, M.S., *Biotransformation of xenobiotics by amine oxidases*. Fundam Clin Pharmacol, 2001. **15**(2): p. 75-84.
64. Herraiz, T. and C. Chaparro, *Human monoamine oxidase is inhibited by tobacco smoke: beta-carboline alkaloids act as potent and reversible inhibitors*. Biochem Biophys Res Commun, 2005. **326**(2): p. 378-86.
65. Herraiz, T. and C. Chaparro, *Human monoamine oxidase enzyme inhibition by coffee and beta-carbolines norharman and harman isolated from coffee*. Life Sci, 2006. **78**(8): p. 795-802.

66. Constantino, L., et al., *Metabolism of primaquine by liver homogenate fractions. Evidence for monoamine oxidase and cytochrome P450 involvement in the oxidative deamination of primaquine to carboxyprimaquine*. *Exp Toxicol Pathol*, 1999. **51**(4-5): p. 299-303.
67. Abad, E., R.K. Zenn, and J. Kastner, *Reaction mechanism of monoamine oxidase from QM/MM calculations*. *J Phys Chem B*, 2013. **117**(46): p. 14238-46.
68. Bailey, K. and E.W. Tan, *Synthesis and evaluation of bifunctional nitrocatechol inhibitors of pig liver catechol-O-methyltransferase*. *Bioorg Med Chem*, 2005. **13**(20): p. 5740-9.
69. Shield, A.J., et al., *Human catechol O-methyltransferase genetic variation: gene resequencing and functional characterization of variant allozymes*. *Mol Psychiatry*, 2004. **9**(2): p. 151-60.
70. Mannisto, P.T. and S. Kaakkola, *Catechol-O-methyltransferase (COMT): biochemistry, molecular biology, pharmacology, and clinical efficacy of the new selective COMT inhibitors*. *Pharmacol Rev*, 1999. **51**(4): p. 593-628.
71. Malherbe, P., et al., *Expression of functional membrane-bound and soluble catechol-O-methyltransferase in Escherichia coli and a mammalian cell line*. *J Neurochem*, 1992. **58**(5): p. 1782-9.
72. Guldberg, H.C. and C.A. Marsden, *Catechol-O-methyl transferase: pharmacological aspects and physiological role*. *Pharmacol Rev*, 1975. **27**(2): p. 135-206.
73. Lotta, T., et al., *Kinetics of human soluble and membrane-bound catechol O-methyltransferase: a revised mechanism and description of the thermolabile variant of the enzyme*. *Biochemistry*, 1995. **34**(13): p. 4202-10.
74. Palma, P.N., et al., *Molecular modeling and metabolic studies of the interaction of catechol-O-methyltransferase and a new nitrocatechol inhibitor*. *Drug Metab Dispos*, 2003. **31**(3): p. 250-8.
75. Brevitt, S.E. and E.W. Tan, *Synthesis and in vitro evaluation of two progressive series of bifunctional polyhydroxybenzamide catechol-O-methyltransferase inhibitors*. *J Med Chem*, 1997. **40**(13): p. 2035-9.
76. Zhang, L., et al., *Detoxication of structurally diverse polycyclic aromatic hydrocarbon (PAH) o-quinones by human recombinant catechol-O-methyltransferase (COMT) via O-methylation of PAH catechols*. *J Biol Chem*, 2011. **286**(29): p. 25644-54.
77. Pelkonen, O., et al., *Inhibition and induction of human cytochrome P450 (CYP) enzymes*. *Xenobiotica*, 1998. **28**(12): p. 1203-53.
78. Spaggiari, D., et al., *A cocktail approach for assessing the in vitro activity of human cytochrome P450s: an overview of current methodologies*. *J Pharm Biomed Anal*, 2014. **101**: p. 221-37.
79. Yuan, R., et al., *Evaluation of cytochrome P450 probe substrates commonly used by the pharmaceutical industry to study in vitro drug interactions*. *Drug Metab Dispos*, 2002. **30**(12): p. 1311-9.
80. Chauret, N., A. Gauthier, and D.A. Nicoll-Griffith, *Effect of common organic solvents on in vitro cytochrome P450-mediated metabolic activities in human liver microsomes*. *Drug Metab Dispos*, 1998. **26**(1): p. 1-4.
81. Yuan, L., et al., *Study of in vitro metabolism of m-nisoldipine in human liver microsomes and recombinant cytochrome P450 enzymes by liquid chromatography-mass spectrometry*. *J Pharm Biomed Anal*, 2014. **97**: p. 65-71.
82. Newton, D.J., R.W. Wang, and A.Y. Lu, *Cytochrome P450 inhibitors. Evaluation of specificities in the in vitro metabolism of therapeutic agents by human liver microsomes*. *Drug Metab Dispos*, 1995. **23**(1): p. 154-8.
83. Yao, M., et al., *Development and full validation of six inhibition assays for five major cytochrome P450 enzymes in human liver microsomes using an automated 96-well microplate incubation format and LC-MS/MS analysis*. *J Pharm Biomed Anal*, 2007. **44**(1): p. 211-23.

84. von Moltke, L.L., et al., *Phenacetin O-deethylation by human liver microsomes in vitro: inhibition by chemical probes, SSRI antidepressants, nefazodone and venlafaxine*. *Psychopharmacology (Berl)*, 1996. **128**(4): p. 398-407.
85. Bourrie, M., et al., *Cytochrome P450 isoform inhibitors as a tool for the investigation of metabolic reactions catalyzed by human liver microsomes*. *J Pharmacol Exp Ther*, 1996. **277**(1): p. 321-32.
86. Rochat, B., et al., *Human CYP1B1 and anticancer agent metabolism: mechanism for tumor-specific drug inactivation?* *J Pharmacol Exp Ther*, 2001. **296**(2): p. 537-41.
87. Mancy, A., et al., *Interaction of sulfaphenazole derivatives with human liver cytochromes P450 2C: molecular origin of the specific inhibitory effects of sulfaphenazole on CYP 2C9 and consequences for the substrate binding site topology of CYP 2C9*. *Biochemistry*, 1996. **35**(50): p. 16205-12.
88. Rasmussen, B.B., T.L. Nielsen, and K. Brosen, *Fluvoxamine inhibits the CYP2C19-catalysed metabolism of proguanil in vitro*. *Eur J Clin Pharmacol*, 1998. **54**(9-10): p. 735-40.
89. Walsky, R.L. and R.S. Obach, *Verification of the selectivity of (+)N-3-benzylirivanol as a CYP2C19 inhibitor*. *Drug Metab Dispos*, 2003. **31**(3): p. 343.
90. Turpeinen, M., et al., *Selective inhibition of CYP2B6-catalyzed bupropion hydroxylation in human liver microsomes in vitro*. *Drug Metab Dispos*, 2004. **32**(6): p. 626-31.
91. Draper, A.J., A. Madan, and A. Parkinson, *Inhibition of coumarin 7-hydroxylase activity in human liver microsomes*. *Arch Biochem Biophys*, 1997. **341**(1): p. 47-61.
92. Moody, G.C., et al., *Fully automated analysis of activities catalysed by the major human liver cytochrome P450 (CYP) enzymes: assessment of human CYP inhibition potential*. *Xenobiotica*, 1999. **29**(1): p. 53-75.
93. Stresser, D.M., et al., *Highly selective inhibition of human CYP3Aa in vitro by azamulin and evidence that inhibition is irreversible*. *Drug Metab Dispos*, 2004. **32**(1): p. 105-12.
94. Walsky, R.L., et al., *Selective inhibition of human cytochrome P4502C8 by montelukast*. *Drug Metab Dispos*, 2005. **33**(3): p. 413-8.
95. Walsky, R.L. and R.S. Obach, *Measurement of in vitro cytochrome P450 2B6 activity*. *Curr Protoc Toxicol*, 2009. Chapter 4: p. Unit4 27.
96. Fukami, T., et al., *CYP2A13 metabolizes the substrates of human CYP1A2, phenacetin, and theophylline*. *Drug Metab Dispos*, 2007. **35**(3): p. 335-9.
97. Nedelcheva, V. and I. Gut, *P450 in the rat and man: methods of investigation, substrate specificities and relevance to cancer*. *Xenobiotica*, 1994. **24**(12): p. 1151-75.
98. Kobayashi, K., et al., *Selectivities of human cytochrome P450 inhibitors toward rat P450 isoforms: study with cDNA-expressed systems of the rat*. *Drug Metab Dispos*, 2003. **31**(7): p. 833-6.
99. Fabrizi, L., et al., *Identification of the cytochrome P450 isoenzymes involved in the metabolism of diazinon in the rat liver*. *J Biochem Mol Toxicol*, 1999. **13**(1): p. 53-61.
100. Wang, D.L., et al., *Identification of ginkgolide B metabolites in urine and rat liver cytochrome P450 enzymes responsible for their formation in vitro*. *Acta Pharmacol Sin*, 2008. **29**(3): p. 376-84.
101. Liu, Y.T., et al., *Metabolism and metabolic inhibition of gambogic acid in rat liver microsomes*. *Acta Pharmacol Sin*, 2006. **27**(9): p. 1253-8.
102. Liu, Z.Y., et al., *In vitro biotransformation and investigation of metabolic enzymes possibly responsible for the metabolism of bisdesoxyolaquinox in the liver fractions of rats, chicken, and pigs*. *Toxicology*, 2011. **279**(1-3): p. 155-66.
103. Kimonen, T., et al., *The inhibition of CYP enzymes in mouse and human liver by pilocarpine*. *Br J Pharmacol*, 1995. **114**(4): p. 832-6.
104. Chang, T., M. Levine, and G.D. Bellward, *Selective inhibition of rat hepatic microsomal cytochrome P-450. II. Effect of the in vitro administration of cimetidine*. *J Pharmacol Exp Ther*, 1992. **260**(3): p. 1450-5.

105. Levine, M. and G.D. Bellward, *Effect of cimetidine on hepatic cytochrome P450: evidence for formation of a metabolite-intermediate complex*. Drug Metab Dispos, 1995. **23**(12): p. 1407-11.
106. Lin Wu, S.W., et al., *Cytochrome P-450A1 catalyzes the formation of MA1 from territrem a in liver microsomes of 7-week-old female Wistar rats*. J Toxicol Environ Health A, 2003. **66**(5): p. 453-67.
107. Makaji, E., et al., *Effects of cytochrome P450 inhibitors on the biotransformation of fluorogenic substrates by adult male rat liver microsomes and cDNA-expressed rat cytochrome P450 isoforms*. Toxicol Sci, 2010. **113**(2): p. 293-304.
108. Su, Q.B., et al., *Biotransformation and pharmacokinetics of the novel anticancer drug, SYUIQ-5, in the rat*. Invest New Drugs, 2008. **26**(2): p. 119-37.
109. Eagling, V.A., J.F. Tjia, and D.J. Back, *Differential selectivity of cytochrome P450 inhibitors against probe substrates in human and rat liver microsomes*. Br J Clin Pharmacol, 1998. **45**(2): p. 107-14.
110. Guo, W., et al., *Identification of the rat liver cytochrome P450 enzymes involved in the metabolism of the calcium channel blocker dipfluzine hydrochloride*. Environ Toxicol Pharmacol, 2014. **38**(3): p. 901-12.
111. Takano, A., et al., *Mapping of the norepinephrine transporter in the human brain using PET with (S,S)-[18F]FMeNER-D2*. Neuroimage, 2008. **42**(2): p. 474-82.
112. Takano, A., et al., *Comparative evaluations of norepinephrine transporter radioligands with reference tissue models in rhesus monkeys: (S,S)-[18F]FMeNER-D2 and (S,S)-[11C]MeNER*. Eur J Nucl Med Mol Imaging, 2009. **36**(11): p. 1885-91.
113. Takano, A., et al., *Imaging the norepinephrine transporter with positron emission tomography: initial human studies with (S,S)-[18F]FMeNER-D2*. Eur J Nucl Med Mol Imaging, 2008. **35**(1): p. 153-7.
114. Takano, A., et al., *Biodistribution and radiation dosimetry of the norepinephrine transporter radioligand (S,S)-[18F]FMeNER-D2: A human whole-body PET study*. J NUCL MED MEETING ABSTRACTS, 2007. **48**(MeetingAbstracts_2): p. 299P-a-.
115. Takano, A., et al., *Saturated norepinephrine transporter occupancy by atomoxetine relevant to clinical doses: a rhesus monkey study with (S,S)-[(18)F]FMeNER-D (2)*. Eur J Nucl Med Mol Imaging, 2009. **36**(8): p. 1308-14.
116. Schou, M., et al., *Synthesis of 11C-labelled (R)-OHDMI and CFMME and their evaluation as candidate radioligands for imaging central norepinephrine transporters with PET*. Bioorg Med Chem, 2007. **15**(2): p. 616-25.
117. Neudorfer, C., *Development of Novel Precursors and Reference Compounds for PET Based Investigations Targeting the Norepinephrine Transporter and Monoamine Oxidase B*. Dec. 2014: p. 124-131, 221-253.
118. Ching, M.S., et al., *Potent inhibition of yeast-expressed CYP2D6 by dihydroquinidine, quinidine, and its metabolites*. Biochem Pharmacol, 1995. **50**(6): p. 833-7.
119. Rami-Mark, C., et al., *[18F]FMeNER-D2: reliable fully-automated synthesis for visualization of the norepinephrine transporter*. Nucl Med Biol, 2013. **40**(8): p. 1049-54.
120. Anzenbacher, P. and E. Anzenbacherova, *Cytochromes P450 and metabolism of xenobiotics*. Cell Mol Life Sci, 2001. **58**(5-6): p. 737-47.
121. Christensen, H., et al., *Different enzyme kinetics of midazolam in recombinant CYP3A4 microsomes from human and insect sources*. Drug Metab Pharmacokinet, 2009. **24**(3): p. 261-8.
122. Nics, L., et al., *The stability of methyl-, ethyl- and fluoroethylesters against carboxylesterases in vitro: there is no difference*. Nucl Med Biol, 2011. **38**(1): p. 13-7.
123. Li, D., et al., *Effect of regular organic solvents on cytochrome P450-mediated metabolic activities in rat liver microsomes*. Drug Metab Dispos, 2010. **38**(11): p. 1922-5.

124. Dolomanov, O.V., et al., *OLEX2: a complete structure solution, refinement and analysis program*. Journal of Applied Crystallography, 2009. **42**(2): p. 339-341.
125. Sheldrick, G., *A short history of SHELX*. Acta Crystallographica Section A, 2008. **64**(1): p. 112-122.
126. Zhang, P., et al., *Synthesis and activity of novel 1- or 3-(3-amino-1-phenyl propyl)-1,3-dihydro-2H-benzimidazol-2-ones as selective norepinephrine reuptake inhibitors*. Bioorg Med Chem Lett, 2008. **18**(23): p. 6067-70.
127. Panagopoulos, A.M., et al., *Apparent alkyl transfer and phenazine formation via an aryne intermediate*. J Org Chem, 2013. **78**(8): p. 3532-40.
128. Varney, M.D., et al., *Synthesis and biological evaluation of -n[4-(2-trans-[[2,6-diamino-4(3H)-oxopyrimidin-5-yl]methyl]thio]cyclobutyl)benzoyl] -l-glutamic acid a novel 5-thiapyrimidinone inhibitor of dihydrofolate reductase*. Journal of Heterocyclic Chemistry, 1995. **32**(5): p. 1493-1498.
129. Fernández, I. and L. Muñoz, *Synthesis of enantiomerically pure (+)- and (-)-protected 5-aminomethyl-1,3-oxazolidin-2-one derivatives from allylamine and carbon dioxide*. Tetrahedron: Asymmetry, 2006. **17**(17): p. 2548-2557.
130. Li, Z., et al., *"Minimalist" Cyclopropene-Containing Photo-Cross-Linkers Suitable for Live-Cell Imaging and Affinity-Based Protein Labeling*. Journal of the American Chemical Society, 2014. **136**(28): p. 9990-9998.
131. Gregory, W.A., et al., *Antibacterials. Synthesis and structure-activity studies of 3-aryl-2-oxooxazolidines. 1. The B group*. Journal of Medicinal Chemistry, 1989. **32**(8): p. 1673-1681.
132. Yu, F., et al., *Copper(II)-Catalyzed Hydrosilylation of Ketones Using Chiral Dipyridylphosphane Ligands: Highly Enantioselective Synthesis of Valuable Alcohols*. Chemistry – A European Journal, 2011. **17**(50): p. 14234-14240.
133. La Regina, G., et al., *1-[(3-Aryloxy-3-aryl)propyl]-1H-imidazoles, New Imidazoles with Potent Activity against Candida albicans and Dermatophytes. Synthesis, Structure–Activity Relationship, and Molecular Modeling Studies*. Journal of Medicinal Chemistry, 2008. **51**(13): p. 3841-3855.
134. Larsen, P.U.J., Dahlstrom, K.; Jensen, M., *Synthesis of [¹¹C]iodomethane by iodination of [¹¹C]methane*. Appl Radiat Isot, 1997(48): p. 153-7.
135. Knies, T., K. Rode, and F. Wuest, *Practical experiences with the synthesis of [11C]CH3I through gas phase iodination reaction using a TRACERlabFXC synthesis module*. Appl Radiat Isot, 2008. **66**(4): p. 482-8.
136. Rochat, B., et al., *Stereoselective biotransformation of the selective serotonin reuptake inhibitor citalopram and its demethylated metabolites by monoamine oxidases in human liver*. Biochem Pharmacol, 1998. **56**(1): p. 15-23.
137. Scott, I.L., et al., *Amine derivatives and their preparation, pharmaceutical compositions and use in the treatment of ophthalmic diseases*. 2009, Acucela, Inc., USA . p. 373pp.

9 APPENDIX

9.1 Supplementary data

9.1.1 Detailed information about batch mixtures for chemical inhibition experiments

Batch-#1:

used for: Quinidine (HLM)

Table 42: Batch-#1

	Conc. [μM]	n [nmol]	Vol. stock [μL]	Vol. buffer [μL]	Vol. buffer + DMSO [μL]
A	0.4	0.12	20	157	80
B	0.8	0.24	40	157	60
C	2.0	0.60	100	157	-
D = Ref	-	-	-	157	100

Batch-#2:

used for: Quinidine (HLM)

Table 43: Batch-#2

	Conc. [μM]	n [nmol]	Vol. stock [μL]	Vol. buffer [μL]	Vol. buffer + DMSO [μL]
A	1	0.3	20	157	80
B	2	0.6	40	157	60
C	5	1.5	100	157	-
D = Ref	-	-	-	157	100

Batch-#3:

used for: Montelukast.Na (RLM)
4-Methylpyrazole.HCl (RLM)

Table 44: Batch-#3

	Conc. [μM]	n [nmol]	Vol. stock [μL]	Vol. buffer [μL]	Vol. buffer + DMSO [μL]
A	1	0.3	10	157	90
B	5	1.5	50	157	50
C	10	3.0	100	157	-
D = Ref	-	-	-	157	100

Batch-#4:

used for: Ketoconazole (HLM, RLM)

Table 45: Batch-#4

	Conc. [μM]	n [nmol]	Vol. stock [μL]	Vol. buffer [μL]	Vol. buffer + DMSO [μL]
A	2	0.6	20	157	80
B	5	1.5	50	157	50
C	10	3.0	100	157	-
D = Ref	-	-	-	157	100

Batch-#5:used for: Quinidine (HLM, RLM)
4-Methylpyrazole.HCl (HLM)*Table 46: Batch-#5*

	Conc. [μM]	n [nmol]	Vol. stock [μL]	Vol. buffer [μL]	Vol. buffer + DMSO [μL]
A	5	1.5	20	157	80
B	10	3.0	40	157	60
C	20	6.0	100	157	-
D = Ref	-	-	-	157	100

Batch-#6:used for: 2-Phenyl-2-(1-piperidiny)propane (HLM, RLM)
Sulfaphenazole (HLM, RLM)*Table 47: Batch-#6*

	Conc. [μM]	n [nmol]	Vol. stock [μL]	Vol. buffer [μL]	Vol. buffer + DMSO [μL]
A	10	3	20	157	80
B	20	6	40	157	60
C	50	15	100	157	-
D = Ref	-	-	-	157	100

Batch-#7:

used for: Montelukast.Na (HLM)
Ticlopidine.HCl (HLM, RLM)

Table 48: Batch-#7

	Conc. [μM]	n [nmol]	Vol. stock [μL]	Vol. buffer [μL]	Vol. buffer + DMSO [μL]
A	10	3	10	157	90
B	50	15	50	157	50
C	100	30	100	157	-
D = Ref	-	-	-	157	100

Batch-#8:

used for: Furafllyline (HLM, RLM)
(+)-N-Benzylirvanol (HLM, RLM)
Ketoconazole (HLM, RLM)

Table 49: Batch-#8

	Conc. [μM]	n [nmol]	Vol. stock [μL]	Vol. buffer [μL]	Vol. buffer + DMSO [μL]
A	20	6	20	157	80
B	50	15	50	157	50
C	100	30	100	157	-
D = Ref	-	-	-	157	100

Batch-#9:

used for: Ticlopidine.HCl (HLM, RLM)

Table 50: Batch-#9

	Conc. [μM]	n [nmol]	Vol. stock [μL]	Vol. buffer [μL]	Vol. buffer + DMSO [μL]
A	50	15	25	157	75
B	100	30	50	157	50
C	200	60	100	157	-
D = Ref	-	-	-	157	100

9.1.2 SPSS analyses

Data of HLM and RLM incubations were corrected for outliers. Raw data is given below (*Figures and Tables 51 + 52*):

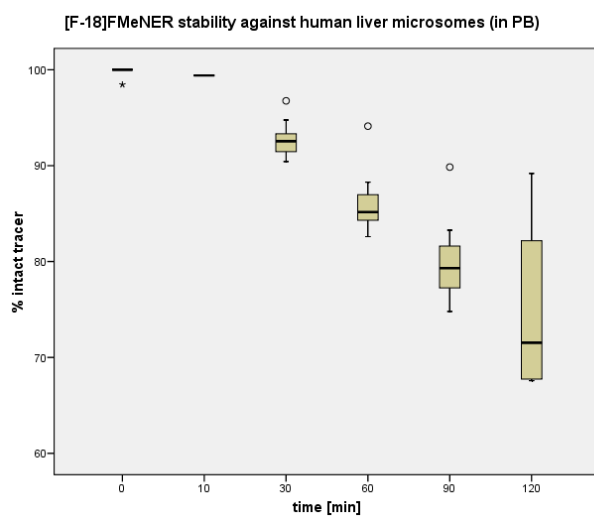


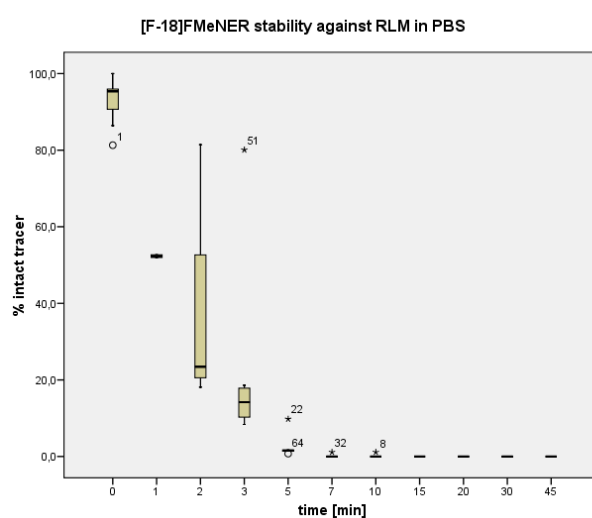
Table 51: Full dataset for HLM incubations in PB.

t [min]	MEAN [% intact tracer]	SD	n
0	99.9	0.5	10
10	99.4	-	1
30	92.8	1.9	10
60	86.1	3.4	10
90	80.2	4.3	10
120	75.0	10.1	4

Figure 51: Boxplot of HLM incubations in PB, not corrected for outliers.

The outlying and highlighted datapoints belong to a single experiment. Due to a probable systematic error not only the single datapoints but the whole experiment was excluded.

Table 52: Full dataset for RLM in PBS.



t [min]	MEAN [% intact tracer]	SD	n
0	93.3	5.2	15
1	52.3	0.5	2
2	36.6	30.0	4
3	21.6	23.9	8
5	3.0	3.8	5
7	0.1	0.4	9
10	0.2	0.4	7
15	0.0	0.0	10
20	0.0	0.0	14
30	0.0	0.0	2
45	0.0	.	1

Figure 52: Boxplot of RLM incubations in PBS, not corrected for outliers.

The highlighted four datapoints (stars) were identified as outliers and eliminated.

9.1.3 Analytical HPLC – chromatogram: Crude [¹⁸F]FMeNER-D2

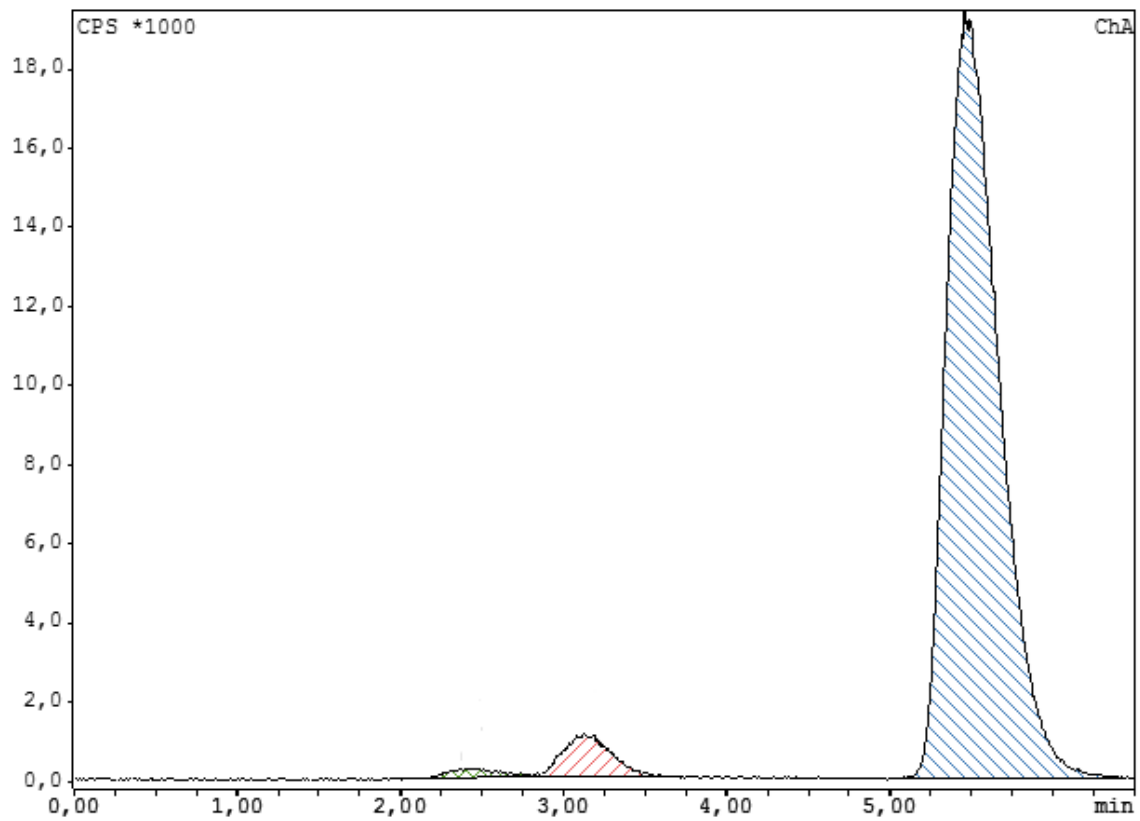


Figure 53: Crude [¹⁸F]FMeNER-D2 after injection onto analytical HPLC.

9.1.4 Complete data table for metabolism experiments

[see next page]

Table 53: Overview of all metabolism studies.

FMN-#	Single enzyme	Microsomes	Inhibitor	Concentration range [µM]	Buffer	% org. solvent	Batch
92		RLM			PBS	2 (EtOH)	300
93	1A1				PBS	0.66(EtOH)	300
	3A4				PBS	0.4 (EtOH)	500
94	1B1				PBS	0.24 (EtOH)	500
		HLM			PBS	0.4 (EtOH)	300
95	CES porcine				PBS	0.17 (EtOH)	500
	MAO A				PBS	0.085 (EtOH)	1000
97	3A4				PBS	3.3 (EtOH)	300
100	1A1				PBS	0.4 (EtOH)	300
	MAO A				PB	0.48 (EtOH)	250
	2E1				PBS	0.4 (EtOH)	500
104		HLM			PBS	0.28 (EtOH)	300
		RLM			PBS	0.28 (EtOH)	300
	2E1				PBS	0.17 (EtOH)	500
	MAO B				PBS	0.34 (EtOH)	250
105		RLM			PB	0.28 (EtOH)	300
		HLM			PB	0.28 (EtOH)	300
106	COMT				PB	0.34 (EtOH)	350
	COMT				PB	0.34 (EtOH)	350
	CES human mix				PB	0.24 (EtOH)	300
107		RLM			PB	0.28 (EtOH)	300
108		RLM	Ketoconazole	2, 5, 10	PB	0.28 (EtOH); 0.19 (DMSO, max.)	300
109		RLM	Ketoconazole	2, 5, 10	PB	0.28 (EtOH); 0.05 (DMSO, max.)	300
		RLM	Ketoconazole	2, 5, 10	PB	0.32 (EtOH)	300
		RLM	Montelukast.Na	1, 5, 10	PB	0.28 (EtOH); 0.03 (DMSO, max.)	300
110		RLM	(+)-N-3-Benzylirvanol	2, 5, 10	PB	0.28 (EtOH); 0.02 (DMSO, max.)	300
		RLM	Furafylline	20, 50, 100	PB	0.28 (EtOH); 0.17 (DMSO, max.)	300
		RLM	4-Methylpivrazole.HCl	1, 5, 10	PB	0.28 (EtOH); 0.003 (DMSO,max.)	300
111	2A6				PB	0.28 (EtOH)	300
	2C19				PB	0.28 (EtOH)	300
112	3A4				PB	0.28 (EtOH)	300
	2C19				PB	0.28 (EtOH)	300
		RLM	Quinidine	5, 10, 20	PB	0.28 (EtOH); 0.02 (DMSO, max.)	300
113		HLM	Quinidine	5, 10, 20	PB	0.28 (EtOH); 0.02 (DMSO, max.)	300
		HLM	Montelukast.Na	10, 50, 100	PB	0.28 (EtOH); 0.3 (DMSO, max.)	300

FMN-#	Single enzyme	Microsomes	Inhibitor	Concentration range [µM]	Buffer	% org. solvent	Batch		
114		RLM	Quinidine	5, 10, 20	PBS	0.28 (EtOH); 0.02 (DMSO, max.)	300		
			HLM	Ketoconazole	2, 5, 10	PB	0.28 (EtOH); 0.05 (DMSO, max.)	300	
			HLM	Furafylline	20, 50, 100	PB	0.28 (EtOH); 0.17 (DMSO, max.)	300	
115			HLM	(+)-N-3-Benzyl nirvanol	20, 50, 100	PB	0.28 (EtOH); 0.19 (DMSO, max.)	300	
			HLM	4- Methylpivrazole.HCl	5, 10, 20	PB	0.28 (EtOH); 0.006 (DMSO, max.)	300	
117	3A4					PB	0.4 (EtOH)	300	
	2C19						0.4 (EtOH)	300	
		RLM		Quinidine	5, 10, 20		0.4 (EtOH); 0.02 (DMSO, max.)	300	
		RLM		(+)-N-3-Benzyl nirvanol	20, 50, 100		0.4 (EtOH); 0.14 (DMSO max.)	300	
			HLM	Quinidine	1, 2, 5	PB	0.4 (EtOH); 0.004 (DMSO max.)	300	
			HLM	Ketoconazole	20, 50, 100	PB	0.28 (EtOH); 0.45 (DMSO, max.)	300	
118	2D6					PB	0.29 (EtOH)	300	
	2D6					PB	0.086 (EtOH)	1000	
	2A6					Tris	0.29 (EtOH)	300	
	1B1					PB	0.29 (EtOH)	300	
	2E1					PB	0.29 (EtOH)	300	
	1A1					PB	0.29 (EtOH)	300	
119			HLM	Ticlopidine.HCl	10, 50, 100	PBS	0.4 (EtOH); 0.08 (DMSO)	300	
				Sulfaphenazole	10, 20, 50	PBS	0.4 (EtOH); 0.01 (DMSO)	300	
				PPP	10, 20, 50	PBS	0.4 (EtOH); 0.01 (DMSO)	300	
				Ketoconazole	20, 50, 100	PBS	0.4 (EtOH); 0.3 (DMSO)	300	
		RLM		Sulfaphenazole	10, 20, 50	PBS	0.4 (EtOH); 0.01 (DMSO)	300	
120				Ticlopidine.HCl	10, 50, 100	PBS	0.4 (EtOH); 0.08 (DMSO)	300	
				PPP	10, 20, 50	PBS	0.4 (EtOH); 0.01 (DMSO)	300	
				Ketoconazole	20, 50, 100	PBS	0.4 (EtOH); 0.3 (DMSO)	300	
				Quinidine	10, 20, 50	PBS	0.4 (EtOH); 0.01 (DMSO)	300	
				(+)-N-3-Benzyl nirvanol	20, 50, 100	PBS	0.4 (EtOH); 0.04 (DMSO)	300	
		RLM		Ticlopidine.HCl	10, 50, 100	PBS	0.4 (EtOH); 0.08 (DMSO)	300	
				PPP	10, 20, 50	PBS	0.4 (EtOH); 0.01 (DMSO)	300	
121	2D6					PB	0.12 (EtOH)	1000	
			HLM	Furafylline	20, 50, 100	PB	0.29 (EtOH); 0.04 (DMSO)	300	
122				Ticlopidine.HCl	50, 100, 200	PB	0.29 (EtOH); 0.16 (DMSO)	300	
				Quinidine	0.4, 0.8, 2	PB	0.29 (EtOH); 0.002 (DMSO)	300	
				(+)-N-3-Benzyl nirvanol	20, 50, 100	PB	0.4 (EtOH); 0.14 (DMSO)	300	
		CYP 3A4			Ketoconazole	1	PB	0.29 (EtOH)	300
		CYP2D6			Quinidine	1	PB	0.29 (EtOH)	300

9.1.5 Data tables for chemical inhibition experiments in RLM

In the interest of completeness, the data tables for inhibitors which did not affect [¹⁸F]FMENER-D2 degradation in RLM are given below (Table 54 – Table 57).

Sufaphenazole

Table 54: Sulfaphenazole in RLM incubations.

% total area				
n = 1	10 μM		20 μM	
t [min]	5.0 (tracer)	3.4	5.0	3.4
0	95.6	4.4	95.0	5.0
3	16.4	83.6	15.3	84.7
7	0.56	99.4	0.7	99.3
15	0.0	100.0	0.0	100.0
20	0.0	100.0	0.0	100.0
% total area				
	50 μM		Ref	
t [min]	5.0	3.4	5.0	3.4
0	96.2	3.8	95.4	4.6
3	14.4	85.6	17.1	82.9
7	0.43	99.6	1.1	98.9
15	0.0	100.0	0.0	100.0
20	0.0	100.0	0.0	100.0

Montelukast sodium

Table 55: Montelukast in RLM incubations.

% total area								
n = 1	1 μM				5 μM			
t [min]	5.5 (tracer)	2.6	3.0	3.6	5.5	2.6	3.0	3.6
0	90.8	0	0	9.2	90.3	0	0	9.7
10	0.0	1.7	4.1	9.2	0.0	0	5.1	94.9
20	0.0	4.3	10.0	85.7	0.0	4.1	8.7	87.3
30	0.0	8.0	12.3	79.7	0.0	5.0	12.7	82.3
45	0.0	12.6	13.5	73.9	0.0	11.1	14.4	74.5
% total area								
	10 μM				Ref			
t [min]	5.5	2.6	3.0	3.6	5.5	2.6	3.0	3.6
0	84.6	0	0	15.4	88.1	0	0	11.9
10	0.0	0	3.5	96.5	0.0	2.5	5.2	92.3
20	0.0	3.3	8.6	88.1	0.0	4.2	10.0	85.8
30	0.0	5.9	12.0	82.2	0.0	7.3	16.0	77.4
45	0.0	8.3	15.0	76.7	0.0	13.6	16.6	69.8

4-Methylpyrazole hydrochloride*Table 56: 4-Methylpyrazole.HCl in RLM incubations.*

% total area								
n = 1	1 μ M				5 μ M			
t [min]	5.6 (tracer)	2.6	3.0	3.6	5.6	2.6	3.0	3.6
0	84.3	0	0	15.7	90.7	0	0	9.3
10	0.0	1.8	7.3	90.9	0.0	1.7	7.2	91.1
20	0.0	4.0	11.3	84.7	0.0	3.9	11.2	84.9
	10 μ M				Ref			
t [min]	5.6	2.6	3.0	3.6	5.6	2.6	3.0	3.6
0	91.6	0	0	8.4	88.2	0	0	11.8
10	0.0	1.9	6.7	91.4	0.0	1.3	7.0	91.7
20	0.0	3.2	12.1	84.7	0.0	2.9	12.7	84.4

Furafylline*Table 57: Furafylline in RLM incubations.*

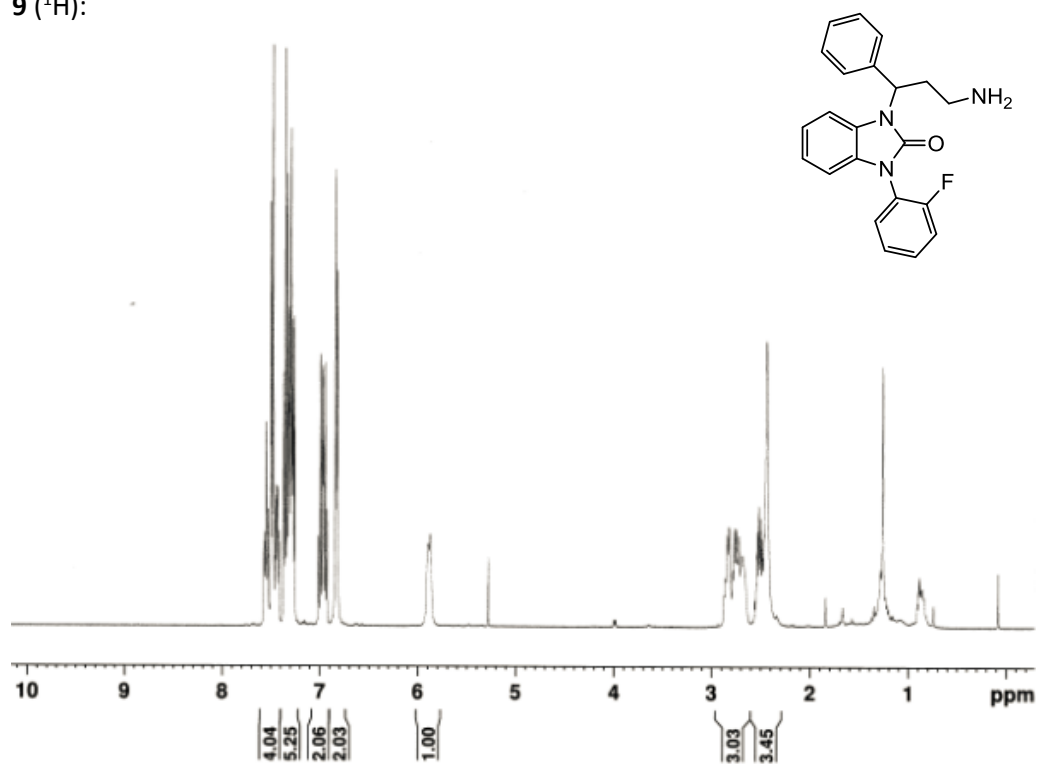
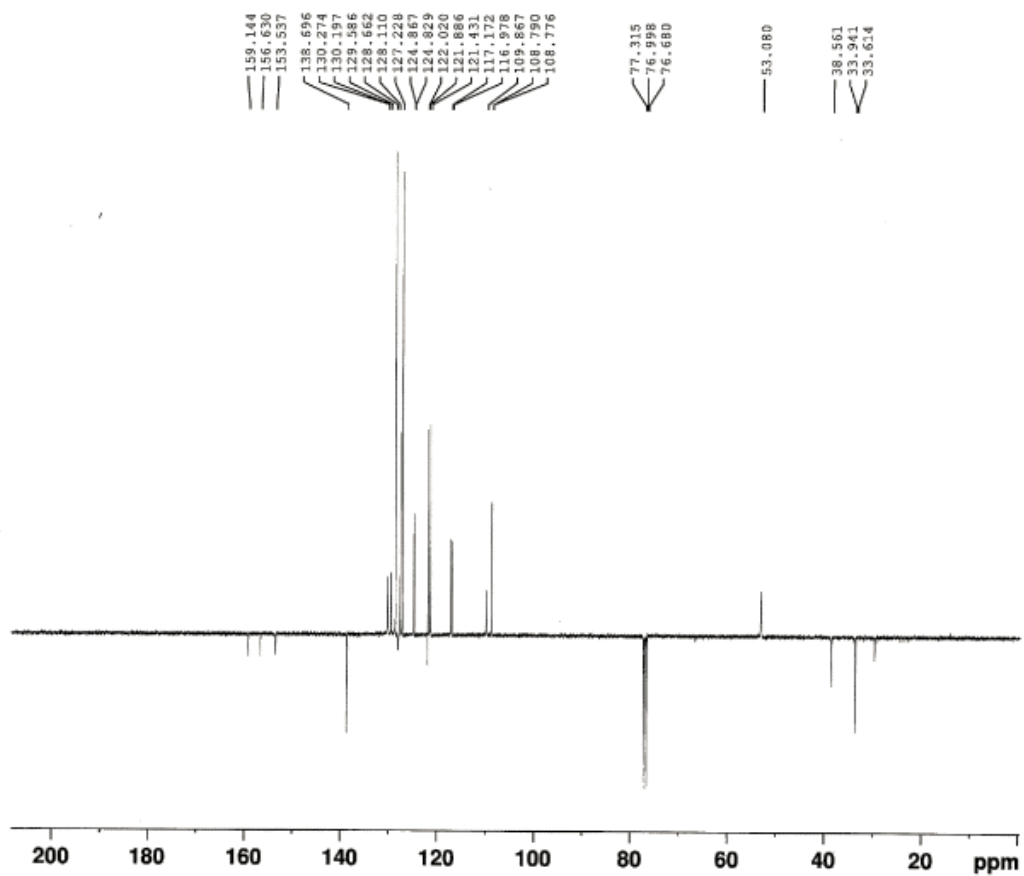
% total area								
n = 1	20 μ M				50 μ M			
t [min]	5.6 (tracer)	2.6	3.0	3.6	5.6	2.6	3.0	3.6
0	85.4	0	0	14.6	82.5	0	0	17.6
10	0.0	1.7	7.0	91.3	0.0	1.8	6.6	91.6
20	0.0	4.2	12.9	81.7	0.0	3.4	12.2	84.4
40	0.0	8.0	20.2	71.8	0.0	8.4	18.5	73.1
	100 μ M				5 μ M			
t [min]	5.6	2.6	3.0	3.6	5.6	2.6	3.0	3.6
0	86.0	0	0	14.0	69.4	0	0	30.6
10	0.0	1.0	5.6	93.4	0.0	1.6	9.3	89.2
20	0.0	0.0	9.1	90.9	0.0		16.9	93.1
40	0.0	5.7	16.5	77.9	0.0	11.3	24.1	64.6

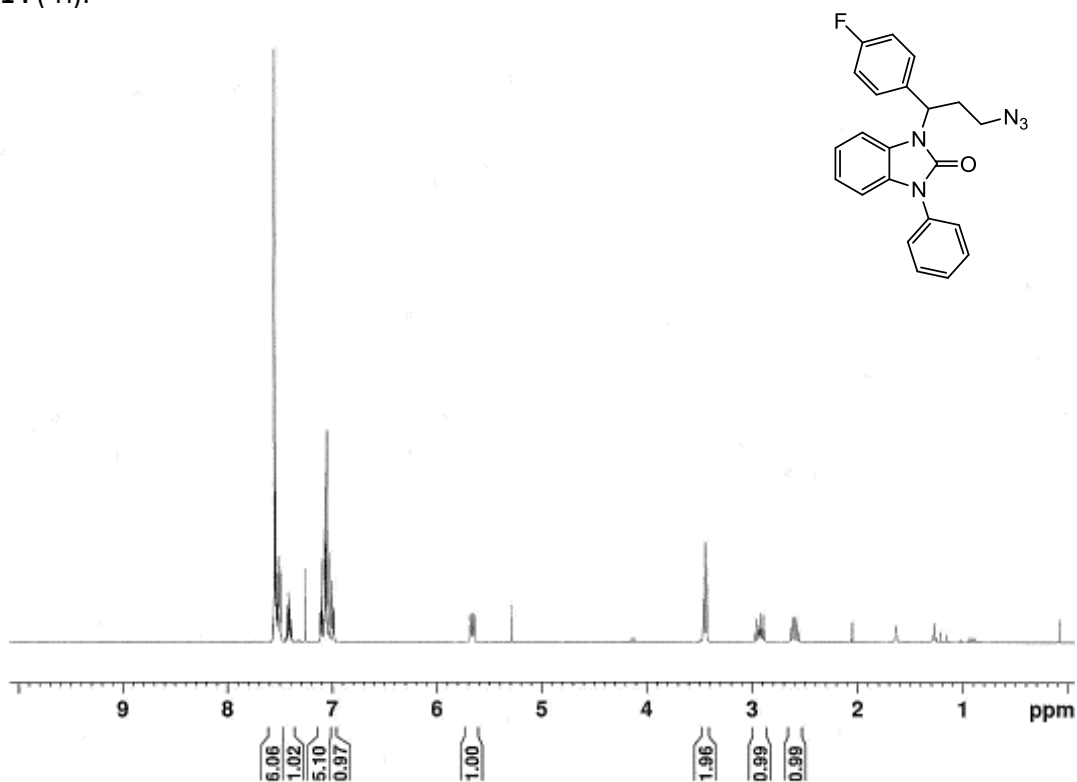
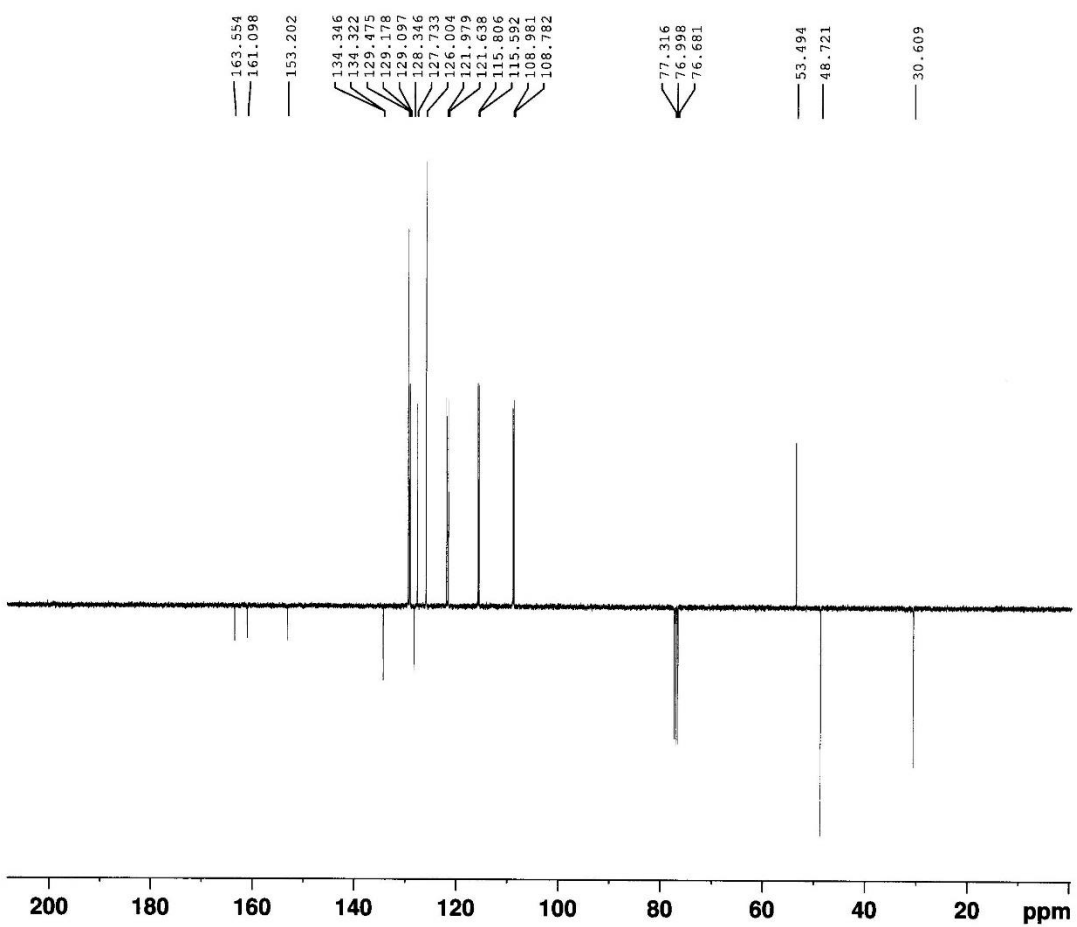
9.1.6 Complete data for bone binding experiments

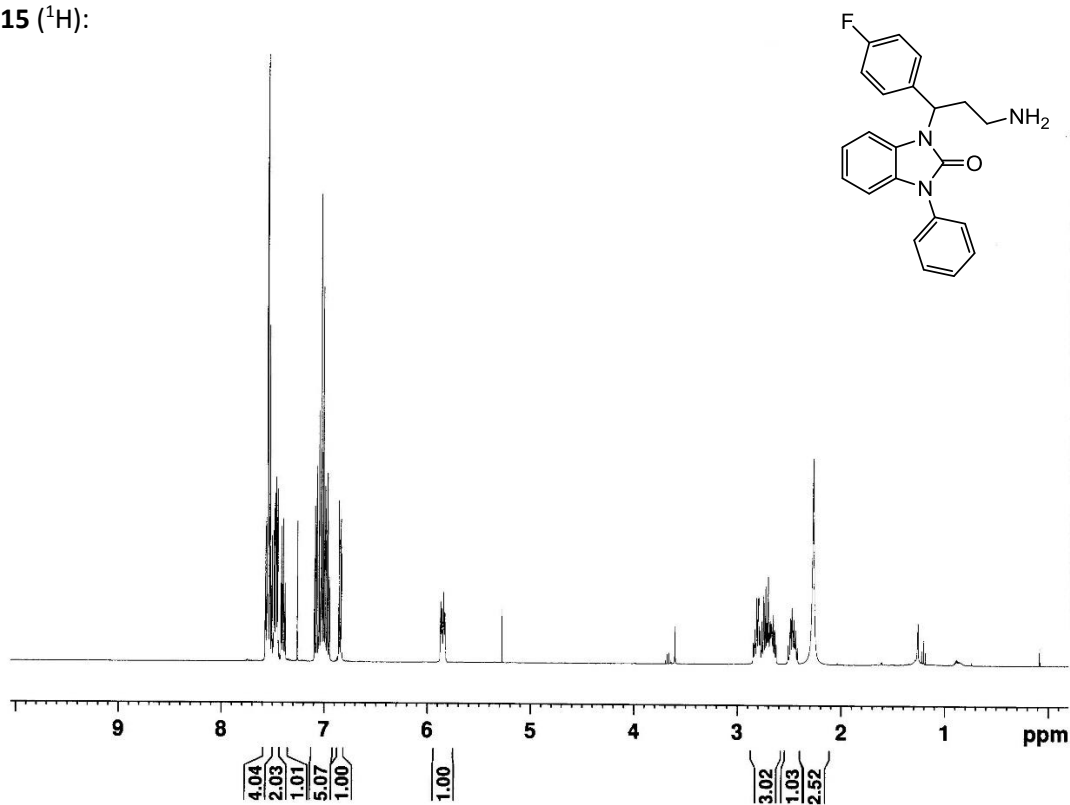
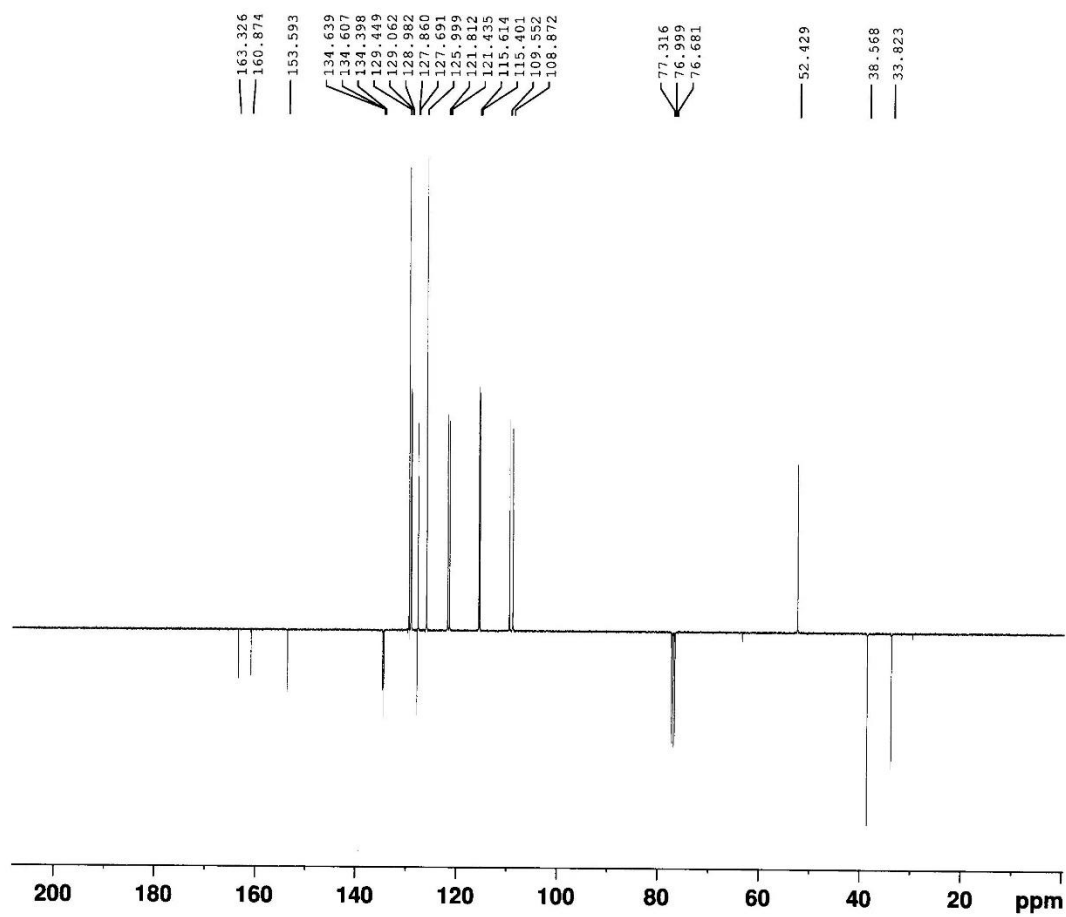
Table 58: Complete data list for bone binding experiments.

tracer		t _i [min]	% bound activity								t _i [min]	% bound activity							
			30		60		90					30		60		90			
			Mean	SD	Mean	SD	Mean	SD				Mean	SD	Mean	SD	Mean	SD		
FMeNER	hydroxyl	pellet	5.8	3.7	6.4	2.5	5.9	1.1	F-Cholin	hydroxyl	pellet	0.9	0.2	0.9	0.3	0.9	0.2		
	n = 6	sup.	88.9	4.6	87.3	4.1	88.0	2.9		n = 7	sup.	97.2	1.0	97.1	0.6	97.2	0.5		
		wash 1	4.7	2.3	4.6	3.8	5.5	2.9			wash 1	1.9	1.0	1.9	0.8	1.8	0.6		
		wash 2	0.7	0.4	1.8	2.1	0.6	0.3			wash 2	0.1	0.0	0.1	0.0	0.1	0.0		
		sum Σ	100.0	0.0	100.0	0.0	100.0	0.0			sum Σ	100.0	0.0	100.0	0.0	100.0	0.1		
		diaphysis	pellet	2.1	0.7	2.9	0.6	2.8		0.3		diaphysis	pellet	1.2	0.3	1.1	0.0	1.0	
		n = 5	sup.	91.8	0.8	91.2	0.6	90.7		0.4		n = 2 or	sup.	97.2	0.0	97.6	0.1	97.3	
		wash 1	5.5	0.3	5.1	0.1	5.6	0.4				wash 1	1.5	0.3	1.3	0.1	1.6		
		wash 2	0.6	0.2	0.7	0.1	0.9	0.2				wash 2	0.1	0.1	0.1	0.0	0.1		
		sum Σ	100.0	0.0	100.0	0.0	100.0	0.0				sum Σ	100.0	0.0	100.0	0.0	100.0		
FMeNER met.	hydroxyl	pellet	4.5	4.9					FDG	hydroxyl	pellet	1.7	0.4	1.7	0.6	1.7	0.5		
	n=3	sup.	92.0	6.9						n = 7	sup.	96.7	0.6	96.3	1.0	96.5	0.5		
		wash 1	3.0	1.5							wash 1	1.5	0.4	1.9	1.0	1.6	0.4		
		wash 2	0.5	0.6							wash 2	0.1	0.1	0.1	0.2	0.1	0.1		
		sum Σ	100.0	0.0							sum Σ	100.0	0.0	100.0	0.0	100.0	0.0		
		diaphysis	pellet	1.6	0.3							diaphysis	pellet	1.7	0.8	1.7	1.8	1.5	0.5
		n = 4	sup.	94.9	1.7							n = 5	sup.	96.8	0.9	97.0	96.7	96.8	0.8
		wash 1	3.3	1.9								wash 1	1.3	0.2	1.3	1.4	1.7	0.3	
		wash 2	0.3	0.1								wash 2	0.1	0.0	0.1	0.1	0.1	0.0	
		sum Σ	100.0	0.0								sum Σ	100.0	0.0	100.0	100.0	100.0	0.0	
APPI	hydroxyl	pellet	17.3	5.8	17.0	3.5	23.4	7.3		cortex	pellet	1.0		1.0		1.1			
	n = 2	sup.	48.8	11.8	46.9	10.7	43.9	8.8		n = 1	sup.	97.9		97.8		97.3			
		wash 1	22.5	1.4	23.2	2.4	21.6	0.2			wash 1	1.0		1.1		1.4			
		wash 2	11.5	4.6	12.9	4.8	11.1	1.3			wash 2	0.0		0.1		0.2			
		sum Σ	100.0	0.0	100.0	0.0	100.0	0.0			sum Σ	100.0		100.0		100.0			

9.1.7 NMR spectra of novel compounds

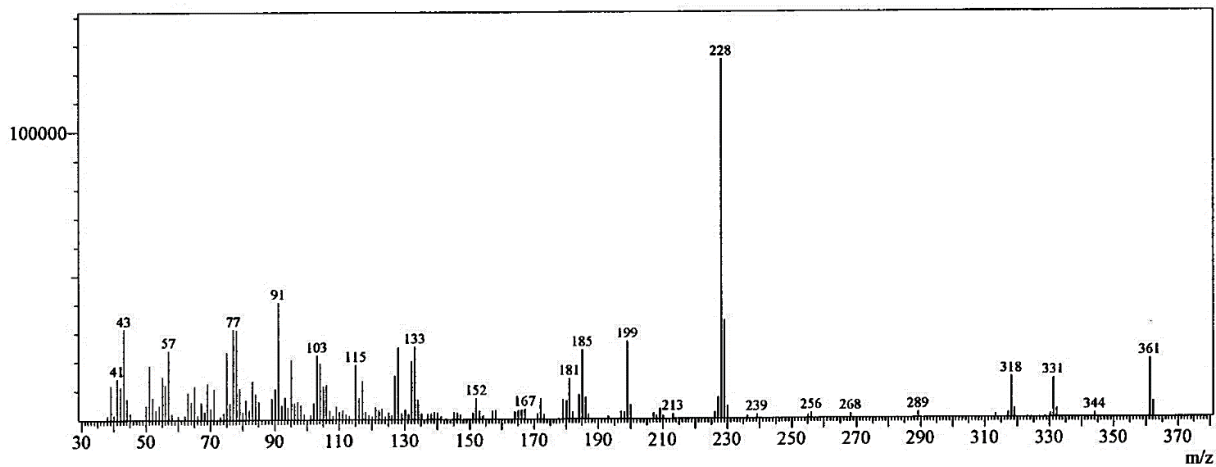
9 (^1H):9 (^{13}C):

14 (^1H):**14** (^{13}C):

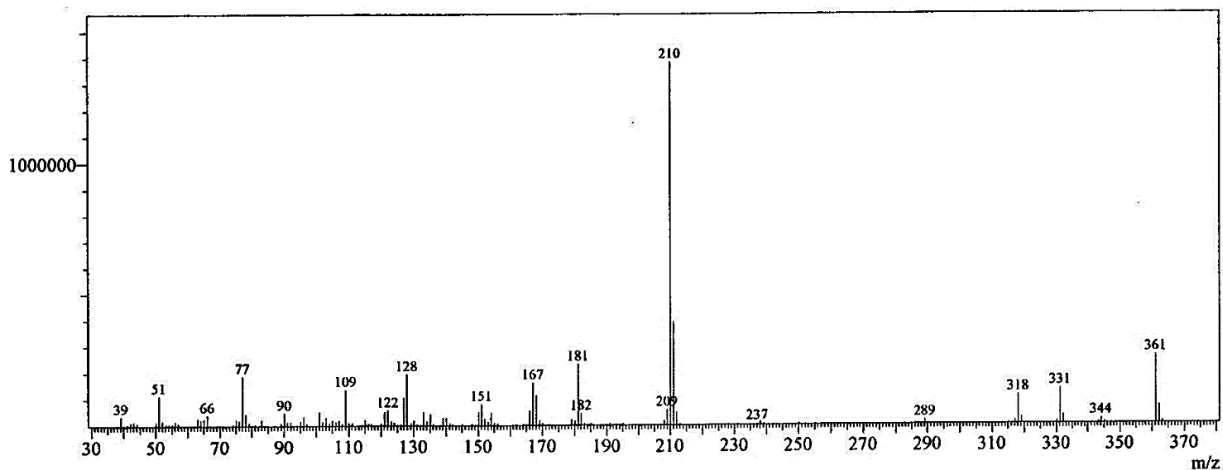
15 (^1H):15 (^{13}C):

9.1.8 EI-MS spectra

9:



15:



9.1.9 Crystallographic data of 1-(1-(4-Fluorophenyl)-3-iodopropyl)-3-phenyl-1,3-dihydro-2H-benzo[d]imidazol-2-one

Table 59: Crystallographic Data

Identification code	naeb_FAPP1_P21
Empirical formula	C ₂₂ H ₁₈ FIN ₂ O
Formula weight	472.28
Temperature/K	100.0
Crystal system	monoclinic
Space group	P2 ₁
a/Å	9.0066(4)
b/Å	8.9734(4)
c/Å	12.0549(5)
α/°	90
β/°	98.5197(13)
γ/°	90
Volume/Å ³	963.52(7)
Z	2
ρ _{calc} /cm ³	1.628
μ/mm ⁻¹	1.685
F(000)	468.0
Crystal size/mm ³	0.313 × 0.217 × 0.074
Radiation	MoKα (λ = 0.71073)
2θ range for data collection/°	4.572 to 60.146
Index ranges	-12 ≤ h ≤ 12, -12 ≤ k ≤ 12, -16 ≤ l ≤ 16
Reflections collected	51824
Independent reflections	5641 [R _{int} = 0.0248, R _{sigma} = 0.0115]
Data/restraints/parameters	5641/1/244
Goodness-of-fit on F ²	1.099
Final R indexes [I ≥ 2σ (I)]	R ₁ = 0.0169, wR ₂ = 0.0444
Final R indexes [all data]	R ₁ = 0.0170, wR ₂ = 0.0445
Largest diff. peak/hole / e Å ⁻³	0.43/-1.04
Flack parameter	-0.025(3)

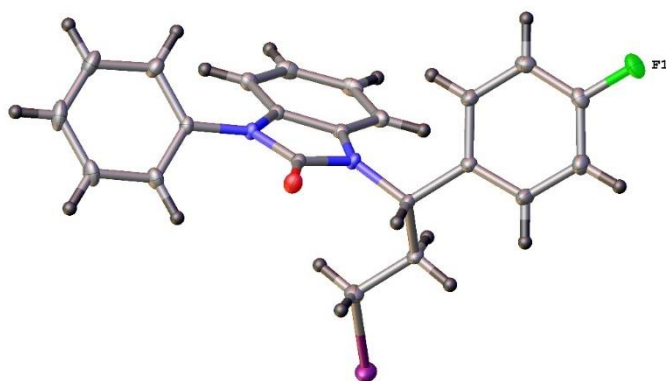


Figure 54: Crystal structure of 1-(1-(4-Fluorophenyl)-3-iodopropyl)-3-phenyl-1,3-dihydro-2H-benzo[d]imidazol-2-one.

9.2 List of abbreviations

Arg	arginine
bs	broad singlet
Bq	Bequerel
δ	chemical shift
d	doublet
CES	carboxyl esterase
CDI	carbonyldiimidazole
COMT	catechol- <i>O</i> -methyltransferase
CYP450	cytochrome P450
DCM	dichloromethane
EtOAc, EE	ethyl acetate
[¹⁸ F]FDG	2-deoxy-2-[¹⁸ F]fluoro-D-glucose
[¹⁸ F]FMN	[¹⁸ F]FMeNER-D2
IC50	half maximal inhibitory concentration
K _i	inhibition constant
K _M	Michaelis-Menten constant
m	multiplet
MAO	monoamine oxidase
MeOH	methanol
HA	hydroxyapatite
Hz	hertz
PE	petroleum ether
R _f	retardation factor
rt	room temperature
s	singlet
SD	standard deviation
TBAH	tetrabutylammonium hydroxide
TEA	triethyl amine
TEAA	triethylammonium acetate
TLC	thin layer chromatography
t _r	retention time
Trp	tryptophan

9.3 List of tables

Table 1: Important generators for nuclear medicine.	5
Table 2: Diagnostically relevant PET nuclides; CYC = cyclotron, GEN = generator.	6
Table 3: Human CYP450s in the liver responsible for drug metabolism.	14
Table 4: CYP families expressed in the brain and their exogenous substrates.	15
Table 5: List of important inhibitors and substrates for hCYP450 enzymes; the main reaction for the given substrate (probe substance) to monitor CYP isozyme activity used for the evaluation of inhibitory effects of a drug candidate is quoted in the rightmost column; K_i values (third column) for inhibitors (second column) are given.	20
Table 6: Inhibitors for RLM; cross-reactivity should be avoided in the given concentration range.	24
Table 7: Components of stock solution A (on the left) and stock solution B (on the right)	33
Table 8: Microsomal incubation batch.	33
Table 9: Chemical inhibitors for CYP450 isozymes.	34
Table 10: HLM Inhibition assay.	36
Table 11: RLM inhibition assays.	36
Table 12: CYP1A1 batch, 300 μ L.	37
Table 13: CYP1B1 batches, 300 μ L (left) and 1000 μ L (right).	37
Table 14: CYP2A6 batch, 500 μ L.	37
Table 15: CYP2C19 batch, 300 μ L.	38
Table 16: CYP2D6 batches, 1000 μ L (left) and 300 μ L (right).	38
Table 17: CYP2E1 batches, 500 μ L (left) and 300 μ L (right).	38
Table 18: CYP3A4 batches, 500 μ L (left) and 300 μ L (right).	39
Table 19: MAO A/B incubation mixtures, 1000 μ L (left) and 250 μ L (right) batch.	39
Table 20: Resulting concentrations for COMT assays.	40
Table 21: Stock solutions for COMT incubation assays.	40
Table 22: Preparation of COMT incubations using stock solutions given above (Table 21).	40
Table 23: hCES batch, 300 μ L.	41
Table 24: porcine CE-batch, 500 μ L.	41
Table 25: Radioactive tracers tested for their binding properties to bone or hydroxyapatite as its inorganic mineral.	42
Table 26: Preparation of [18 F]FMeNER-D2; Yields and loss of radioactivity between reaction steps and required time (MEAN \pm SD); R1 = reactor 1, R2 = reactor 2, TW-waste = target water waste.	45
Table 27: List showing all FMN syntheses and special modifications in the procedures.	46
Table 28: Data for Figure 13.	47
Table 29: Data for Figure 15.	48
Table 30: Data for Figure 17.	50
Table 31: Data table for Figure 22; Standard deviations (SD) are given for experiments, which were carried out more than once.	54
Table 32: Data table for Figure 23.	55
Table 33: Averaged data for Figure 29 including standard deviations.	59
Table 34: Data list for Figure 30.	59
Table 35: Data table for RLM inhibition via quinidine gives MEAN (\pm SD).	60
Table 36: Data list for Figure 32.	61
Table 37: Data set for Figure 33.	62
Table 38: Overview on inhibition experiments in HLM and RLM.	63
Table 39: Degradation via CYP2D6, 1000 μ L batch.	66
Table 40: Radioactive signals listed for all experiments where degradation was observed (MEAN(\pm SD)); main signals are highlighted in bold.	69
Table 41: Overview on large scale syntheses performed for Me@FAPPI1 and Me@FAPPI3 using different chromatographic systems; overall yield for Me@FAPPI1 given below is less than the real turnover as not the whole product peak was collected.	100
Table 42: Batch-#1.	114
Table 43: Batch-#2.	114
Table 44: Batch-#3.	114
Table 45: Batch-#4.	115
Table 46: Batch-#5.	115
Table 47: Batch-#6.	115
Table 48: Batch-#7.	116

Table 49: Batch-#8.....	116
Table 50: Batch-#9.....	116
Table 51: Full dataset for HLM incubations in PB.....	117
Table 52: Full dataset for RLM in PBS.....	117
Table 53: Overview of all metabolism studies.....	119
Table 54: Sulfaphenazole in RLM incubations.....	121
Table 55: Montelukast in RLM incubations.....	121
Table 56: 4-Methylpyrazole.HCl in RLM incubations.....	122
Table 57: Furfurylline in RLM incubations.....	122
Table 58: Complete data list for bone binding experiments.....	123
Table 59: Crystallographic Data.....	129

9.4 List of figures

Figure 1:	Schematic representation of NET with its 12 transmembrane segments (shown as numbered rectangles): C- and N-terminus are located on the cytoplasmic side of the plasma membrane, glycosylation sites were found on the largest loop between helix 3 and 4. ^[20, 21]	7
Figure 2:	Schematic figure showing norepinephrine homeostasis: biosynthesis, release, reuptake and metabolism. Legend: COMT = catechol-O-methyl transferase, DA = dopamine, DBH = dopamine β -hydroxylase, DD = DOPA decarboxylase, DOPA = 3,4,-dihydroxyphenylalanine, MAO = monoamine oxidase, MHPG = 3-methoxy-4-hydroxyphenylglycol, NE = norepinephrine, NET = norepinephrine transporter, TH = tyroxine hydroxylase. ^[22]	8
Figure 3:	PET images of [¹⁸ F]FMeNER-D2: a. transaxial (left), coronal (upper right) and sagittal (lower right) images in a healthy volunteer ^[31] ; b. PET-MR images in a healthy subject, white crosses display the thalamus (upper row) and the LC (lower row) ^[32] ; both PET scans indicate extensively high uptake in extra-cerebral tissue such as cranial bone and nasal mucosa.	9
Figure 4:	Diagnostically and therapeutically active ligands for norepinephrine transporter (NET): (a) (S,S)-[¹⁸ F]FMeNER-D2, (b) (S,S)-[¹¹ C]MeNER, (c) reboxetine, (d) atomoxetine; c) and d) are clinically approved therapeutics used for the treatment of depression and ADHD, respectively. Novel tracers for NET are listed in the bottom row: Me@APPI (e) and Me@HAPTHI (f).....	10
Figure 5:	Overview of clearance mechanisms for the top 200 drugs in the US in 2002 ^[41] : UGT, UDP-glucuronosyltransferase; FMO, flavin monooxygenase; NAT, N-acetyltransferase; MAO, monoamine oxidase.	12
Figure 6:	Cytochrome P450 catalytic cycle.....	13
Figure 7:	Fractions of CYP450 subfamilies responsible for the metabolism of cytochrome P450 substrates.	14
Figure 8:	Reaction catalyzed by MAO.....	16
Figure 9:	NADPH regeneration converting glucose 6-phosphate into 6-phosphogluconate.....	19
Figure 10:	Synthesis steps for preparation of [¹⁸ F]FMeNER-D2.	29
Figure 11:	Process flow chart of [¹⁸ F]FMeNER-D2 synthesis.	30
Figure 12:	Exemplary preparative (left) and analytical (right) HPLC chromatograms of [¹⁸ F]FMeNER-D2 (FMN-# 121)..	45
Figure 13:	Boxplots showing degradation of radiotracer [¹⁸ F]FMeNER-D2 in HLM within 2 h; based on data from Table 28; statistically corrected for outliers (see appendix, chapter 9.1.2).	47
Figure 14:	Individual series of measurements (n = 9) which were averaged in Figure 13.....	47
Figure 15:	Shows higher stability of [¹⁸ F]FMeNER-D2 in PBS than in PB according to data from Table 29.	48
Figure 16:	Analytical HPLC chromatograms showing radiosignals of metabolites and intact [¹⁸ F]FMeNER-D2 (t _r = 5 min) in HLM incubations after 60 min with different tracer concentrations.	49
Figure 17:	Boxplots showing degradation of radiotracer [¹⁸ F]FMeNER-D2 in RLM within 20 min; based on data from Table 30; statistically corrected for outliers (see appendix, chapter 9.1.2).	50
Figure 18:	Individual datapoints of all series of measurements, which were averaged in Figure 17.	50
Figure 19:	Effect of preincubation; n = 1.	51
Figure 20:	Supernatant of different RLM incubations showing up to three radioactive signals besides the tracer signal (t _r = 5 min).....	52
Figure 21:	Inhibition of HLM metabolism of [¹⁸ F]FMeNER-D2 via ketoconazole; (a) 20, 50, 100 μ M inhibitor in PB, (b) 20, 50, 100 μ M inhibitor in PBS, (c) 2, 5, 10 μ M inhibitor in PB; n = 1.	53
Figure 22:	Inhibition of HLM activity with quinidine in a concentration range of 0.4 - 20 μ M.	54
Figure 23:	Inhibitor (+)-N-3-benzyl Nirvanol tested for its effect in HLM incubations of [¹⁸ F]FMeNER-D2; 20, 50, 100 μ M in PB; n = 2.	55
Figure 24:	Ticlopidine.HCl inhibits metabolism of [¹⁸ F]FMeNER-D2 in HLM; a) 50, 100, 200 μ M in PB; b) 10, 50, 100 μ M in PBS.	56
Figure 25:	10, 20, 50 μ M incubations with inhibitor PPP in HLM, n = 1.	56
Figure 26:	Selective CYP2C9 inhibitor sulfaphenazole used in 3 different concentrations in HLM incubations; 10, 20, 50 μ M in PBS; n = 1.....	57
Figure 27:	CYP450 inhibitor Montelukast sodium was tested for impairment of [¹⁸ F]FMeNER-D2 degradation; 10, 50, 100 μ M in PB; n = 1.....	57
Figure 28:	Involvement of 4-methylpyrazole.HCl in the metabolic stability of [¹⁸ F]FMeNER-D2; 5, 10, 20 μ M batches in PB were investigated; n = 1.	58
Figure 29:	Stability of [¹⁸ F]FMeNER-D2 in HLM incubations spiked with three different concentrations of furafylline; 20, 50, 100 μ M in PB; n = 2.....	58
Figure 30:	Inhibition of RLM enzymatic activity via ketoconazole; a) 2, 5, 10 μ M in PB, n = 3, b) 20, 50, 100 μ M in PBS, n=1.....	59

Figure 31: Inhibition via (+)-N-3-benzylrivanol in RLM, a) 20, 50, 100 μ M in PBS; 0.04 μ M DMSO, n = 1, b) 20, 50, 100 μ M, 0.14 μ M DMSO in PB, n = 1.....	60
Figure 32: Evaluation of the effect of ticlopidine on RLM breakdown of [18 F]FMeNER-D2; 10, 50, 100 μ M in PBS; n = 2.	61
Figure 33: Inhibition of microsomal degradation of [18 F]FMeNER-D2 via PPP in RLM; 10, 20, 50 μ M in PBS; n = 2.	62
Figure 34: Time-dependent cleavage of [18 F]FMeNER-D2 via CYP3A4; (MEAN \pm SD); n = 4.	65
Figure 35: Exemplary chromatogram of CYP3A4 incubation showing the resulting radiosignals of metabolites after 60 min.	65
Figure 36: Full depletion of NET-ligand [18 F]FMeNER-D2 via the CYP2D6 isoform using 1000 μ L batch; (MEAN \pm SD)...	66
Figure 37: HPLC chromatogram showing enzymatic breakdown with CYP2D6 after 45 min incubation time, 1000 μ L batch (t_r (FMN) = 6 min, t_r (metabolite) = 4 min).	66
Figure 38: In-vitro depletion of intact [18 F]FMeNER-D2 via CYP2C19; (MEAN \pm SD); n = 5.	67
Figure 39: RP-chromatography reveals one major metabolite (t_r = 4.5 min) formed in enzymatic decomposition of [18 F]FMeNER-D2 (t_r = 6 min) with CYP2C19; after 15 min of incubation time.....	67
Figure 40: CYP2D6 inhibition via quinidine (1 μ M) in the presence of [18 F]FMeNER-D2 versus control.....	68
Figure 41: Effect of single enzyme CYP3A4 inhibition on tracer degradation; 1 μ M ketoconazole versus control without inhibitor.	69
Figure 42: Overview on bone binding studies using the same amount (3 mg) of hydroxy apatite (HA), diaphysis (DIA) or corticalis (C), FMeNER met. stands for radiometabolites taken from RLM incubations; the complete data table is given in the appendix (see Table 58).	71
Figure 43: Reagents and Conditions: (i) KF, K ₂ CO ₃ , 180°C, 2 d, (1, 23%); (ii) CH ₂ Cl ₂ , DMF, Ar, Zn, 2 h: 0°C to rt (2, 97%); (iii) CDI, DMF, Ar, reflux, 2 h (3, 75%); (iv) EtOH/THFdry, NaBH ₄ , -10°C to rt, 3 - 4 h [(4, 92%), (10, 98%)]; (v) HBr (47%), rt, 3h (5, 95%), 18 h (11, 93%); (vi) K ₂ CO ₃ , DMF, rt, 24 h (6, 68%), 7 h or 24 h (12, 17%); (vii) NaI, acetone _{dry} , reflux, 18 - 20 h [(7, 52%), (13, 89%)]; (viii) NaN ₃ , DMF, 75%, 12 h [(8, 60%), (14, 98%)]; (ix) (1) PPh ₃ , THF, rt, 8-10 h; (2) H ₂ O, 12 - 16 h [(9, 57%), (15, 85%)].	75
Figure 44: Radiosynthesis of [11 C]Me@FAPPI derivatives.	91
Figure 45: Production flow chart of [11 C]Me@FAPPI synthesis.	92
Figure 46: Synthesis of 9 and 15 with ammonia solutions: both precursors cannot be obtained under the abovementioned conditions due to no conversion (1) and the formation of numerous side products (2 + 3); synthesis route (4) was able to give the pure precursors.	96
Figure 47: Influence of reaction time and temperature on radiochemical yield using different bases (NaOH, TEA and TBAH) in 2-butanone (n = 1).....	97
Figure 48: Dependence of radiochemical incorporation yield of the tracer [11 C]Me@FAPPI3 for the shown reaction conditions (n = 1).	98
Figure 49: Semi-preparative (a.) and corresponding analytical (b.) HPLC chromatograms for both [11 C]Me@FAPPI3 syntheses: best separation was achieved via analytical separation showing retention times of 5.45 min for the precursor FAPPI3:0 (UV-channel) and 6.97 min.	101
Figure 50: HPLC chromatograms of first [11 C]Me@FAPPI1 synthesis showing insufficient resolution. Analytical HPLC of the product peak shows very similar retention times of precursor (5.62 min) and tracer (7.25 min) compared to their analogues FAPPI3:0 and Me@FAPPI3.....	101
Figure 51: Boxplot of HLM incubations in PB, not corrected for outliers.....	117
Figure 52: Boxplot of RLM incubations in PBS, not corrected for outliers.	117
Figure 53: Crude [18 F]FMeNER-D2 after injection onto analytical HPLC.....	118
Figure 54: Crystal structure of 1-(1-(4-Fluorophenyl)-3-iodopropyl)-3-phenyl-1,3-dihydro-2H-benzo[d]imidazol-2-one.	129

9.5 Curriculum vitae

Personal Data

Name: Nadine Yvonne Eberherr, B.Sc.
 Date of birth: 4. Mai 1990
 Nationality: Austria
 E-mail: nadine.eberherr@outlook.com

Education

10/2014 – 09/2015 Master thesis at the at the Department of Biomedical Imaging and Image-Guided Therapy, Division of Nuclear Medicine, Medical University of Vienna.

10/2012 – to date Study of Medicine at the Medical University of Vienna

01/2012-10/2014 Master program Chemistry, University of Vienna

10/2008 – 01/2012 Bachelor program Chemistry, University of Vienna; *Title of Bachelor Thesis: "Synthesis and characterization of Copper(II) complexes with new Indolo[3,2-c]quinoline-based ligands"*

09/2000 – 07/2008 Secondary School: Bundesgymnasium Braunau am Inn

09/1996– 07/2000 Elementary School: Volksschule in Geretsberg

Experience

08 – 09/2014 Student employee at Vinnolit GmbH & Co. KG, Gendorf, Germany; Process control monomer

07 – 09/2013 Student employee at Vinnolit GmbH & Co. KG, Gendorf, Germany; Process control monomer

03 – 06/2012 Tutor in undergraduate lab courses at the Institute of Organic Chemistry, University of Vienna

10/2012 – 01/2013 Tutor in undergraduate lab courses at the Institute of Organic Chemistry, University of Vienna

09/2011

Research scholarship at the Institute of Inorganic Chemistry,
University of Vienna**Personal Skills**

IT-Skills MS Office, basic knowledge of SPSS

Languages German: mother tongue

English: fluent, spoken and written

French: basic knowledge

Publications

Primik, M.F.; Göschl, S; Meier, S.M.; Eberherr, N; Jakupec, M.A.; Enyedy, É; Novitchi, G; Arion, V.B., *Dicopper(II) and dizinc(II) complexes with nonsymmetric dinucleating ligands based on indolo[3,2-c]quinolines: synthesis, structure, cytotoxicity, and intracellular distribution*. Inorg Chem, 2013. **52**(17): p. 10137-46.